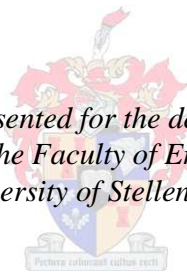


Perimeter Fan Performance in Forced Draught Air-cooled Steam Condensers

by
Sybrand Johannes van der Spuy

*Dissertation presented for the degree of Doctor of
Philosophy in the Faculty of Engineering at the
University of Stellenbosch*



Promoters:
Prof T.W. von Backström
Prof. D.G. Kröger
Faculty of Engineering
Department of Mechanical and Mechatronic Engineering

December 2011

DECLARATION

By submitting this dissertation electronically, I declare that the entirety of the work contained therein is my own, original work, that I am the sole author thereof (save to the extent explicitly otherwise stated), that reproduction and publication thereof by Stellenbosch University will not infringe any third party rights and that I have not previously in its entirety or in part submitted it for obtaining any qualification.

December 2011.

Copyright © 2011 Stellenbosch University

All rights reserved

ABSTRACT

Axial flow fan arrays form part of air-cooled steam condensers in direct dry-cooled power plants. This dissertation investigates the performance of axial flow fans when located at the perimeter of a fan array. The perimeter (or edge) fans may experience a reduction in air flow through the fan due to the prevalence of distorted inlet conditions upstream of the fan. The reduction in air flow leads to a reduction in the heat transfer capability of the steam condenser and a consequent reduction in the electricity output of the power plant.

Due to the physical size of an air-cooled condenser, full-scale experiments are often impractical and computational fluid dynamics (CFD) is used to model its performance under various conditions. To limit the size of the CFD model the axial flow fans in the CFD analysis are represented by means of simplified methods. Three different simplified methods are presented and applied to a CFD model of a single axial flow fan, namely the pressure jump method (PJM), actuator disc method (ADM) and extended actuator disc method (EADM). The results are compared to experimental values. The comparison highlights the limitations of the models: The ADM fails to model fan performance correctly at low flow rates, while the PJM ignores the variation in fan blade properties at different locations within the fan rotor. The EADM is presented as an improvement on both the other two models.

A multiple fan test facility is constructed, consisting of three 630 mm diameter fans extracting air from a common inlet chamber. The inlet chamber is constructed in such a way that one of the three fans act as the perimeter (edge) fan. The floor of the inlet chamber can be adjusted to increase or reduce the inlet flow distortion experienced by the edge fan. Six different fan configurations are tested in the position of the edge fan and an empirical method is derived by which the volumetric effectiveness of an edge fan can be predicted. The experimental results are compared to CFD results for the same facility using the three different simplified simulation methods investigated previously. Particle image velocimetry (PIV) measurements are also performed upstream of the edge fan and the velocity profiles at the inlet of the fan are compared to the profiles obtained numerically. The comparisons show that the EADM predicts the performance of the edge fan more accurately than the ADM en PJM.

The effect of adding a walkway and removing the bell mouth upstream of the edge fan was investigated using the EADM. The results are used to show the location of the loss mechanisms upstream of the edge fan. The addition of a walkway moves the location of the pressure loss away from the edge fan bell mouth towards the edge of the walkway. Consequently the distortion directly upstream of the edge fan is reduced and its volumetric effectiveness increased. The effect of removing the edge fan's bell mouth is similar to the effect of adding a walkway upstream of the edge fan.

OPSOMMING

Aksiaalwaaiermatrikse vorm deel van lugverkoelde kondensors in direk droë-verkoelde kragstasies. Hierdie verhandeling ondersoek die werkverrigting van aksiaalwaaiers wat geleë is op die rand van 'n groot waaiermatriks. Die randwaaiers kan 'n vermindering in deurvloei ondervind as gevolg van versteurde inlaattoestande stroom-op vanaf die waaier. Die vermindering in lugvloei lei tot 'n vermindering in die warmetoordagvermoë van die stoomkondensor en 'n gepaardgaande afname in die elektrisiteitslewering van die kragstasie.

As gevolg van die fisiese grootte van die lugverkoelde kondensor is volskaalse eksperimente gewoonlik onprakties en word berekeningsvloeimeganika (BVM) gebruik om die werking van die aanleg onder verskeie toestande te modelleer. Ten einde die grootte van die BVM model te beperk, word die aksiaalwaaiers in so 'n BVM analiese voorgestel met behulp van vereenvoudigde metodes. Drie verskillende vereenvoudigde metodes word aangebied en toegepas op 'n BVM model van 'n enkelwaaier, naamlik die druksprongmetode, die aksieskyfmetode en die verlengde aksieskyfmetode. Die resultate word vergelyk met eksperimentele waardes. Die vergelyking benadruk die beperkings van die modelle: Die aksieskyfmetode kan nie die werking van die waaier akkuraat voorspel by lae vloeië nie en die druksprongmetode ignoreer die variasie in lemeienskappe op verskillende liggings binne-in die waaierrotor. Die verlengde aksieskyfmetode word voorgestel as 'n verbetering op die ander twee metodes.

'n Veelvuldige waaiertoetsfasiliteit is saamgestel, bestaande uit drie 630 mm deursnee waaiers wat lug uit 'n gemeenskaplike inlaatkamer suig. Die inlaatkamer is so saamgestel dat een van die waaiers in die fasiliteit 'n randwaaier verteenwoordig. Die vloerhoogte van die inlaatkamer kan aangepas word om die inlaatversteuring wat deur die raandwaaier ondervind word te vermeerder of te verminder. Ses verskillende waaierkonfigurasies is getoets in die randwaaierposisie. 'n Empiriese metode waarmee die volumetriese effektiwiteit van 'n randwaaier voorspel kan word is afgelei. Die eksperimentele resultate word vergelyk met ooreenstemmende BVM resultate vir dieselfde fasiliteit deur gebruik te maak van die drie verskillende vereenvoudigde metodes wat vroeër ondersoek is. Partikelbeeld snelheidsmetings word ook stroom-op vanaf die randwaaier uitgevoer en die snelheidsprofiële by die inlaat van die waaier word vergelyk met profiële wat numeries bereken word. Die vergelykings wys dat die verlengde aksieskyfmetode die werkverrigting van 'n aksiaalwaaier meer akkuraat voorspel as die aksieskyf- of druksprongmetodes.

Die effek van die installering van 'n loopvlak en die verwydering van die randwaaier se inlaatmondstuk word ondersoek met behulp van BVM deur gebruik te maak van die verlengde aksieskyfmetode. Die resultate word spesifiek gebruik om die ligging van die verliesmeganismes stroom-op vanaf die randwaaier aan te dui. Die resultate wys dat die installering van 'n loopvlak die ligging van die drukverlies wegneem vanaf die rand van die waaierinlaat na die rand van die loopvlak. Dit verminder die inlaatversteuring stroom-op vanaf die randwaaier en

die volumetriese effektiwiteit word verhoog. Die verwydering van die randwaaier se inlaatmondstuk het 'n soortgelyke effek as die installering van 'n loopvlak stroom-op vanaf die randwaaier.

Aan Elana, dankie.

ACKNOWLEDGEMENTS

The following people and entities are acknowledged for their contribution towards this thesis:

- My supervisors, Professors von Backström and Kröger, for sharing their time, patience and wisdom.
- The family – my wife and three children, my parents, brothers, sisters, the whole lot. Thanks for not asking every time I saw you.
- The personnel from the Mechanical and Mechatronic Workshop: Cobus, Ferdi, Anton, Graham, Calvin, Nathi, Julian and Clive for doing the impossible yesterday.
- My colleagues: Thomas, Hanno, Chris, Richard and the late Gerrie, for sharing the workload.
- Marilie, for proofreading the thesis report at such short notice.
- Eugene, for assisting with the PIV tests.
- My students, both under- and postgraduate who assisted with various investigations related to this thesis.
- The National Research Foundation (NRF) of South Africa, for providing funding for the project.
- Eskom TESP, for providing funding for the project.
- Stellenbosch University, for providing the facilities, infrastructure as well as funding for the project.
- The high performance cluster (HPC) at Stellenbosch University was used for all computer simulations.
- Laastens, aan die Here, wat ons al die talente en geleenthede gee, al gebruik ons net so 'n klein fraksie daarvan.

TABLE OF CONTENTS

LIST OF FIGURES xiii

LIST OF TABLESxxiv

NOMENCLATURE.....xxvi

ACRONYMS.....xxxi

1 INTRODUCTION1

1.1 Background 1

1.2 Air-cooled heat exchangers and ACCs4

1.3 Axial flow fans.....5

1.3.1 Velocity triangles5

1.3.2 Isolated airfoil theory6

1.3.3 An air-cooled condenser fan system8

1.3.4 The layout of an axial flow fan8

1.4 Objectives10

1.5 Methodology11

1.6 Summary12

2 LITERATURE REVIEW13

2.1 Introduction.....13

2.2 Axial flow fans and their application in air-cooled condensers.....13

2.3 Axial flow fan testing for air-cooled condensers.....16

2.4 Simulation of axial flow fans in air-cooled condensers.....19

2.4.1 The actuator disc method20

2.4.2 The pressure jump method22

2.4.3 The extended actuator disc method.....23

2.5 Summary24

3 AXIAL FLOW FAN EXPERIMENTS25

3.1 Introduction.....25

3.2 Facilities.....27

3.2.1 Standard axial flow fan test facilities27

3.2.2 Multiple axial flow fan test facility28

3.3 Description of Experiments29

3.3.1 Individual fan performance tests29

3.3.2 Multiple fan performance tests.....30

3.3.3 Detailed flow field measurements.....30

3.4 Results and discussion32

3.4.1 Individual fan performance32

3.4.2 Multiple fan performance.....35

3.4.3	Detailed edge fan inlet flow field.....	42
3.5	Summary	46
3.5.1	Overall individual fan characteristics.....	46
3.5.2	Multiple fan performance.....	46
3.5.3	Edge fan inlet flow field.....	47
4	AXIAL FAN MODELS FOR ACCs.....	48
4.1	Introduction.....	48
4.2	The actuator disc method (ADM) applied to individual fans	49
4.2.1	Geometry and mesh.....	50
4.2.2	Boundary and cell zone conditions	57
4.2.3	Simulation	58
4.3	The pressure jump method (PJM) applied to individual fans.....	59
4.3.1	Geometry and mesh.....	59
4.3.2	Boundary and cell zone conditions	60
4.3.3	Simulation	62
4.4	The extended actuator disc method (EADM) applied to individual fans	62
4.5	Results and discussion for individual axial flow fans.....	64
4.6	The simulation of multiple axial flow fans.....	67
4.6.1	Geometry and mesh.....	67
4.6.2	Boundary and cell zone conditions	69
4.6.3	Simulation	71
4.7	Multiple fan simulation results and discussion.....	71
4.7.1	N_N_N multiple fan facility simulations.....	71
4.7.2	Results for B_N_N multiple fan facility simulations.....	81
4.7.3	Results for H10_N_N multiple fan facility simulations	89
4.8	Summary	98
4.8.1	Single fan simulations	98
4.8.2	Multiple fan simulations	98
4.8.3	Advantages and disadvantages of simplified fan models	101
5	APPLICATION OF THE EXTENDED ACTUATOR DISC METHOD TO ACCs.....	103
5.1	Introduction.....	103
5.2	Edge fan installation with bell mouth and no walkway – results and discussion	103
5.3	The effect of a walkway on the performance of multiple axial flow fans	109
5.3.1	CFD model for edge fan investigation with walkway	110
5.3.2	Results and discussion for walkway investigation.....	111
5.4	The performance of an edge fan with no bell mouth inlet.....	118
5.4.1	Results and discussion for inlet section investigation.....	119
5.5	Comparison of pressure plots for different inlet configurations.....	125

5.6	Summary	130
6	CONCLUSIONS AND RECOMMENDATIONS	132
6.1	Conclusions.....	132
6.1.1	The effect of fan configuration on edge fan performance.....	132
6.1.2	The use of simplified numerical models to simulate edge fan performance.....	134
6.1.3	The format of the inlet flow field of an edge fan	136
6.1.4	A guideline for improved edge fan performance	137
6.2	Recommendations for future work	138
6.3	Summary.....	138
	REFERENCES.....	140
	APPENDIX A: AXIAL FLOW FANS	147
A.1.	Individual fans	147
A.1.1.	B-fan.....	147
A.1.2.	V-fan	148
A.2.	Multiple fans	150
A.2.1.	H-fan	150
A.2.2.	N-fan	152
A.2.3.	630 mm diameter B-fan	153
	APPENDIX B: THE ACTUATOR DISC METHOD.....	154
B.1.	Introduction.....	154
B.2.	Application of the actuator disc method to calculate fan performance curves	156
B.2.1.	Basic method	156
B.2.2.	Geometry	159
B.2.3.	Mesh.....	161
B.2.4.	Boundary conditions	163
B.2.5.	Turbulence modelling	164
B.2.6.	Discretization model	167
B.2.7.	Results	169
B.3.	Modelling 3-dimensional effects in actuator discs	173
B.3.1.	Coriolis force.....	175
B.3.2.	Blade cross-flow.....	175
B.3.3.	Rotational augmentation of aerodynamic loads	178
B.3.4.	Integration of rotational augmentation into the actuator disc method	181
B.3.5.	Results for extended actuator disc method (EADM)	183
B.4.	Summary.....	184

APPENDIX C: MODELLING 2D AIRFOIL PROFILES187

C.1.	Introduction.....	187
C.2.	Standard CFD analysis.....	189
C.2.1.	Airfoil profile	189
C.2.2.	Solver	189
C.2.3.	Geometry and mesh.....	190
C.2.4.	Boundary conditions	191
C.3.	Low Reynolds number analyses	191
C.3.1.	Xfoil solver.....	191
C.3.2.	Transitional CFD-modelling.....	193
C.4.	Results.....	194
C.4.1.	Verification of CFD model	194
C.4.2.	Blade profile modelling.....	196
C.5.	Discussion.....	199
C.5.1.	Verification results	199
C.5.2.	Blade profile results	199
C.6.	Summary.....	200

APPENDIX D: THE PRESSURE JUMP METHOD.....201

D.1.	Introduction.....	201
D.2.	Application of the Pressure Jump Model to calculate fan performance curves	202
D.2.1.	Description	202
D.2.2.	Geometry.....	206
D.2.3.	Boundary conditions	206
D.2.4.	Solver settings	206
D.2.5.	Results	206
D.3.	Summary.....	207

APPENDIX E: MULTIPLE FAN TEST FACILITY208

E.1.	Facility configuration.....	208
E.1.1.	Layout	208
E.1.2.	Instrumentation	211
E.1.3.	Calibration.....	212
E.2.	Fan testing.....	213
E.2.1.	Individual fan performance calculations.....	214
E.2.2.	Individual fan performance curves.....	217
E.2.3.	Multiple fan performance curves	218
E.3.	Particle image velocimetry (PIV)	221
E.3.1.	PIV test equipment.....	221
E.3.2.	PIV test lay-out	223
E.3.3.	Preliminary PIV test results	227
E.3.4.	Hot-film measurement comparison with PIV test results	228

APPENDIX F: EXPERIMENTAL RESULTS	232
F.1. Individual fans	232
F.1.1. N-fan	232
F.1.2. 630 mm diameter B-fan	234
F.1.3. H5-fan	236
F.1.4. H10-fan	238
F.1.5. H7-fan	240
F.1.6. H14-fan	242
F.2. Multiple fans	244
F.2.1. N_N_N configuration.....	244
F.2.2. B_N_N configuration.....	246
F.2.3. H10_N_N configuration.....	249
F.3. PIV data for multiple fans.....	252
F.3.1. N_N_N configuration.....	252
F.3.2. B_N_N configuration.....	253
F.3.3. H10_N_N configuration.....	254
APPENDIX G: DETAILED VELOCITY PROFILES	255
G.1 Experimental velocity profiles.....	255
G.2 Comparison of CFD and experimental velocity profiles	261

LIST OF FIGURES

Figure 1.1: Schematic lay-out and T-s diagram of power plant Rankine cycle (re-drawn from van Wylen and Sonntag, 1985). 1

Figure 1.2: Photographs showing the Matimba ACC from below, above and the side (Photos with permission of Eskom (Pty) Ltd.)..... 3

Figure 1.3: Sketch showing distorted inlet conditions for a perimeter fan. 4

Figure 1.4: Sketch showing lay-out of ACC A-frame heat exchanger and axial flow fan. 5

Figure 1.5: Velocity triangles for axial flow fan blade element. 6

Figure 1.6: Isolated airfoil lay-out of a fan blade element..... 7

Figure 1.7: Sketch showing a fan shroud and rotor lay-out..... 9

Figure 2.1: Test set-up used by Stinnes for 45° pipe angle (copied directly from Stinnes and von Backström, 2002). 17

Figure 2.2: Test set-up used of Salta and Kröger for 6 fan rows (copied directly from Salta and Kröger, 1995). 19

Figure 3.1: Array configuration of multiple axial flow fans in an ACC. 25

Figure 3.2: Lay-out of original multiple fan test facility in 3-fan format (redrawn from Visser, 1990) 26

Figure 3.3: Schematic of single test tunnel for multiple fan facility. 28

Figure 3.4: Photo of multiple fan test facility, inlet side. 28

Figure 3.5: Operation of PIV system. 31

Figure 3.6: Layout of PIV system while in operation..... 32

Figure 3.7: Fan static pressure curves for individual fans. 33

Figure 3.8: Combined fan static pressure results for individual fans. 34

Figure 3.9: Edge fan volumetric effectiveness vs. platform height for different fan configurations. 35

Figure 3.10: Correlation between open tunnel loss coefficient and hub-to-tip ratio. 36

Figure 3.11: Distribution of remaining loss coefficient ratios with solidity at lowest platform height. 38

Figure 3.12: Comparison of calculated and measured volumetric effectiveness for different fan configurations.	39
Figure 3.13: Summary of fan shaft power for different fan configurations at different platform heights.	40
Figure 3.14: Power ratio for different fan configurations at different platform heights.	41
Figure 3.15: Location of detailed velocity profiles.	43
Figure 3.16: U-velocity component vs. distance from bell mouth edge along line 4 for different fan configurations at 2.5 x fan diameter platform height.	43
Figure 3.17: V-velocity component vs. distance from bell mouth edge along line 4 for different fan configurations at 2.5 x fan diameter platform height.	44
Figure 3.18: U-velocity component vs. distance from bell mouth edge along line 4 for different fan configurations at 1.0 x fan diameter platform height.	45
Figure 3.19: V-velocity component vs. distance from bell mouth edge along line 4 for different fan configurations at 1.0 x fan diameter platform height.	45
Figure 4.1: CFD geometry of single fan test facility.	52
Figure 4.2: CFD geometry showing structured and unstructured meshes.	53
Figure 4.3: Static pressure vs. volume flow rate for unstructured mesh density investigation.	54
Figure 4.4: Static pressure vs. volume flow rate for fan section mesh density investigation.	55
Figure 4.5: Static pressure vs. volume flow rate for upstream disc position investigation.	56
Figure 4.6: Static pressure vs. volume flow rate for downstream disc position investigation.	56
Figure 4.7: Location of PJM cell face relative to ADM rotor disc.	60
Figure 4.8: Illustration of extended lift coefficient curve for B-fan blade profile.	63
Figure 4.9: Comparison of fan static pressure for N-fan.	64
Figure 4.10: Comparison of fan static pressure for B-fan.	65
Figure 4.11: Comparison of fan static pressure for H10-fan.	65
Figure 4.12: CFD geometry of multiple fan test facility.	68

Figure 4.13: CFD mesh of multiple fan test facility.	69
Figure 4.14: Comparison of N_N_N system volumetric effectiveness.	72
Figure 4.15: Comparison of edge N-fan volumetric effectiveness.	73
Figure 4.16: Comparison of U- and V-velocity profiles for N-fan at horizontal line from edge of bell mouth for infinite floor height.	74
Figure 4.17: Vector plots for (a) PJM, (b) ADM and (c) EADM at infinite floor height, N-fan.	76
Figure 4.18: Comparison of U- and V-velocity profiles for N-fan at horizontal line from edge of bell mouth for 2.5 x fan diameter floor height.	77
Figure 4.19: Vector plots for (a) PJM, (b) ADM and (c) EADM at 2.5 x fan diameter floor height, N-fan.	78
Figure 4.20: Comparison of U- and V-velocity profiles for N-fan at horizontal line from edge of bell mouth for 1.0 x fan diameter floor height.	79
Figure 4.21: Vector plots for (a) PJM, (b) ADM and (c) EADM at 1.0 x fan diameter floor height, N-fan.	80
Figure 4.22: Comparison of B_N_N system volumetric effectiveness.	81
Figure 4.23: Comparison of edge B-fan volumetric effectiveness.	82
Figure 4.24: Comparison of U- and V-velocity profiles for B-fan at horizontal line from edge of bell mouth for infinite floor height.	83
Figure 4.25: Vector plots for (a) PJM, (b) ADM and (c) EADM at infinite floor height, B-fan.	84
Figure 4.26: Comparison of U- and V-velocity profiles for B-fan at horizontal line from edge of bell mouth for 2.5 x fan diameter floor height.	85
Figure 4.27: Vector plots for (a) ADM, (b) PJM and (c) EADM at 2.5 x fan diameter floor height, B-fan.	86
Figure 4.28: Comparison of U- and V-velocity profiles for B-fan at horizontal line from edge of bell mouth for 1.0 x fan diameter floor height.	87
Figure 4.29: Vector plots for (a) PJM, (b) ADM and (c) EADM at 1.0 x fan diameter floor height, B-fan.	89
Figure 4.30: Comparison of H10_N_N system volumetric effectiveness.	90
Figure 4.31: Comparison of edge H10-fan volumetric effectiveness.	91

Figure 4.32: Comparison of U- and V-velocity profiles for H10-fan at horizontal line from edge of bell mouth for infinite floor height.....92

Figure 4.33: Vector plots for (a) PJM, (b) ADM and (c) EADM at infinite floor height, H10-fan.93

Figure 4.34: Comparison of U- and V-velocity profiles for H10-fan at horizontal line from edge of bell mouth for 2.5 x fan diameter floor height.94

Figure 4.35: Vector plots for (a) PJM, (b) ADM and (c) EADM at 2.5 x fan diameter floor height, H10-fan.95

Figure 4.36: Comparison of U- and V-velocity profiles for H10-fan at horizontal line from edge of bell mouth for 1.0 x fan diameter floor height.96

Figure 4.37: Vector plots for (a) PJM, (b) ADM and (c) EADM at 1.0 x fan diameter floor height, H10-fan.97

Figure 5.1: Comparison of numerical (left) and experimental (right) results for edge fan..... 104

Figure 5.2: Simulated pathlines at different floor heights. 105

Figure 5.3: Simulated pathlines along centre plane, at different floor heights. 106

Figure 5.4: Streamline plot at centre plane, 2.5 x fan diameter floor height. 107

Figure 5.5: Streamline plot at centre plane, 1.0 x fan diameter floor height. 107

Figure 5.6: Total pressure contours at different floor heights. 108

Figure 5.7: Lay-out of multiple fan test facility with walkway added. 109

Figure 5.8: Experimental results of tests for B_N_N configuration with and without walkway..... 110

Figure 5.9: Detail of walkway in CFD model. 110

Figure 5.10: Volumetric effectiveness of edge fan for B_N_N configuration with walkway. 111

Figure 5.11: Comparison of numerical (left) and experimental (right) results for edge fan with walkway. 112

Figure 5.12: Simulated pathlines at various floor heights, with walkway..... 114

Figure 5.13: Simulated pathlines along centre plane, at different floor heights, with walkway..... 115

Figure 5.14: Streamline plot at centre plane, 2.5 x fan diameter floor height. 116

Figure 5.15: Total pressure contours at different floor heights, with walkway...	117
Figure 5.16: Lay-out of multiple fan test facility without edge fan inlet bell mouth.	119
Figure 5.17: Volumetric effectiveness of edge fan for B_N_N configuration with and without bell mouth.	120
Figure 5.18: Vector field distribution at different floor heights, without bell mouth.	121
Figure 5.19: Simulated pathlines at various floor heights, without bell mouth...	122
Figure 5.20: Simulated pathlines along centre plane, at different floor heights, without bell mouth.	123
Figure 5.21: Total pressure contours at different floor heights, without bell mouth.	124
Figure 5.22: Reference surfaces for tracking of pressure values.	125
Figure 5.23: Total pressure values for edge fan with bell mouth and no walkway.	126
Figure 5.24: Static pressure values for edge fan with bell mouth and no walkway.	127
Figure 5.25: Total pressure values for edge fan with bell mouth and walkway. .	127
Figure 5.26: Static pressure values for edge fan with bell mouth and walkway.	128
Figure 5.27: Total pressure values for edge fan without bell mouth.	128
Figure 5.28: Static pressure values for edge fan without bell mouth.	129
Figure A.1: B-fan, as tested by le Roux (2010).	148
Figure A.2: B-fan blade properties.	148
Figure A.3: V-fan replacement fan, referred to as the S-fan.	149
Figure A.4: V-fan blade properties.	150
Figure A.5: H-fan configurations.....	151
Figure A.6: H-fan blade properties.	152
Figure A.7: N-fan.....	153
Figure A.8: 630 mm diameter B-fan.....	153
Figure B.1: Fan static pressure vs. volume flow curve, (copied directly from Meyer and Kröger, 2001).....	155

Figure B.2: Curved control volume.	157
Figure B.3: Lay-out of blade element.	158
Figure B.4: Schematic representation of BS 848 (2007) fan test facility.	159
Figure B.5: Lay-out of CFD geometry.	161
Figure B.6: Mesh size investigation for B-fan.	162
Figure B.7: Mesh type investigation for B-fan.	163
Figure B.8: One-dimensional control volume (redrawn from ANSYS Fluent [®] , 2009).	167
Figure B.9: Fan static pressure, B-fan.	170
Figure B.10: Fan shaft power, B-fan.	171
Figure B.11: Fan static efficiency, B-fan.	171
Figure B.12: Fan static pressure at different blade angles, B-fan.	172
Figure B.13: Fan shaft power at different blade angles, B-fan.	172
Figure B.14: Vector plot for B-fan in wind tunnel test facility at 6 m ³ /s, simulated using the actuator disc method.	174
Figure B.15: Blade cross-flow.	176
Figure B.16: Fan static pressure simulated using Coriolis and cross flow terms (B-fan).	178
Figure B.17: Measured lift coefficients for rotating wing, plotted for various values of r/R (Himmelskamp, 1945).	179
Figure B.18: Illustration of Coriolis force effect on boundary layer stability.	180
Figure B.19: Illustration of extended lift coefficient curve for B-fan blade profile.	182
Figure B.20: Effect of different limiting ratios on fan static pressure curve using the EADM.	183
Figure B.21: Fan static pressure obtained using EADM, B-fan.	183
Figure B.22: Fan shaft power obtained using EADM, B-fan.	184
Figure B.23: Fan static efficiency obtained using EADM, B-fan.	184
Figure B.24: Post processed lift coefficients at different radius ratios for B-fan at 16 m ³ /s and 6 m ³ /s, compared to published airfoil data.	186

Figure C.1: Example of a composite blade profile characteristic at $Re = 1.9 \times 10^6$ (Copied from Meyer and Kröger, 2001).....	187
Figure C.2: Lay-out of CFD-model for airfoil analyses.	191
Figure C.3: Comparison of lift coefficient for CFD-simulation and experimental results (LS(1)-0413, $Re = 2.1 \times 10^6$).....	194
Figure C.4: Comparison of drag coefficient for CFD-simulation and experimental results (LS(1)-0413, $Re = 2.1 \times 10^6$).....	195
Figure C.5: Comparison of lift coefficients using the Spalart Allmaras, Xfoil and transitional model (LS(1)-0413, $Re = 2.97 \times 10^5$).....	195
Figure C.6: Comparison of drag coefficients using the Spalart Allmaras, Xfoil and transitional model (LS(1)-0413, $Re = 2.97 \times 10^5$).....	196
Figure C.7: Complete lift coefficient curve for B-fan hub blade profile (LS(1)-0413, $Re = 2.97 \times 10^5$).....	197
Figure C.8: Complete drag coefficient curve for B-fan hub blade profile (LS(1)-0413, $Re = 2.97 \times 10^5$).....	197
Figure C.9: Complete lift coefficient curve for B-fan tip blade profile (LS(1)-0409, $Re = 6.19 \times 10^5$).....	198
Figure C.10: Complete drag coefficient curve for B-fan tip blade profile (LS(1)-0409, $Re = 6.19 \times 10^5$).....	198
Figure D.1: Conversion between measured and simulated pressure value.....	203
Figure D.2: Fan static pressure curve with polynomial curve fit.....	203
Figure D.3: Application of PJM in Fluent®	205
Figure D.4: Fan static pressure, B-fan	207
Figure E.1: Lay-out of multiple fan test facility used in this investigation.	209
Figure E.2: Single fan test facility (including instrumentation lay-out).	210
Figure E.3: Hexcore mesh flow resistance characteristic curve	211
Figure E.4: Comparison of the 1.542 m diameter V-fan results to that of the 630 mm diameter N-fan.....	217
Figure E.5: Comparison of the 1.542 m diameter B-fan results to that of the 630 mm diameter B-fan.	218
Figure E.6: Fan test tunnel with fixed resistance at tunnel outlet.....	219

Figure E.7: Comparison of measured (N-N-N configuration) volumetric effectiveness to predicted effectiveness.....	221
Figure E.8: PIV test lay-out.	223
Figure E.9: Glass window in upper floor of inlet chamber.	224
Figure E.10: PIV camera frame structure.	225
Figure E.11: PIV calibration target positioned inside facility.	226
Figure E.12: Lay-out of calibration targets relative to test facility.....	226
Figure E.13: Photo showing particle seeding upstream of edge fan.....	227
Figure E.14: 2D PIV and PJM results for inlet flow field of edge fan (N-fan configuration) with infinite floor height.	228
Figure E.15: Location of measuring points for hot-film measurements.....	229
Figure E.16: Hot-film probe installed at position 4.	229
Figure E.17: Comparison of velocities for points 1 and 2 at platform height of 1.0 x fan diameter.	230
Figure E.18: Comparison of velocities for points 3 and 4 at platform height of 1.0 x fan diameter.	230
Figure E.19: Comparison of velocities for points 1 and 2 at infinite platform height.	231
Figure E.20: Comparison of velocities for points 3 and 4 at infinite platform height.	231
Figure F.1: N-fan fan static pressure curve.....	233
Figure F.2: N-fan fan shaft power curve.....	233
Figure F.3: B-fan fan static pressure curve.....	235
Figure F.4: B-fan fan shaft power curve.....	235
Figure F.5: H5-fan fan static pressure curve.....	237
Figure F.6: H5-fan fan shaft power curve.....	237
Figure F.7: H10-fan fan static pressure curve.....	239
Figure F.8: H10-fan fan shaft power curve.....	239
Figure F.9: H7-fan fan static pressure curve.....	241
Figure F.10: H7-fan fan shaft power curve.....	241
Figure F.11: H14-fan fan static pressure curve.....	243

Figure F.12: H14-fan fan shaft power curve.....	243
Figure F.13: Volumetric effectiveness vs. platform height of edge fan for N_N_N configuration.....	245
Figure F.14: Volumetric effectiveness vs. platform height of 3-fan system for N_N_N configuration.	245
Figure F.15: Edge fan shaft power vs. platform height for N_N_N configuration.	246
Figure F.16: Volumetric effectiveness vs. platform height of edge fan for B_N_N configuration.....	247
Figure F.17: Volumetric effectiveness vs. platform height of 3-fan system for B_N_N configuration.	248
Figure F.18: Edge fan shaft power vs. platform height for B_N_N configuration.	248
Figure F.19: Volumetric effectiveness vs. platform height of edge fan for H10_N_N configuration.	250
Figure F.20: Volumetric effectiveness vs. platform height of 3-fan system for H10_N_N configuration.	250
Figure F.21: Edge fan shaft power vs. platform height for H10_N_N configuration.....	251
Figure F.22: PIV vector field for N_N_N configuration without walkway (left) and with walkway (right).....	252
Figure F.23: PIV vector field for B_N_N configuration without walkway (left) and with walkway (right).....	253
Figure F.24: PIV vector field for H10_N_N configuration without walkway (left) and with walkway (right).....	254
Figure G.1: U- and V-velocity components vs. distance from platform edge along line 1 for N_N_N fan configuration.	255
Figure G.2: U- and V-velocity components vs. distance from platform edge along line 2 for N_N_N fan configuration.	255
Figure G.3: U- and V-velocity components vs. distance from bell mouth edge along line 3 for N_N_N fan configuration.....	256

Figure G.4: U- and V-velocity components vs. distance from bell mouth edge along line 4 for N_N_N fan configuration.....256

Figure G.5: U- and V-velocity components vs. distance from platform edge along line 1 for B_N_N fan configuration.....257

Figure G.6: U- and V-velocity components vs. distance from platform edge along line 2 for B_N_N fan configuration.....257

Figure G.7: U- and V-velocity components vs. distance from bell mouth edge along line 3 for B_N_N fan configuration.....258

Figure G.8: U- and V-velocity components vs. distance from bell mouth edge along line 4 for B_N_N fan configuration.....258

Figure G.9: U- and V-velocity components vs. distance from platform edge along line 1 for H10_N_N fan configuration.259

Figure G.10: U- and V-velocity components vs. distance from platform edge along line 2 for H10_N_N fan configuration.....259

Figure G.11: U- and V-velocity components vs. distance from bell mouth edge along line 3 for H10_N_N fan configuration.....260

Figure G.12: U- and V-velocity components vs. distance from bell mouth edge along line 4 for H10_N_N fan configuration.....260

Figure G.13: Comparison of velocity profiles for N-fan at horizontal line from edge of plenum for infinite floor height.....261

Figure G.14: Comparison of velocity profiles for N-fan at vertical line from edge of plenum for infinite floor height.261

Figure G.15: Comparison of velocity profiles for N-fan at vertical line from edge of bell mouth for infinite floor height.262

Figure G.16: Comparison of velocity profiles for N-fan at horizontal line from edge of bell mouth for infinite floor height.262

Figure G.17: Comparison of velocity profiles for N-fan at horizontal line from edge of plenum for 2.5 x fan diameter floor height.263

Figure G.18: Comparison of velocity profiles for N-fan at vertical line from edge of plenum for 2.5 x fan diameter floor height.....263

Figure G.19: Comparison of velocity profiles for N-fan at vertical line from edge of bell mouth for 2.5 x fan diameter floor height.264

Figure G.20: Comparison of velocity profiles for N-fan at horizontal line from edge of bell mouth for 2.5 x fan diameter floor height.264

Figure G.21: Comparison of velocity profiles for N-fan at horizontal line from edge of plenum for 1.0 x fan diameter floor height.265

Figure G.22: Comparison of velocity profiles for N-fan at vertical line from edge of plenum for 1.0 x fan diameter floor height.265

Figure G.23: Comparison of velocity profiles for N-fan at vertical line from edge of bell mouth for 1.0 x fan diameter floor height.266

Figure G.24: Comparison of velocity profiles for N-fan at horizontal line from edge of bell mouth for 1.0 x fan diameter floor height.266

LIST OF TABLES

Table 3.1: Summary of all experiments.....29

Table 3.2: Calculated loss coefficients, K_{loss} , for different fans at various platform heights.....36

Table 3.3: Remaining loss coefficients for different fans at various platform heights.....37

Table 3.4: Ratios of remaining loss coefficients for different fans at various platform heights.....37

Table 3.5: Single fan static efficiency at operating point ($\dot{V} = 1.45 \text{ m}^3/\text{s}$ and $p_{sf} = 56.38 \text{ Pa}$).....42

Table 4.1: Summary of all CFD simulations.....49

Table 4.2: Summary of boundary or cell zone conditions.....57

Table 4.3: Radius ratios used for extended actuator disc method63

Table 4.4: Summary of boundary or cell zone conditions.....70

Table 4.5: Reference volume flow rates obtained for individual fan simulations using fixed system resistance.....70

Table 4.6: Summary of error percentages for N- edge fan volumetric effectiveness.....99

Table 4.7: Summary of error percentages for B- edge fan volumetric effectiveness.....99

Table 4.8: Summary of error percentages for H10- edge fan volumetric effectiveness.....99

Table 4.9: Summary of advantages and disadvantages of different simplified fan models.....101

Table A.1: B-fan properties.....147

Table A.2: V-fan properties.....149

Table A.3: H-fan properties.....150

Table A.4: N-fan properties.....152

Table A.5: 630 mm diameter B-fan properties.....153

Table B.1: Relaxation factors169

Table E.1: Measured performance values for B-fan (tested on tunnel 3).....	214
Table E.2: Fan operating point.	219
Table F.1: Measured data for single N-fan test.	232
Table F.2: Processed data for single N-fan test.	232
Table F.3: Measured data for single B-fan test.....	234
Table F.4: Processed data for single B-fan test.	234
Table F.5: Measured data for H5-fan test.	236
Table F.6: Processed data for H5-fan test.	236
Table F.7: Measured data for H10-fan test.	238
Table F.8: Processed data for H10-fan test.	238
Table F.9: Measured data for H7-fan test.	240
Table F.10: Processed data for H7-fan test.	240
Table F.11: Measured data for H14-fan test.	242
Table F.12: Processed data for H14-fan test.	242
Table F.13: Test data for N_N_N configuration without walkway.	244
Table F.14: Test data for N_N_N configuration with walkway.	244
Table F.15: Test data for B_N_N configuration without walkway.	246
Table F.16: Test data for B_N_N configuration with walkway.	247
Table F.17: Test data for H10_N_N configuration without walkway.	249
Table F.18: Test data for H10_N_N configuration with walkway.	249

NOMENCLATURE

Symbol	Description	Unit
A	area	m^2
A_0	turbulence model constant	-
A_s	turbulence model constant	-
C	absolute velocity	m/s
	coefficient of force	-
	inertial resistance coefficient	m^{-1}
C_D	outer layer dissipation coefficient	-
C_f	coefficient of friction	-
$C_{\epsilon 1}$	turbulence model constant	-
$C_{\epsilon 2}$	turbulence model constant	-
C_{μ}	turbulence model constant	-
C_{τ}	shear stress coefficient	-
C_1	turbulence model constant	-
C_2	turbulence model constant	-
c	chord length	m
D	drag force	N
	diameter	m
$delp$	pressure change	N/m^2
F	force term	N
g	gravitational acceleration	m/s^2
H	platform height	m
	shape parameter	-
H^*	kinetic energy shape parameter	-
H^{**}	density shape parameter	-
H_k	kinematic shape factor	-
K	loss factor	-
	loss coefficient	-
k	turbulent kinetic energy	m^2/s^2

L	lift force	N
N	rotational speed	rpm
m	mass defect	m^2/s
M	Mach number	-
n	thickness	m
\tilde{n}	amplitude of the Tollmien-Schlichting wave	m
p	pressure	N/m^2 or Pa
P	power	W
Q	torque	Nm
Re	Reynolds number	-
r	radius	m
	vector magnitude between point at s and field point	m
	radial distance in coordinate field	m
S	momentum source	N/m^3
	strain rate	s^{-1}
	cell side length	m
s	blade pitch	m
	coordinate along vortex and source sheet	m
T	torque	Nm
T	thrust force	N
t	time	s
U	rotational velocity	m/s
	velocity in coordinate field	m/s
$U^{(*)}$	mean flow field characteristic	s^{-1}
u	fluctuating velocity component	m/s
\dot{V}	volume flow rate	m^3/s
V	voltage	V
v	velocity	m/s
W	relative velocity	m/s
X	dimensionless platform height	-

x	distance in coordinate field	m
z	number of blades	-
	axial distance in coordinate field	m
α	angle of attack	°
$1/\alpha$	viscous resistance coefficient	m ⁻²
β	relative flow angle	°
Δ	delta or change	-
δ	boundary layer thickness	m
δ^*	displacement thickness	m
ε	rate of dissipation of turbulent energy	m ² /s ³
ϕ	flow coefficient	-
	variable value in interpolation equation	-
γ	blade stagger angle	°
	vortex sheet strength	m/s
η	efficiency	-
λ	hub-to-tip ratio	-
μ	viscosity	Ns/m ²
π	constant = 3.14159264...	-
θ	circumferential distance in coordinate field	-
	vector angle between point at s and field point	rad
	momentum thickness	m
	weight value in interpolation equation	-
ρ	density	kg/m ³
σ	solidity	-
	source sheet strength	m/s
σ_k	turbulence model constant	-
σ_ε	turbulence model constant	-
τ	shear stress	N/m ²
Ω	rotational speed	rad/s

$\tilde{\Omega}$	mean rotation rate	s^{-1}
ξ	thin shear layer coordinate	m
Ψ	stream function	m^2/s
ψ	head coefficient	-
ζ	cross flow angle	$^{\circ}$

Subscript

Description

<i>air</i>	air
<i>amb</i>	ambient
<i>B</i>	B-fan
<i>c</i>	coriolis
<i>con</i>	converted
<i>D</i>	drag
<i>d</i>	dynamic
<i>e</i>	boundary layer edge
<i>F</i>	fan
<i>h</i>	hydraulic
<i>hex</i>	hexcore
<i>hub</i>	fan hub
<i>i</i>	index in coordinate field
<i>inlet</i>	fan inlet section
<i>inletOD</i>	fan inlet excluding hub section
<i>j</i>	index in coordinate field
<i>loss</i>	system loss
<i>loss open</i>	open tunnel loss
<i>loss platform</i>	platform loss
<i>L</i>	lift
<i>m</i>	mean
<i>mesh</i>	porous mesh
<i>op</i>	operating point

<i>pipe</i>	pipe
<i>r</i>	radial direction
<i>s</i>	static
<i>sf</i>	static fan
<i>shroud</i>	fan shroud
<i>static-to-static</i>	difference between two static values
<i>t</i>	turbulent
<i>tip</i>	blade tip
<i>z</i>	axial direction
θ	tangential direction
	momentum thickness
∞	infinity, free stream
<i>1</i>	leading edge or upstream of fan
<i>2</i>	trailing edge or downstream of fan
<i>3</i>	position at plenum chamber inlet
<i>4</i>	position after porous mesh
<i>2D</i>	2-dimensional
<i>3D</i>	3-dimensional

Superscript

Description

‘ indicates transformation to cross-flow direction

ACRONYMS

ACC	air-cooled condenser
ADM	actuator disc method
B_N_N	3-fan facility consisting of B-fan at perimeter and two N-fans as inner fans
CFD	computational fluid dynamics
EADM	extended actuator disc method
H10_N_N	3-fan facility consisting of H10-fan at perimeter and two N-fans as inner fans
N_N_N	3-fan facility consisting of N-fan at perimeter and two N-fans as inner fans
PIV	particle image velocimetry
PJM	pressure jump method

1 INTRODUCTION

This chapter contains background information on the application and use of axial flow fans in air-cooled condensers.

1.1 Background

The Rankine cycle is considered ideal for a steam power plant (van Wylen and Sonntag, 1985). This is based on the practical feasibility of the pumping and constant pressure superheating processes, compared for example to similar processes in the Carnot cycle. Figure 1.1 shows a simple schematic lay-out, as well as a temperature-entropy (T-s) diagram, of the Rankine cycle.

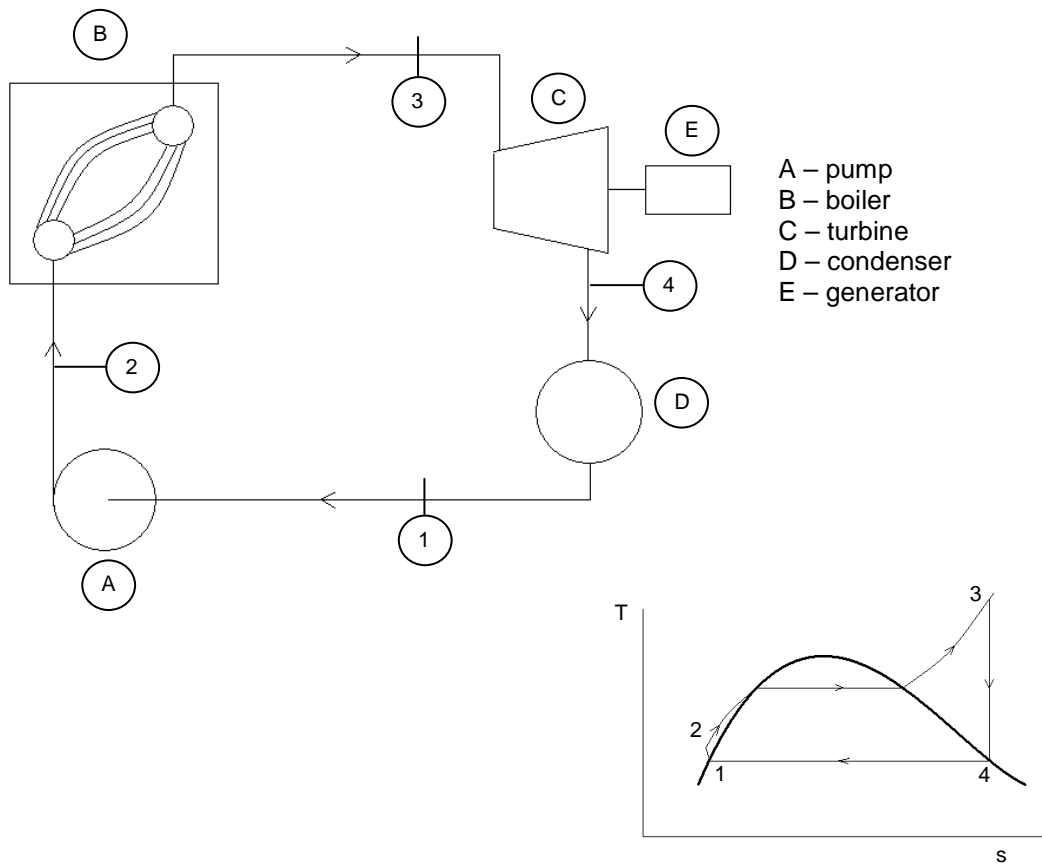


Figure 1.1: Schematic lay-out and T-s diagram of power plant Rankine cycle (re-drawn from van Wylen and Sonntag, 1985).

A Rankine power plant cycle consists of a pump (A) that pumps the water to a boiler (B) where it is heated (in this case superheated), typically using coal. From the boiler the steam passes through the turbine (C) where it expands over the rotor. Work is transferred from the turbine rotor through a shaft to a generator (E)

where it is converted to electrical energy. The expanded steam leaves the turbine and condenses in a condenser (D).

The condensation process removes the excess heat from the working fluid and transfers it into the hydrosphere or atmosphere by means of a cooling system. Various cooling systems exist, each with its own advantages or disadvantages. One of the major factors determining the choice of cooling system is the availability of the cooling medium. Wet-cooling systems (cooling towers using evaporative cooling) are the most economical option in terms of capital cost, provided that a sufficient supply of make-up water is available. Kröger (2004) shows that a 600 MW(e) coal-fired power plant with a wet-cooling system, operating at 70% annual capacity factor may require as much as 10×10^6 m³ of make-up water (in other words about 2.5 litre per kWh(e)). The use of dry-cooling becomes viable where the availability of cooling water is limited and expensive. However, dry-cooling plants are more expensive to build than wet-cooling plants. A report by EPRI (2004) shows that the capital cost of a direct dry-cooled condenser system for a coal power plant is between 3.2 and 3.6 times the cost of a traditional wet-cooling system. The same report estimates that the use of dry-cooling may reduce plant output by about 2%.

Two types of dry-cooling systems are used, namely indirect or direct systems. In an indirect system the cooling water is circulated in a closed loop through a natural or forced draft cooling tower, before being returned to the steam condenser. The interface with the steam can either be through surface or spray condensers (Kröger, 2004). In a direct dry-cooled system, the turbine exhaust steam is fed to an air-cooled condenser (ACC) that consists of finned tube bundles. Air is forced over the outside of these finned tubes using axial flow fans. The Matimba coal-fired power plant (located at Lephalale in Limpopo province, South Africa) has 6 x 665 MW(e) units. It is a direct dry-cooled power plant that is operated by the South African electricity supplier, Eskom (Pty) Ltd. Its condenser has 384 heat exchanger bundles per unit, arranged in an A-frame format. 905 MW of heat is rejected per unit. The complete Matimba ACC uses 288 vertically axis orientated axial flow fans. The fans are 9.145 m in diameter and are installed 45 m above ground level. Each of the fans is driven by a 270 kW electric motor. The total designed energy consumption for the 288 fans (assuming 55% fan static efficiency) is in the order of 65 MW. Figure 1.2 shows a collection of photos of the Matimba ACC, photographed and shown with the permission of Eskom (Pty) Ltd.

Eskom is currently building two additional coal-fired power plants, named Medupi and Kusile (respectively located at Lephalale and Witbank, South Africa). Both Medupi and Kusile will be 6 x 794 MW(e) direct dry-cooled power plants (Eskom, 2011).



Figure 1.2: Photographs showing the Matimba ACC from below, above and the side (Photos with permission of Eskom (Pty) Ltd.).

During operation of the Matimba power plant it became apparent that wind has a major effect on the performance and the stable operation of the plant (Du Toit et al., 1993). Goldschagg et al. (1997) showed that the thermal effectiveness of one of the units of the Matimba plant was as low as 62.5% when a 6 m/s wind was blowing. Strong cross-winds underneath the ACC platform cause distorted inlet flow conditions upstream of the axial flow fans and consequently lower flow rates through the fans. This effect is especially severe for fans located along the perimeter of the ACC (see Figure 1.3). Distorted inlet conditions exist when the vector field upstream of the fan differs from the corresponding conditions experienced by the fan in a standard test facility at the same flow rate.

It is known that the rate of heat transfer to a cooling medium fluid stream is directly proportional to its mass flow rate. The heat transferred from the steam to the ambient air flowing through an ACC will therefore decrease as the mass flow rate of the air decreases. This means that the performance of the ACC under distorted flow conditions deteriorates. During operation the aim is to keep the turbine load (or output) of a specific power plant unit constant. Under normal, stable operating conditions the turbine would therefore be operating at a set steam flow rate and back pressure. This requires the ACC to maintain a stable heat rejection rate. If the ACC cannot maintain the heat rejection rate, for instance due to a change in air mass flow rate or temperature, the turbine back pressure and

outlet steam temperature will increase and the energy output of the turbine is reduced.

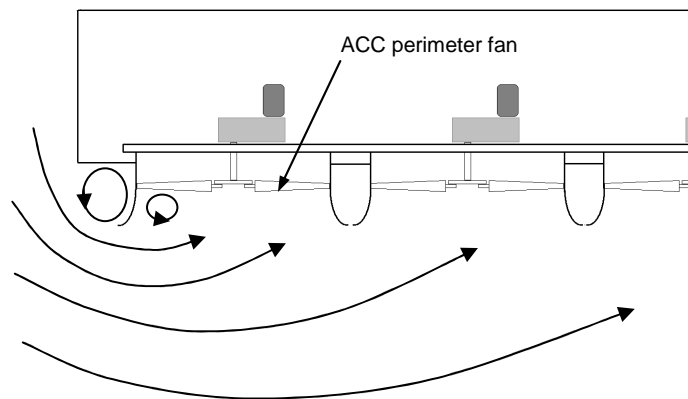


Figure 1.3: Sketch showing distorted inlet conditions for a perimeter fan.

1.2 Air-cooled heat exchangers and ACCs

An air-cooled heat exchanger can be defined as a device where heat is transferred from a high-temperature process fluid, to a lower temperature air stream. This definition would include both natural draught (buoyancy-driven) cooling towers and mechanical draught (fan-driven) heat exchangers.

Air-cooled heat exchangers using axial flow fans to provide air movement may be found in automotive vehicles (referred to as radiators), home-use air conditioners and in air-cooled condensers in large power plants, to name but a few examples. The fans can be installed either in a forced draft layout (the fan is installed upstream of the heat exchanger) or induced draft layout (the fan is installed downstream of the heat exchanger). Forced draught ACC installations are preferred because of their lower fan motor power consumption (due to higher air density) and their lower motor running temperature.

In a power plant steam is supplied to an ACC by means of a large diameter duct that runs from the turbine exhaust. The large diameter is required to minimise pipe friction losses. Minimal friction losses would also require a short steam duct length. An interesting optimisation problem therefore arises; if the ACC is located too close to the main plant buildings (with a short duct length) the buildings may have a detrimental effect on the air flow distribution over the plant (Du Toit et al., 1993).

The air-cooled heat exchangers consist of finned tube bundles that are arranged in an A-frame format (see Figure 1.4). The steam supply duct (1) connects to the heat exchangers (2) at the apex of the A-frame from where the steam is fed down

into the heat exchangers. Air is forced over the outside of the heat exchangers by means of an axial flow fan (3) that is located below the heat exchanger. The fan is driven by an electric motor and gearbox (4) that is suspended from a bridge that in turn rests on the ACC platform (5). The platform is located on top of a series of concrete pillars (shown in the photos in Figure 1.2). The space downstream of the fan and upstream of the heat exchanger is referred to as the plenum chamber (6). The fan shroud (7) forms the duct between the atmospheric air volume underneath the platform and the plenum chamber and is suspended from the ACC platform. Based on the analysis of Salta and Kröger (1995), it is clear that the platform height has a significant influence on the performance of the axial flow fans in a multiple fan installation. The platform height is illustrated in Figure 1.4.

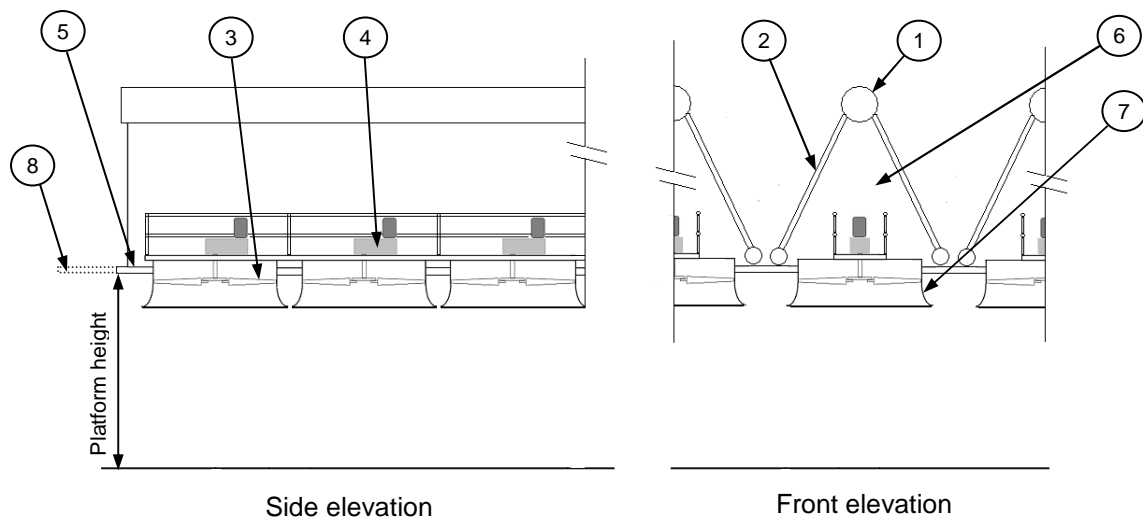


Figure 1.4: Sketch showing lay-out of ACC A-frame heat exchanger and axial flow fan.

One disadvantage of a forced draught installation is its susceptibility to recirculation of the heated outlet air. This occurs under windy conditions. To prevent recirculation a wind wall is usually installed around the outside perimeter of the A-frame heat exchangers. Salta and Kröger (1995) have also shown that the addition of a “walkway” or skirt (8) around the perimeter of the platform may help to increase the volumetric flow rate produced by fans located at the edge of a fan array.

1.3 Axial flow fans

1.3.1 Velocity triangles

A set of inlet and outlet velocity triangles for an axial flow fan blade segment is shown in Figure 1.5. For the velocity triangles shown all radial velocities are ignored and it is assumed that there is no pre-swirl at the inlet of the fan (in other

words $C_{\theta 1} = 0$ and $C_1 = C_{z1}$). The relative circumferential velocity at the inlet is therefore given by the rotational speed of the fan blade ($W_{\theta 1} = U = \Omega r$).

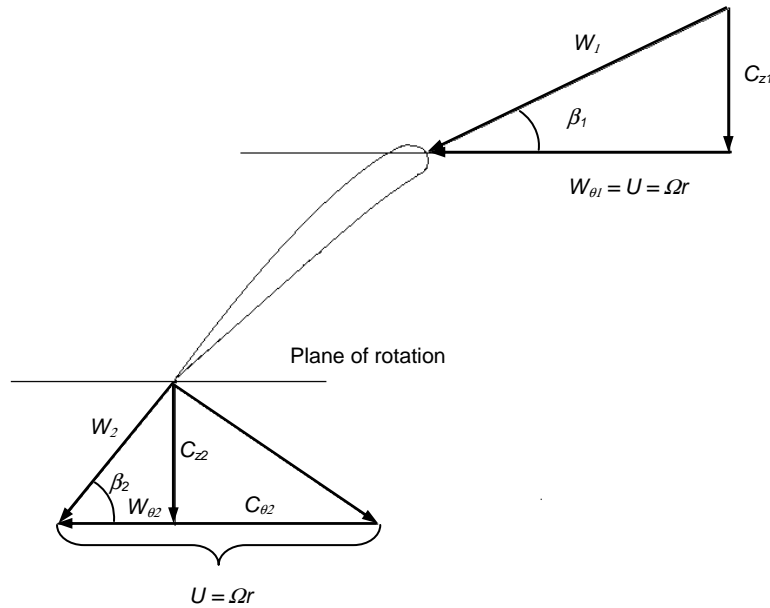


Figure 1.5: Velocity triangles for axial flow fan blade element.

1.3.2 Isolated airfoil theory

In its simplest form an axial flow fan can be regarded as a set of airfoils that rotates around a central axis. The combined effect of the airfoils can be obtained from summing the effect of the individual airfoils together. This approach is referred to as “isolated airfoil theory”. Isolated airfoil theory is appropriate for designing or analysing axial flow fans when the fan solidity (c/s) is less than 0.7 (Bruneau, 1994).

Wallis (1983) describes isolated airfoil theory while referring to a sketch similar to the one shown in Figure 1.6. The flow is assumed to follow a 2-dimensional path over the blade and any radial velocities are ignored. Radial variation in the fan blade properties are accommodated by dividing the blade into radial blade segments, each with its own chord length (c) and blade angle (γ). The blade segment is analysed using the average relative velocity vectors given in terms of the absolute velocities as (Wallis, 1983):

$$W_z = \frac{C_{z1} + C_{z2}}{2} \quad (1.1)$$

$$W_\theta = \Omega.r - \frac{C_{\theta 1} + C_{\theta 2}}{2} \quad (1.2)$$

$$W_{\infty} = \sqrt{W_{\theta}^2 + W_z^2} \quad (1.3)$$

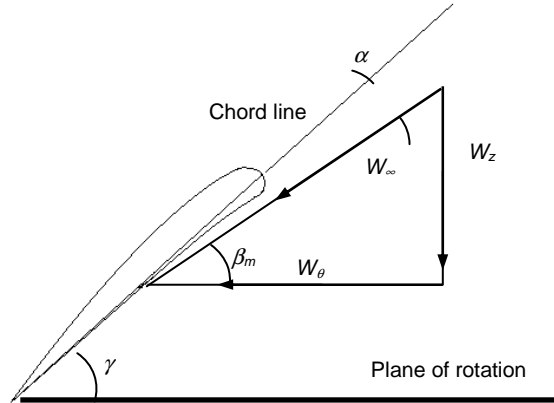


Figure 1.6: Isolated airfoil lay-out of a fan blade element.

Assuming that the blade segment resembles a standard airfoil profile, its 2-dimensional lift and drag properties can be obtained from literature. The lift and drag properties are given in terms of non-dimensional lift and drag coefficients vs. the angle of attack of the airfoil. For isolated airfoil theory the angle of attack is defined as the angle between the blade chord and the average relative velocity vector over the blade. The angle of attack is then calculated as:

$$\alpha = \gamma - \beta_m \quad (1.4)$$

where

$$\tan \beta_m = \frac{1}{2}(\tan \beta_1 + \tan \beta_2) \quad (1.5)$$

Once the angle of attack is known, the lift and drag forces exerted by the blade on the flow can be calculated from the lift and drag coefficients as:

$$L = C_L \frac{1}{2} \rho W_{\infty}^2 c \Delta r \quad (1.6)$$

$$D = C_D \frac{1}{2} \rho W_{\infty}^2 c \Delta r \quad (1.7)$$

It should be noted that these forces act in a direction perpendicular and in line with the average relative velocity vector and therefore need to be transformed to the appropriate direction of the flow field. When using isolated airfoil theory to assess the effect of distorted inlet conditions, the effect of radial flow would be

ignored and the reduction or increase in the upstream and downstream velocity vectors is incorporated into equation (1.1) to (1.7). This approach is followed when applying the actuator disc method (ADM), which is discussed in more detail in Chapter 4.

1.3.3 An air-cooled condenser fan system

Wallis (1983) defines three categories of axial flow fans: free fans, diaphragm mounted fans and ducted fans. Based on this classification, the axial flow fans that are used in ACCs would fall in-between diaphragm-mounted and ducted fans and may be referred to as “shrouded fans”. A diaphragm-mounted fan transfers air from one relatively large space to another, while in a ducted fan the air is enclosed by a duct with length in excess of the distance between the blade inlet and outlet. An ACC fan transfers air from the open atmosphere to a plenum chamber. Although the plenum chamber is often regarded as a large open space, Meyer (1998) has shown that, depending on its geometry and dimensions, a degree of pressure recovery may actually take place in the plenum chamber. Kröger (2004) regards the plenum chamber as a “fan system” component, along with the fan shroud or casing. Since there is no cylindrical pipe section in front of the fan blades, the inlet is regarded as part of the shroud.

It is hence important to distinguish between the fan and the fan system. This is especially relevant when referencing fan performance. A standard fan test facility (BS 848, 2007) is equipped with its own shroud and bell mouth inlet, manufactured to specific dimensions. The fan tests are performed on a scaled-down version of the actual fan using a specially manufactured test rotor. It is essential that the test conditions are referenced correctly and that these test conditions are considered when designing a fan installation. Authors that discuss axial flow fan installations often list the loss factors associated with different inlet types and give examples of the effect of different tip clearance values on fan performance (Kröger, 2004). If the test conditions are referenced correctly it would be possible to make provision for the variation between the properties of the test system and the installed fan system and give an accurate prediction of the performance of the fan.

1.3.4 The layout of an axial flow fan

So the question still remains: “What does a typical axial flow fan in an ACC like the one shown in Figure 1.2 look like?” The technical specifications of the Matimba fans are listed in Section 1.1. Wallis (1983) lists the possible components of a ducted fan as a rotor, rotor-straightener, prerotor, nose cone and tail fairing. For practical reasons (considering the size of the fan and the location of its installation) the ACC fans shown in Figure 1.2 consist of a rotor only. Bruneau (1994) designed a rotor-only axial flow fan for an ACC with a nose cone. However, tests performed by Bruneau (1994) himself showed minimal differences between fan performance with or without the nose cone.

The rotor would typically consist of a hub and a set of fan blades (see Figure 1.7). The hub diameter is reflected in the hub-to-tip (or “boss”) ratio. A large hub-to-tip ratio gives a higher axial velocity through the fan annulus and consequently a higher relative velocity over the fan blade. This leads to higher blade loads (see equations (1.6) and (1.7)) and a higher pressure increase over the fan. The increased velocity would however increase the annular losses through the fan and therefore a lower efficiency may be expected. The number of fan blades, combined with the blade chord length, gives the fan blade solidity as follows:

$$\sigma = \frac{c}{s} = \frac{cz}{2\pi r} \quad (1.8)$$

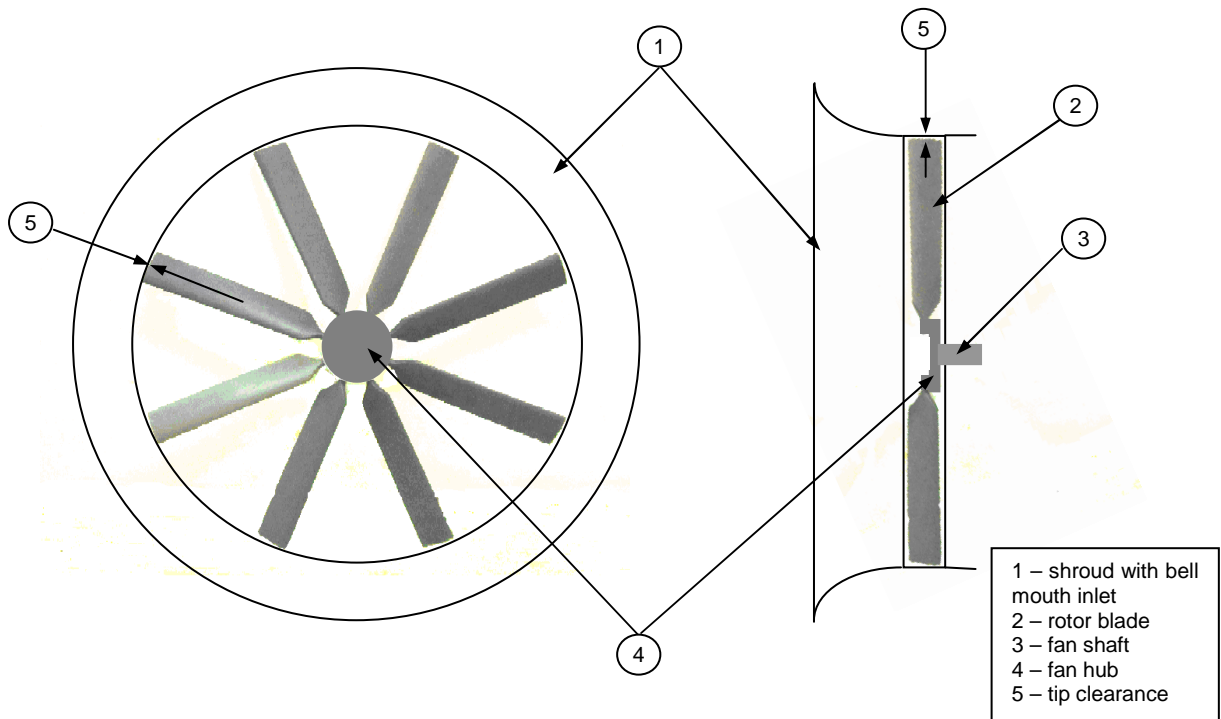


Figure 1.7: Sketch showing a fan shroud and rotor lay-out.

The chord length increases the load transferred from the blade to the fluid (see equations (1.6) and (1.7)) and since isolated airfoil theory assumes that the effect of multiple blades is simply the effect of a single blade times the number of blades, it is clear that an increase in solidity would increase the load transferred to the fluid. However, if the solidity increases beyond a certain limit, the blades can no longer be regarded as isolated airfoils and cascade theory should be used to analyse fan performance.

The inner diameter of the shroud is used when referring to the size of an axial flow fan – in other words a “2 m diameter fan” has a shroud inner diameter of 2

m. The fan rotor diameter is obtained by subtracting twice the tip clearance value from the shroud inner diameter. The fan tip clearance value has a definite influence on the performance of the fan (Venter and Kröger, 1992). An excessive tip clearance leads to a decrease in fan efficiency due to air leakage around the tip of the blade from the high pressure to the low pressure side of the blade.

The blade angles (γ) of a large diameter axial flow fan are adjustable and can be set on-site. The angles are usually set at the blade tip, between the underside (pressure side) of the blade and the fan plane of rotation. When analysing or designing a fan blade, it is important to reference the blade angle correctly and to allow for a possible offset between the blade chord line and the blade angle. The difference between the blade angle (if in line with the chord line) and the flow angle is used to calculate the angle of attack (see equation (1.4)). A larger blade angle, with the same velocity vector, would give a larger angle of attack, which means that larger lift and drag forces are exerted by the blade onto the fluid.

1.4 Objectives

The performance of the axial flow fans in an ACC when subjected to distorted inlet conditions has an immediate implication for the electrical output of a power plant. The requirements for the present study were formulated after Bredell et al. (2006) completed a simplified numerical investigation into the performance of two different fan configurations installed in a multiple fan arrangement typical of an ACC. Bredell et al. (2006) concluded that one of the fan configurations (namely the one that had a steeper fan static pressure vs. volume flow rate curve) performed better in a multiple fan installation than the other. This was originally investigated by Stinnes and von Backström (2002), who found that an edge fan with a high fan static pressure to volume flow ratio (non-dimensionalised with respect to the design point) would have a higher volumetric effectiveness than a fan with a lower ratio.

Following the completion of Bredell's investigation, a number of questions arose regarding the performance of fans under distorted inlet conditions and the objectives of this investigation are formulated around these questions. The objectives can be summarised as follows:

- An empirical curve for the performance of multiple fan installations under different platform heights was derived by Salta and Kröger (1995). The curve was originally derived based on results obtained using a specific fan configuration. An objective of the present investigation is to determine the effect of fan configuration (different hub-to-tip ratios and fan blade solidities) on the performance of fans that are subjected to distorted inlet conditions.
- In order to reduce computational requirements, the operation of axial flow fans in a multiple fan arrangement are modelled using simplified numerical fan models. Previous investigations using these simplified models have shown differences in performance between different fan

configurations at lower platform heights. The effect that the simplified fan model had on these results is not shown. To shed more light on this issue, it was decided to investigate and possibly improve the use of simplified numerical models when simulating axial flow fans that experience distorted inlet conditions.

- To assist the above investigations, it was decided to measure a distorted fan inlet flow field. This would give the following information:
 - It would visualise the interaction of the inlet flow field with different fan configurations and different numerical fan models.
 - It would enable the characterisation of the inlet flow field and show what a typical distorted inlet flow field looks like.
- A number of previous investigations have been done to evaluate possible configurations for multiple fan installations, primarily using simplified fan models and computational fluid dynamics (see Chapter 2). If the use of simplified fan models can be improved such a model can be used to determine the total pressure loss mechanisms upstream of the edge fan and explain why certain multiple fan installations perform better than others.
- The experiments and simulations that would form part of this investigation will provide a large amount of information on edge fan performance for different fan and plant configurations. A final objective of this investigation is to improve the design of a multiple fan installation by evaluating the use of different fan configurations, walkways and fan inlets.

1.5 Methodology

Based on the abovementioned objectives, the investigation uses both numerical and experimental tools. These tools are used as follows:

- The performance of different fan configurations under distorted inlet flow conditions were evaluated by focussing on the performance of the edge fan of a 3-fan multiple fan test facility with variable platform height. The performance values were obtained from experiments and numerical analyses. Six different fan configurations were evaluated. All of these fans were tested and their blade angles set using a single fan test tunnel before being installed in the multiple fan facility. The fans that were evaluated in this investigation are detailed in Appendix A. The experimental facility and test results are discussed in Chapter 3 as well as Appendices E and F.
- To investigate the use of simplified numerical fan models, computational fluid dynamic simulations using different fan models at different levels of inlet flow distortion and for different fan configurations were performed. Before performing the multiple fan analyses the simplified models were developed and verified for single

fan simulations that were compared to single fan experimental results. The numerical analyses are discussed in Chapter 4 as well as Appendices B, C and D.

- The inlet flow field measurements were performed using Particle Image Velocimetry (PIV). The measurements were performed on a central plane upstream of the perimeter (edge) fan in the 3-fan multiple fan test facility. The results from the PIV measurements are discussed and shown in Chapter 3 and Appendices F and G.
- The numerical and experimental techniques and facilities were extended to evaluate various fan configurations. The results from these are detailed in Chapter 5.

1.6 Summary

This chapter gave a short technical overview of air-cooled condensers and axial flow fans. It highlighted the relevance and importance of ACCs to the South African electricity generation industry. It pointed out that the electricity output of an ACC is influenced by the performance of the axial flow fans, specifically those located at its perimeter. These fans experience a reduction in volume flow rate due to the occurrence of distorted inlet flow conditions upstream of the fans.

The chapter listed the objectives of the proposed study. These are centred on improving the performance (and performance prediction) of multiple fan installations, with specific focus on the perimeter or edge fans. Finally a proposed methodology for this study was presented, along with references to the individual chapters where the different tools are applied.

Following the presentation of the argument in Chapter 1, Chapter 2 details the literature study that was performed to prepare and assist in the execution of this study.

2 LITERATURE REVIEW

2.1 Introduction

This chapter highlights the literature that is consulted during the investigation. The literature study focuses on ACCs and axial flow fans in particular. Numerous articles are obtained from the scientific databases, ScienceDirect and Elsevier, the databases of the American Society of Mechanical Engineers (ASME), the Electrical Power Research Institute (EPRI), the American Institute of Aeronautics and Astronautics (AIAA), the Institution of Mechanical Engineers (IMEche) and the South African Institute of Mechanical Engineering (SAIMEchE), to name a few. In that regard access provided to these databases by the University is particularly helpful. Where individual access to databases can not be obtained, articles are sourced through the Engineering Library of Stellenbosch University. This also includes copies of a number of these documents that are obtained from other universities. Contact is also established with at least two individual authors where copies of their work can not be obtained in the public domain. Finally, the database of completed post graduate thesis documents, conference proceedings and academic books on related subjects that are available from the University's own library is extensive and ample use is made of this facility.

The literature study is divided into three sections, namely the application of axial flow fans in ACCs, the testing of axial flow fans and the simulation of axial flow fans. More detailed aspects of literature that is consulted, specifically information on 2-dimensional airfoil profiles and the augmentation of airfoil properties due to 3-dimensional flow over the blade of an axial flow fan are discussed in the relevant chapters or appendices.

2.2 Axial flow fans and their application in air-cooled condensers

Monroe (1979) presented a paper on the improvement of fan system efficiencies in dry- and wet-cooled cooling towers. He lists a number of possible causes of a reduction in the performance of an air-cooled heat exchanger and specifically highlights the fan itself. Monroe (1979) points to the improved efficiency that can be obtained by using a moulded fibreglass fan blade as opposed to using an extruded aluminium blade. This is primarily because the moulded blade can be manufactured with a chord width and blade angle that varies with the fan radius and would have a specific airfoil profile for the cross section of the blade. He advocates the use of a hub disc to minimise reverse flow close to the hub of the fan and emphasises the loss in performance that may be associated with excessive fan tip clearances. He also discusses the importance of selecting the fan speed and blade angle to coincide with the maximum efficiency point of the fan.

One of the most comprehensive books available on the subject of axial flow fans was written by Wallis (1983). He gives extensive details of the design and application of axial flow fans, starting with low solidity, open fans and ending

with high solidity, ducted fans. Of particular use are the results from experimental investigations that are summarised in the book. Wallis (1983) also gives information on fan blade airfoil profiles and specifically refers to the use of the F-series profile in axial flow fans (Wallis, 1977).

A more recent publication is a book by McKenzie (1997) which deals with the design and performance of axial flow fans and compressors. Although axial fans and compressors may be grouped together (their basic velocity diagrams are the same) the subject becomes very broad and specific information on low solidity axial flow fans (as found in air-cooled heat exchangers) is limited. However, the field of axial flow compressors is much more intensively researched than that of axial flow fans. Consequently secondary aspects of axial flow compressors, such as low flow behaviour and the handling of distorted inlet conditions, are discussed in the book of McKenzie (1997). McKenzie (1997) discusses the use of the method of “compressors in parallel” to simulate distorted inlet conditions. This principle corresponds with the “pressure jump model” discussed and used later in this document. However, the low flow behaviour of an axial flow fan is different from that of an axial flow compressor (McKenzie and Yu, 1990). McKenzie and Yu (1990) tested a low-solidity axial flow fan at low flow rates and showed that the pressure rise over the fan increases with decreasing flow rates, compared to an axial flow compressor where the pressure rise decreases. They ascribe the increasing pressure rise to the centrifugal forces that exist in the rotor at low flow rates.

Venter (1990) reports on tests that were performed to determine the effect of up- and downstream obstacles on fan performance in an ACC. Venter used a 1.5 m diameter scaled model of an industrial fan, referred to as the V-fan (see Appendix A) for his investigations. The maximum fan static efficiency for this fan was measured to be 56%. Venter (1990) gives details of aspects such as safety grids and support beams and derives loss factors that represent these components. He also looks at the potential use of a highly cambered fan blade profile (referred to as the GH-fan). Although the efficiency of the GH-fan was slightly higher than that of the V-fan, Venter concludes that the efficient range of operation of the GH-fan was narrower than that of the V-fan and that the V-fan would be more suitable for use in ACCs. Venter and Kröger (1992) published a paper detailing the effect of blade tip clearance on fan performance and conclude that in the region of maximum efficiency of a fan, the fan pressure and volume flow rate decrease linearly with increasing blade tip clearance. Venter (1990) also considered the installation of hub discs on a small hub-to-tip ratio fan and found that the installation of a disc on the downstream side of the fan hub increases the fan efficiency by 1.7% at its operating point.

Using the operating values for the V-fan as specified by Venter (1990), Bruneau (1994) developed an axial flow fan for specific use in ACCs. He based his design on the methods detailed by Wallis (1983) and developed an 8-bladed fan with a hub-to-tip ratio of 0.4. This was considerably larger than the hub-to-tip ratio of

0.153 for the V-fan tested by Venter (1990). Bruneau (1994) put a lot of emphasis on the specification of the airfoil profile for the fan blade and designed two sets of fan blades. The first set was referred to as the B₁-fan and made use of a Clark-Y airfoil profile. The second set was referred to as the B₂-fan and made use of a NASA-LS airfoil profile. The B₂-fan is referred to as only the B-fan later on in this document (see Appendix A). Both fans performed well, with fan static efficiencies in excess of 60%. Bruneau (1994) designed the fan with research in mind; consequently the fan had adjustable blade tip clearances and was supplied with its own equipment for setting the blade angles. The blade angles were set at the root of the blade (in other words at the hub) and were based on the blade chord line and not the underside of the blade surface, as often used in practice. The fan was also supplied with a nose cone, which Bruneau (1994) later found to contribute very little to the performance of the fan. Bruneau (1994) neglected to take the helical path of the relative streamlines through the rotor into account when he distributed the blade profiles along the radial length of the blade. The result of this was a flat blade root surface which did not conform to the cylindrical contour of the fan hub. Consequent leakage flows at the fan hub detracted from the expected fan performance. This was corrected by manufacturing inserts that were fitted between the blade roots and the fan hub, and the fan performance was improved considerably. The design process followed by Bruneau did not consider possible distorted inlet flow conditions.

Van der Spuy (1997) designed a series of rotor-only axial flow fans, ranging from 315 mm diameter to 1200 mm diameter. These fans were intended for use in general industrial applications. Although the size of these fans fall outside the range of ACC fans, the principle of having a single blade design that is adapted for different sizes, blade angles and solidities is similar to the principle used for large diameter ACC fans. Van der Spuy (1997) followed the same design process used by Bruneau (1994) and Wallis (1983). He based the design of the fan series on the minimisation of the fan exit kinetic energy, as detailed in a paper by von Backström et al. (1996). The eventual fan series was designed to have two different hub diameters (150 mm and 250 mm), each with a different number of blades (10 blades were used for the 150 mm hub and 14 blades for the 250 mm hub). The different hubs could also be used in a half-solidity configuration (in other words half the number of blades). Van der Spuy (1997) used the F-series profile described by Wallis (1977) for his fan blade profiles. An interesting feature of the F-series airfoil shape is its ability to incorporate nose droop that increases the stall margin of the airfoil profile.

Although Kröger (2004) focuses on air-cooled heat exchangers, he devotes a chapter to axial flow fans, which summarizes the work of a number of authors, including Venter (1990) and Meyer (1998). The first part of the chapter details the testing of fans, while the remainder discusses fan tip clearance values, fan upstream and downstream obstacles, plenum chamber losses, shroud losses and the advantages of adding a diffuser downstream of the fan.

Salta and Kröger (1995) and Duvenhage et al. (1995) point to the inlet losses experienced by axial flow fans in a multiple fan installation. Salta and Kröger (1995) mention that fans located at the periphery of an ACC (referred to as the edge fans) are particularly affected by distorted inlet conditions. They also point out that very little information is available on inlet flow distortion and its effect in ACCs. To evaluate the effect of “off-axis” inflow Stinnes (1998) conducted experiments using three different test fans with an angled inlet duct. In a subsequent paper, Stinnes and von Backström (2002) conclude that fan power consumption and fan total-total pressure rise is independent of the angle of off-axis inflow, up to 45°. This was explained by Hotchkiss et al. (2006) by means of a CFD analysis, which showed that the effect of the off-axis inflow effectively cancels out on either side of the axial flow fan (see Section 2.3.1).

Bredell (2005) performed a numerical analysis of a single street multiple fan installation, similar to the test facility used by Salta and Kröger (1995). Bredell (2005) evaluated the performance of the multiple fan installation using two different fan configurations. The first configuration was similar to the V-fan, while the second configuration was the B-fan (see Appendix A). Bredell found that an installation using the B-fan has a higher volumetric effectiveness (\dot{V}/\dot{V}_{ref}) than an installation using the other fan (referred to as the A-fan). He pointed out that the B-fan has a much steeper fan static pressure gradient than the A-fan – consequently an additional flow loss caused by inlet flow distortion would result in a smaller change in flow rate for the B-fan than for the A-fan. He concluded that fan configuration influences the volumetric effectiveness of a forced draught air-cooled heat exchanger. This was repeated in a publication by van der Spuy et al. (2009) who also concluded that a fan with a steeper fan static pressure curve is less susceptible to distorted inflow conditions and that its air-cooled heat exchanger would have a higher volumetric effectiveness. Conradie (2010) tested two different edge fan configurations, the B-fan and N-fan (see Appendix A) and found that the edge fan with the steeper pressure curve has a higher volumetric effectiveness in a multiple fan installation.

2.3 Axial flow fan testing for air-cooled condensers

Axial flow fans used in ACCs are tested using a facility with a configuration that resembles a large open inlet and outlet space. A BS 848 part 1, type A fan test facility comprises an inlet settling chamber from where the test fan extracts air to an atmospheric outlet space (BS 848, 2007). The settling chamber has an inlet pipe fitted with a flow measuring and flow control device. To overcome the flow resistance of the flow control device the inlet pipe also has an in-line booster fan. This necessitates the use of flow straighteners to remove the swirl that may be present in the fluid entering the settling chamber. This facility is similar to the facility prescribed by AMCA (AMCA-210, 1974) although the recommended ratio for settling chamber cross sectional area to test fan area of the BS 848 Standards are slightly larger than that of the AMCA Standards. BS 848 part 1 has been revised a number of times over the years (1980, 1997 and 2007). For the

sake of brevity only the latest version is referenced in this document. BS 848 part 1 of 2007 is also referred to as ISO 5801:2008.

Venter (1990) designed and built a “large” fan test facility based on the BS 848 Standards of 1980. The details of this facility are discussed briefly in Appendix B. The fan drive was considered part of the test facility and consisted of a hydraulic power pack and motor. Venter (1990) used the facility to test the 1.5 m diameter scaled industrial fan mentioned in Section 2.1. The facility was subsequently also used by Bruneau (1994) to test the B₁- and B₂-fans and by Stinnes (1998) to test the effect of off-axis flow through an axial flow fan. For this purpose Stinnes fitted extension pipes at different angles between the settling chamber and the test fan (see Figure 2.1). Stinnes (1998) found that fitting a straight section of pipe between the settling chamber and the test fan had no effect on the performance of the fan except for the additional system losses due to the presence of the pipe. Stinnes (1998) also paid particular attention to setting the fan tip clearance. By machining the cylindrical section of the fan shroud on a boring mill and by using a very stiff fan support frame Stinnes was able to set tip clearances as small as 1.5 mm on the experimental fans.

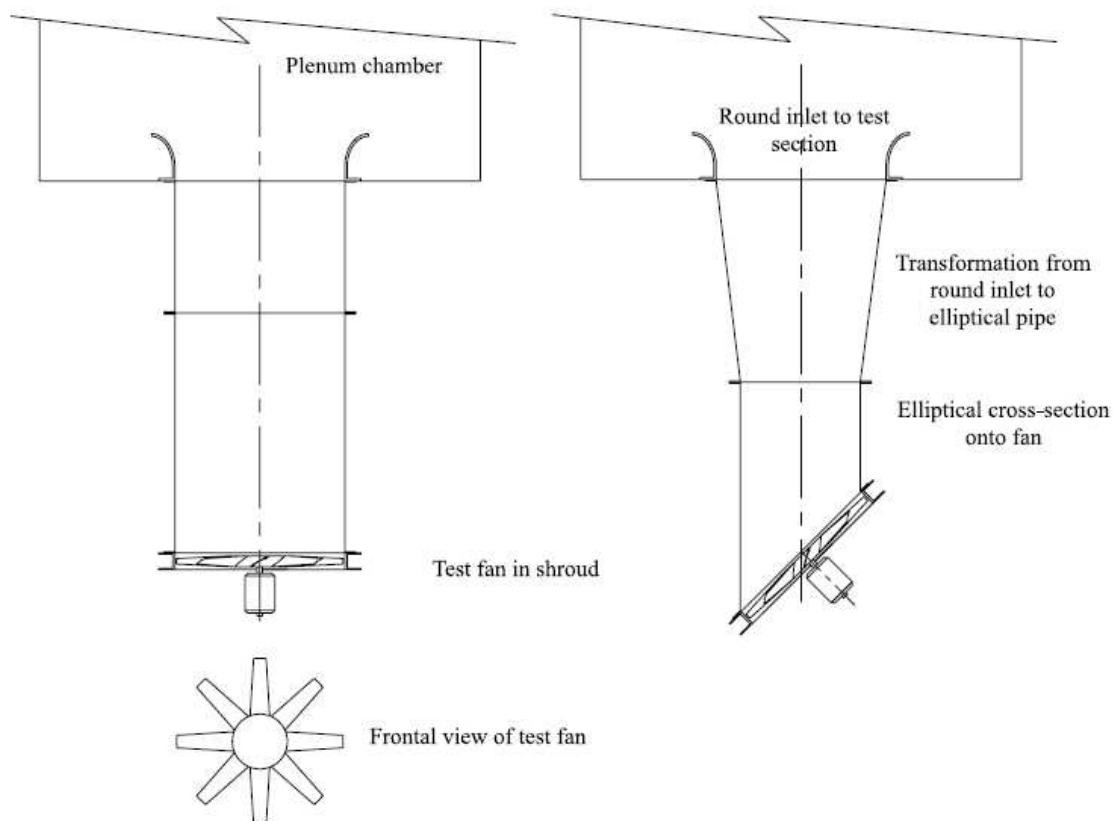


Figure 2.1: Test set-up used by Stinnes for 45° pipe angle (copied directly from Stinnes and von Backström, 2002).

Le Roux (2010) used the large fan test tunnel to test the performance of the B₂-fan as verification of his numerical simulation of the same fan. Le Roux (2010) was able to obtain remarkable repeatability in his results and showed that the atmospheric conditions when running a test on the large fan test facility influences the results considerably. He was, however, unable to reproduce the test results of Stinnes (1998) exactly.

When testing an axial flow fan using the BS 848 test standards, the fan is subjected to axisymmetric inflow conditions, which may be considered ideal. However, as mentioned previously, fans installed at the periphery of an ACC experience distorted inlet conditions. Russel and Peachey (1982) investigated “poor inlet effects” in fans by testing a single model air-cooled heat exchanger with air coming from one side only (the floor and other three sides are closed off). They concluded that the experimental results compared well with full-scale results but that more work was needed on such a facility.

As part of his work to develop a numerical method for simulating fans, Thiart (1990) tested a single 620 mm diameter fan installed at the side of the large wind tunnel at Stellenbosch University. The velocity distribution downstream of the fan was measured and compared to the numerical results. Visser (1990) designed and built a multiple fan test facility that was similar to the facility of Russel and Peachey (1982). He could test up to a maximum of six fan rows with 630 mm diameter axial flow fans and could vary the platform height between 4.5 x - and 1.0 x fan diameter. Visser (1990) found that for 6 fan rows, the edge fan experienced a 19% reduction in volume flow rate at the lowest platform height. This value was reduced to 13% by adding a 150 mm wide walkway upstream of the edge fan. Salta and Kröger (1995) continued the work of Visser and published an empirical curve that predicted the volumetric effectiveness of a multiple fan installation for a variable number of fan rows and fan platform height. The facility of Salta and Kröger (1995) is shown in Figure 2.2.

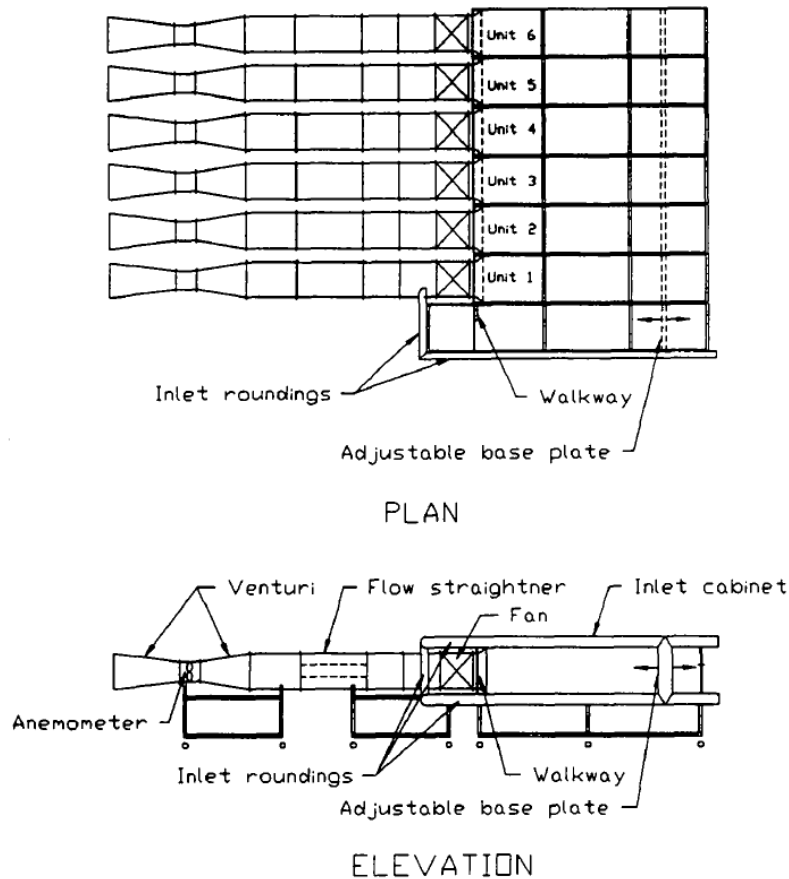


Figure 2.2: Test set-up used of Salta and Kröger for 6 fan rows (copied directly from Salta and Kröger, 1995).

Conradie (2010) used the facility of Visser (1990) to test two different edge fan configurations for a 3-fan row format. He also studied the effect of high Reynolds number flow on the performance of the edge fan by installing a trip-wire on the blades of the edge fan. He found that the effect of a trip wire was to increase the required blade setting angle of the experimental fan to achieve the desired volume flow rate. However, the effect on the volumetric effectiveness of the multiple fan installation was negligible. This correlates with the recommendation of Stinnes and von Backström (2002) who concluded that experimental fans used to simulate off-axis inlet flow should have the same dimensionless slope for the fan characteristic as the actual fans that they represent (even though the experimental and actual fans are not identical).

2.4 Simulation of axial flow fans in air-cooled condensers

The size of an ACC means that accurate airflow measurements are difficult to perform and the need exists to simulate the operation of the ACC using CFD in order to evaluate the effect of atmospheric conditions and possible design

alterations on the performance of the plant. The large number of axial flow fans used in an ACC like the one shown in Figure 1.2 means that simplified models are needed to simulate the operation of the fans. The ability of these models to represent the performance of an axial flow fan correctly is often questioned. Le Roux (2010) conducted a steady state numerical analysis of the performance curve of a full 3-dimensional rotating B-fan. He found that the use of “rotor-stator” interfaces up- and downstream of the fan section in his numerical simulation gave inaccurate results within the normal operating range of the fan (the static pressure rise over than fan that he was simulating was in the order of 200 Pa). He resorted to solving the entire computational domain in the rotating reference frame and in doing this was able to obtain very accurate results in the normal operating range of the fan. However, he was still unable to simulate the axial flow fan accurately at low flow rates.

2.4.1 The actuator disc method

Thiart and von Backström (1993) developed a numerical model, using the actuator disc method, to represent the operation of an axial flow fan in CFD. The actuator disc method replaces the discrete individual fan blades with source terms distributed over an annular disc. The values of the source terms are based on the blade airfoil properties at a specific radial location in the fan. Thiart and von Backström (1993) concluded that the “general performance” of the actuator disc method is good but that it requires excessive computational time. However, the actuator disc method was used by du Toit et al. (1993) and Goldschagg et al. (1997) to model the performance of the Matimba ACC under specific windy conditions by only simulating certain pre-selected fans. They evaluated the effect of wind on both plume recirculation and volumetric effectiveness and were able to conclude that the reduction in volumetric effectiveness under windy conditions was far more prominent than the effect of plume recirculation. Goldschagg et al. (1997) showed that the thermal effectiveness of Unit 1 of the Matimba plant was 62.5% with a 6 m/s north westerly wind blowing compared to a thermal effectiveness of 96.9% for Unit 4 under the same wind conditions.

Duvenhage et al. (1995) used the actuator disc method to simulate a single street, 2-fan row installation for a 4.3 m diameter axial flow fan air-cooled heat exchanger. They used the results from the simulation to evaluate different fan inlet configurations (bell mouth, conical and cylindrical). They concluded that the format of the fan inlet is an important component of the installation and consideration should be given to its design. They also showed that the results from their numerical analyses compare favourably with the experimental results of Salta and Kröger (1995) and recommended that the empirical curve of Salta and Kröger (1995) be used when designing air-cooled heat exchangers. The actuator disc method is investigated further by Meyer and Kröger (2001). They compared the results obtained using the actuator disc method to the experimental results obtained for the B₂-fan on the large fan test facility at Stellenbosch University. The performance curves for the B₂-fan are evaluated at different blade angles. The

correlation between the experimental and numerical performance curves is good. However, differences between the shaft power curves are noticeable. The relative size of these differences vary according to the blade angle being simulated. Meyer and Kröger (2001) also point out that the actuator disc ignores the effect of radial flow between the fan blades. Meyer and Kröger (2004) investigated the effect of Reynolds number (based on the blade chord length) on the accuracy of actuator disc simulations and showed that the fan power consumption values obtained by scaling using the fan laws are between 3% and 4% lower than values obtained from numerical analyses.

Hotchkiss et al. (2006) used the actuator disc method to simulate the experiments of Stinnes (1998) where off-axis flow is channelled through an axial flow fan at a predetermined angle. They were able to repeat the experimental results for the B₂-fan to such an extent that the numerical results confirmed the conclusions of Stinnes and von Backström (2002), namely that the fan power consumption and fan static-to-static pressure rise is independent of the off-axis inflow angle. The numerical results were analysed to show that the effect of off-axis inflow effectively cancels out on either side of the axial flow fan. The investigation of Hotchkiss et al. (2006) was repeated by Jidayi (2008). Jidayi simulated off-axis inflow at various angles for the V-fan (with a much smaller hub-to-tip ratio) and showed that, despite the much smaller hub, the fan power consumption and fan static-to-static pressure rise were still independent of the off-axis inflow angle.

Bredell (2005) simulated different axial flow fan configurations in a forced draught air-cooled steam condenser set-up using the actuator disc method. He validated his numerical model by comparing his results to single fan test results before simulating a single street of a 9.1 m fan diameter six-fan row installation. In a subsequent publication by Bredell et al. (2005) the authors concluded that fan configuration does indeed have an influence on the effectiveness of a forced draught air-cooled steam condenser. They also concluded that inlet flow distortions have an adverse effect on fan flow rate due to off-axis inflow, flow maldistribution and increased inlet flow losses. Bredell et al. (2006) used the actuator disc method to calculate the expected aerodynamic loading on the fan blades due to distorted inflow conditions. They found that the predicted bending moment in the flapping direction experienced by a fan blade fluctuated significantly with the azimuthal position of the blade.

Van Rooyen (2007) simulated the effect of wind on a generic 30-fan ACC using the actuator disc model of Bredell (2005). He used a “manual parallel method” where solutions obtained from a large scale atmospheric simulation using constant velocity outlet profiles for the fans were used to compile inlet velocity profiles for specific fans. The results from these fans were then used as input boundaries to update the large-scale atmospheric flow field simulation. Van Rooyen and Kröger (2008) conclude that wind does indeed affect the performance of an air-cooled steam condenser due to the flow distortions upstream of the edge fans. They are

also able to show that, under certain circumstances, the wind may actually improve the performance of some of the fans in the ACC.

2.4.2 The pressure jump method

Van Staden (2000) simulated the performance of the Matimba air-cooled condenser using CFD. One of the main purposes of his simulation was to predict the variation in power plant output due to changes in atmospheric conditions (basically the wind strength and direction). For that purpose he incorporated the characteristics of the steam turbine into his model and was able to obtain realistic values for the power output of the plant. In his simulations he used a fan model that consisted of source terms in the main flow direction to give a static-to-static pressure increase at the centre of the plane of rotation of the fan, based on the volume flow rate passing through the fan annulus. The value for the static-to-static pressure increase was obtained from the manufacturer's fan static pressure curve. Van Staden (2000) adapted the values for the static-to-static pressure increase from the fan static pressure curve by "calibrating" a model of a single fan air-cooled heat exchanger.

Van der Spuy et al. (2009) showed that the calibrated static-to-static pressure values used by van Staden (2000) can be obtained directly from the fan static pressure curve by considering the properties of a typical BS 848 fan test facility. Van der Spuy et al. (2009) referred to this method as the "pressure jump method". The pressure jump method was subsequently used by Joubert (2010) to model the same generic 30-fan ACC modelled by van Rooyen (2007). Joubert obtained similar overall results to those of van Rooyen (2007). However, Joubert (2010) refrains from analysing differences in the results noted for specific fan units.

Van der Spuy et al. (2010) modelled a single street 6-fan installation with different platform heights. They compared results obtained for two fans (the B-fan and another industrial fan) using the pressure jump method to results obtained for the same fans using an actuator disc method. They also compared the results to the empirical curve of Salta and Kröger (1995). They found that correlation between the results from different fans and different numerical models at large platform heights was good but that there were specific differences at low platform heights. Although these differences could partly be ascribed to the different fan configurations simulated, the different numerical models also contributed to the difference in results.

Louw (2011) used the pressure jump method to simulate the performance of a large ACC with 380 axial flow fans. He was able to show that the size of the ACC, compared to the ACC simulated by Joubert (2010), affects the performance of the axial flow fans under windy conditions. He subsequently makes recommendations regarding the walkway width, screen distribution and ACC orientation, based on the results of his analyses. The pressure jump method was also applied to ACC investigations by Gao et al. (2010) and Shi et al. (2009).

However, the fan model is referred to very briefly and it is unclear whether any provision for the difference between fan static pressure and the static-to-static pressure increase in the plane of rotation of the fan was made in these analyses.

2.4.3 The extended actuator disc method

The extended actuator disc method was formulated during the course of this study. It is based on the augmentation of the 2-dimensional blade profile lift capabilities of a rotating blade, as described by Himmelskamp (1945). He tested a 2-bladed ducted rotor and instrumented one of the blades to measure the chordwise pressure distribution at different radial locations along the length of the blade. Himmelskamp found that the maximum lift coefficient of a rotating blade increased in the presence of radial flow and that stall occurs at a larger angle of attack when a blade is rotating than when it is stationary.

Snel (1991) derived momentum equations for the boundary layer of a rotating wind turbine airfoil and for separated flow over the same airfoil using boundary layer theory. However, the boundary layer derivation of Snel (1991) is investigated further by Corten (2001), who concludes that Snel's use of the boundary layer equations (with its associated simplifications) to solve the flow in the separated region is incorrect. Corten (2001) used the "full" momentum equations to describe the boundary layer of a rotating wind turbine airfoil. A number of other researchers have also investigated this effect, all of them referring to its application on wind turbines. Tangler (2004) investigated the appearance of stall on a wind turbine blade and advocates the use of an empirical model to account for stall delay at small radial locations. Lindenburg (2004) summarised the effect of rotation on a rotor blade as follows:

1. The rotational velocity of the fan blade is directly related to its radius. Consequently there exists a radial variation in relative flow velocity (and dynamic pressure) over the blade. At low flow rates the relative flow over the blade is dominated by the rotational velocity and the radial variation in relative flow velocity becomes more prominent. The radial variation in dynamic pressure is the strongest near the suction peak (location of lowest static pressure) of the blade profile.
2. The air that rotates with the blade (entrained in the boundary layer and separated flow) is subjected to a centrifugal force.
3. The radial velocity originating from the centrifugal force gives rise to a Coriolis force that reduces the extent of trailing edge pressure build-up on the suction side of the airfoil and reduces the volume of the stalled area on the blade.

Hu et al. (2006) concludes that rotation generally has a beneficial effect in delaying separation of flow over an airfoil. Schreck et al. (2007) concludes that regions where the boundary layer proceeds in a radial, or even forward direction, experience the highest level of rotational augmentation.

The above publications all refer to the application of rotational augmentation on wind turbine blades. Corrigan and Schillings (1994) published an empirical model for stall delay on helicopter rotor blades, largely based on the results of the work of Banks and Gadd (1963). The model of Corrigan and Schillings calculates a value for stall delay (in degrees) based on a separation parameter that is intrinsic to a blade's shape. Gur and Rosen (2005) derived a correlation which they based on the proposal of Snel that the true value for the lift coefficient of a rotating airfoil section would lie between the 2-dimensional, non-rotating value (often obtained from wind tunnel testing) and the inviscid flow solution where there is no stall. Gur and Rosen then proceeded to use a hyperbolic tangent function based on the value of chord length divided by radius to interpolate between these two extremes.

Despite all of the above, no reference to the application of the above "rotational augmentation" on axial flow fans could be found.

2.5 Summary

This chapter gave an overview of the literature that was consulted during the course of this study. The main sources of literature that lay the basis for this study were detailed as follows:

- As mentioned in Chapter 1, this study originated from the work of Bredell (2005) where he evaluated the performance of a multiple fan installation using different fan configurations by means of the actuator disc method.
- The work of Visser (1990) and the publication by Salta and Kröger (1995) detail the testing of axial flow fans in a multiple fan environment, while Venter (1990) describes the testing of an individual axial flow fan.
- Meyer and Kröger (2000) explain the use of the actuator disc method to model the performance of an axial flow fan in CFD, while van Staden (2000) uses the pressure jump method to model the performance of multiple axial flow fans in an ACC arrangement.
- An investigation into the effect of three-dimensional flow in an axial flow fan by Himmelskamp (1945) provided insight into improving the modelling of axial flow fans in CFD. The extended actuator disc method that was eventually used was largely based on the work of Gur and Rosen (2005).

A number of aspects were however lacking in the literature that was surveyed. The first was a lack of experimental performance data for axial flow fans of different configurations operating in a multiple fan environment. Secondly no direct comparisons between experimental and numerical results for axial flow fans in a multiple fan environment, particularly edge fans, could be found and thirdly no experimental data on the flow field that exists upstream of an edge fan could be found. This formed the motivation behind the execution of this project.

3 AXIAL FLOW FAN EXPERIMENTS

This chapter is used to describe the test facilities, test procedures and test results that formed part of this investigation. Details like test facility dimensions, calculations and tabulated test results are shown in Appendix E and Appendix F.

3.1 Introduction

The purpose of these axial flow fan experiments was to quantify the performance of different axial flow fan configurations when subjected to distorted inlet flow conditions. The experimental results were also used to derive correlations for the performance of different edge fan configurations to validate results obtained from CFD simulations and to obtain insight into the operation of an edge fan.

The concept of evaluating a single fan as part of a multiple fan installation was proposed by Russell and Peachey (1982), who tested a single axial flow fan as if installed in a 2-fan row array configuration (with flow coming from one side only) and investigated the effect of poor inlet conditions on fan performance. Visser (1990) also identified the need for testing the performance of an axial flow fan within an array configuration. Figure 3.1 shows three fans that form part of a fan array that has six fan rows. The numbering of the fans in Figure 3.1 correlates with the numbering used in the eventual multiple fan test facility.

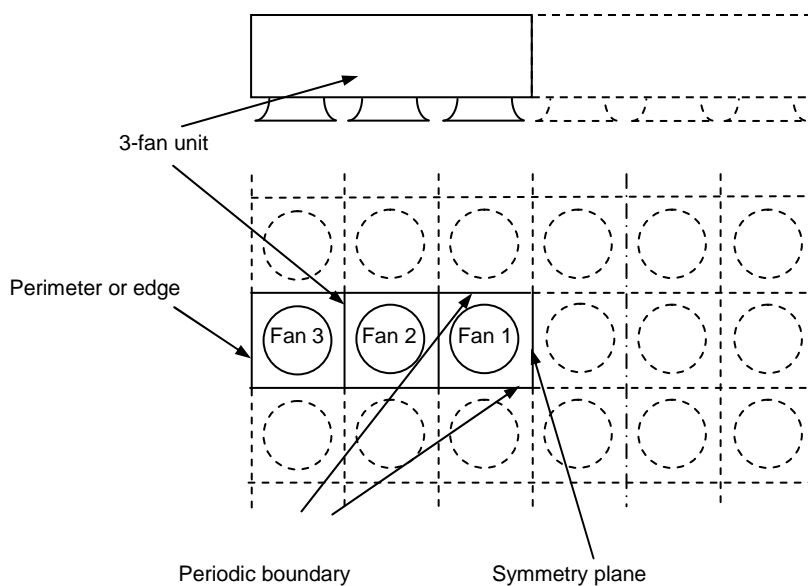


Figure 3.1: Array configuration of multiple axial flow fans in an ACC.

Visser (1990) designed, built and tested a facility with multiple fan rows with variable ground clearance height (ground clearance height can also be referred to as platform height). The fan systems are installed in parallel, with their inlets

extracting air from a common wooden boxed structure. Since the fans are intended to form part of a large array of fans, the sides of the wooden box resemble symmetry planes.

The platform height of the apparatus is adjustable with removable floor boards that can be positioned at pre-determined heights (see Figure E.1). Each of the single fan systems included in the multiple fan row represented a BS 848 type B testing configuration (see Figure 3.2).

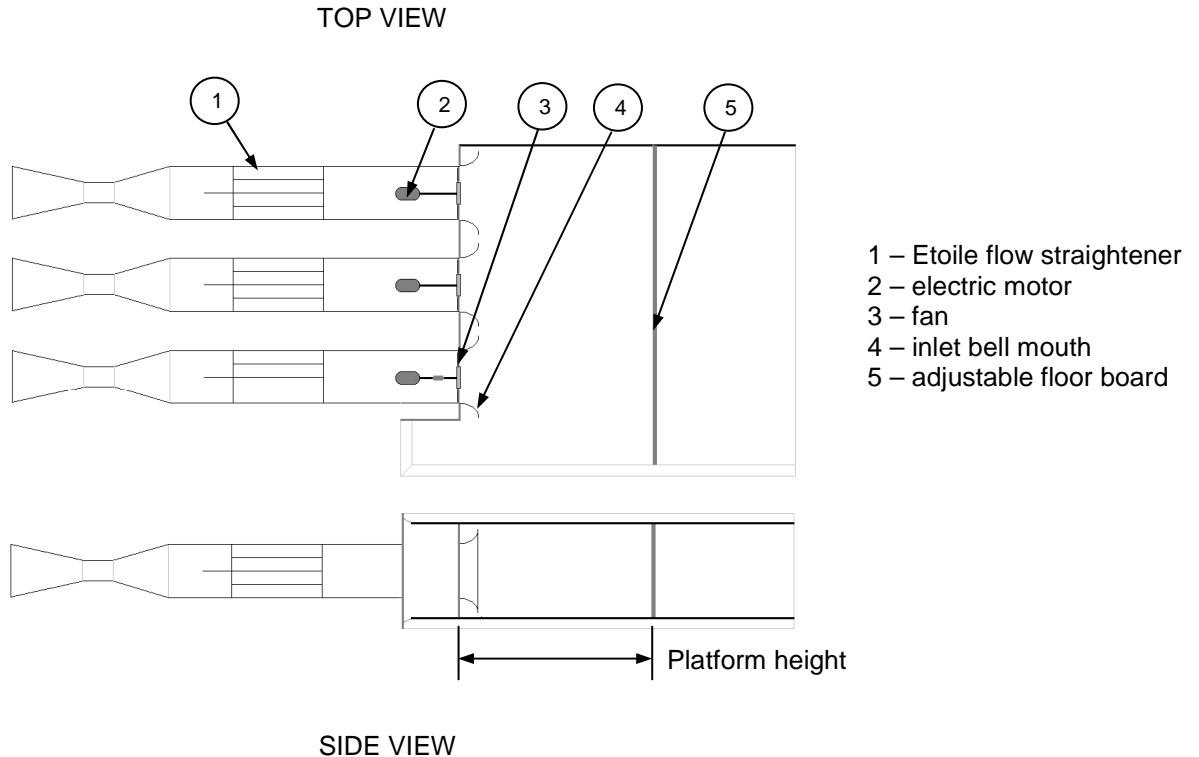


Figure 3.2: Lay-out of original multiple fan test facility in 3-fan format (redrawn from Visser, 1990)

Visser used the facility to investigate the effect of ground clearance height, inlet guide vane configuration, walkway (or skirt) width and bell mouth depth on the performance of fans in an array configuration. The facility of Visser was re-commissioned in a 3-fan row format by Conradie (2010) to test the effect of fan configuration on the performance of a multiple fan installation. All of these investigations showed that the edge fan of a multiple fan installation experiences distorted inlet conditions due to its location at the side of the fan row. The extent of inlet flow distortion is increased by lowering the platform height.

This investigation extends the work of Conradie (2010) by testing 6 different axial flow edge fans (also 630 mm diameter) with different hub-to-tip ratios (0.15 to

0.4) and solidity ratios (0.33 to 0.84). The details of the different axial flow fans that formed part of this investigation are given in Appendix A.

3.2 Facilities

The BS 848 part 1 standard (BS 848, 2007) provides for the testing of four different fan system configurations, namely open inlet to open outlet (type A), open inlet to ducted outlet (type B), ducted inlet to open outlet (type C) and ducted inlet to ducted outlet (type D). The standard is very specific regarding the layout and methods applicable to each of these configurations with the purpose of ensuring that fans are tested under well-defined and repeatable test conditions. Consequently, the condition of the inlet flow of a fan installed in such a test facility can be termed “ideal”. The standard test facilities make provision for air flow into the fan along the fan longitudinal axis and do not investigate the effect of distorted inlet flow.

Two types of fan experiments were performed as part of this investigation. The first type of experiment was the testing of axial flow fans under ideal inlet conditions with a bell mouth inlet. The second type of experiment was the testing of different axial flow fans installed at the location of the edge fan in a 3-fan multiple fan arrangement (the configuration of the two inner fans were kept the same). The facilities used in this investigation are described in detail in Appendix E.

3.2.1 Standard axial flow fan test facilities

The BS 848 type A test configuration is considered appropriate for the testing of axial flow fans used in forced draught ACC fan applications since the plenum chamber into which the axial flow fan discharges may be regarded as an open outlet. The results generated for the 1.542 mm diameter B- and V-fan referred to in Appendix A were obtained on a type A test facility that was developed by Venter (1990) (see Figure B.4).

The three 630 mm diameter test tunnels that formed part of the multiple flow fan test facility were similar to type B test tunnels. The reason for using a type B tunnel in this application was a practical one in that the volume flow through each of the test tunnels had to be measured independently. Since the three fans were supplied with a common inlet area, the flow rate through each of the fans was measured using outlet ducts with an axial flow vane anemometer in each of the ducts (see Appendix E). The original format of the tunnels in the multiple fan test facility corresponded to a type B facility and used 8-vane “Etoile” flow straighteners to remove the swirl after the fans. The format of these tunnels was, however, adapted to correspond more closely to the actual installation by replacing the straightener section with a plenum chamber and porous mesh sheet (see Figure 3.3).

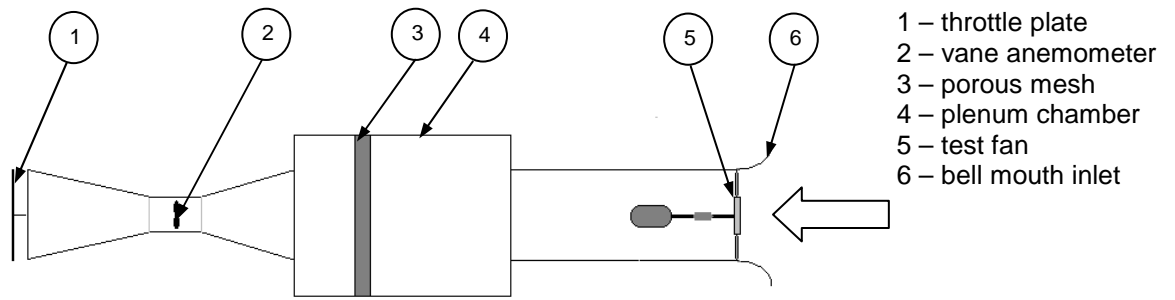


Figure 3.3: Schematic of single test tunnel for multiple fan facility.

3.2.2 Multiple axial flow fan test facility

The multiple axial flow fan test facility was assembled from the three individual fan tunnels and included a common inlet chamber that represented the area underneath a typical horizontal ACC installation (see Figure 3.4), where the upper and lower sides of the inlet chamber represented symmetry planes. Provision was made for the installation of a floor at various distances in front of the fans so that the platform height of the installation could be changed. Each of the tunnel outlets were supplied with a fixed flow resistance plate (the throttle plates shown in Figure 3.3 were removed) to ensure that the individual, single tunnel, operating point of each of the tunnels correspond to the values given in Table E.2.



Figure 3.4: Photo of multiple fan test facility, inlet side.

3.3 Description of Experiments

The individual performance of each of the test fans described in Appendix A was determined on the free standing single tunnel format shown in Figure 3.3. Once the individual performance of each of the fans was determined, the multiple fan test facility was assembled and the performance of the fans inside the facility was measured. Table 3.1 shows a summary of all experiments that were performed as part of this study.

Table 3.1: Summary of all experiments.

Single fan variable resistance	Single fan fixed resistance	Multiple fan bell mouth no walkway	Multiple fan bell mouth with walkway	Multiple fan PIV no walkway	Multiple fan PIV with walkway	Multiple fan hot-film
		7 different floor heights	7 different floor heights	Infinite, 2.5 and 1.0 floor height	Infinite, 2.5 and 1.0 floor height	Infinite and 1.0 floor height
N-fan	N-fan	N_N_N	N_N_N	N_N_N	N_N_N	
B-fan	B-fan	B_N_N	B_N_N	B_N_N	B_N_N	B_N_N
H5-fan		H5_N_N	H5_N_N			
H10-fan	H10-fan	H10_N_N	H10_N_N	H10_N_N	H10_N_N	
H7-fan		H7_N_N	H7_N_N			
H14-fan		H14_N_N	H14_N_N			

3.3.1 Individual fan performance tests

The individual fan performance tests of each of the fans described in Section A.2 were conducted using tunnel 3 of the multiple fan test facility (see Section E.3). During the tests the static pressure after the porous mesh sheet, the volume flow through the tunnel and the fan shaft torque was measured while progressively adjusting the throttle plate at the tunnel outlet. The tests were performed at 1000 RPM, taking into account the limited capacity of the electric motors. This meant that the tip speed of the test fan rotor was 33 m/s, compared to a tip speed of 24 m/s for the tests performed by Visser (1990).

The blade angles of each of the fans were set to ensure that the fan static pressure curves of all the fans crossed the operating point detailed in Table E.2, namely $1.45 \text{ m}^3/\text{s}$ and 56.38 N/m^2 . The subsequent measured values were processed according to the calculations detailed in Section D.3.1, using reference values of

1000 RPM and 1.2 kg/m^3 . The individual fan static pressure curves were measured twice to confirm the repeatability of the facility.

The shaft power transferred to the fan was also measured using an in-line torque transducer and speed proximity sensor.

3.3.2 Multiple fan performance tests

The multiple fan performance tests were performed using 3 fans. The two inner fans were N-fans (see Appendix A) and were considered representative of fans in industrial installations. Each of the individual fans tested previously were tested in the edge fan (also referred to as fan number 3 during the experiments) position under different platform heights ranging from $1.0 \times$ fan diameter to infinite platform height. Where applicable, the multiple fan test facilities are classified according to their configuration, where N_N_N would refer to a configuration with an N-fan, B_N_N a B-fan and H10_N_N an H10-fan as the edge fan.

Since all the tunnels were supplied with an identical, fixed resistance, the decrease in volume flow rate through the tunnel when it is in its multiple fan format at a specific platform height, compared to the volume flow rate measured in its individual format, gives an indication of the susceptibility of the fan installation to distorted inlet flow. This ratio of volume flow rates is referred to by Salta and Kröger (1995) as the volumetric effectiveness of a specific fan installation or collection of fans.

The shaft power transferred to the edge fan at the different platform heights was also measured.

3.3.3 Detailed flow field measurements

Particle Image Velocimetry (PIV) was used to measure the vector field upstream of the edge fan. In short, a PIV system consists of high speed cameras that take photos at set intervals of very fine particles in a flow field. The particles are illuminated by means of a laser light. By comparing the location of particles shown on two successive photographs, the direction and speed of the particles can be calculated to form a vector field. The PIV system and its lay-out for this specific experiment are described in Section E.3. Figure 3.5 shows a photo of the laser light from the PIV system being directed into the flow field upstream of the test fans (while testing the B_N_N configuration with an “infinite” platform height).

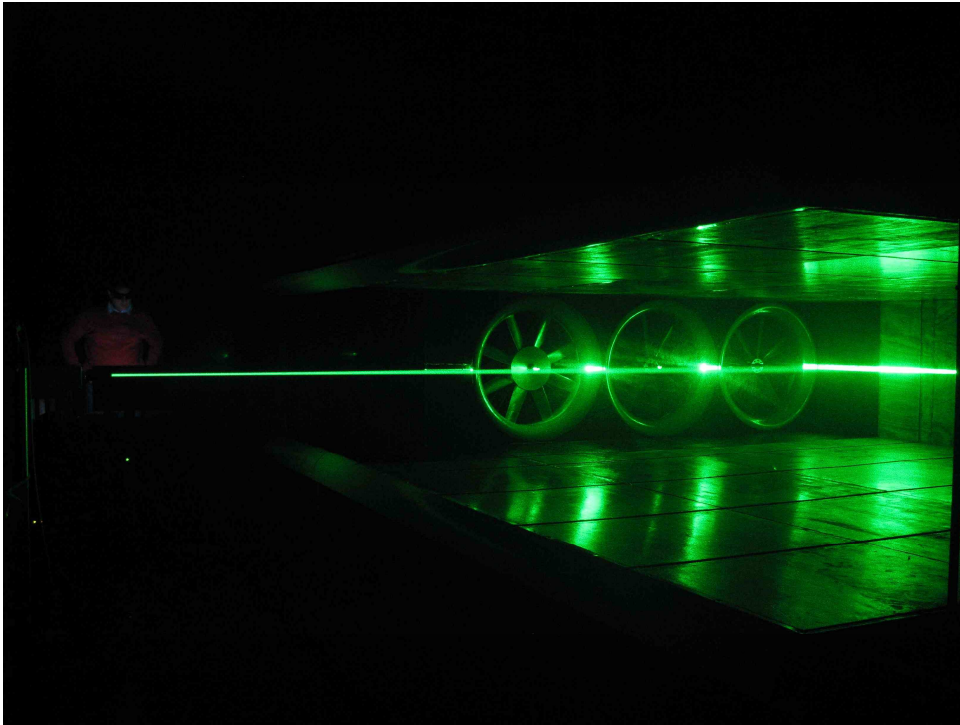


Figure 3.5: Operation of PIV system.

Figure 3.6 shows a photo of the PIV system while in operation (note that the intensity of the laser light was turned down to give a clearer photo of the equipment). The volume flow rate measurements and PIV measurements were conducted separately from each other. The PIV experiments were performed for the N_N_N, B_N_N and H10_N_N multiple fan configurations at infinite, 2.5 x - and 1.0 x fan diameter platform heights (see Figure 3.2 and Figure E.1).

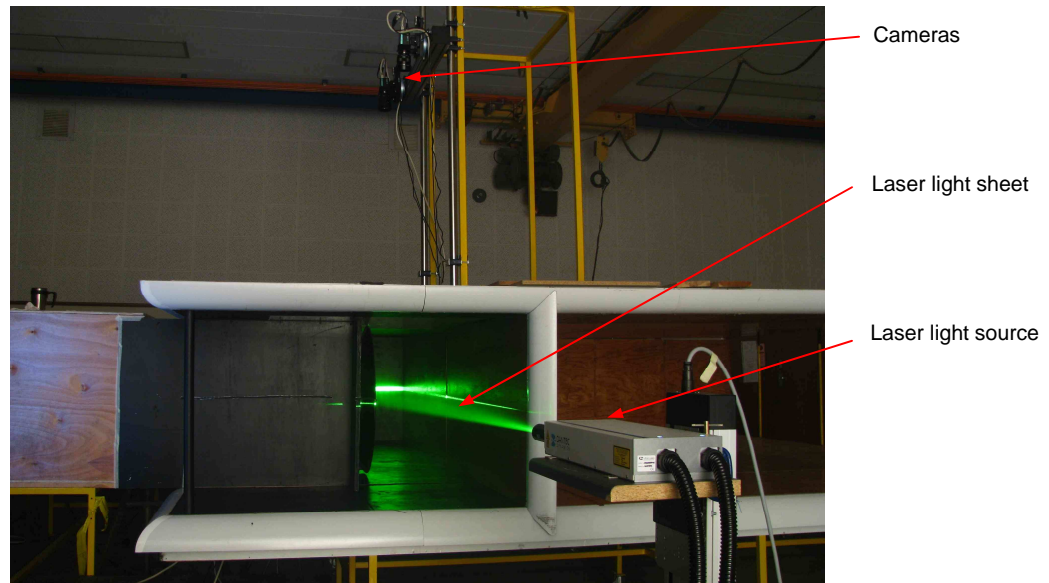


Figure 3.6: Layout of PIV system while in operation.

3.4 Results and discussion

3.4.1 Individual fan performance

The individual test results of the various fans are shown in Figure 3.7. Tables containing the measured and processed test results are included in Appendix F. The test results shown in Figure 3.7 were combined into a single data set by referencing the pressure and flow characteristics of each of the fans to that of the 630 mm diameter B-fan. The motivation for using the B-fan as a reference was the fact that its fan static pressure curve lies in the centre of all the test data, as well as the large amount of background information available for the fan. The different sets of fan test results were consolidated by first converting all the test data to dimensionless flow and head coefficients (Balje, 1981) where:

$$\phi = \left(\frac{\dot{V}}{\pi r_{tip}^2 (1 - \lambda^2)} \right) / U_{tip} \quad (3.1)$$

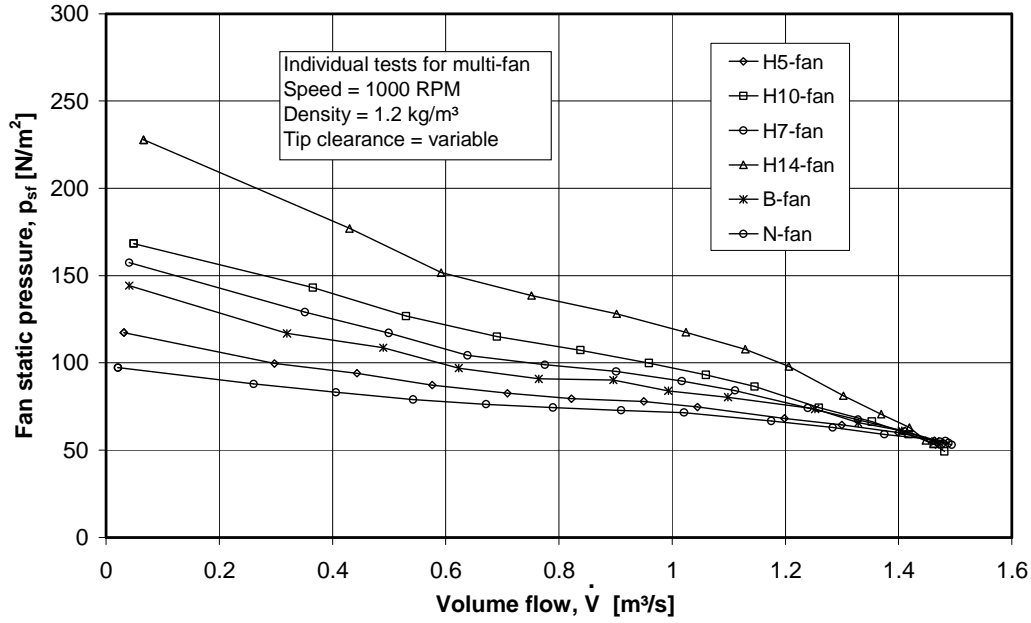


Figure 3.7: Fan static pressure curves for individual fans.

and

$$\psi = \left(\frac{P_{sf}}{\rho_{air}} \right) / U_{tip}^2 \quad (3.2)$$

The calculated flow coefficients for the different fans were referenced to the B-fan by multiplying their values with a flow conversion factor as follows:

$$\phi_{con} = \phi \left(\frac{\phi_{op}}{\phi_{Bop}} \right)^{-0.18} \quad (3.3)$$

where the operating point flow coefficients are calculated for each of the fan configurations using the operating point data given in Table E.2. The head coefficients were referenced to the B-fan data by following the same process used for the flow coefficients:

$$\psi_{con} = \psi_{op} + (\psi - \psi_{op}) \left[\frac{\sigma_B}{\sigma} \right]^{1.2} \left[\frac{\lambda_B}{\lambda} \right]^{0.5} \quad (3.4)$$

where the operating point head coefficient is also based on the operating point data of Table E.2. The resultant data distribution following the above referencing process is shown in Figure 3.8.

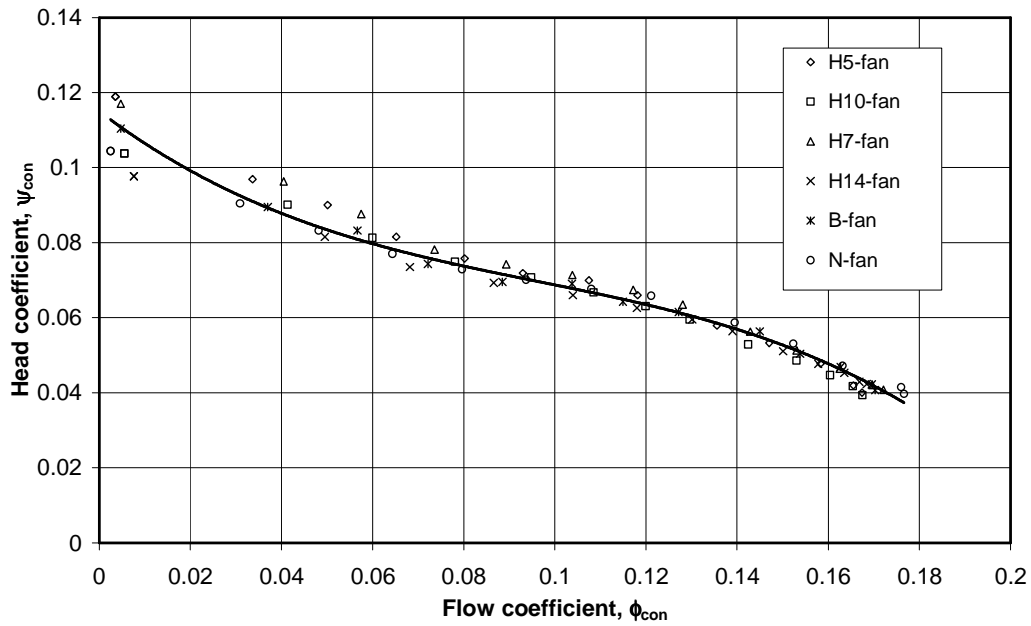


Figure 3.8: Combined fan static pressure results for individual fans.

Finally a curve was fitted through the dimensionless B-fan data as follows:

$$\psi_B = -24.272\phi_B^3 + 7.015\phi_B^2 - 0.921\phi_B + 0.115 \quad (3.5)$$

In principle a single equation was obtained that could be used to predict the fan static pressure vs. volume flow rate curve at low flow rates (below the operating point) of a wide range of axial flow fans by taking into account their solidity and hub-to-tip ratios. Since the operating point forms part of the derivation (see equation 3.3 and 3.4) this equation is only valid for the specific operating point and for the specific dimensionless curve of the B-fan shown in Figure 3.8. The applicability of the equation to a wider operating range (other blade setting angles and operating points) should still be investigated.

3.4.2 Multiple fan performance

The performance of a multiple fan system with different platform heights was described and quantified by Salta and Kröger (1995). In broad terms, the distorted inlet conditions prevailing upstream of the edge fan can be ascribed to the cross flow velocity originating from the inner fans inducing a flow of air past the edge fan inlet. The higher the cross flow velocity becomes, for instance due to a lower platform height, the higher the level of distortion in front of the edge fan inlet and, consequently, the lower the volumetric effectiveness of the edge fan would be. Figure 3.9 shows the volumetric effectiveness of the different edge fan configurations at various dimensionless platform heights. Tables containing the measured data are included in Appendix F.

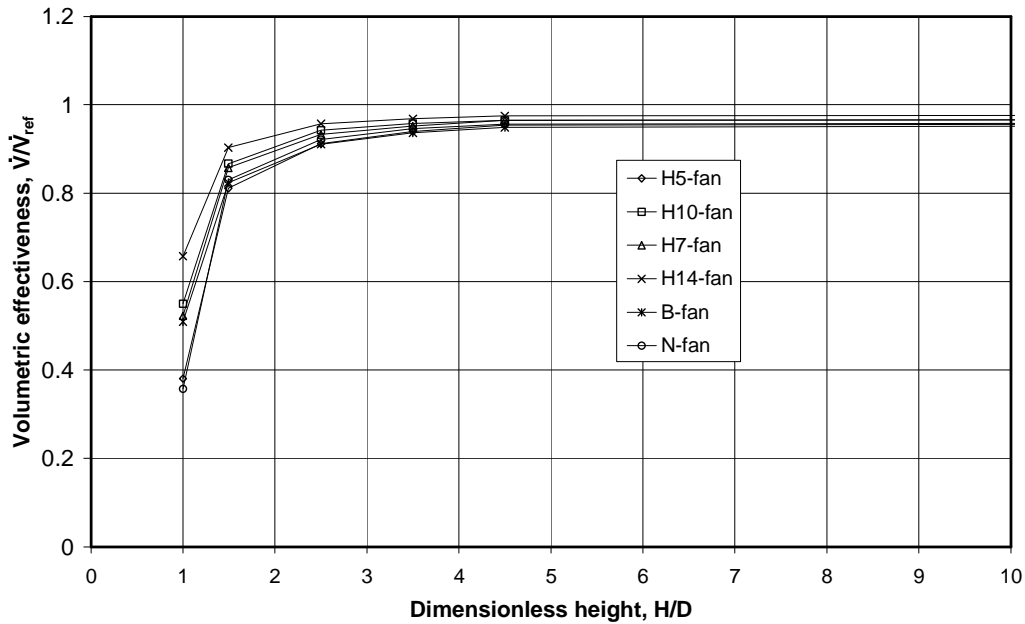


Figure 3.9: Edge fan volumetric effectiveness vs. platform height for different fan configurations.

To derive an empirical correlation for the effect of platform height on edge fan volumetric effectiveness, the volume flow rate measured at each of the points was written as a flow coefficient using equation (3.1). These flow coefficients were then converted to universal values using equation (3.3). Assuming that the fans would operate along their fan static pressure curves, the universal head coefficients were then calculated using equation (3.5). By inserting these universal head coefficients as the dependent variable into equation (3.4), the head coefficient applicable to the specific fan was calculated. A system loss coefficient specific to every fan and every platform height was then calculated from:

$$\psi = K_{loss}\phi^2 \tag{3.6}$$

The calculated set of loss coefficients are shown in Table 3.2.

Table 3.2: Calculated loss coefficients, K_{loss} , for different fans at various platform heights.

Dimensionless floor height, H/D	H5-fan	H10-fan	H7-fan	H14-fan	B-fan	N-fan
Individual fan	1.990	2.021	1.541	1.502	1.480	2.028
Infinite floor	2.197	2.275	1.733	1.707	1.667	2.221
4.5	2.309	2.390	1.797	1.809	1.840	2.345
3.5	2.415	2.465	1.894	1.893	1.934	2.422
2.5	2.637	2.638	2.045	2.032	2.139	2.620
1.5	3.606	3.583	2.712	2.773	2.941	3.484
1	20.094	12.074	9.573	8.060	9.719	23.321

The aim of the investigation was to see if a relationship between fan solidity, hub-to-tip ratio and platform height could be derived that can be used to predict the loss coefficients shown in Table 3.2. The first row of loss coefficients shown in Table 3.2 was considered to be tunnel specific only and excludes the effect of the inlet chamber. A linear correlation between the fan frontal flow area (based on the hub-to-tip ratio) and the individual fan loss coefficient was assumed (based on the evidence of Figure 3.10). The linear relationship was derived as:

$$K_{loss\ open} = 4.459(1 - \lambda^2) - 2.251 \tag{3.7}$$

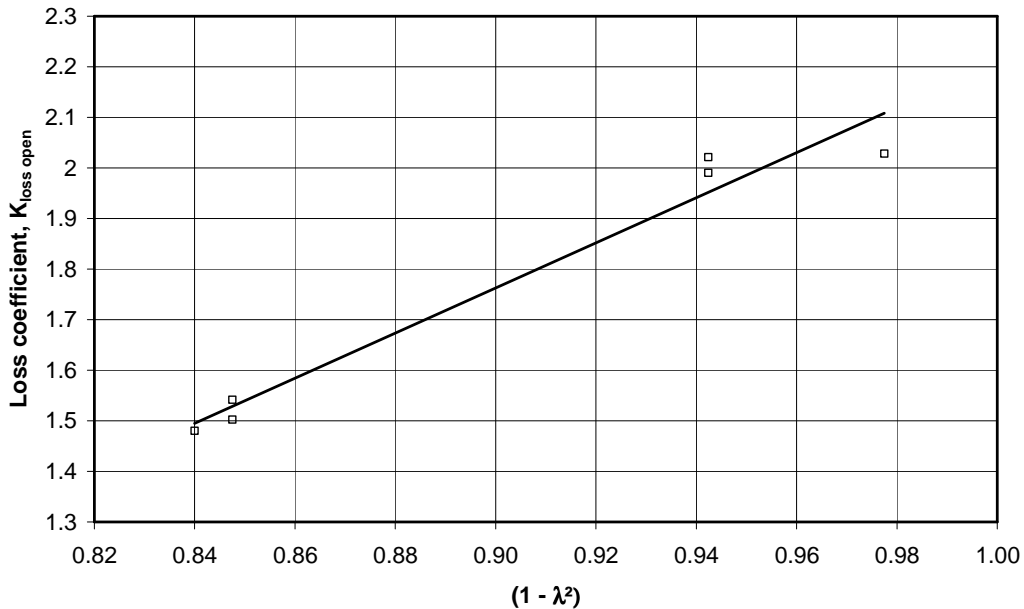


Figure 3.10: Correlation between open tunnel loss coefficient and hub-to-tip ratio.

The next step was to subtract the open tunnel loss coefficient for each of the fans from the loss coefficients shown in Table 3.2. The resulting “remaining loss coefficients” are shown in Table 3.3.

Table 3.3: Remaining loss coefficients for different fans at various platform heights.

Dimensionless floor height, H/D	H5-fan	H10-fan	H7-fan	H14-fan	B-fan	N-fan
Infinite floor	0.207	0.254	0.192	0.205	0.186	0.192
4.5	0.319	0.369	0.256	0.307	0.360	0.317
3.5	0.425	0.444	0.353	0.391	0.454	0.393
2.5	0.647	0.617	0.504	0.529	0.659	0.591
1.5	1.616	1.562	1.171	1.271	1.460	1.456
1	18.104	10.053	8.032	6.558	8.239	21.292

Since the B-fan was considered to be the reference fan a correlation for the variation in the remaining loss coefficient of the B-fan with a variation in platform height was derived from the B-fan values shown in Table 3.3 as follows:

$$K_{loss \ platform} = \frac{0.216}{\left[1 - 1.272 e^{(-0.267H/D)}\right]} \quad (3.8)$$

The exponential form of equation (3.8) was based on the equation derived by Salta and Kröger (1995). The last variable that needed to be included was the solidity of the different fans. Numerous analyses were performed and no clear relationship could be established. Looking at the remaining loss coefficients in Table 3.3, it is clear that the largest variation in remaining loss coefficient between the different fans was at the lowest platform height of $H/D = 1$. Dividing the remaining loss coefficients of Table 3.3 by the remaining loss coefficients of the B-fan (which was chosen as the platform height reference) gave the remaining loss coefficient ratios as shown Table 3.4.

Table 3.4: Ratios of remaining loss coefficients for different fans at various platform heights.

Dimensionless floor height, H/D	H5-fan	H10-fan	H7-fan	H14-fan	B-fan	N-fan
Infinite floor	1.112	1.365	1.028	1.101	1.000	1.032
4.5	0.885	1.026	0.712	0.852	1.000	0.880
3.5	0.937	0.979	0.777	0.862	1.000	0.867
2.5	0.982	0.936	0.765	0.804	1.000	0.897
1.5	1.107	1.070	0.802	0.870	1.000	0.997
1	2.197	1.220	0.975	0.796	1.000	2.584

A graph of the variation in loss coefficient ratio with solidity for the lowest platform height showed the following:

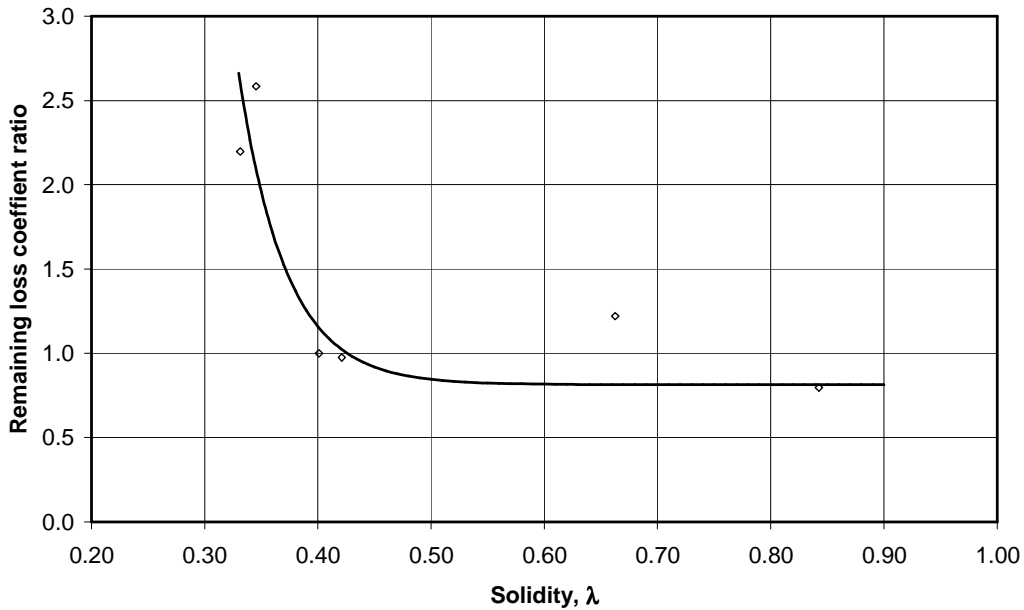


Figure 3.11: Distribution of remaining loss coefficient ratios with solidity at lowest platform height.

The solid line in Figure 3.11 is for an equation of the form $y = A + B.e^{(C.x)}$. Fitting a curve through the data in Figure 3.8 showed that A would be close to a value of 1, B would be about 1000 and C would be about -20.

Looking at the remaining loss coefficient ratios at higher platform heights, it is clear that the value of $B.e^{(C.x)}$ would have to decrease with increasing platform height, so the anticipated format was adjusted to $y = A + (B.e^{(C.x)})/(H/D)^E$. A crude optimisation exercise was conducted, where the calculated loss coefficient was compared to the loss coefficients shown in Table 3.2 and the difference between the two minimised by changing the values for A , B , C and E . The final form of the loss coefficient equation was calculated as:

$$K_{loss} = 4.459(1 - \lambda^2) - 2.251 + \left(\frac{0.216}{[1 - 1.272 e^{(-0.267H/D)}]} \right) \times \left(0.91 + \frac{2100}{(H/D)^{6.0}} e^{-21.7\sigma} \right) \quad (3.9)$$

To evaluate the accuracy of the above equation values for the loss coefficients of the different fan configurations and platform heights were calculated using equation (3.9). These values were inserted into equation (3.6) which was solved simultaneously with equation (3.5) to obtain the flow coefficients for the different fan configurations and platform heights. These were converted to values for flow rate using equation (3.1) and the volumetric effectiveness for every fan was calculated by dividing the flow rate by the calculated individual fan, open tunnel volume flow rate. Figure 3.12 shows a comparison between the calculated and measured values for volumetric effectiveness of the different fan configurations.

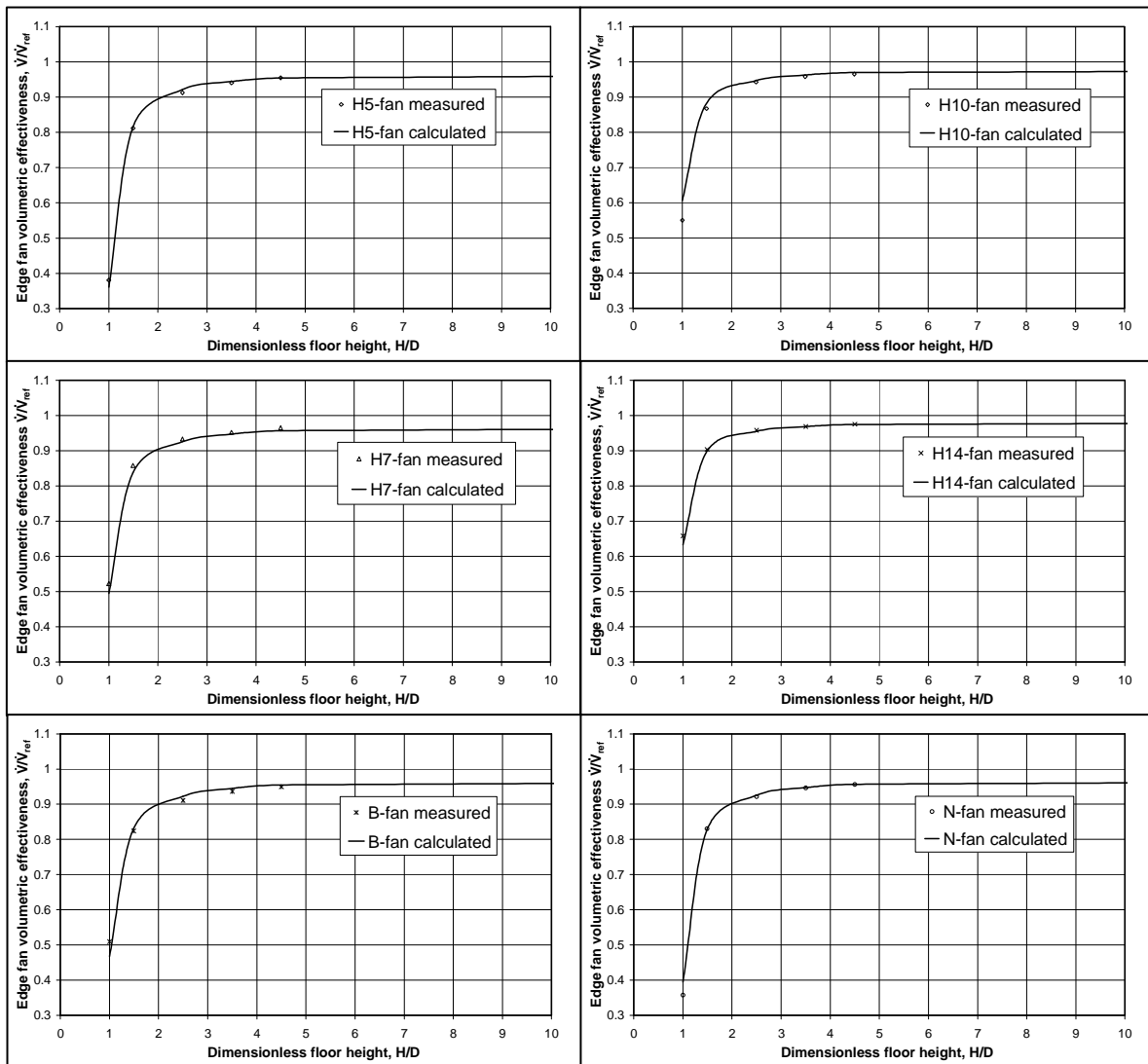


Figure 3.12: Comparison of calculated and measured volumetric effectiveness for different fan configurations.

The level of agreement shown in Figure 3.12 is excellent. It illustrates that it is possible to derive an empirical correlation that relates the velocity of the cross

flow underneath an ACC platform to the volumetric effectiveness of the edge fans while also considering the hub-to-tip ratio and solidity of the edge fans. Two issues should however be highlighted:

1. The deviation between the calculated and measured volumetric effectiveness values at $1.0 \times$ fan diameter platform height can be attributed to the assumption that the fans would operate along their fan static pressure characteristic curves (given by equation (3.5)) at all times. This assumption is invalid in instances where the flow field upstream of the fan (or fan hub-to-tip section) differs from the flow field that would exist in the relevant fan test facility at the corresponding flow rate through the fan (or fan hub-to-tip section). The fan test facility refers to the specific facility used to measure the fan static pressure characteristic curve.
2. Although the actual derived loss coefficient correlation can be applied in practice, it would have to be adapted to take into account the configuration of the specific fan system. The details of the fan system used to compile this correlation are shown in Figure E.1.

When considering the volumetric effectiveness of a fan, its efficiency and power consumption should also be taken into account. Figure 3.13 shows the variation in fan shaft power that was measured at different platform heights for the various fan configurations. Looking at Figure 3.13 it is interesting to note that the variation in shaft power with platform height is generally small.

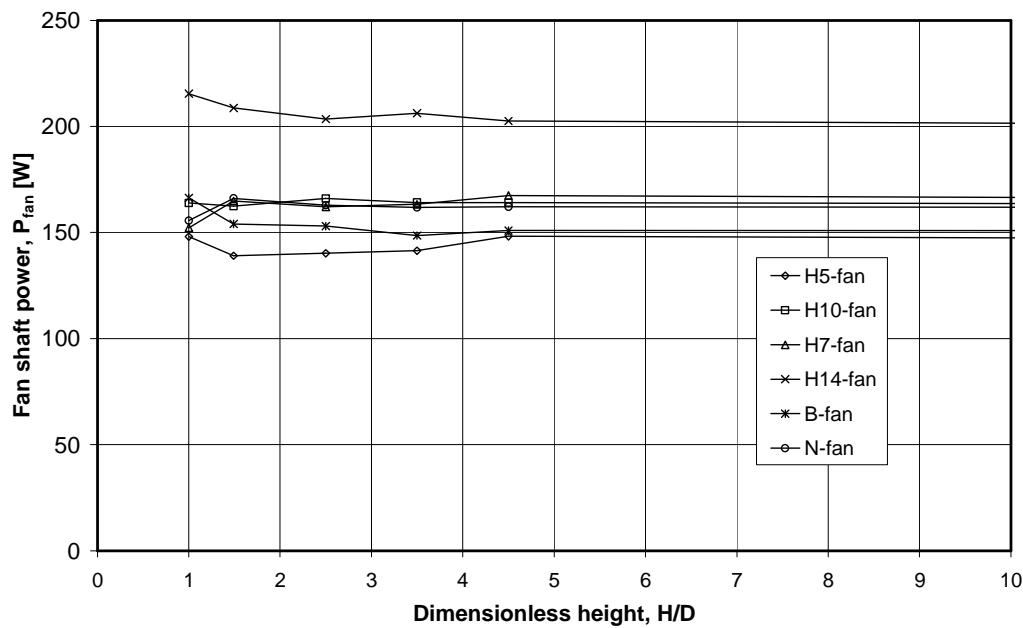


Figure 3.13: Summary of fan shaft power for different fan configurations at different platform heights.

Kröger (2004) gives the following equation for the heat transfer rate of a condenser A-frame unit:

$$Q = m_{air} \cdot c_p (T_{steam} - T_{air}) \left(1 - e^{(-UA/m_{air}c_p)}\right) \quad (3.10)$$

The function of the fan is to supply air movement that enables the transfer of energy from the steam to the surrounding atmosphere. To achieve the movement of air, the fan is supplied with energy from the fan motor, through the fan shaft. If we assume that the heat transfer rate is directly proportional to the air mass flow rate we can compare the mass flow rate to the fan shaft power to obtain a “power ratio” as follows (using an air density of 1.2 kg/m³ and undistorted volume flow rate of 1.45 m³/s):

$$PR = \frac{v_{oleff} \times 1.2 \times 1.45}{P_{fan}} \quad (3.11)$$

If we now plot the power ratio (x1000) vs. platform height, we obtain Figure 3.14.

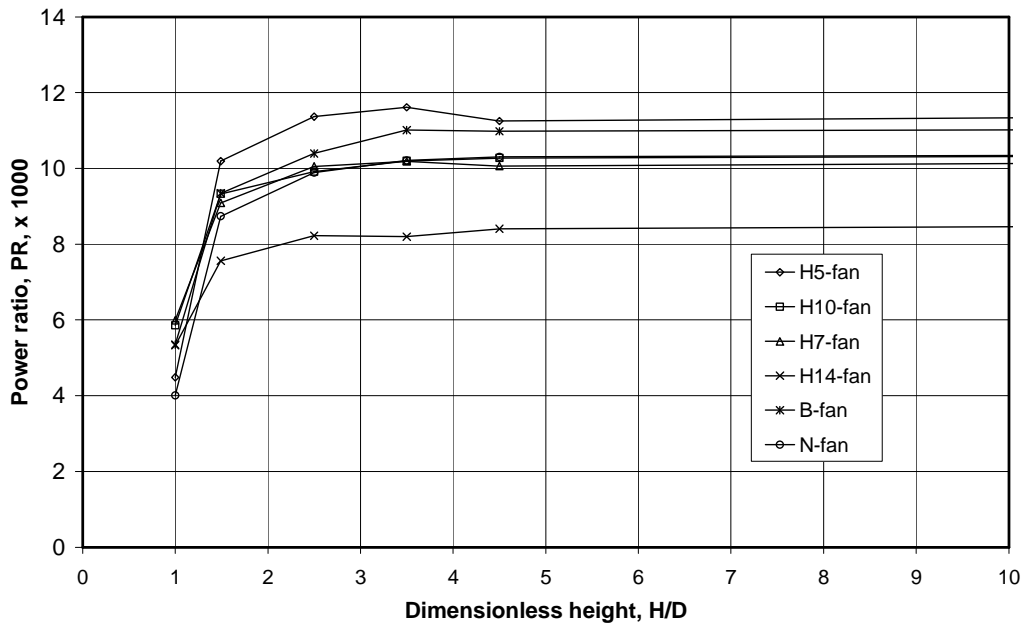


Figure 3.14: Power ratio for different fan configurations at different platform heights.

Figure 3.14 gives an indication of the relative efficiency of the various edge fan configurations. It is interesting to compare the power ratio of the fans in their undistorted state (at an infinite platform height) to their most distorted state (at 1.0 x fan diameter platform height). In the undistorted state, the power ratios of the H5-fan and the B-fan are the highest, with a value of 11 to 11.2. The

remainder of the fans have a ratio of 10 while the H14-fan has a power ratio of 8.5. These values are related to the efficiency of the particular fan being chosen for a specific operating point under undistorted inlet conditions. The fan static efficiency for the different fan configurations, measured during the single fan performance tests, is shown in Table 3.5 (the values represent test points that are located close to the operating point used for the multiple fan tests). The efficiency values in Table 3.4 correlate with the distribution of power ratio values at an infinite floor height shown in Figure 3.14. The H5- and B-fans have the highest efficiency values (about 55%), while the H10-, H7- and N-fans all have similar values (about 49%) and the H14-fan has the lowest efficiency value (39%).

Table 3.5: Single fan static efficiency at operating point ($\dot{V} = 1.45 \text{ m}^3/\text{s}$ and $p_{sf} = 56.38 \text{ Pa}$).

	H5-fan	H10-fan	H7-fan	H14-fan	B-fan	N-fan
Fan static efficiency	54	48	49	39	55	49

In the distorted state, the H10- and H7-fans have a power ratio of 6, the B- and H14-fans have a power ratio of 5.3 and the H5- and N-fans a power ratio of less than 5. This shows that the power ratio of an edge fan at its undistorted operating point is different from its distorted operating condition and that a fan with a relatively high power ratio (and efficiency) at its operating point may perform very poorly under distorted inlet conditions, as is the case with the H5-fan.

3.4.3 Detailed edge fan inlet flow field

To measure the effect of fan configuration on the inlet flow field and to evaluate the flow field predicted by the CFD analyses it was decided to measure the flow distribution adjacent and upstream of the edge fan in the multiple fan test facility using a PIV system (see Section E.3). Pictures of the resulting vector fields are given in Section F.3. To compare the results for the different combinations of edge fans and platform heights, velocity vectors were extracted directly from the measured data along specific lines, as shown in Figure 3.15. Graphs were compiled for the “U” and “V” components of the velocity vectors along these lines with the data referenced according to the platform edge and the bell mouth edge (as shown in Figure 3.15).

A complete set of the U- and V-velocity graphs is included in Section G.1. The velocity graphs along lines 1, 2 and 3 (as shown in Figure 3.15) for the different fan configurations are similar and it may be concluded that, at these locations, the inlet flow field is largely independent of fan configuration. The different flow field distributions are presented in terms of absolute velocity. Differences that occur between the velocity graphs can be attributed to small differences in the volume flow rates of the different multiple fan systems.

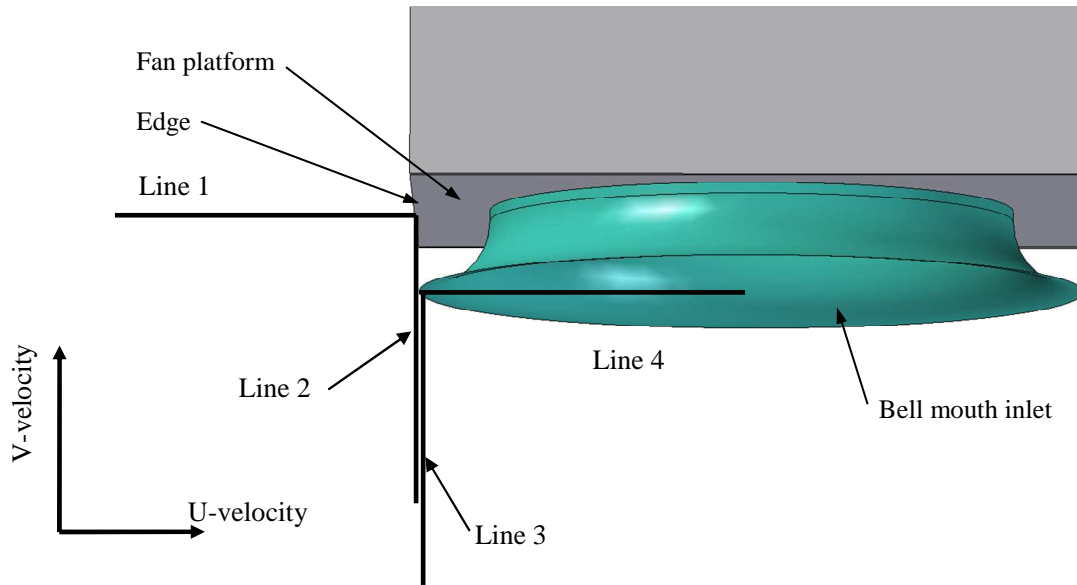


Figure 3.15: Location of detailed velocity profiles.

Figure 3.16 and 3.17 show the velocity distributions for three different fan configurations along line 4 (see Figure 3.15) at a platform height of 2.5 x fan diameter.

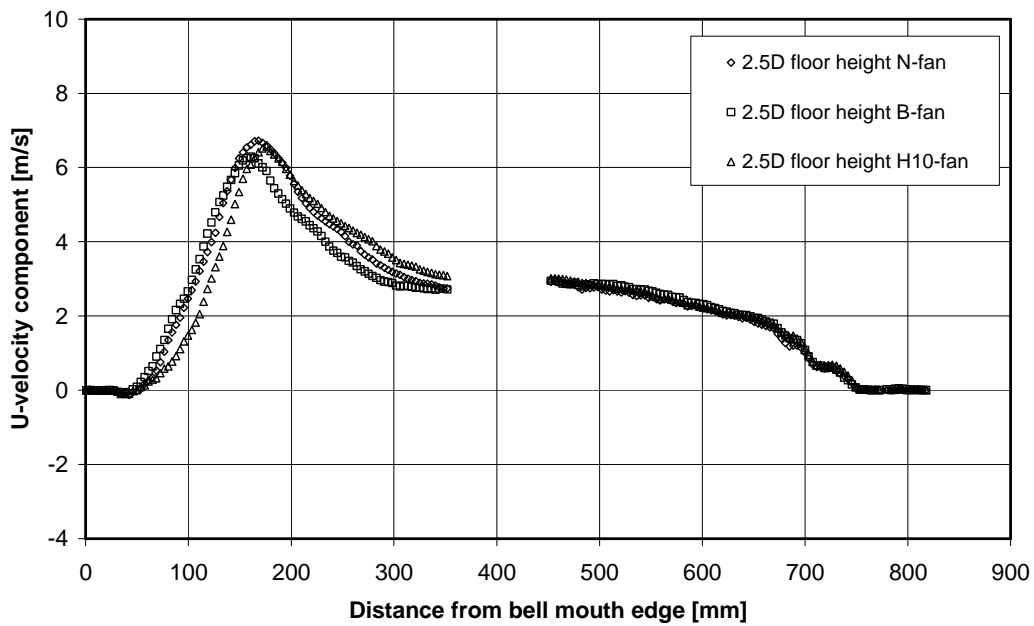


Figure 3.16: U-velocity component vs. distance from bell mouth edge along line 4 for different fan configurations at 2.5 x fan diameter platform height.

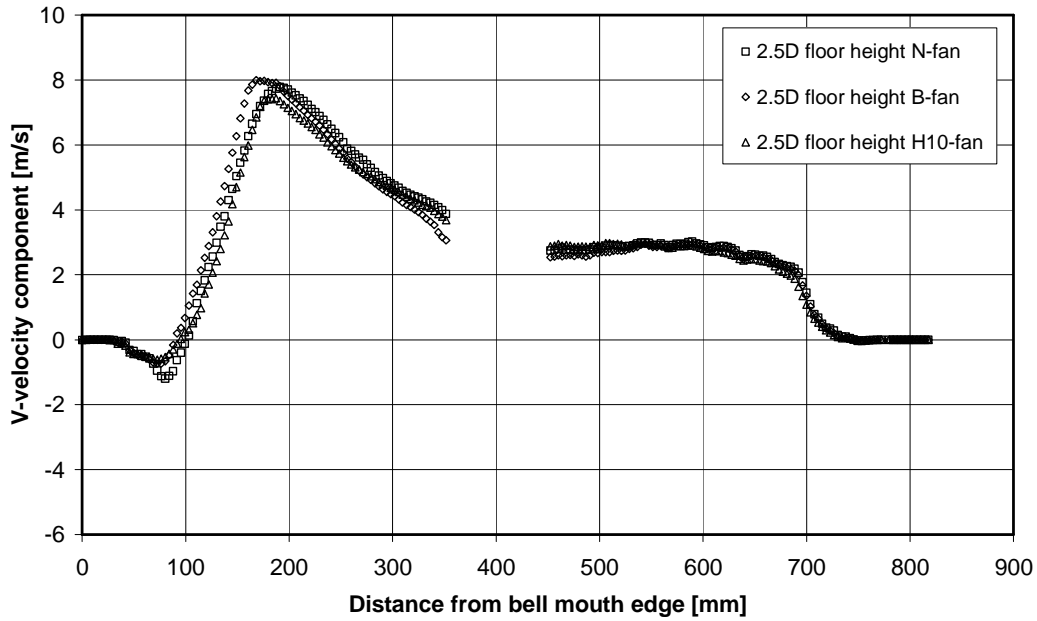


Figure 3.17: V-velocity component vs. distance from bell mouth edge along line 4 for different fan configurations at 2.5 x fan diameter platform height.

Figures 3.16 and 3.17 clearly show a negligible difference in inlet flow field distribution for the different fan configurations. All the velocity distributions along line 4 display a central gap in the velocity profile which is directly attributed to the presence of the fan shaft which protrudes quite far forward. Because of reflections caused by the shaft, its image is “blanked” out and consequently a large zero velocity zone is shown.

The only significant difference between the different fan configurations can be observed at a platform height of 1.0 x fan diameter along line 4 (see Figures 3.18 and 3.19). At first glance the difference in velocity distribution along line 4 for the different fan configurations seems to counter the results from the multiple fan tests shown in Figure 3.9. Figure 3.9 shows that the B-fan and H10-fan both have considerably higher volumetric effectiveness values (in the order of 0.5 compared to 0.37) than the N-fan. This does not necessarily agree with the results of Figure 3.17 which shows a lower V-velocity distribution for the B-fan compared to the other two fan configurations. However, the velocity profile is shown along a single 2-dimensional plane while the inlet flow field at this platform height is actually highly 3-dimensional. The shape of the flow field is investigated further in Chapter 5.

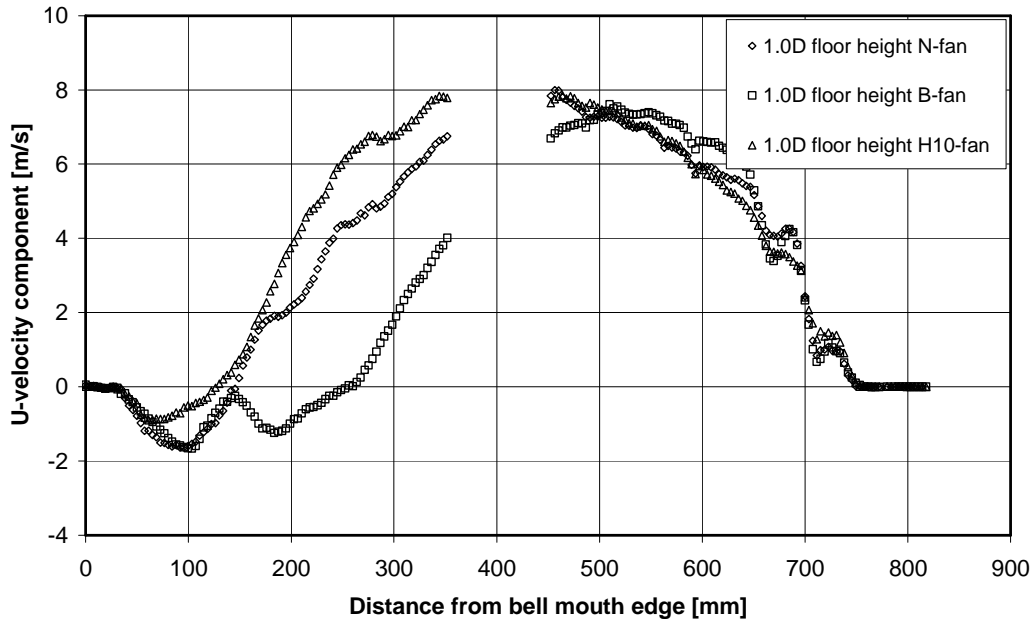


Figure 3.18: U-velocity component vs. distance from bell mouth edge along line 4 for different fan configurations at 1.0 x fan diameter platform height.

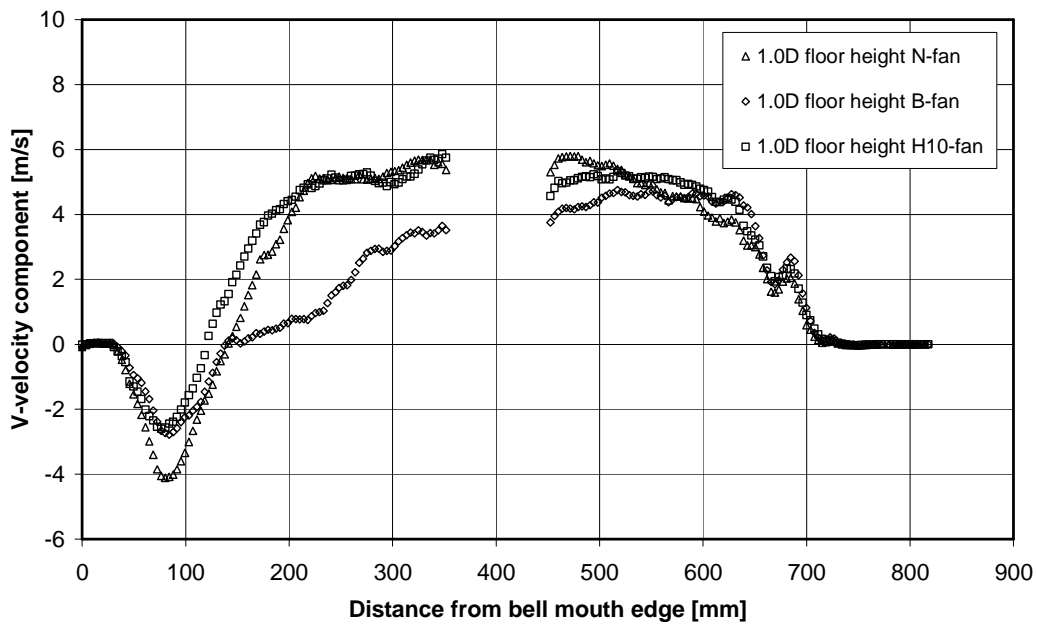


Figure 3.19: V-velocity component vs. distance from bell mouth edge along line 4 for different fan configurations at 1.0 x fan diameter platform height.

3.5 Summary

3.5.1 Overall individual fan characteristics

The individual fan performance curves (fan static pressure vs. volume flow rate) in Figure 3.7 show a difference in the slope of the curves, depending on the hub-to-tip ratio and average blade solidity of the fan. An empirical method is derived that correlates the performance curves of the different fans to the performance curve of the small diameter B-fan. Since the method is essentially non-dimensional it can, in principle, be applied to any fan configuration (blade solidity and hub-to-tip ratio) within the envelope of the experimental fans used in this study to determine an approximate performance curve for the fan configuration. This performance curve may then be used in the pressure jump method detailed in Chapter 4 to predict the performance of multiple fan installations.

3.5.2 Multiple fan performance

The individual fans tested previously were used as edge fans in an experimental 3-fan installation. The volumetric effectiveness of the edge fan at different platform heights was measured and shows a direct correlation with the slope of the individual fans tested previously, i.e. edge fans with a performance curve with a steep slope (fan static pressure vs. volume flow rate) have a higher volumetric effectiveness when operating at high levels of inlet flow distortion. This confirms the results of Bredell et al. (2006) who showed that a fan with a steep performance curve has a relatively high volumetric effectiveness when used as an edge fan.

The volumetric effectiveness of a fan installation under distorted inlet conditions should never be the sole consideration when selecting a fan. The efficiency and power consumption of the fan should always be taken into account. A fan configuration that exhibits high volumetric effectiveness at low platform heights may have a particularly low efficiency (and high power consumption). The increased power generation ability that results from higher volumetric effectiveness should be offset against the possible higher fan power consumption associated with a particular fan configuration to ensure that the net effect of the proposed installation is positive.

- To predict the volumetric effectiveness of an edge fan with different hub-to-tip ratios and blade solidities at different platform heights an empirical correlation was derived that calculates a loss coefficient for the fan system. Assuming that the fan would operate along its single fan performance curve, the intersection between the performance and system curve gives the operating point of the edge fan. The edge fan system loss coefficient is separated into an open tunnel loss component and a platform height loss component. The open tunnel loss component is assumed to be dependant on the annular flow area of the fan while the platform loss coefficient is assumed to be a function of the platform height and the fan solidity. The correlation is only applicable to the specific system format that was tested

and its possible use to analyse other system formats should be investigated. The intention was however not to investigate the effect of platform height as such and the variation in platform height was actually used to vary the level of flow distortion upstream of the edge fan.

3.5.3 Edge fan inlet flow field

The inlet flow field of the edge fan was measured at three different heights and for three different fan configurations. The results show a negligible difference between the inlet flow field distributions of the different fan configurations, except at 1.0 x fan diameter platform height where a difference in the flow field distribution for the three configurations immediately upstream of the fan rotor was noted. At this particular platform height the flow field distributions for the N-fan and H10-fans are similar, while the distribution for the B-fan is completely different. The N- and H10-fans both have small hub-to-tip ratios (0.15 and 0.24 respectively) while the B-fan has a hub-to-tip ratio of 0.4. This may indicate that the hub-to-tip ratio of the edge fan affects the velocity distribution immediately upstream of the fan at a low platform height (and a high level of inlet flow distortion).

4 AXIAL FAN MODELS FOR ACCs

This chapter describes the CFD models and results that formed part of this investigation. Details of the different simplified fan modelling methods are included in Appendices B, C, and D. Results of the CFD analyses are also included in Appendix G.

4.1 Introduction

The modelling of an axial flow fan in CFD can serve one of two purposes. The first purpose of a CFD analysis would be to simulate the axial flow fan as part of the fan development process. The fan model would be highly detailed and will include, for instance, the blade tip clearance along with the exact blade tip geometry. The second purpose would be to simulate the effect of the fan, typically when evaluating the performance of a system. The fan itself does not have to be modelled and can be represented by momentum source terms based on the geometric properties and operational parameters of the fan (excluding details such as the tip clearance of the fan). When evaluating the height of an ACC platform ranging from 20 m to 50 m, the fact that the fan model excludes the detail of a 20 mm blade tip clearance would have a small effect on the results.

When modelling the performance of an axial flow fan that is subjected to distorted inlet conditions, one is forced to consider a combination of the above two approaches. The performance of the axial flow fan, typically evaluated under “ideal” standard conditions (BS 848, 2007), has to be combined with the effect of the system into which it is installed. The system includes the proximity of other fans, the proximity of structures and the orientation of the fan being investigated, relative to these other fans and structures. This investigation considers the specific approach where the fan that is being investigated is modelled in the system as a collection of momentum source terms, to such a level of accuracy that the effect of varying various geometric parameters of the fan can be evaluated.

To follow this approach, the first step in the CFD process would be to show that the performance of the axial flow fan under standard inlet conditions can be replicated using the simplified CFD model (described in Sections 4.2, 4.3 and 4.4). Once it has been confirmed that the simplified fan model performs acceptably under standard conditions (see Section 4.5), the fan model is used to investigate the performance of the flow system (described in Section 4.6). This is the approach followed by Meyer and Kröger (2001), Meyer (2005) and Bredell et al. (2005) when using the actuator disc method to simulate an axial flow fan in a multiple fan environment. In Section 4.7 this investigation takes the CFD process a step further by considering the results of the CFD simulations of the flow system and compares these results to experimental measurements of the fan inlet flow field and system performance results.

Axial flow fans can be modelled using various methods. Ultimately, it can be argued that the most accurate method would be to model the fan blade geometry in full detail, including the tip clearance and blade-to-hub connection geometry. However, such a CFD model would require large computational resources (van der Spuy et al., 2010). When the flow is axisymmetric around the rotational axis of the fan, the size of the CFD model can be reduced by modelling only one blade sector and using periodic boundaries to represent the other blade sectors (Le Roux, 2010). When considering multiple axial flow fans in a system, the flow through the fans is not axisymmetric and a full 360° representation of the fan is required. The focus is therefore on using simplified axial flow fan models. The actuator disc (see Section 4.2) and pressure jump methods (see Section 4.3) are used to compile two such models. An additional, third method, the extended actuator disc method is introduced in Section 4.4. A summary of all CFD simulation that were performed as part of this study is shown in Table 4.1

Table 4.1: Summary of all CFD simulations.

Single fan variable resistance	Single fan fixed resistance	Multiple fan bell mouth no walkway	Multiple fan bell mouth with walkway	Multiple fan no bell mouth no walkway
		7 different floor heights	7 different floor heights	7 different floor heights
PJM, ADM and EADM	PJM, ADM and EADM	PJM, ADM and EADM for edge fan	EADM for edge fan	EADM for edge fan
N-fan	N-fan	N_N_N	N_N_N	N_N_N
B-fan	B-fan	B_N_N	B_N_N	B_N_N
H10-fan	H10-fan	H10_N_N	H10_N_N	H10_N_N

4.2 The actuator disc method (ADM) applied to individual fans

The ADM represents the effect of an axial flow rotor by a step change in the tangential velocity through a parallel annulus, where the position of the step change coincides with the centre of the plane of rotation of the rotor. This particular method simulates the operation of an axial flow fan by calculating the effect of the individual fan blades on the flow through the machine, based on the lift and drag characteristics of the blade elements. Thiart and von Backström (1993) made use of empirical correlations to establish the lift and drag characteristics of the blade profiles used in simulations. The ADM was developed further by Meyer and Kröger (2001). The authors provide extensive details of the ADM by modelling a specific axial flow fan, referred to as the B-fan (see Appendix A). The actuator disc method (ADM), its implementation and its initial verification are described in Appendix B. The CFD modelling of fan blade elements to obtain their lift and drag characteristics for use in the ADM is shown in Appendix C.

In Appendix B, the CFD results are verified by comparing them to experimental data obtained on a BS 848 part 1 (BS 848, 2007) Type A test facility (see Figure B.4). The investigation described in this chapter was however conducted on a test facility with a different test format (see Chapter 3) and therefore the use of the ADM on this specific facility also had to be confirmed.

4.2.1 Geometry and mesh

The CFD model that was used in this investigation represented the single fan test facility shown in Figure 3.3. Figure 4.1 shows the details of the corresponding CFD geometry, as used to model the 630 mm diameter B-fan (see Appendix A). The pre-processing was performed using Gambit® version 2.4.6. The same geometry was used to represent all the fans used in this investigation, with provision being made for different hub diameters and lengths only.

The geometry was modelled with a cubical open air space with a 3.0 m side length in front of the bell mouth inlet. To enable the specification of different flow rates through the fan the sides of the open air space were modelled as inviscid boundaries with the one end specified as a velocity inlet. The bell mouth inlet was modelled as thin wall boundaries protruding into the open air inlet space. The fan section was modelled separately to allow for the specification of the actuator disc and included the obstruction formed by the hub. The fan axis of rotation coincided with the z-axis of the geometry. The hub was modelled as a wall rotating counter-clockwise (when viewed from the upstream direction) around the z-axis. The fan section was connected to the inlet chamber and the outlet pipe using unmatched boundaries. The fan outlet pipe section also included the flow obstruction formed by the electric motor. The plenum chamber section included a porous section to simulate the mesh sheet as detailed in Figure 4.1. The outlet of the test facility was modelled as a pressure boundary.

To ensure a cell size growth rate and direction that would be suitable for the entire operating range of the fan it was decided to use unstructured mesh elements. The geometry was meshed in Gambit® using tetrahedral cells that were converted to polyhedral cells using the standard routine in ANSYS Fluent®. The use of polyhedral cells reduced the total mesh volumes in the reference model from 2.4 million to 1.4 million.

For this specific test facility the distance that the bell mouth protrudes into the computational domain is 120 mm, with its bell diameter extending from 630 mm to 800 mm at its outer edge (in other words about 100 mm on either side). The length of a typical fan blade is between 200 and 250 mm with a thickness of 5 mm. The cell size next to the fan bell mouth was therefore set to have a 10 mm side length using a size function expanding at a ratio of 1.1 to a maximum size of 50 mm, a distance of 1m upstream of the bell mouth. The cell side length on the outside boundaries of the inlet chamber was set to 100 mm. The cell size at the

fan outlet perimeter was set to have a 5 mm side length, expanding to a maximum size of 50 mm at the end of the outlet pipe, before it enters the plenum chamber. Although shown to have a small effect on the results (see Appendix B) the bell mouth was modelled with a boundary layer mesh having a cell height of 5 mm at the bell mouth wall. The fan outlet pipe wall was modelled with a boundary layer cell height of 2 mm at the wall.

The ADM determines the momentum source terms at a central disc (coinciding with the rotor centre plane) using velocity values obtained from reference discs upstream and downstream of the central disc. The cell structure is manipulated so that a domain of one cell thickness coincides with the location of each of the centre and reference discs. The values of the momentum source terms are calculated in a user-defined subroutine. The subroutine was developed further from the routine used by Bredell (2005). To simplify referencing between individual cells inside the discs, a structured mesh was used for these discs (see Figure 4.2). As mentioned in the previous paragraph, the fan section (structured mesh) and inlet chamber and outlet pipe (unstructured meshes) were connected to each other using unmatched boundaries. The fan section was modelled using 8 mm thick discs. The annular section of the fan was modelled using 40 radial elements and 200 circumferential elements. The discs directly upstream and downstream of the hub section were meshed using unstructured hexahedral elements with a maximum side length of 5 mm.

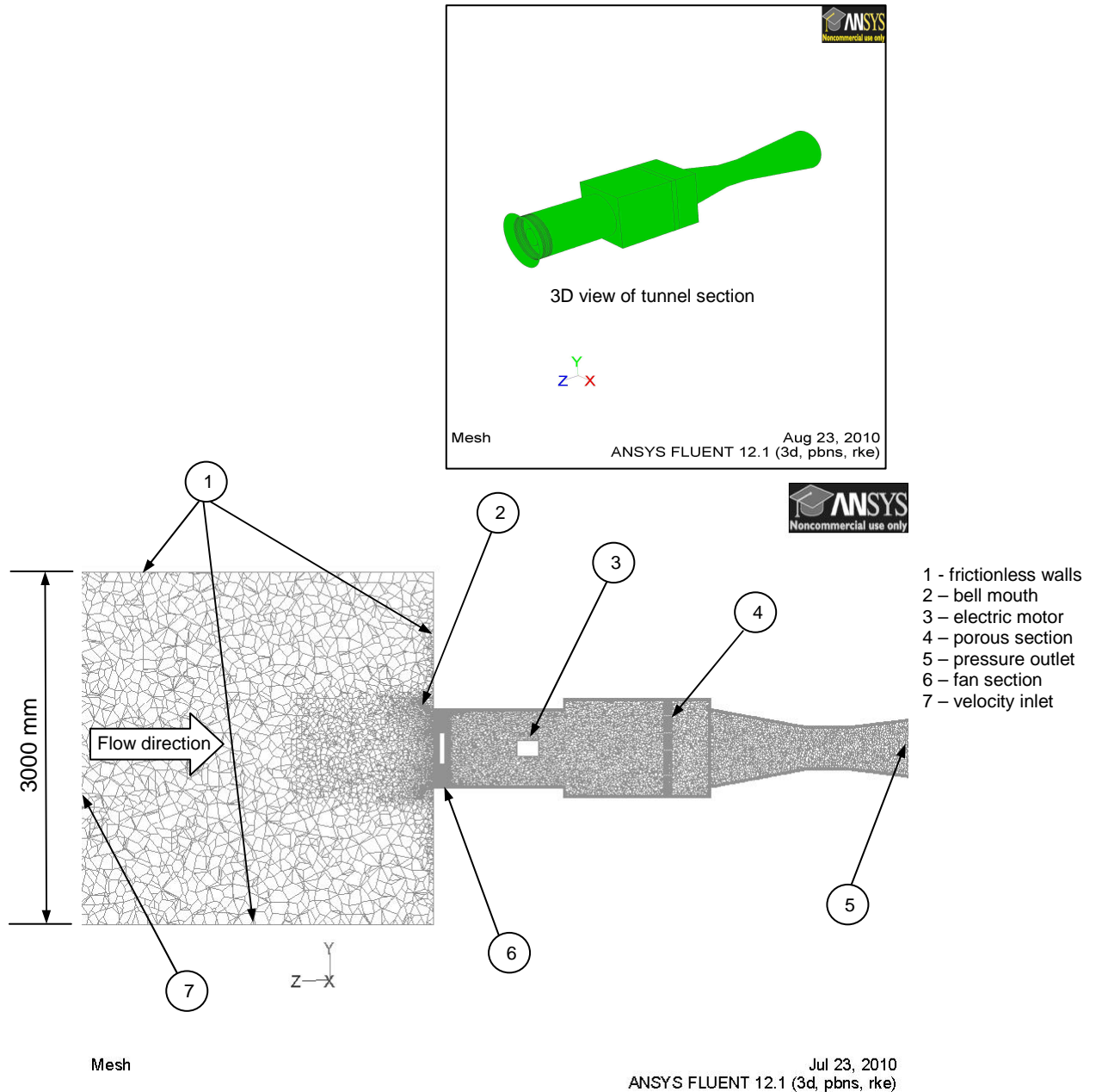


Figure 4.1: CFD geometry of single fan test facility.

The intention was to use the same mesh for all the single fan simulations (in other words for all the different flow rate values and fan configurations). The same mesh settings (initial size and growth rate) were also used for the multiple fan simulations. The mesh size, as detailed in Figure 4.1 was considered conservative. However, to confirm the integrity of the mesh, the unstructured mesh density and the structured fan section mesh density were investigated. All simulations were performed using the 630 mm diameter B-fan parameters.

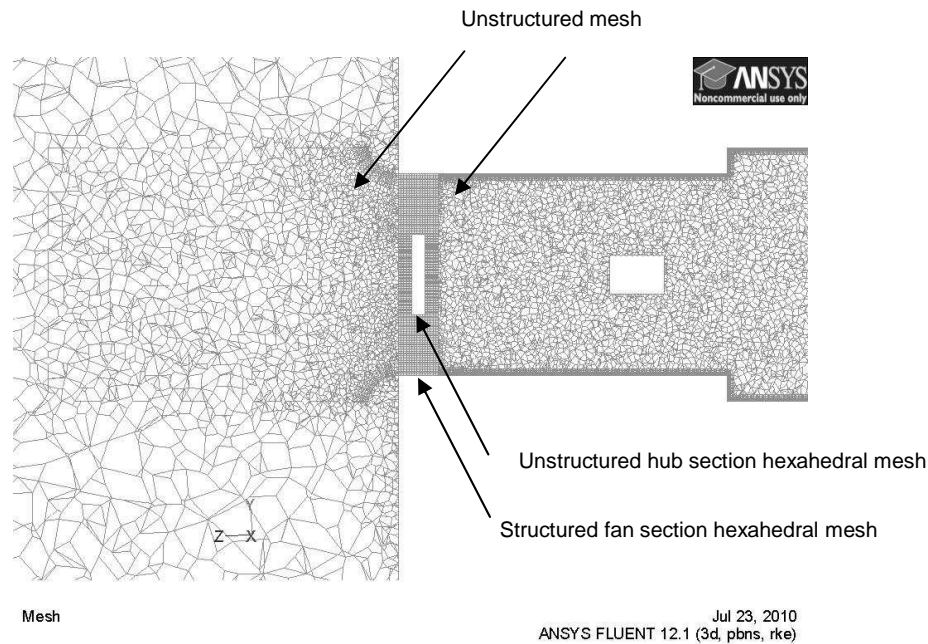


Figure 4.2: CFD geometry showing structured and unstructured meshes.

Since the initial mesh was already considered conservative, it was decided to evaluate the effect of coarsening the mesh. The investigation focussed on the effect of the inlet flow field on the fan's performance, therefore the mesh was coarsened by changing the side lengths of the elements directly up- and downstream of the fan section and not the entire mesh count. Starting from the initial mesh count of 1.4 million elements, the unstructured mesh density was adjusted as follows:

Mesh model 1: the mesh was set to have a size function with 20 mm side length elements expanding to 100 mm side length elements upstream of the fan and 10 mm side length elements expanding to 100 mm downstream of the fan section. The sides of the inlet chamber were meshed with 200 mm side length elements. The total cell count for this model was 800 000.

Mesh model 2: the mesh was set to have a size function with 40 mm side length elements expanding to 200 mm side length elements upstream of the fan and 20 mm side length elements expanding to 200 mm downstream of the fan section. The sides of the inlet chamber were meshed with 400 mm side length elements. The total cell count for this model was 690 000.

The results of the unstructured mesh density investigation are shown in Figure 4.3. The investigation shows that the change in simulation results with a change in the indicated mesh density from 1.4 million to 800 000 to 690 000 elements is negligible. The good correlation achieved between experimental and numerical results (specifically when using the PJM in Figures 4.9, 4.10 and 4.11) confirmed the quality of the mesh that was used.

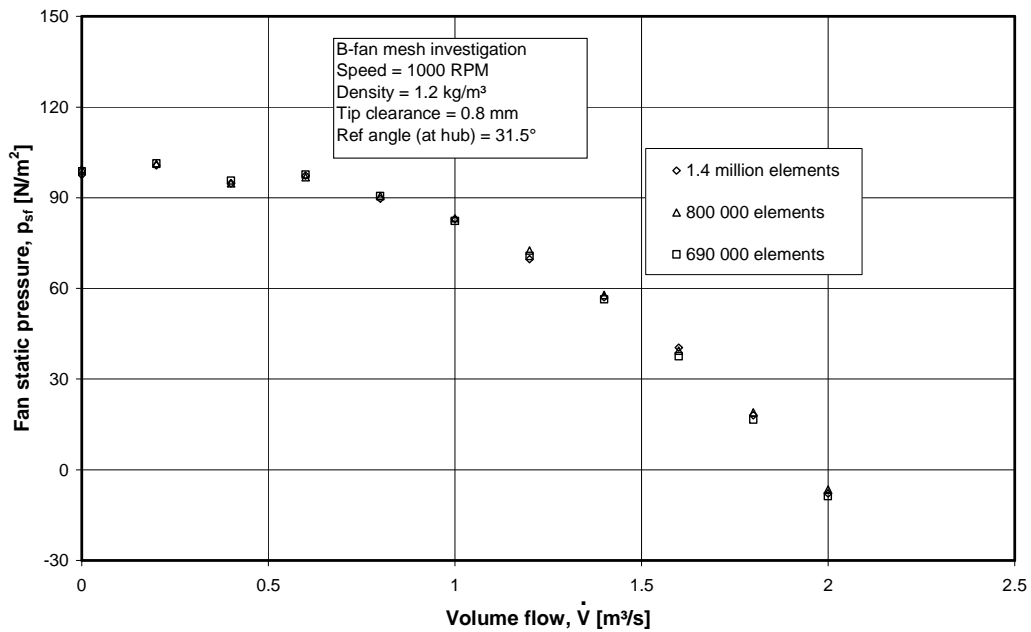


Figure 4.3: Static pressure vs. volume flow rate for unstructured mesh density investigation.

Starting from the initial model that contained 8000 elements, the structured fan section mesh density was adjusted as follows:

Disc model 1: the mesh in the fan section was adjusted to have 30 radial and 160 circumferential elements. The rest of the geometry was left unchanged, as per the reference model.

Disc model 2: the mesh in the fan section was adjusted to have 20 radial and 120 circumferential elements. The rest of the geometry was left unchanged, as per the reference model.

The results of the fan section mesh density investigation are shown in Figure 4.4. Once again the investigation shows that the change in simulation results with a change in mesh density for the fan section is negligible.

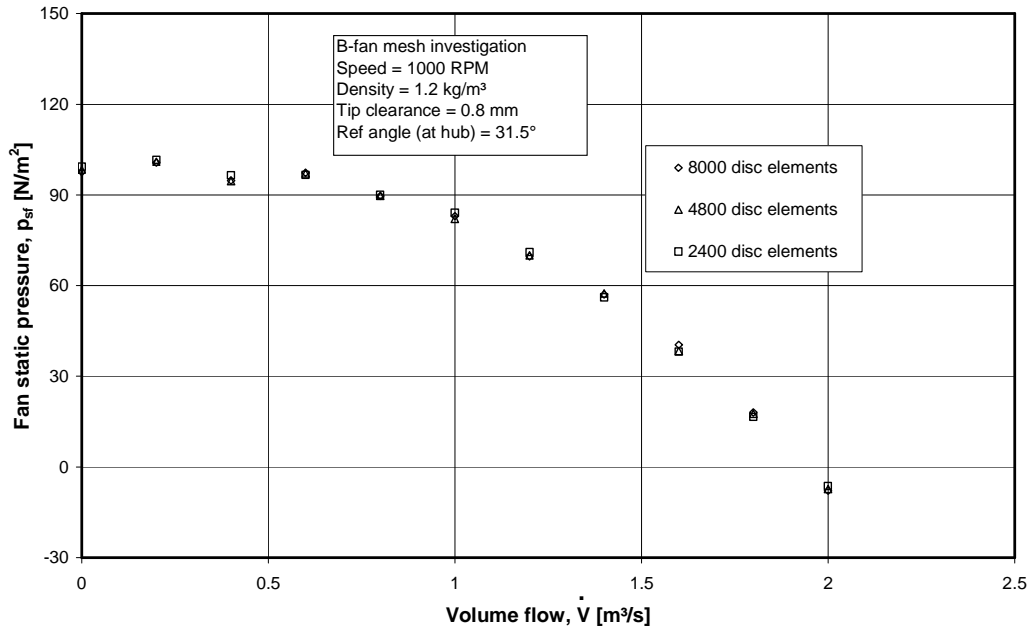


Figure 4.4: Static pressure vs. volume flow rate for fan section mesh density investigation.

The possibility that the position of the reference upstream and downstream discs might influence the results of the ADM analyses was considered by performing a disc position investigation. The investigation was conducted as follows (with all axial distances indicated relative to the fan plane of rotation):

Upstream disc: the geometry and mesh of the reference model was used. Four positions for the upstream reference disc were investigated.

Downstream disc: the geometry and mesh of the reference model was used. Four positions for the downstream reference disc were investigated.

The results of the disc position investigation are shown in Figures 4.5 and 4.6. The results show that the position of the upstream disc has very little effect on the fan pressure curve. The downstream disc has a more visible effect, although also relatively small. Based on these results, it was decided to use a minimum distance of 50 mm for the downstream disc position, while the upstream disc position was selected to be more than 33 mm.

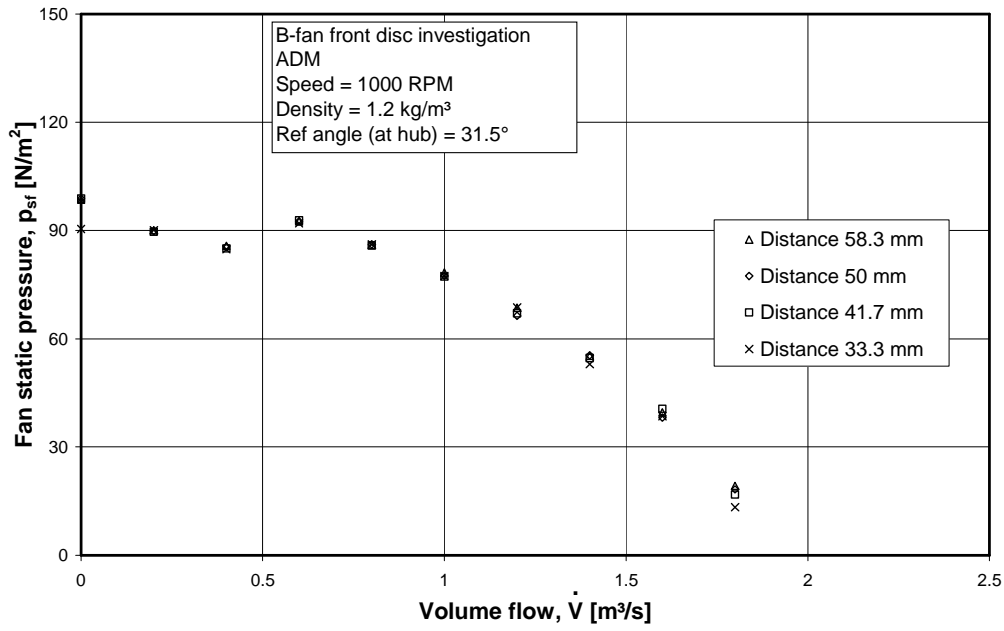


Figure 4.5: Static pressure vs. volume flow rate for upstream disc position investigation.

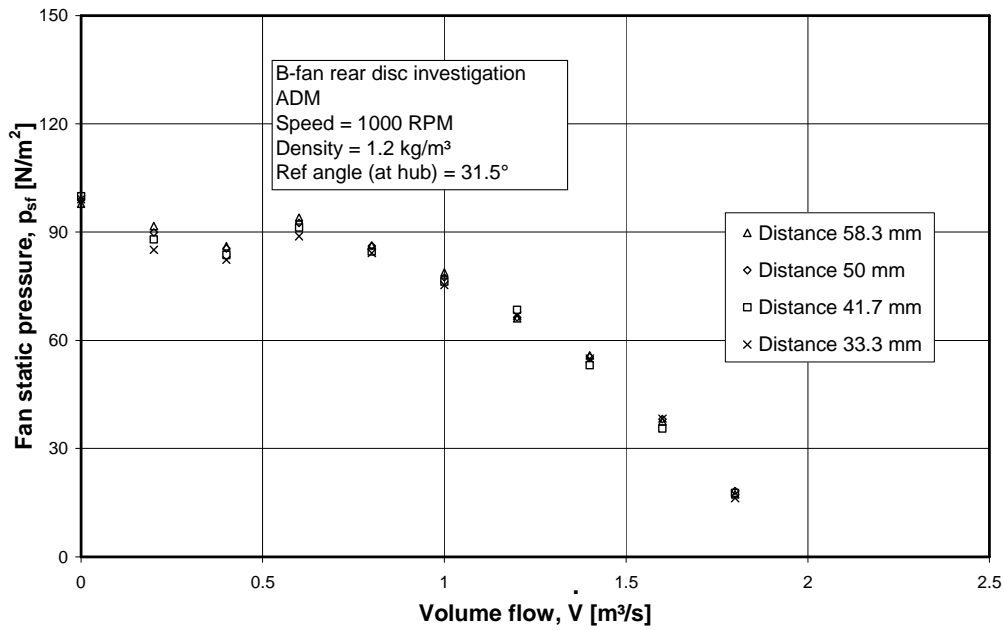


Figure 4.6: Static pressure vs. volume flow rate for downstream disc position investigation.

4.2.2 Boundary and cell zone conditions

The boundary or cell zone conditions that were applied to the model detailed in Section 4.2.1 are shown in Table 4.2.

Table 4.2: Summary of boundary or cell zone conditions

Boundary or zone name	Values
Inlet	Mass flow set according to operating point Turbulence intensity = 3% Turbulence length scale = 0.02 m
Outlet	Static pressure = 0 N/m ²
Inlet chamber walls	Wall shear = 0 N/m ²
Hub walls	Rotational speed = 104.7 rad/s
Rotor disc	Source terms set in x-, y-, and z-direction, linked to user subroutine
Porous mesh (modelled using a porous zone)	Inertial resistance factor = 2.442 m ⁻¹ Viscous resistance factor = 1173168 m ⁻² Applied in z-direction

The values for turbulence intensity and length scale were based on estimates obtained following the guidelines set in the ANSYS Fluent[®] user manual (ANSYS Fluent[®], 2009) taking into account the location of the test facility inside a closed off laboratory, as well as the distance between the inlet boundaries and the fan inlet faces of the numerical model. The turbulence intensity in the flow entering the fans was confirmed by doing hot-film measurements upstream of the edge fan (see Appendix E).

ANSYS Fluent[®] uses a boundary condition referred to as a “porous zone”. The porous mesh section in the facility was modelled as a porous zone. The pressure loss through the porous zone is modelled as a source term in the momentum equation:

$$S_{i, mesh} - \frac{\partial p}{\partial x_i} - \frac{\partial}{\partial x_i}(\tau_{ij}) = \frac{\partial}{\partial t}(\rho U_i) + \frac{\partial}{\partial x}(\rho U_i U_j) \quad (4.1)$$

where the source term is related to the pressure drop over the mesh as (note that the negative sign indicates a momentum sink):

$$S_{i,mesh} = \frac{-delp_{mesh}}{\Delta n} \quad (4.2)$$

The porous resistance values were obtained from the measured resistance curve, at a density of 1.2 kg/m^3 (see Appendix E):

$$delp_{mesh} = 0.0981v^2 + 1.4782v \quad (4.3)$$

The resistance over the porous medium is divided into an inertial and a viscous term. The inertial resistance factor was calculated from:

$$0.0981 = C_z \frac{1}{2} \rho \Delta n \quad (4.4)$$

With the density equal to 1.2 kg/m^3 and the length of the porous medium equal to 0.07 m , the value for the inertial resistance coefficient was calculated as:

$$C_z = 2.442 \text{ m}^{-1}$$

Similarly the viscous resistance factor was calculated from:

$$1.4782 = \frac{\mu}{\alpha_z} \Delta n \quad (4.5)$$

With the viscosity equal to $1.8 \cdot 10^{-5} \text{ Ns/m}^2$, the value for the viscous resistance coefficient was calculated as:

$$\frac{1}{\alpha_z} = 1173168 \text{ m}^{-2} \quad (4.6)$$

4.2.3 Simulation

All CFD analyses were simulated as steady state, incompressible flow using ANSYS Fluent[®] version 12.1. In all instances the working fluid was air at $20 \text{ }^\circ\text{C}$ and 1 atmosphere pressure (density 1.2 kg/m^3 and viscosity $1.8 \cdot 10^{-5} \text{ Ns/m}^2$ (White, 2008)). The simulations were performed using the k- ϵ realizable turbulence model because of its ability to handle large flow field strains (see Appendix B). Second order discretisation schemes were used for all the flow variables forming part of the simulations (see Appendix B). To calculate the gradients of the variables in the flow equations the least squares cell based method was used because of its ability to handle unstructured meshes. The simulations made use of the default under-relaxation factors in ANSYS Fluent[®].

To set up the data matrices for the velocity information in the upstream and downstream discs of the ADM and to establish the correct referencing system

between these discs and the central disc, the simulations had to be initialised using a specific user subroutine that formed part of the user subroutine described in Section 4.2.1. The simulations were set to converge to normalised residual values of 10^{-4} within a maximum of 2000 iterations. Convergence of the momentum and turbulence quantities was within the mentioned limits. The continuity residuals converged to between 10^{-3} and 10^{-4} (or lower), depending on the flow rate being simulated.

All simulations were performed using four processors in parallel. The mesh was partitioned so that the entire fan rotor section was contained within one of the partitions. This was required to enable the transfer of data between the fan rotor and upstream and downstream discs. The simulations were performed on Stellenbosch University's "High Performance Cluster". Simulations were performed for the N-fan, B-fan, and H10-fan (see Appendix A).

4.3 The pressure jump method (PJM) applied to individual fans

The PJM utilises a static-to-static pressure increase that occurs at the location of the fan rotation plane. The value of the static pressure increase is based on the value of the volume flow rate passing through the fan rotation plane. The main advantage of the PJM lies in the minimal amount of information required for its implementation compared to the ADM. The ADM requires detailed information on the fan blade layout and profiles. This information is often considered proprietary to the manufacturer of a specific fan and would not necessarily be available when performing the simulation or design of an ACC-system. The PJM is based on the published fan static pressure vs. volume flow rate curve of the fan manufacturer. Besides the fan static pressure curve, information regarding the test facility used to compile the fan static pressure curve is also required.

Van Staden (2000) used the fan static pressure vs. volume flow rate curve of a particular fan to derive axial momentum source terms for use in his simulation of an ACC. He used an iterative process to refine the source terms, while van der Spuy et al. (2009) describes an explicit method of implementing the PJM by converting the fan total-to-static pressure characteristics of the fan to a static-to-static pressure characteristic. The pressure jump method (PJM), its implementation and its initial verification are described in detail in Appendix D. This section describes the application of the PJM to the test facility referred to in Chapter 3.

4.3.1 Geometry and mesh

The same geometry and mesh were used for the PJM and the ADM. For simulations using the PJM, the hub was modelled as a stationary wall centred around the z-axis. Although the structured mesh of the rotor section used for the ADM was no longer required, using the same mesh for both configurations meant that the same unmatched boundaries were used in the PJM and ADM model. The PJM calculates a momentum source term in the axial flow direction for the cells

downstream of a specified cell face. The standard ANSYS Fluent® “fan” boundary condition is applied to this cell face.

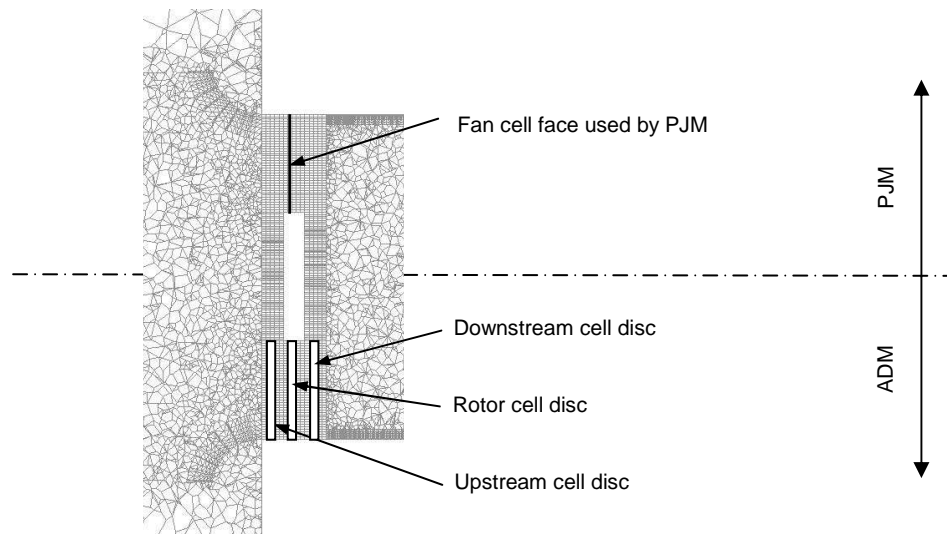


Figure 4.7: Location of PJM cell face relative to ADM rotor disc.

The “fan” face was therefore specified as the upstream face of the rotor cell disc used in the ADM (see Figure 4.7).

4.3.2 Boundary and cell zone conditions

The same boundary conditions were applied to both the ADM and PJM (see Table 4.2), with the only exception being the use of the ANSYS Fluent® “fan” boundary in the PJM instead of the user subroutine with its central rotor and upstream and downstream reference discs. As mentioned in Section 4.1.2, the pressure jump method specifies a static-to-static pressure increase based on the value of volume flow rate passing through a particular cell face. As explained in Appendix D, the static-to-static pressure increase can be derived from a static pressure curve of a fan by taking into account the fact that the curve is actually a fan total-to-static pressure curve. Besides converting the total-to-static pressure to a static-to-static pressure value the flow losses incurred between the measuring points used to determine the curve and the location of the fan rotor also have to be calculated. As an example the conversion of the fan static pressure curve of the 630 mm diameter B-fan is described. The fan static pressure curve is shown in Figure 3.7. Fitting a 3rd order polynomial equation through the curve, the following equation is obtained:

$$p_{sf} = -32.572V^3 + 85.114V^2 - 119.07V + 148.23 \quad (4.7)$$

The “fan” model in ANSYS Fluent® is based on the axial velocity through the fan and therefore equation 4.7 has to be converted to represent fan static pressure in

terms of axial velocity by multiplying each coefficient with a flow area term as follows:

$$p_{sf} = -32.572A^3v^3 + 85.114A^2v^2 - 119.07Av + 148.23 \quad (4.8)$$

where the flow area is given by:

$$\begin{aligned} A &= \pi(r_{shroud}^2 - r_{hub}^2) = \pi(0.315^2 - 0.125^2) \\ &= 0.263m^2 \end{aligned} \quad (4.9)$$

giving

$$p_{sf} = -0.59v^3 + 6.501v^2 - 31.272v + 148.23 \quad (4.10)$$

Equation 4.10 represents the difference between the total pressure value (equal to atmospheric pressure) upstream of the fan bell mouth and a static pressure value immediately downstream of the fan. The static pressure value downstream of the fan is obtained from a static pressure value measured after the porous mesh section in the plenum chamber (see Figure 3.3), which is converted by means of the calculations shown in Section E.2.1. To accommodate the difference between the total pressure in front of the bell mouth inlet and the static pressure immediately upstream of the fan, the dynamic pressure present in the flow immediately upstream of the fan rotor, as well as the anticipated losses (even though very small) in the bell mouth inlet have to be taken into account (see also Appendix D) as follows:

$$\begin{aligned} p_{static-to-static} &= -0.59v^3 + 6.501v^2 - 31.272v \\ &+ 148.23 + \frac{1}{2}\rho v^2 + \frac{1}{2}\rho K_{inlet}v^2 \end{aligned} \quad (4.11)$$

A density value of 1.2 kg/m^3 was used for all equations. The inlet loss coefficient is given in terms of the area defined by the shroud diameter as (Idelchik, 1994):

$$K_{inletOD} = 0.07$$

This value is converted to reference the actual flow area as follows:

$$\begin{aligned} K_{inlet} &= K_{inletOD} \frac{A}{\pi r_{shroud}^2} = 0.07 \frac{0.263}{0.312} \\ &= 0.03 \end{aligned} \quad (4.12)$$

4.3.3 Simulation

Identical simulation settings were used for both the ADM and PJM with the only difference being that simulations using the PJM did not incorporate a user-defined subroutine. PJM simulations were performed for the B-fan, N-fan and H10-fan.

4.4 The extended actuator disc method (EADM) applied to individual fans

The actuator disc method only predicts fan performance accurately within the normal operating range of an axial flow fan (at flow rates where the flow over the fan blade is predominantly in the axial and tangential directions). This is attributed to the fact that radial flow occurs through the fan at low flow rates (Meyer and Kröger, 2001). The radial flow affects the loads exerted by the fan blade on the flow due to possible stabilisation of the boundary layer over the blade, the presence of “Coriolis” forces in the blade and the larger effective chord length of the blade (see Appendix B). Himmelskamp (1945) estimated the blade airfoil properties of a “rotating airscrew” by measuring the pressure distribution over the blade profiles at specific radial locations and at different flow rates. At relatively low flow rates he measured lift coefficient values as high as three and attributed the augmentation of the lift properties to the stabilisation of the boundary layer and the delay of stall due to the presence of radial flow over the blade surface. Gur and Rosen (2005) describe the application of a simplified numerical model for an aircraft propeller. To incorporate lift augmentation into their numerical model they fit a hyperbolic function between the 2-dimensional airfoil properties and the potential flow solution for the same airfoil profile.

The extended actuator disc method (EADM) is therefore based on the model of Gur and Rosen (2005). It uses the same methods and equations used in the actuator disc method but compensates for the ADM’s inability to simulate the operation of an axial flow fan accurately at low flow rates by extending the linear section of the airfoil lift coefficient vs. angle of attack curve (see Figure 4.8).

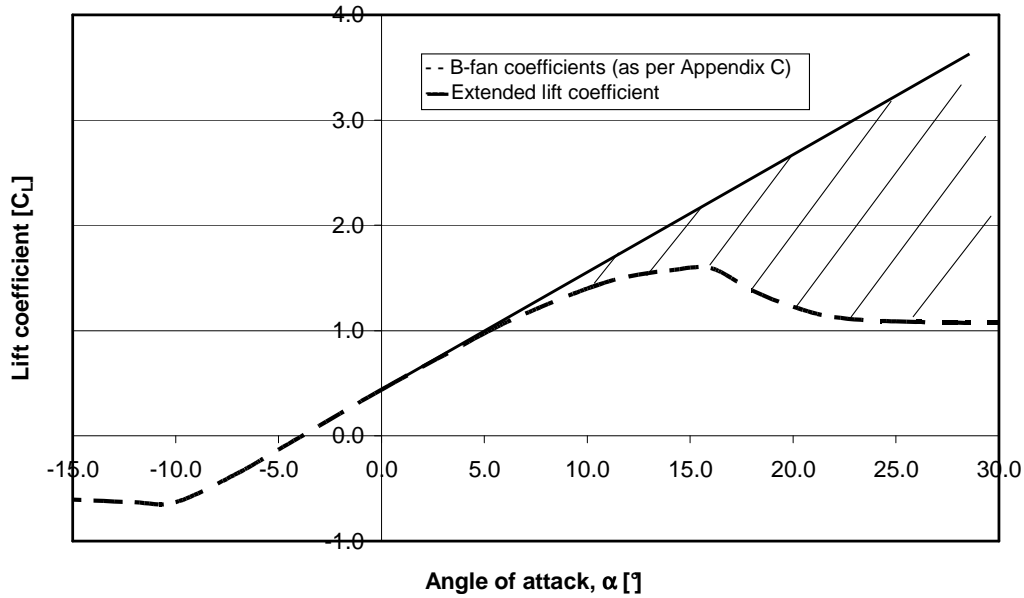


Figure 4.8: Illustration of extended lift coefficient curve for B-fan blade profile.

Stall does eventually occur along the radius of an axial flow fan blade (starting at the hub radius) as the volume flow through the fan is lowered. The EADM therefore provides for the increased lift coefficient to occur only at radii above a specified radius ratio. These radius ratios were selected to ensure that the simulated fan static pressure vs. volume flow rate curve followed the measured pressure curve from 30% to 100% of the maximum flow rate value that was measured. The different radius ratios that were used for the different fans are shown in Table 4.3.

Table 4.3: Radius ratios used for extended actuator disc method

	Radius ratio
B-fan	0.59
N-fan	0.52
H10-fan	0.48

The drag coefficient is increased in direct proportion to the increase in the lift coefficient by maintaining the lift-to-drag ratio for the corresponding angle of attack used in the ADM. A more detailed discussion of the EADM is given in Appendix B. Simulations using the EADM and ADM used identical meshes, boundary conditions and solver settings. The only difference between the two simulations existed in the calculations that form part of the user subroutine used to calculate values for the momentum source terms.

4.5 Results and discussion for individual axial flow fans

The simulation results for the N-fan, B-fan and H10-fan are shown for the ADM, PJM and EADM. Figure 4.9 shows the simulation results compared to the experimental results obtained for the N-fan.

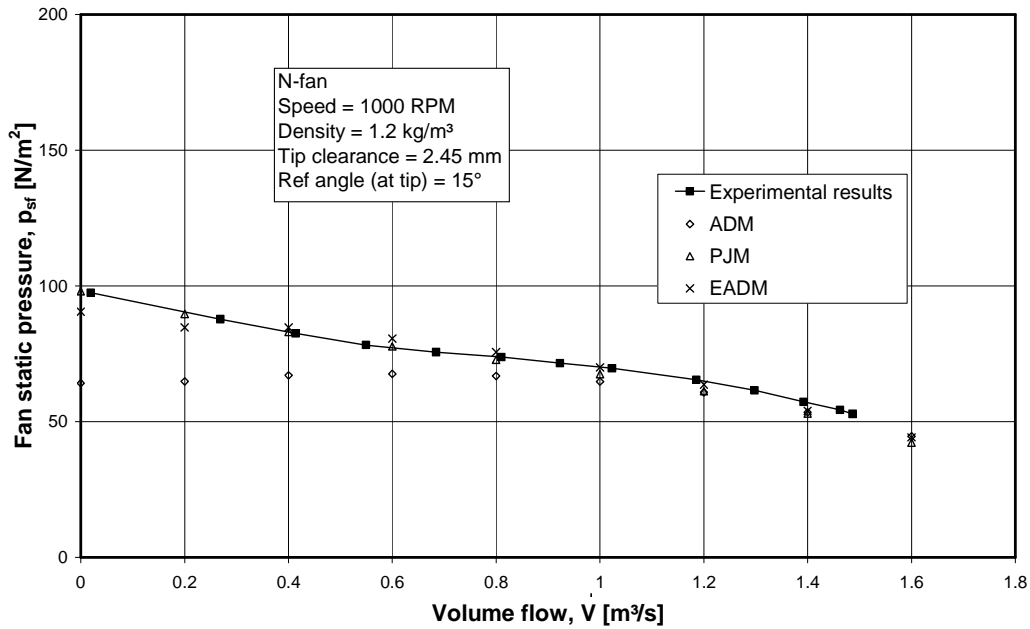


Figure 4.9: Comparison of fan static pressure for N-fan.

Figure 4.10 shows the simulation results compared to the experimental results obtained for the B-fan.

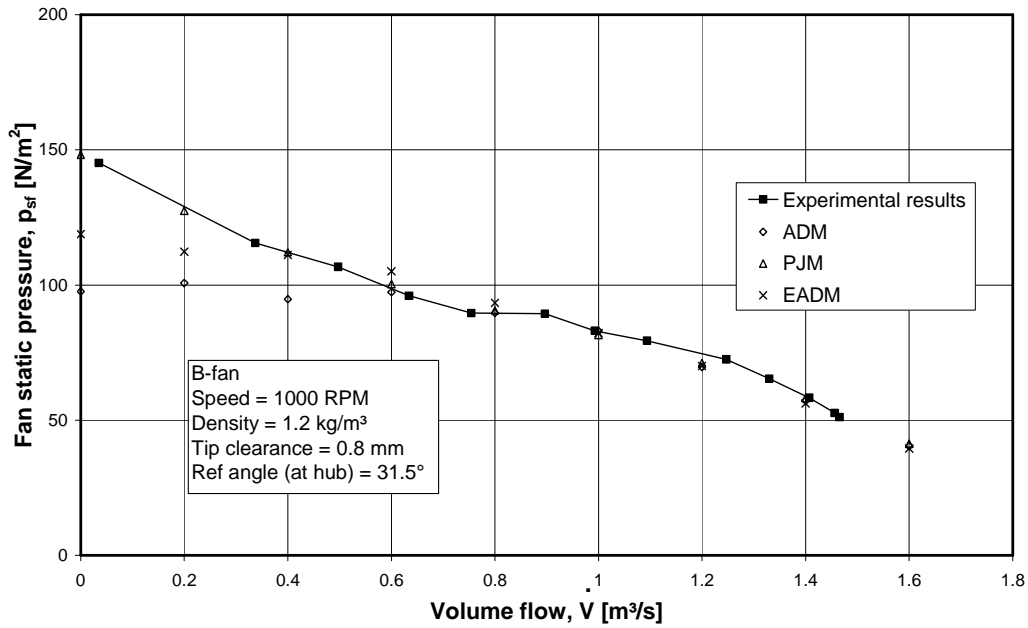


Figure 4.10: Comparison of fan static pressure for B-fan.

Figure 4.11 shows the simulation results compared to the experimental results obtained for the H10-fan.

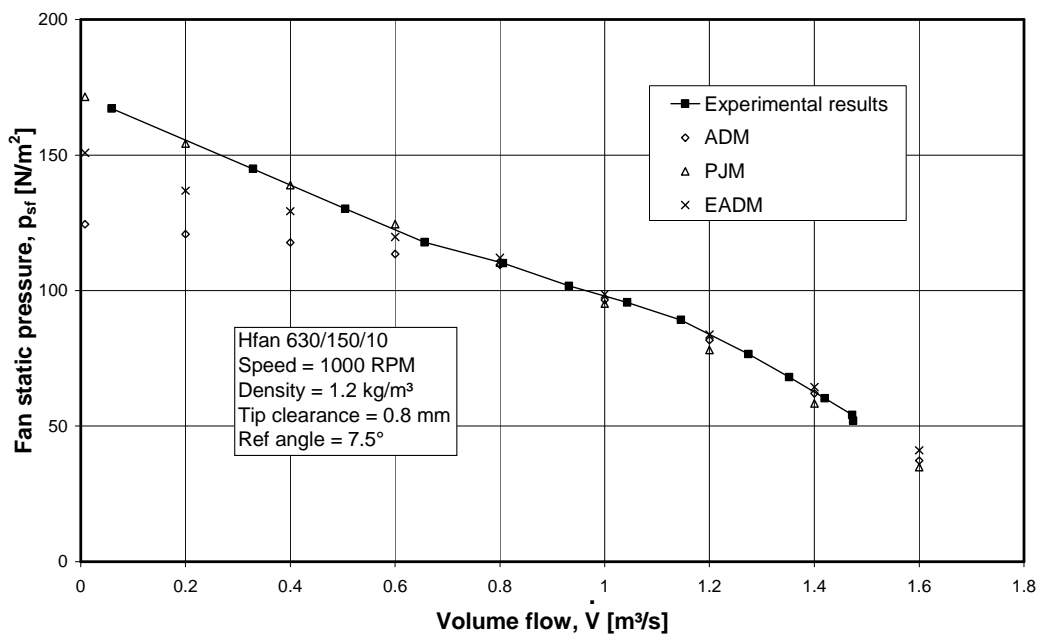


Figure 4.11: Comparison of fan static pressure for H10-fan.

The results shown in Figures 4.9 to 4.11 are discussed according to the three methods used to represent the axial flow fans in the CFD simulations. The

simplest of these three methods, the pressure jump method (PJM), enables the user to model an axial flow fan by using the fan static pressure vs. volume flow rate curve. The details of the fan test facility are incorporated into the fan static pressure curve to convert it to a fan static-to-static pressure curve. The equation representing the static-to-static pressure curve is applied at the fan rotation plane (see Figure 4.7) as a static pressure increase based on the average volume flow rate through the fan annulus. The biggest advantage of this method is the ease with which it can be applied and the availability of fan performance information (if not available, the generic fan curve shown in Figure 3.8 may be used). The value of the static pressure increase used in the PJM is however independent of the configuration of the fan at a specific position within the fan plane of rotation and is determined solely by the volume flow rate through the fan annulus. It would therefore be the same at a position close to the rotor casing and at a position close to the rotor hub. This in itself also holds an advantage in that the mesh structure does not have to be related to the design of the fan blade in any way. Consequently the acceptable coarseness of the mesh structure would be determined by the detail of the flow field surrounding the fan installation. Therefore, applying the PJM to an individual axial flow fan with undistorted inlet conditions shows close correlation between the experimental and the simulated results at all flow rates for the N-, B- and H10-fans (see Figures 4.9 to 4.11).

The actuator disc method (ADM) incorporates the properties of the fan rotor, namely hub-to-tip ratio, blade number, rotational speed, stagger angle, chord length and blade airfoil lift and drag coefficients into the analysis. As shown in Figure 1.4 and equations 1.1 to 1.7, these values combine to determine the local lift and drag forces that would be exerted by a fan blade on the flow field. The advantage of this method is therefore its ability to take the inlet velocity distribution into account when predicting the performance of the fan, as experienced by a fan under distorted inlet conditions. This was the main motivation behind the use of the ADM (and actually the EADM) as the basis for this study. The ADM assumes that the flow at a specific radial location passes through the fan rotor on a cylindrical surface without the presence of radial flow in the rotor. The big disadvantage of the ADM is therefore its inability to take the effect of radial flow through the fan rotor into account when predicting the performance of a fan. Radial flow typically occurs at low flow rates and therefore the actuator disc method predicts fan performance incorrectly at low flow rates (see Figures 4.9 to 4.11). Although the ADM can still be regarded as a simplified fan model, the mesh size of the actual fan section would influence the accuracy of the simulation, and a finer mesh structure may be required to obtain accurate answers. This, along with the additional blade information required, makes the ADM more complicated to incorporate into a simulation than the PJM.

The purpose of the extended actuator disc method (EADM) is to compensate for the inability of the actuator disc method to correctly predict the performance of an axial flow at low flow rates. This is done by extending the linear section of the blade airfoil profile lift coefficient vs. angle of attack curve. This method is based

on the observations of a number of other authors, as referenced in Section 2.4.3. A comparison of the experimental and numerical results shows that the EADM increases the predicted fan static pressure rise for all the fans that were evaluated. However, at very low flow rates the EADM still under-predicts the performance of these fans. This indicates the existence of more than one mechanism that may be linked to increased fan pressure rise caused by the radial flow through the fan rotor. This under-prediction at low flow rates is most evident for the B-fan (see Figure 4.10) while it is less prominent for the N-fan (see Figure 4.9). This difference in prediction accuracy between two different fan configurations also indicate that fan configuration influences the mechanisms that cause pressure rise at low flow rates.

4.6 The simulation of multiple axial flow fans

Once the individual performance of each of the above fans was modelled numerically, a multiple fan simulation model was compiled to simulate the performance of the 3-fan test facility detailed in Figure 3.1. The multiple fan facility simulations investigated the use of different fan configurations, as well as different fan simulation methods for the edge fan. The two inner fans were simulated as N-fans (corresponding to the experiments described in Chapter 3) using the PJM.

4.6.1 Geometry and mesh

The geometry of the multiple fan CFD simulation resembled the test facility shown in Figure 3.1. The geometry consisted of three fan tunnels connected to a common inlet chamber (see Figure 4.12). The geometry and mesh layout of the three tunnels, as well as the volume directly upstream of each of the three fans, in the multiple facility simulation model were exactly the same as the geometry and mesh of the individual tunnels detailed in the Sections 4.3 to 4.5. The model had twenty mesh elements between the upper and lower surfaces of the inlet chamber at the point furthest from the fans.

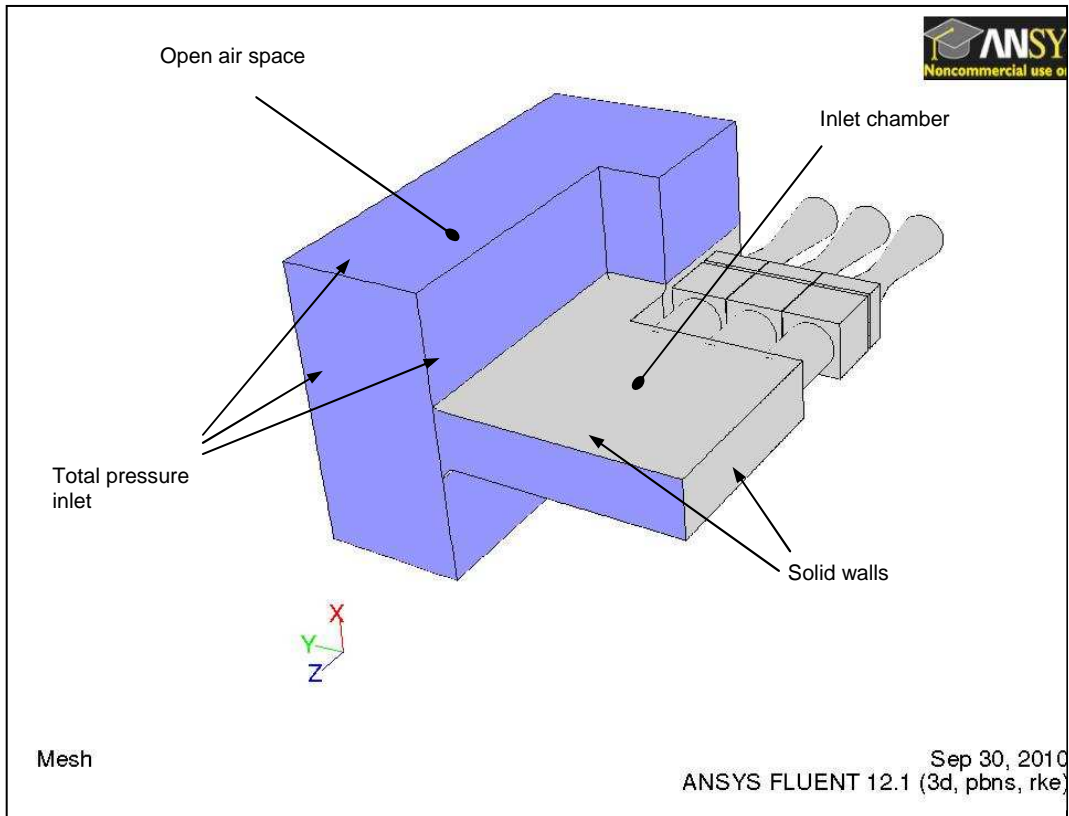
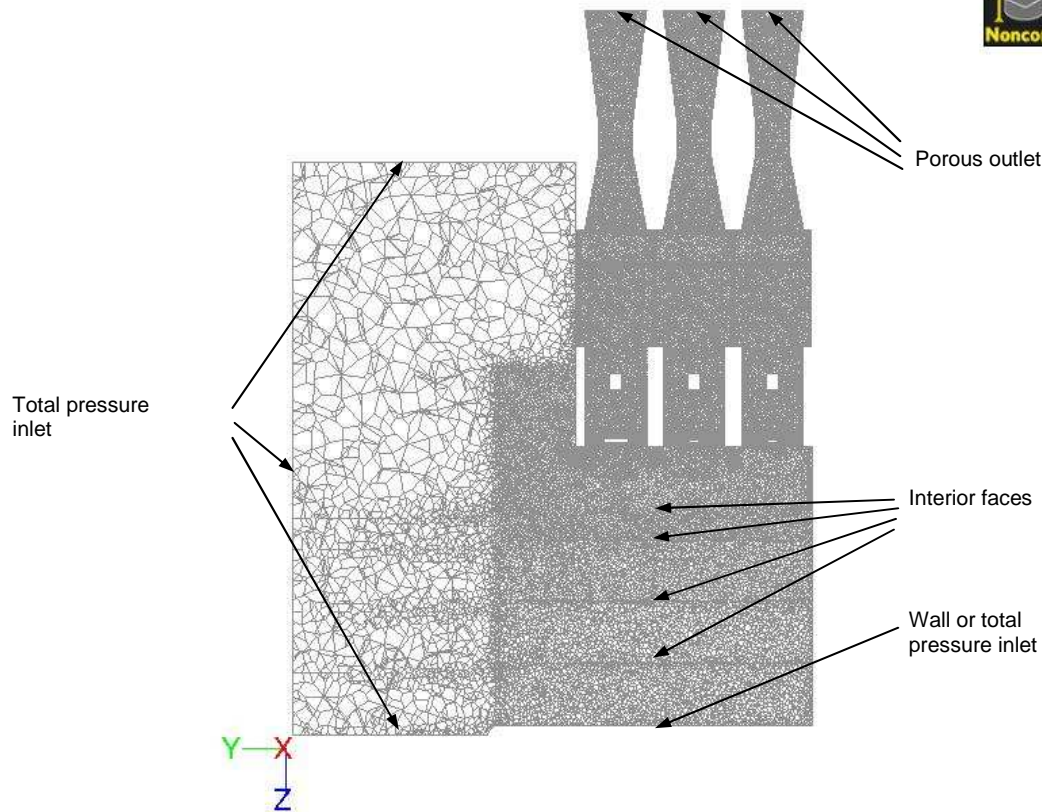


Figure 4.12: CFD geometry of multiple fan test facility.

The single inlet open air space with frictionless walls shown in Figure 4.1 was replaced by a common inlet chamber with solid walls and an open air space upstream from the inlet chamber. The dimensions of the inlet chamber corresponded to that of the test facility. The inlet chamber was modelled in sections corresponding to the different floor heights at which the fans were tested. The interfaces between the sections were specified as “interior” faces which could be converted to wall boundaries to adjust the floor height below the fans. The sides of the inlet chamber were modelled as wall boundaries, while the floor surface furthest from the fan faces was specified as either a wall boundary or pressure inlet. The sides of the open air inlet and the edges were all modelled as total pressure boundaries. The face definitions for the tunnel geometries used in the multiple fan model (see Figure 4.13) were identical to those used for the individual fan model, except for the tunnel outlet, where the static pressure outlet was replaced by a porous outlet, corresponding to the fixed system resistance used in the experimental facility (see Figure E.6).



Mesh

 Aug 23, 2010
 ANSYS FLUENT 12.1 (3d, pbns, rke)

Figure 4.13: CFD mesh of multiple fan test facility.

The same structured hexahedral grid used for the fan section in the individual fan simulations was used for all three fan sections in the multiple fan simulation. The transitions between the hexahedral elements and tetrahedral elements were modelled using unmatched boundaries. The model of the multiple fan facility was meshed with a total of 10.5 million tetrahedral and hexahedral volumes. By converting the tetrahedral cells to polyhedral cells, the mesh size was reduced to 5.5 million volumes.

4.6.2 Boundary and cell zone conditions

The boundary or cell zone conditions that were applied to the model detailed in Section 4.6.1 are shown in Table 4.4.

The loss coefficient specified for the porous sheet outlet boundary is based on data obtained from Idelchik (1994) and was adjusted slightly to ensure that volume flow rates were obtained for the individual fan tunnel simulation that corresponded to values obtained experimentally. These values were used as

reference values when calculating the fan volumetric effectiveness and are shown in Table 4.4.

Table 4.4: Summary of boundary or cell zone conditions.

Boundary or zone name	Values
Inlet	Total pressure = 0 N/m ² Turbulence intensity = 3% Turbulence length scale = 0.02 m
Outlet	Porous sheet with constant loss coefficient, $K_L = 2.3$, followed by static pressure = 0 N/m ²
Open air space walls	Symmetry boundaries
Inlet chamber walls	Stationary walls
Hub walls	Rotational speed = 104.72 rad/s (only for simulations using ADM and EADM)
Rotor disc	Source terms set in x-, y-, and z-direction, linked to user subroutine (only for simulations using ADM and EADM)
Fan face	Static-to-static pressure increase as described in Section 4.3.2 (only for PJM fan models)
Porous mesh	Inertial resistance factor = 2.442 m ⁻¹ Viscous resistance factor = 1173168 m ⁻² Applied in z-direction

Table 4.5: Reference volume flow rates obtained for individual fan simulations using fixed system resistance.

	PJM [m ³ /s]	ADM [m ³ /s]	EADM [m ³ /s]
N-fan	1.450	1.430	1.437
B-fan	1.485	1.450	1.450
H10-fan	1.463	1.486	1.484

4.6.3 Simulation

Similar to the individual fan simulations all multiple fan CFD analyses were simulated as steady state, incompressible flow using ANSYS Fluent[®] version 12.1. In all instances the working fluid was air at 20 °C and 1 atmosphere pressure. The simulations were performed using the $k-\varepsilon$ realizable turbulence model and second order discretisation schemes were used for all the flow variables forming part of the simulations. The least squares cell based method was used to calculate the gradients of the variables in the flow equations.

Where applicable (for the ADM and EADM) the multiple fan simulations used the same disc reference system and user-defined subroutines as used for the individual fan simulations. The simulations were performed using 8 computational processors in parallel. To simplify execution of the user subroutine, the model was partitioned in such a way that the entire rotor assembly of the edge fan (centre disc plus upstream and downstream discs) was located on one partition.

The simulations were set to converge to scaled residual values of 10^{-4} within a maximum of 2000 iterations. As with the individual fan simulations, convergence of the momentum and turbulence quantities were within the mentioned limits, while the continuity residuals converged to between 10^{-3} and 10^{-4} (or lower), depending on the floor height being simulated. Simulations were performed for the multiple fan facility using the B-fan, N-fan and H10-fan in the edge fan position at floor heights of infinite, 4.5, 3.5, 2.5, 1.5 and 1.0 x fan diameter.

4.7 Multiple fan simulation results and discussion

The multiple fan simulation results are evaluated by comparing the simulated and measured values for system volumetric effectiveness and edge fan volumetric effectiveness, and by comparing the detailed velocity profile results obtained using the CFD simulations to experimental PIV results. The results are classified according to the composition of the multiple fan facility, where N_N_N would refer to an N-fan configuration, B_N_N a B-fan configuration and H10_N_N an H10-fan configuration being used for the edge fan.

4.7.1 N_N_N multiple fan facility simulations

The volumetric effectiveness values for the different fan configurations and CFD methods were obtained by dividing the resulting volume flow rate through each of the fan test tunnels in the multiple fan facility by the applicable reference flow rate shown in Table 4.5.

Figure 4.14 compares the simulated 3-fan system volumetric effectiveness for the N_N_N configuration to the measured values, as well as the curve published by Salta and Kröger (1995) (referred to as the Salta curve). Compared to the

experimental values, all three methods under-predict the measured system volumetric effectiveness but correlate well with the Salta curve. This agrees with the results of previous investigators (Bredell, 2005) who found that the numerically simulated volumetric effectiveness of a multiple fan system correlates with the Salta curve, even when the fan configuration simulated is different from that used by Salta and Kröger (1995).

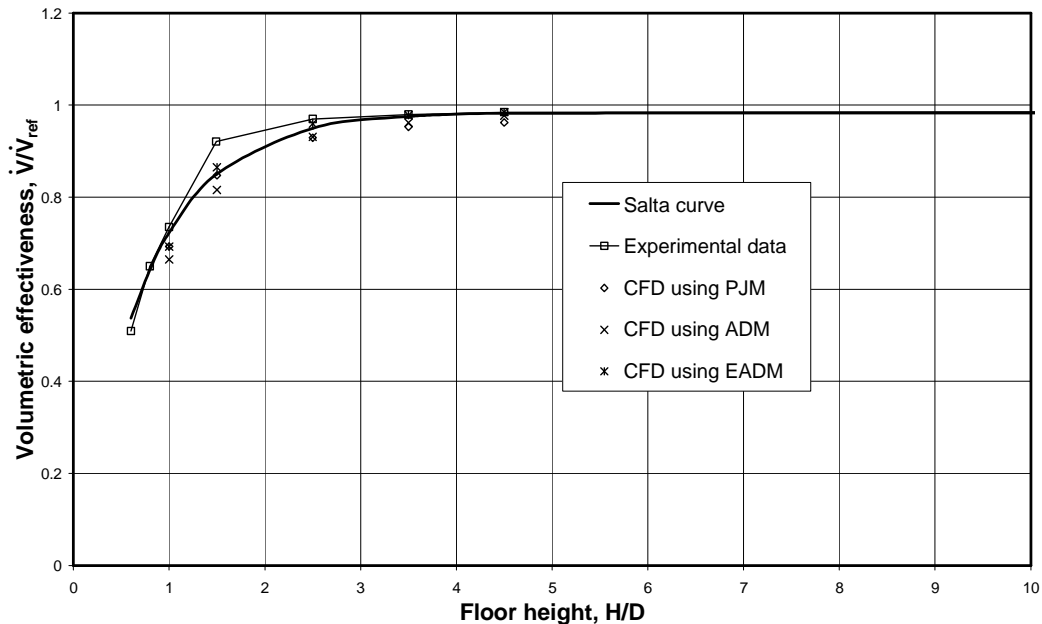


Figure 4.14: Comparison of N_N_N system volumetric effectiveness.

Figure 4.15 compares the simulated edge fan volumetric effectiveness for the N-fan to the measured values. It shows that the EADM predicts the volumetric effectiveness of the edge fan accurately at a floor height of 2.5 x fan diameter and higher. The ADM predicts fan volumetric effectiveness well at a floor height of 3.5 x fan diameter and higher, while the PJM only predicts the volumetric effectiveness of the edge fan accurately at an infinite floor height. At a floor height of 1.5 x fan diameter the EADM gives the highest estimate of edge fan volumetric effectiveness (0.7), compared to an experimental value of 0.83. At this height the ADM predicts a volumetric effectiveness of 0.56. At a floor height of 1.0 x fan diameter the PJM and EADM predict the experimental value exactly, although, based on the results at larger floor heights, this may be fortuitous.

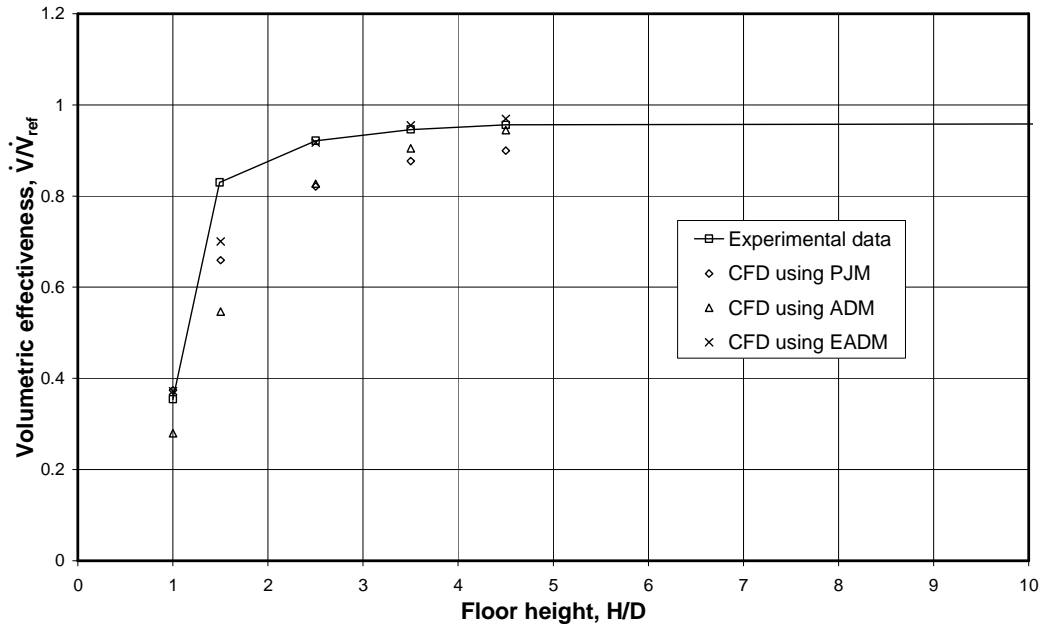


Figure 4.15: Comparison of edge N-fan volumetric effectiveness.

Detailed velocity profiles were obtained from the CFD results at the same locations as that of the velocity profiles for the PIV results (see Figure 3.15 in Section 3.4.3). From the experimental results shown in Chapter 3 it is apparent that the velocity distributions along the horizontal and vertical lines running from the edge of the plenum chamber and the vertical line running from the edge of the bell mouth (all located at the central plane between the walls of the inlet chamber) are independent of the fan configuration. A set of results, comparing experimental and simulation data, for the N_N_N system configuration only is shown in Appendix G. The simulation results of the flow into the multiple fan facility correlate well with the measured flow distributions at locations corresponding to line 1, 2 and 3. Considering its simplicity and the level of accuracy obtained using it, the PJM gives a good representation of the general flow field around the fan installation.

Only the results for the horizontal line drawn from the edge of the edge fan bell mouth directly upstream of the edge fan (line 4) are shown in this section. Figure 4.16 shows the velocity profiles along line 4 for an infinite floor height.

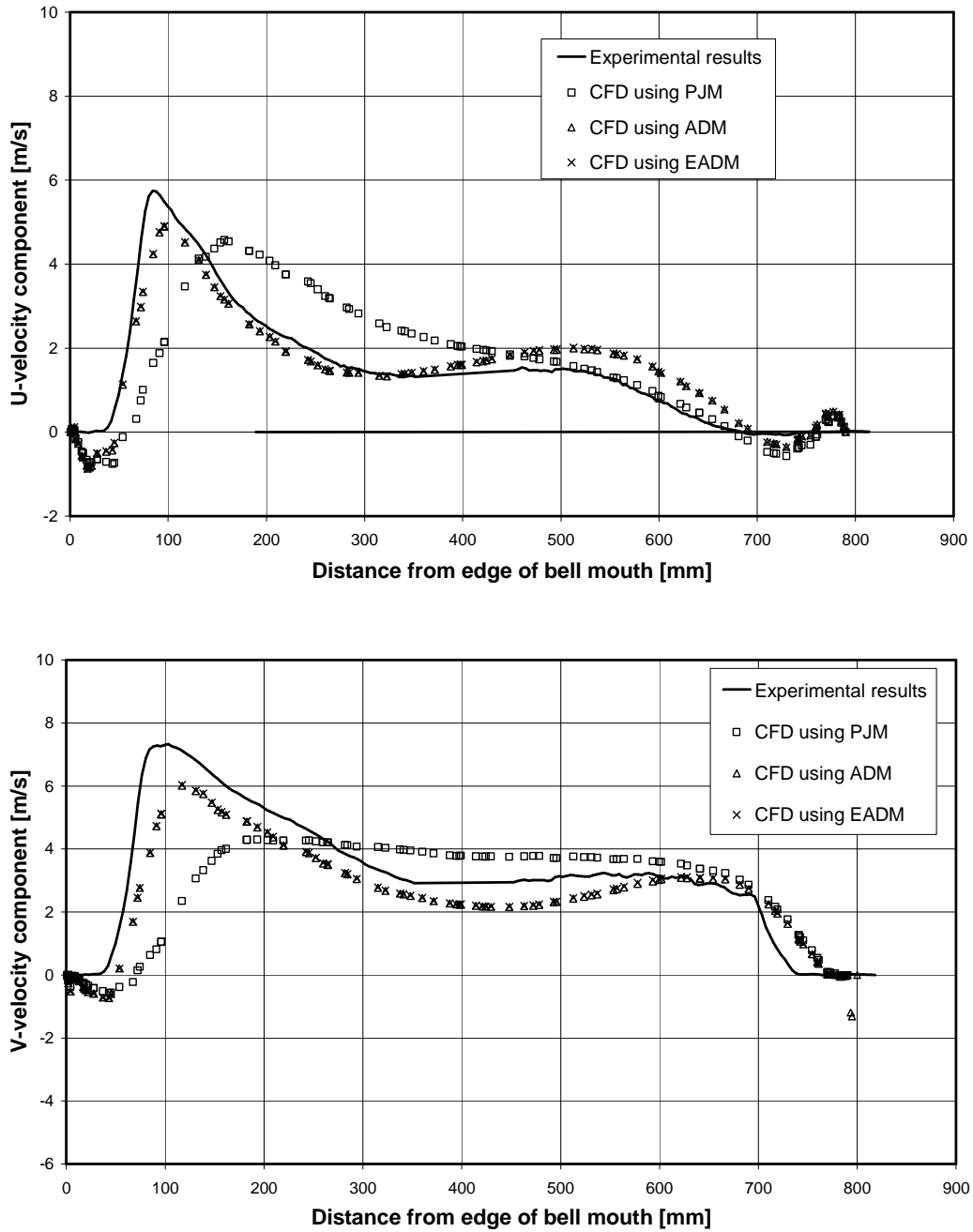
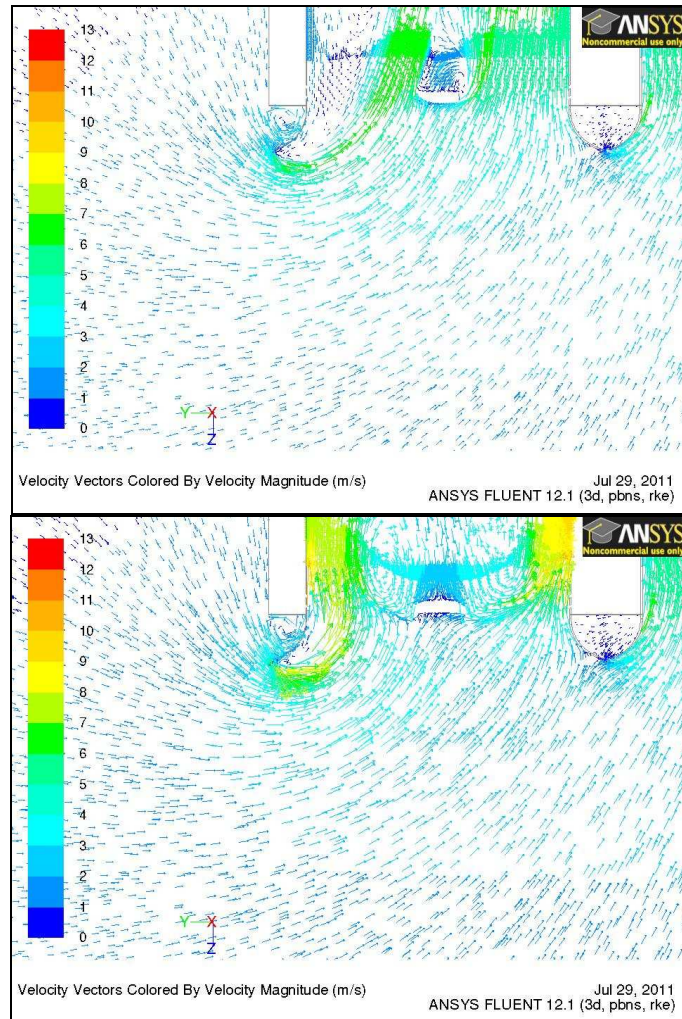


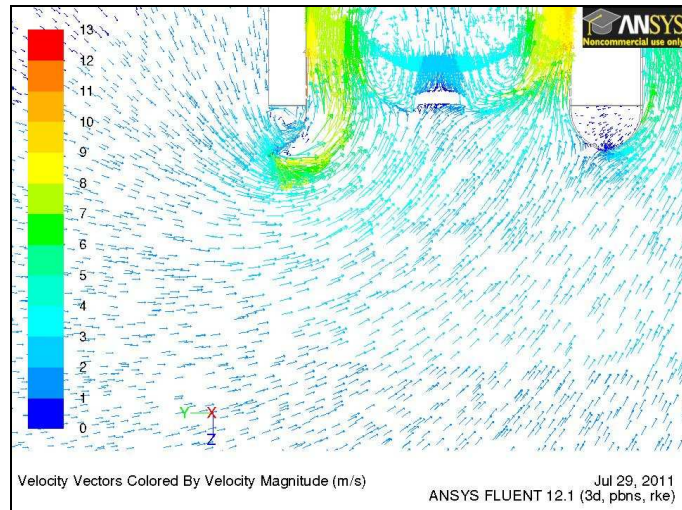
Figure 4.16: Comparison of U- and V-velocity profiles for N-fan at horizontal line from edge of bell mouth for infinite floor height.

Figure 4.16 shows that the results from the EADM and ADM are identical and correlate with the experimental results with a maximum deviation of 1.5 m/s at an infinite floor height. The results from the PJM, although it shows the same tendency as the experimental results, under-predicts the velocity values in both the U- and V-directions by as much as 4 m/s close to the bell mouth edge. The lack of flow exhibited by the experimental results at the edges and the centre of the bell

mouth is attributed to the absence of measured values caused by masking the reflection of the lazer light during PIV testing.

To compare the different numerical models to each other, vector plots were made of the centre plane flow upstream of the edge fan. It should however be noted that the flow through the plane of rotation of the fan is 3-dimensional in nature, and a more complete evaluation of the flow through the edge fan is presented in Section 5.1. Figure 4.17 shows a vector plot for results obtained using the PJM, ADM and EADM (seen from top to bottom) at an infinite floor height.



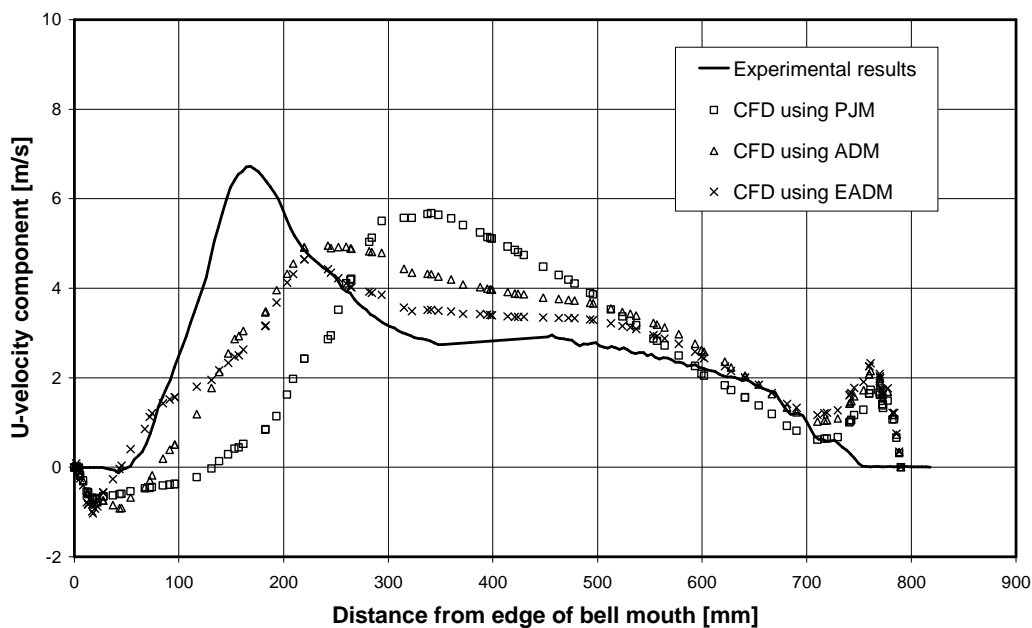


(c)

Figure 4.17: Vector plots for (a) PJM, (b) ADM and (c) EADM at infinite floor height, N-fan.

The vector plots in Figure 4.17 correlate with the results from Figure 4.15 which show that the results from the three different numerical techniques are quite close together at an infinite floor height. The vector plot of results using the EADM and ADM are identical, while the vector plot for results using the PJM predicts a slightly lower maximum velocity along the centre plane.

Figure 4.18 shows the velocity profiles along a horizontal line drawn from the edge of the edge fan bell mouth for a 2.5 x fan diameter floor height.



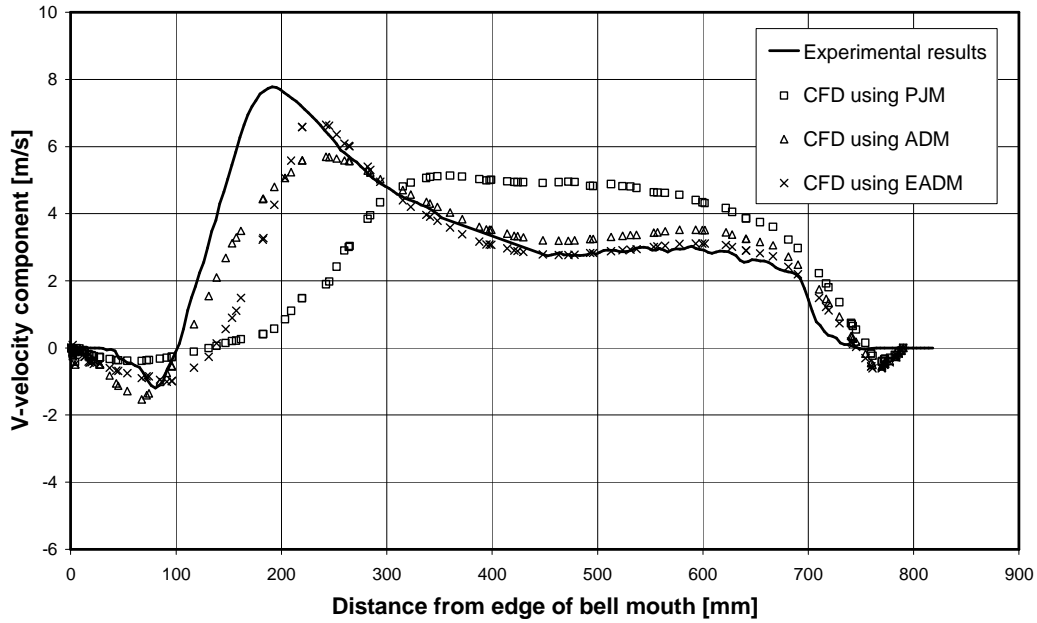
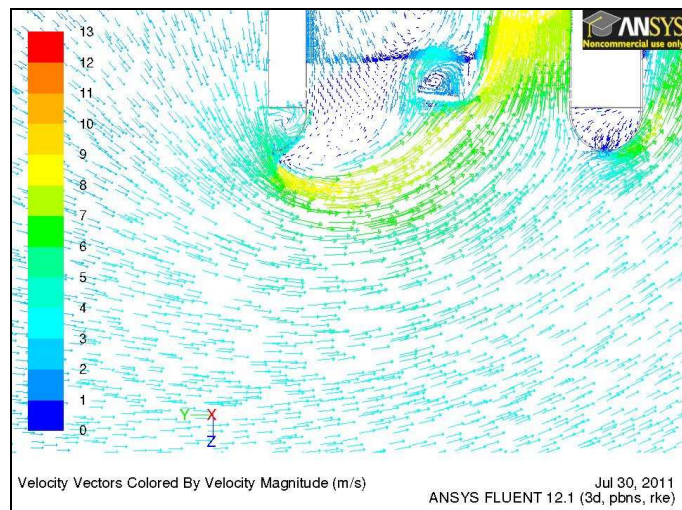


Figure 4.18: Comparison of U- and V-velocity profiles for N-fan at horizontal line from edge of bell mouth for 2.5 x fan diameter floor height.

Figure 4.18 shows that as the floor height is reduced to a value of 2.5 x fan diameter the correlation between the results from the numerical analyses and the experimental results deteriorates, although the numerical values still show the same trend as the experimental values.

Figure 4.19 shows a vector plot for results obtained using the PJM, ADM and EADM (seen from top to bottom) at 2.5 x fan diameter floor height.



(a)

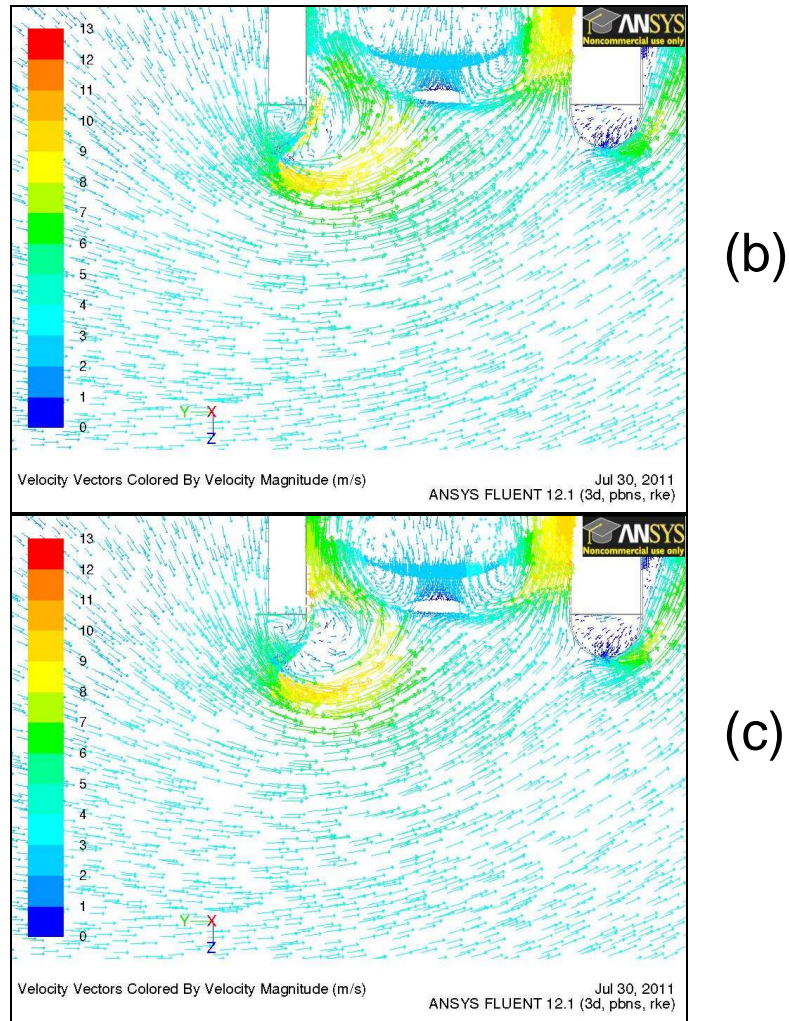


Figure 4.19: Vector plots for (a) PJM, (b) ADM and (c) EADM at 2.5 x fan diameter floor height, N-fan.

The vector plots in Figure 4.19 show that the PJM predicts a large separation zone on the inside of the bell mouth, upstream of the fan rotor. The ADM and EADM both predict a relatively small separation zone. The EADM shows significant redistribution of the flow through the fan rotor (in other words radial flow) by transferring the air from the inside radius to the outside radius of the fan rotor downstream of the fan.

Figure 4.20 shows the velocity profiles along a horizontal line drawn from the edge of the edge fan bell mouth for 1.0 x fan diameter floor height. The correlation between the numerical results and the experimental results is poor.

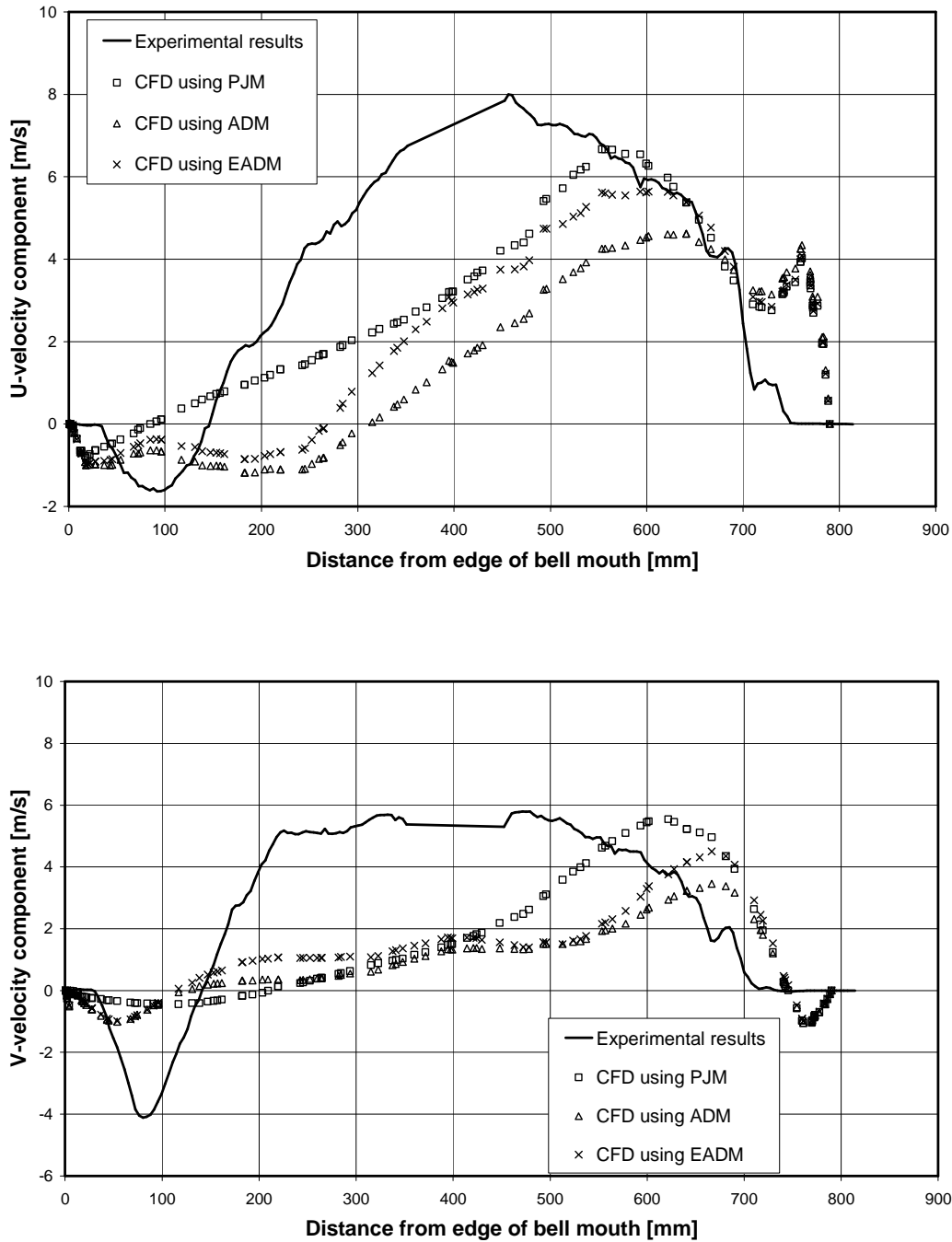
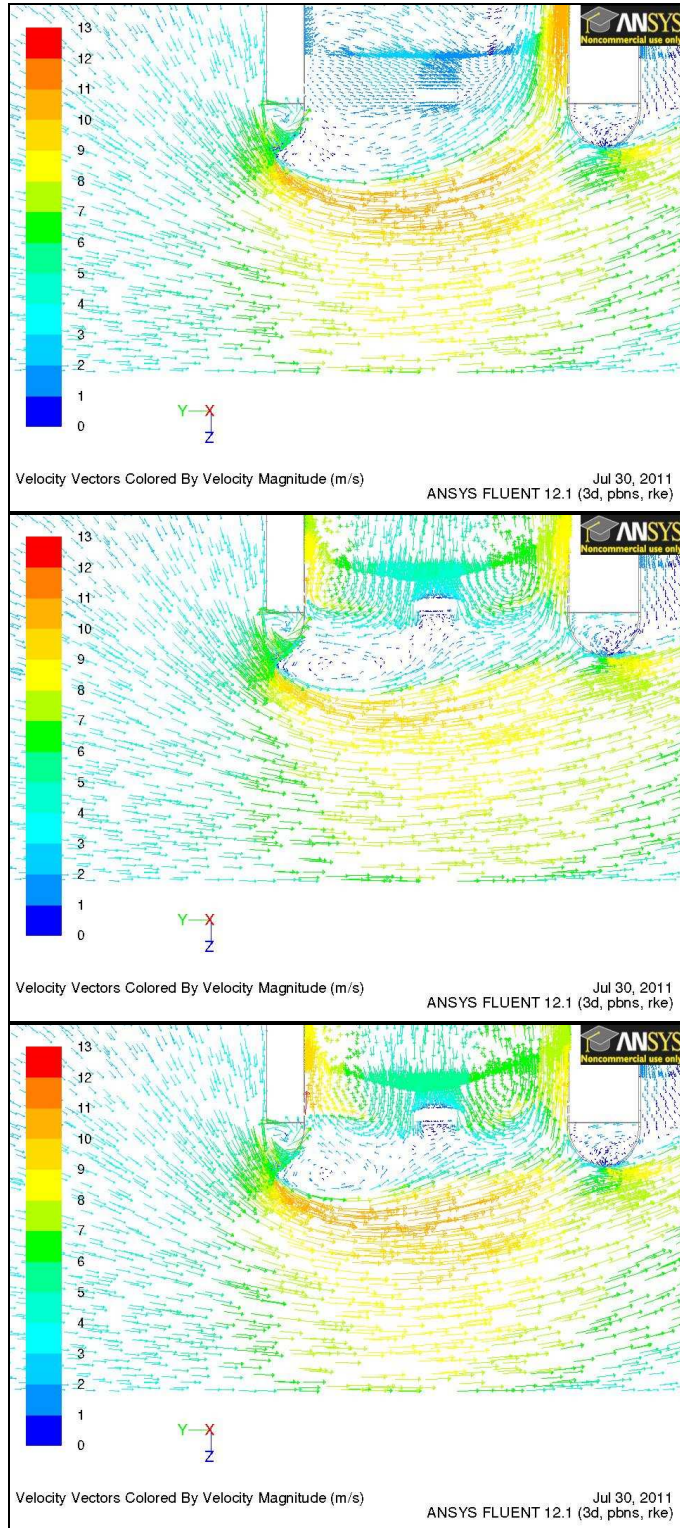


Figure 4.20: Comparison of U- and V-velocity profiles for N-fan at horizontal line from edge of bell mouth for 1.0 x fan diameter floor height.

Figure 4.21 shows that the PJM and EADM predict a separation zone of almost the same size. This correlates with the results shown in Figure 4.15, where the volumetric effectiveness obtained using the PJM and EADM is almost identical. However, based on Figure 4.20, none of these methods predict edge fan operation accurately at this particular floor height.



(a)

(b)

(c)

Figure 4.21: Vector plots for (a) PJM, (b) ADM and (c) EADM at 1.0 x fan diameter floor height, N-fan.

4.7.2 Results for B_N_N multiple fan facility simulations

Figure 4.22 compares the simulated 3-fan system volumetric effectiveness for the B_N_N configuration to the measured values, as well as the curve published by Salta and Kröger (1995). Compared to the experimental values all three methods under-predict the system volumetric effectiveness but correlate well with the Salta curve.

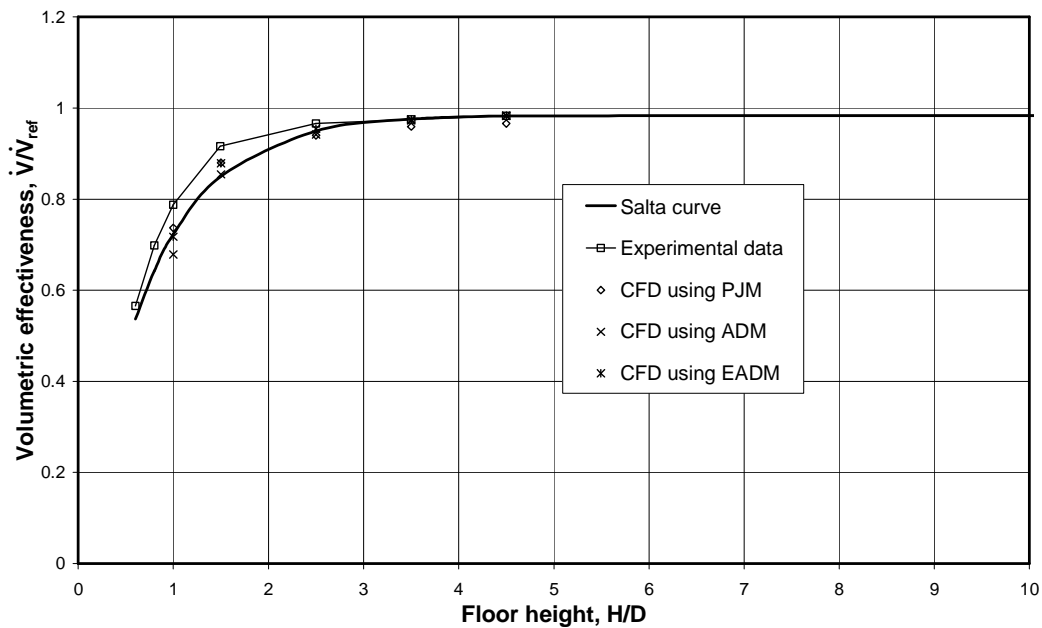


Figure 4.22: Comparison of B_N_N system volumetric effectiveness.

Figure 4.23 compares the simulated edge fan volumetric effectiveness for the B-fan to the measured values. It shows that the EADM predicts the volumetric effectiveness of the edge fan accurately at a floor height of 2.5 x fan diameter and higher. The ADM predicts fan volumetric effectiveness well at a floor height of 3.5 x fan diameter and higher, while the PJM only predicts the volumetric effectiveness of the edge fan accurately at an infinite floor height. At a floor height of 1.5 x fan diameter the EADM predicts an edge fan volumetric effectiveness of 0.75 compared to an experimental value of 0.82. At this height the ADM predicts a volumetric effectiveness of 0.67. At a floor height of 1.0 x fan diameter, the PJM predicts a volumetric effectiveness of 0.5 and the EADM a value of 0.45, compared to a measured value of 0.53. At this floor height the ADM predicts a value of 0.37.

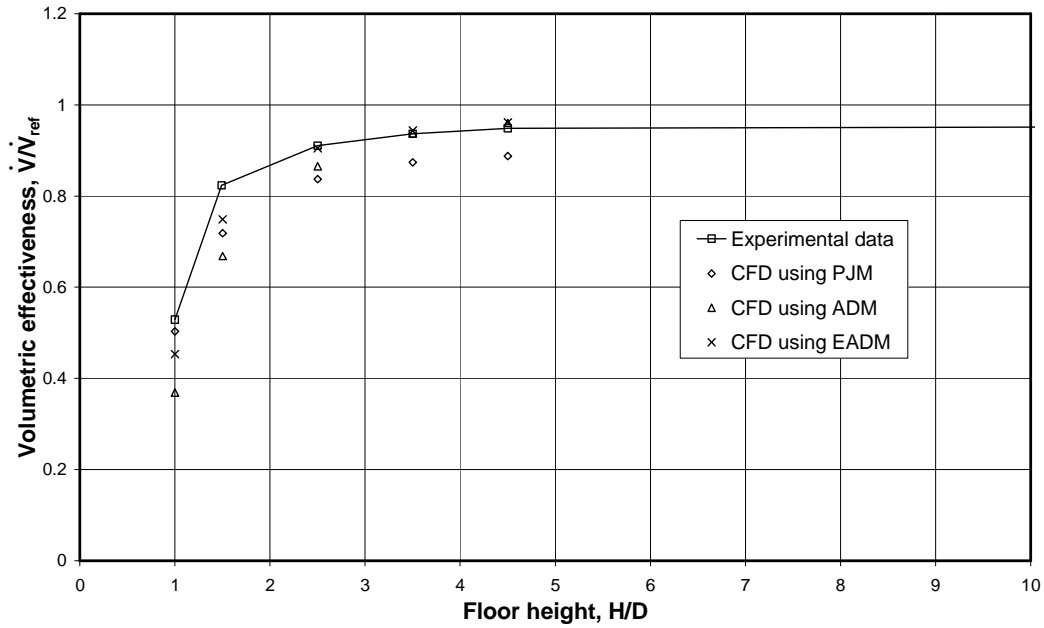
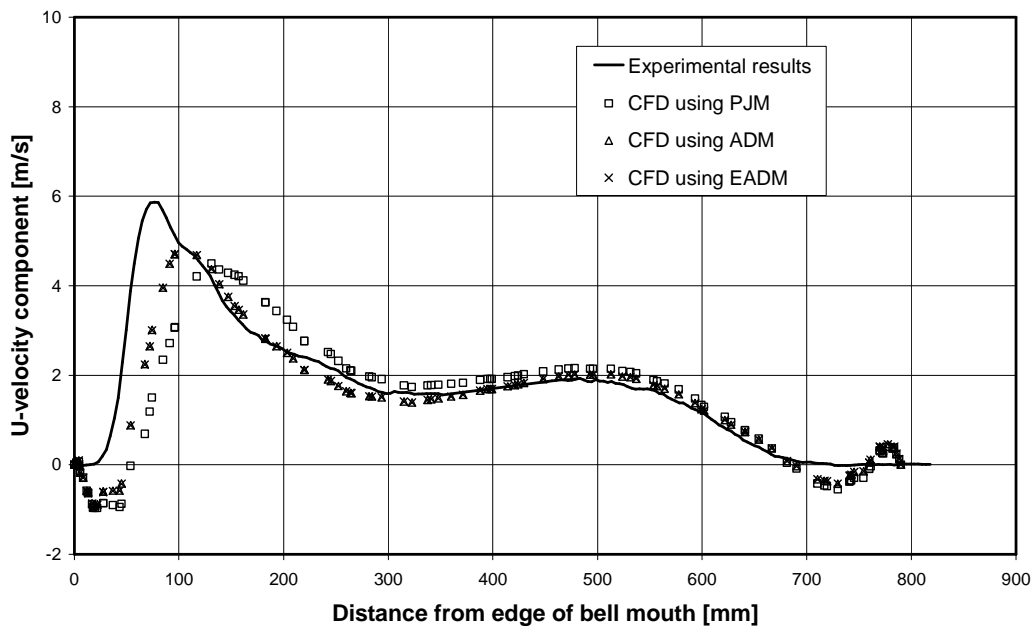


Figure 4.23: Comparison of edge B-fan volumetric effectiveness.

Figure 4.24 shows the velocity profiles along a horizontal line drawn from the edge of the edge fan bell mouth for an infinite floor height. It shows that the results from the numerical analyses correlate with the experimental results with a maximum deviation of 2.0 m/s in the U-direction and 1 m/s in the V-direction close to the edge of the bell mouth. The correlation observed for the B-fan is almost identical to the correlation observed for the N-fan, except for the PJM, where the level of correlation for the B-fan is better than that of the N-fan.



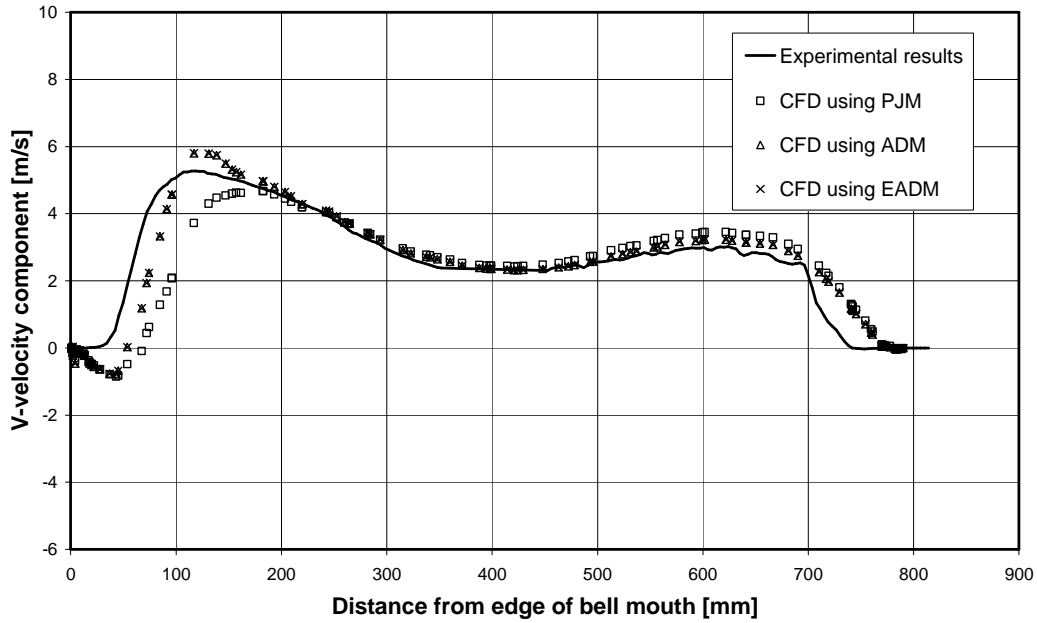
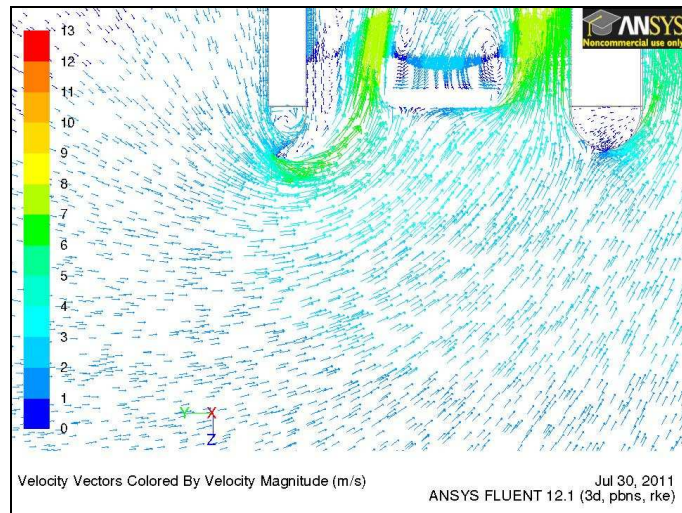
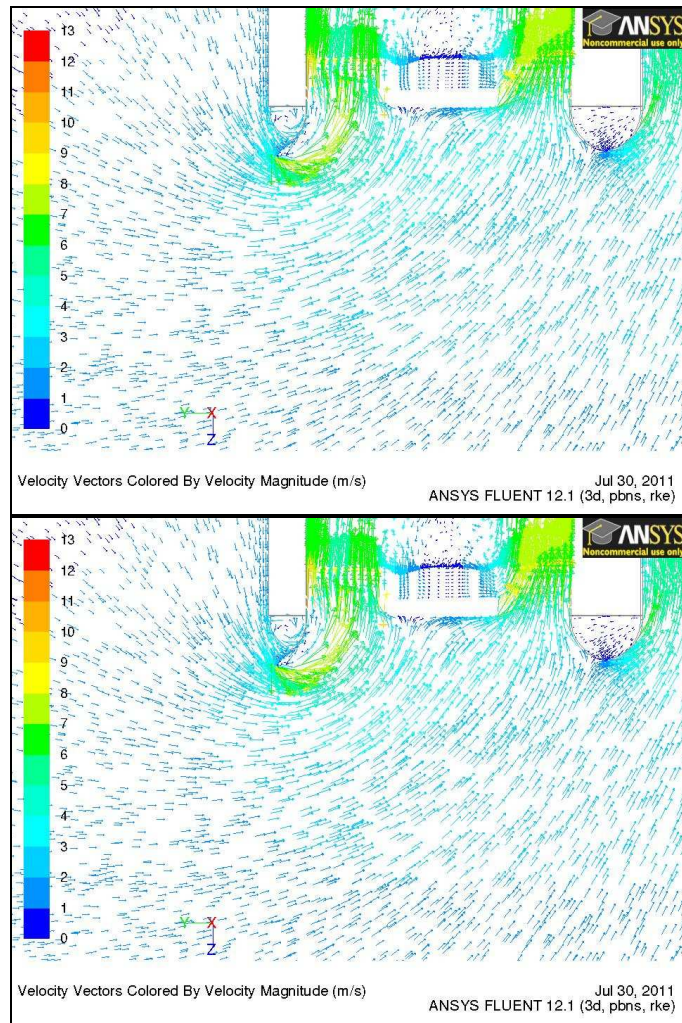


Figure 4.24: Comparison of U- and V-velocity profiles for B-fan at horizontal line from edge of bell mouth for infinite floor height.

Figure 4.25 shows a vector plot for results obtained using the PJM, ADM and EADM for the B-fan (seen from top to bottom) at an infinite floor height. Similar to the N-fan, the vector plots of results using the EADM and ADM are identical, while the vector plot for results using the PJM predicts a slightly lower maximum velocity along the centre plane.



(a)



(b)

(c)

Figure 4.25: Vector plots for (a) PJM, (b) ADM and (c) EADM at infinite floor height, B-fan.

Figure 4.26 shows the velocity profiles for a 2.5 x fan diameter floor height. Similar to the results for the N-fan, as the floor height is reduced to a value of 2.5 x fan diameter the correlation between the results from the numerical analyses and the experimental results deteriorates, although the numerical values still show the same trend as the experimental values.

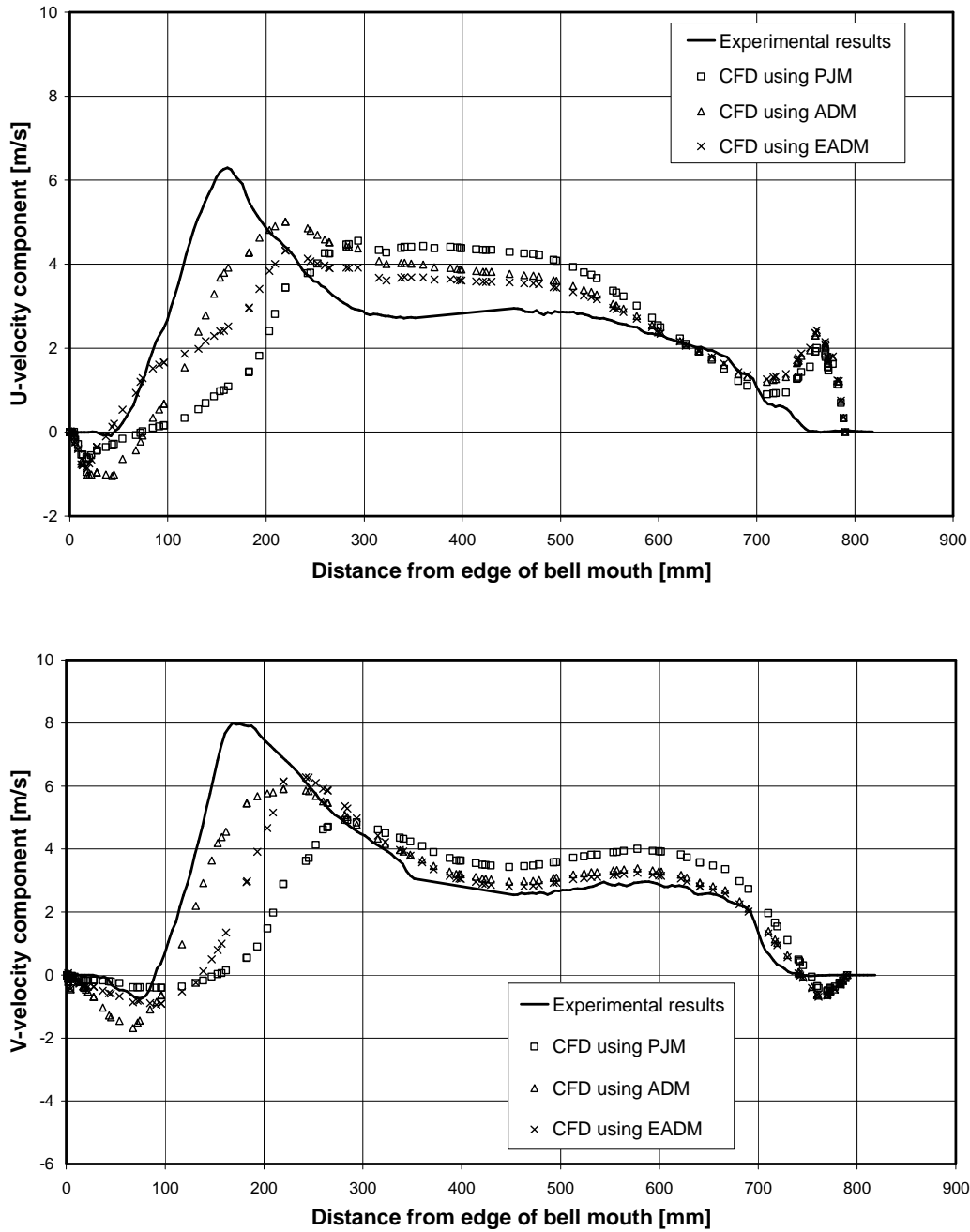
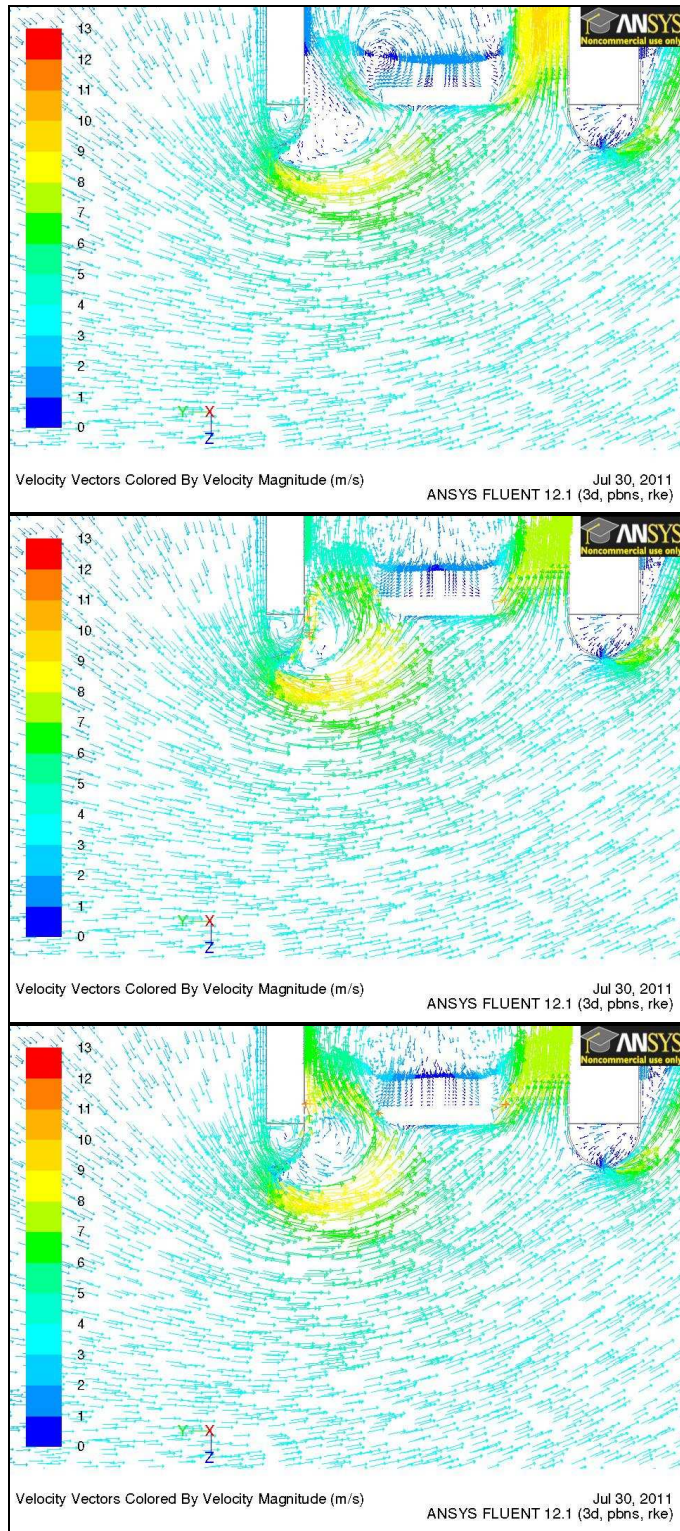


Figure 4.26: Comparison of U- and V-velocity profiles for B-fan at horizontal line from edge of bell mouth for 2.5 x fan diameter floor height.

Figure 4.27 shows a vector plot for the results obtained using the PJM, ADM and EADM (seen from top to bottom) at 2.5 x fan diameter floor height. The vector plots show that the ADM and EADM predict an identical, relatively small separation zone on the inside of the bell mouth, upstream of the fan rotor, while the PJM predicts a larger separation zone. The EADM predicts transfer of air from the inside radius to the outside radius of the fan rotor downstream of the fan.



(a)

(b)

(c)

Figure 4.27: Vector plots for (a) ADM, (b) PJM and (c) EADM at 2.5 x fan diameter floor height, B-fan.

Figure 4.28 shows the velocity profiles for 1.0 x fan diameter floor height. Whereas the numerical results for the N-fan are considered inaccurate at a height of 1.0 x fan diameter, there is some correlation between the EADM results and the experimental results for the B-fan. The correlation in the U-direction is within 2 m/s, while the correlation in the V-direction is within 1 m/s.

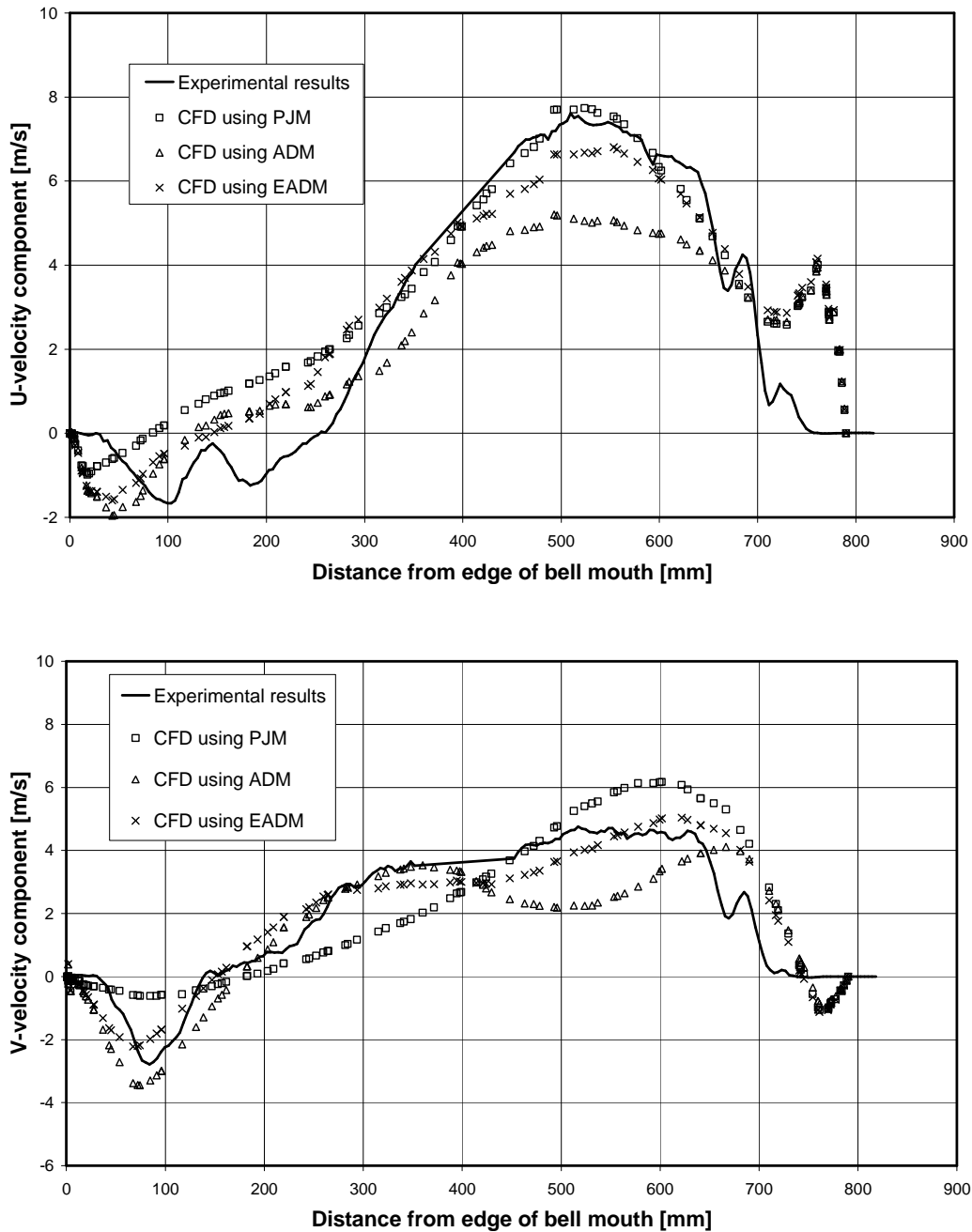
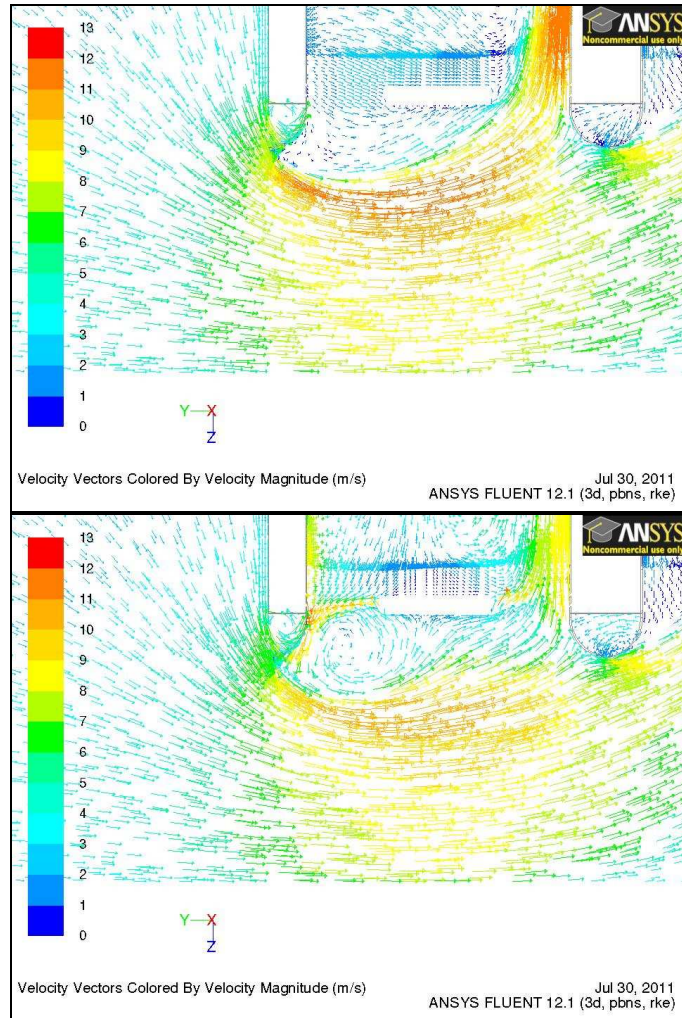


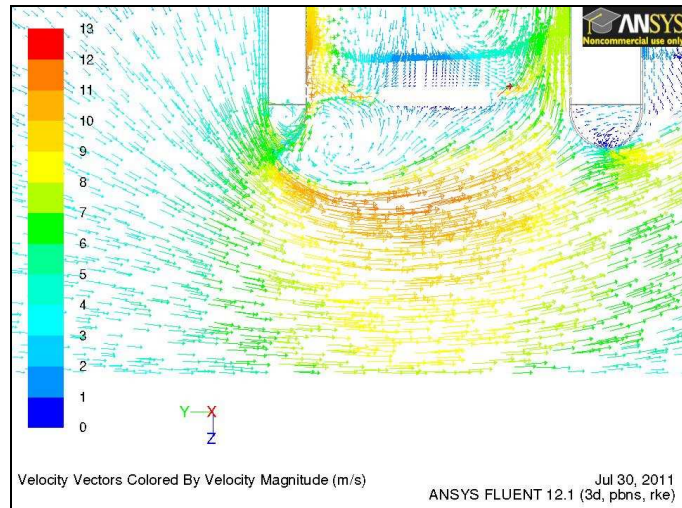
Figure 4.28: Comparison of U- and V-velocity profiles for B-fan at horizontal line from edge of bell mouth for 1.0 x fan diameter floor height.

Figure 4.29 shows a vector plot of results obtained using the PJM, ADM and EADM (seen from top to bottom) at 1.0 x fan diameter floor height. The vector plots show that the ADM predicts the largest separation zone upstream of the fan rotor, while the PJM and EADM predict smaller separation zones. These observations correlate with the results shown in Figure 4.23 where the volumetric effectiveness predicted by the ADM is the lowest, with the results from the prediction using the EADM and PJM being similar.



(a)

(b)



(c)

Figure 4.29: Vector plots for (a) PJM, (b) ADM and (c) EADM at 1.0 x fan diameter floor height, B-fan.

4.7.3 Results for H10_N_N multiple fan facility simulations

Figure 4.30 compares the simulated 3-fan system volumetric effectiveness for the H10_N_N configuration to the measured values, as well as the curve published by Salta and Kröger (1995). Compared to the experimental values at floor heights below 3.5 x fan diameter, all three numerical methods slightly under-predict the system volumetric effectiveness, while it over-predicts the results when compared to the Salta curve. However, compared to the other two fan formats, the numerical results for the H10-fan correlate the closest with their respective experimental values.

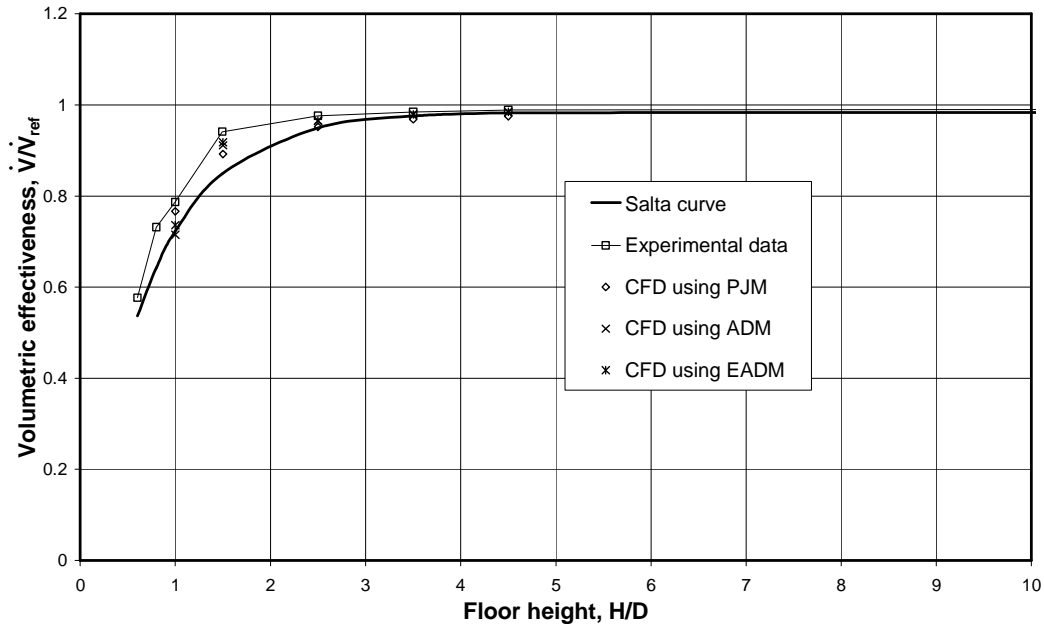


Figure 4.30: Comparison of H10_N_N system volumetric effectiveness.

Figure 4.31 compares the simulated edge fan volumetric effectiveness for the H10-fan to the measured values. It shows that the EADM predicts the volumetric effectiveness of the edge fan accurately at all floor heights and that the ADM predicts the volumetric effectiveness of the edge fan accurately at a floor height of 1.5 x fan diameter and higher. The PJM under-predicts the volumetric effectiveness of the edge fan at all floor heights (except at a floor height of 1.0 x fan diameter). At a floor height of 1.0 x fan diameter the ADM predicts an edge fan volumetric effectiveness of 0.47, compared to an experimental value of 0.55.

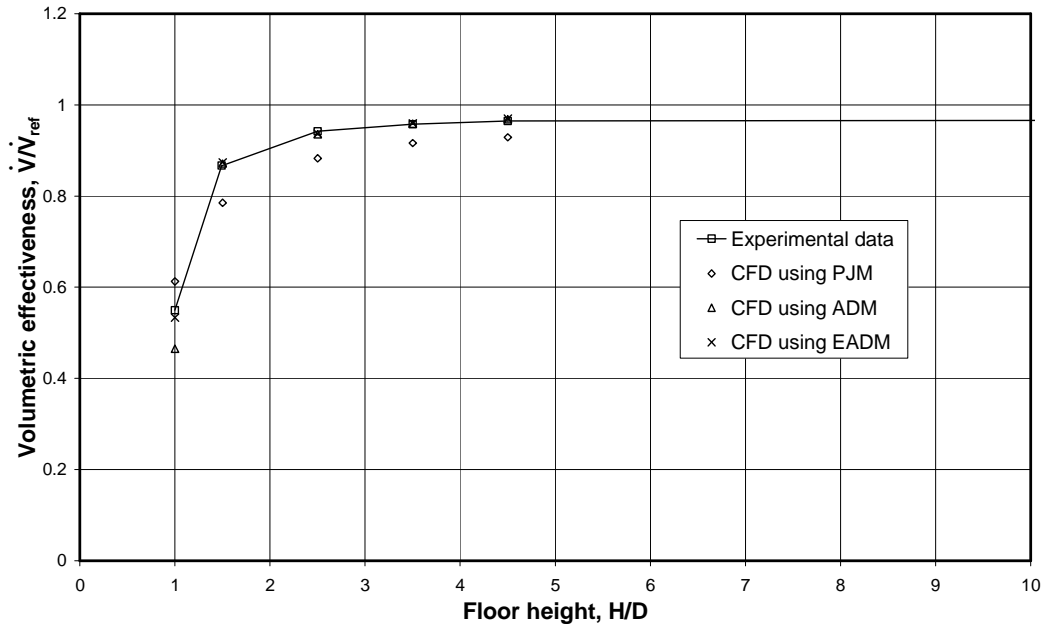
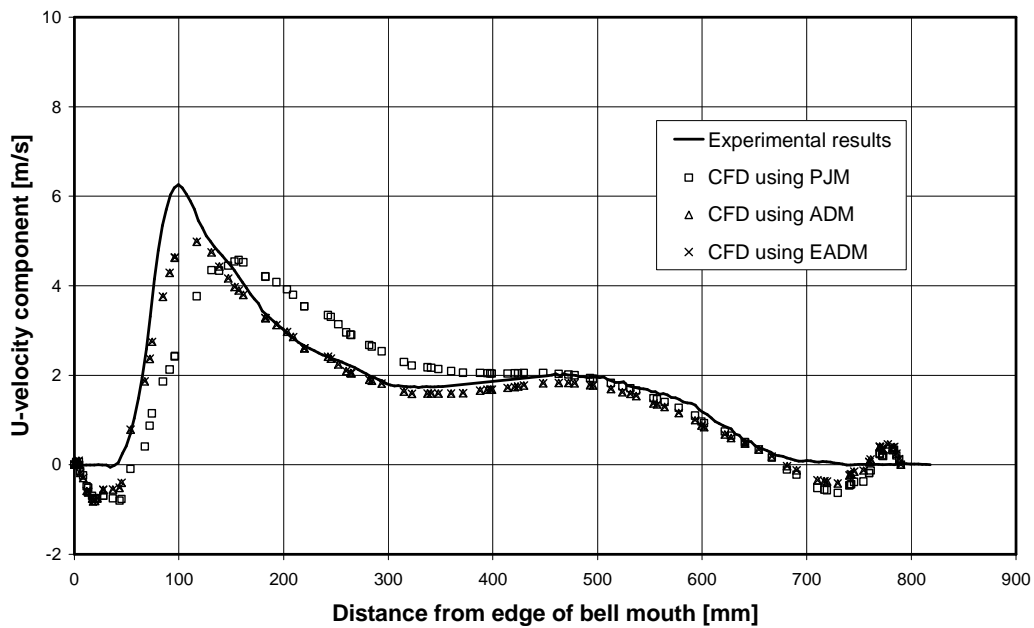


Figure 4.31: Comparison of edge H10-fan volumetric effectiveness.

Figure 4.32 shows the velocity profiles along a horizontal line drawn from the edge of the edge fan bell mouth for an infinite floor height. It shows that the results from the EADM and ADM correlate well with the experimental results in both the U- and V-direction. The results from the PJM follow the trend of the experimental curves in both the U- and V-directions within a maximum margin of 2 m/s. The good correlation observed for the EADM and ADM is also evident in the results of both the B-fan and N-fan.



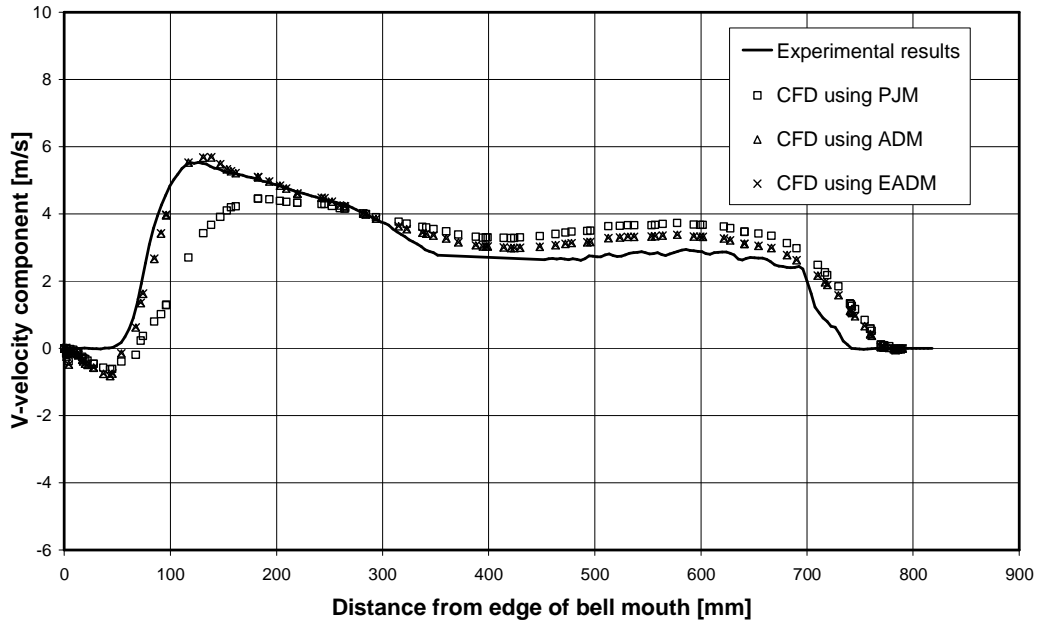
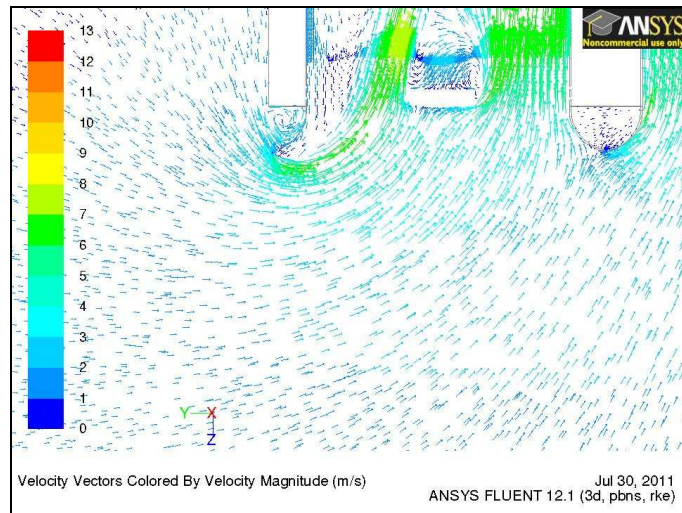


Figure 4.32: Comparison of U- and V-velocity profiles for H10-fan at horizontal line from edge of bell mouth for infinite floor height.

Figure 4.33 shows a vector plot for results obtained using the PJM, ADM and EADM for the H10-fan (seen from top to bottom) at an infinite floor height. Similar to the N- and B-fan, the vector plots of results obtained using the EADM and ADM are identical, while the vector plot for results obtained using the PJM predicts a slightly lower maximum velocity along the centre plane.



(a)

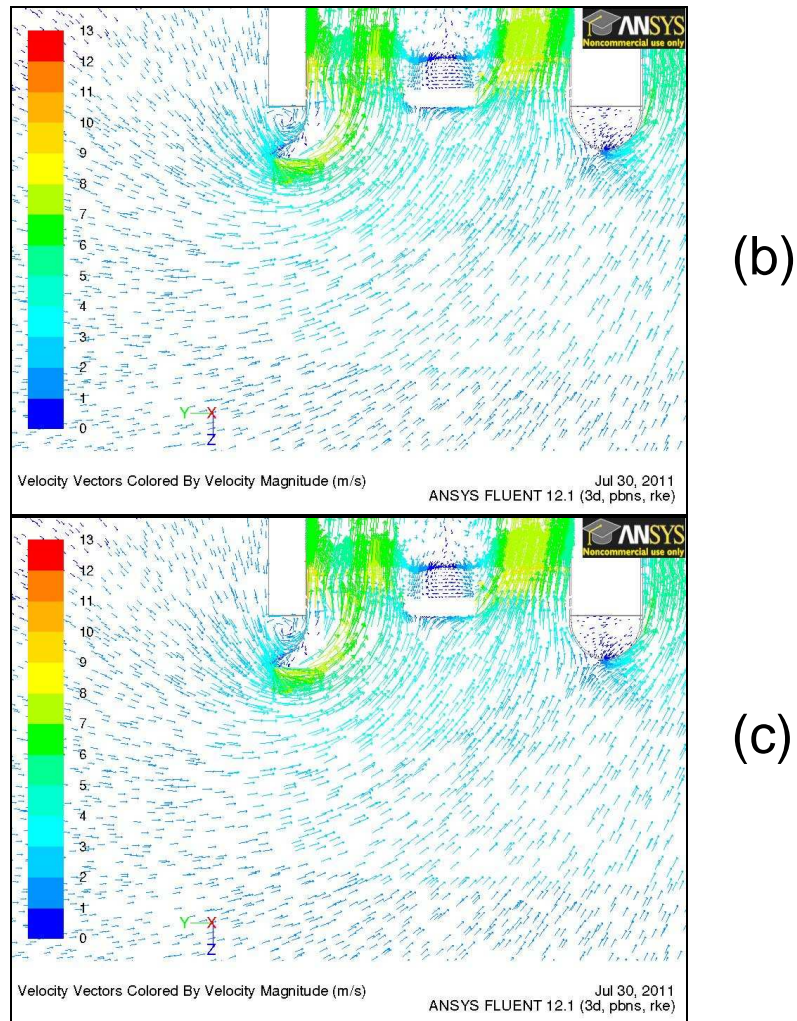


Figure 4.33: Vector plots for (a) PJM, (b) ADM and (c) EADM at infinite floor height, H10-fan.

Figure 4.34 shows the velocity profiles along a horizontal line drawn from the edge of the edge fan bell mouth for a 2.5 x fan diameter floor height. Similar to the results for the B- and N-fan, as the floor height is reduced to a value of 2.5 x fan diameter the correlation between the results from the EADM and ADM and the experimental results deteriorates, although the numerical values still show the same trend as the experimental values.

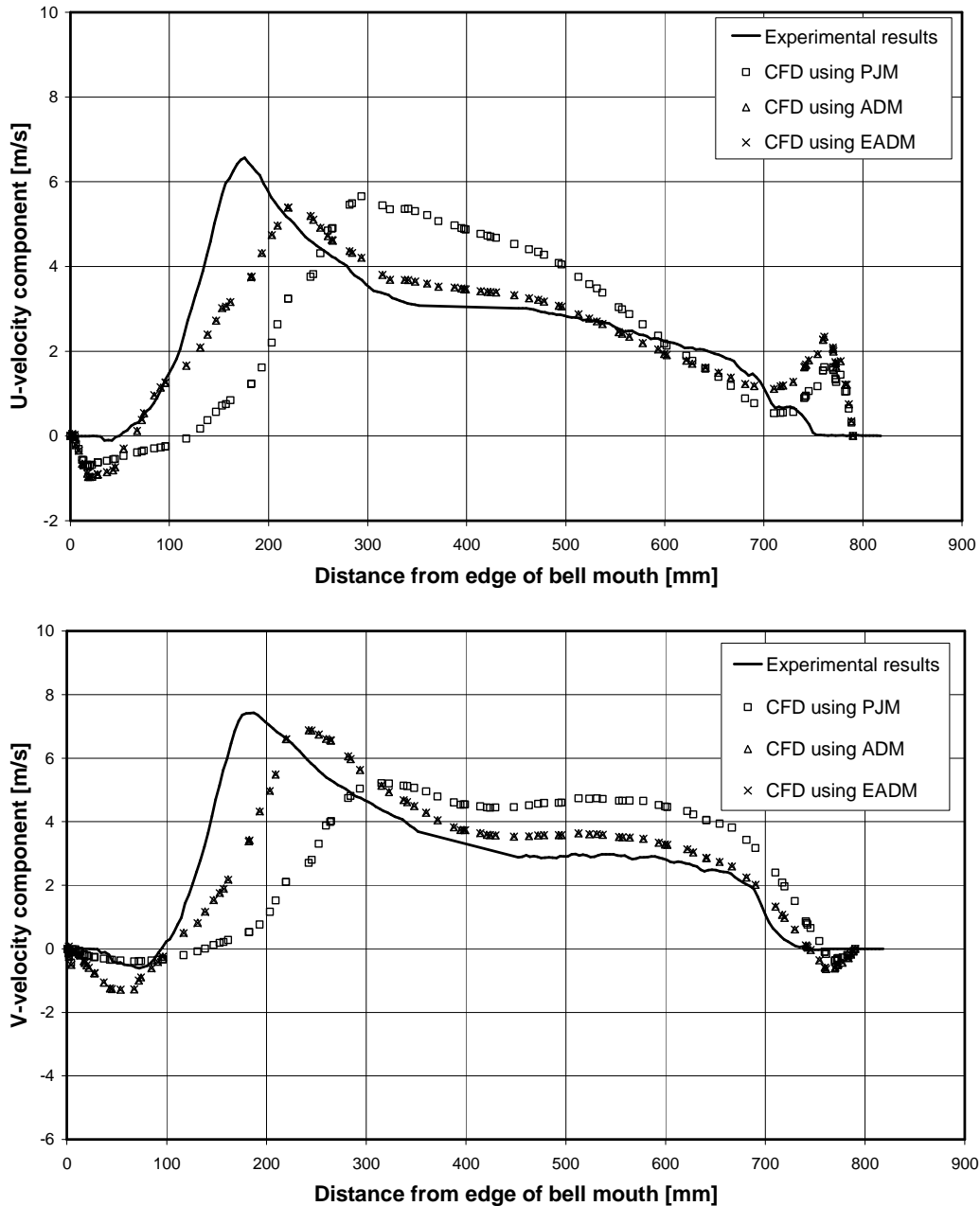


Figure 4.34: Comparison of U- and V-velocity profiles for H10-fan at horizontal line from edge of bell mouth for 2.5 x fan diameter floor height.

Figure 4.35 shows a vector plot for results obtained using the PJM, ADM and EADM (seen from top to bottom) at 2.5 x fan diameter floor height. The vector plots show how the ADM and EADM predict an identical, relatively small separation zone on the inside of the bell mouth, upstream of the fan rotor, while the PJM predicts a larger separation zone. The ADM and EADM also predict a similar transfer of air from the inside radius to the outside radius of the fan rotor downstream of the fan.

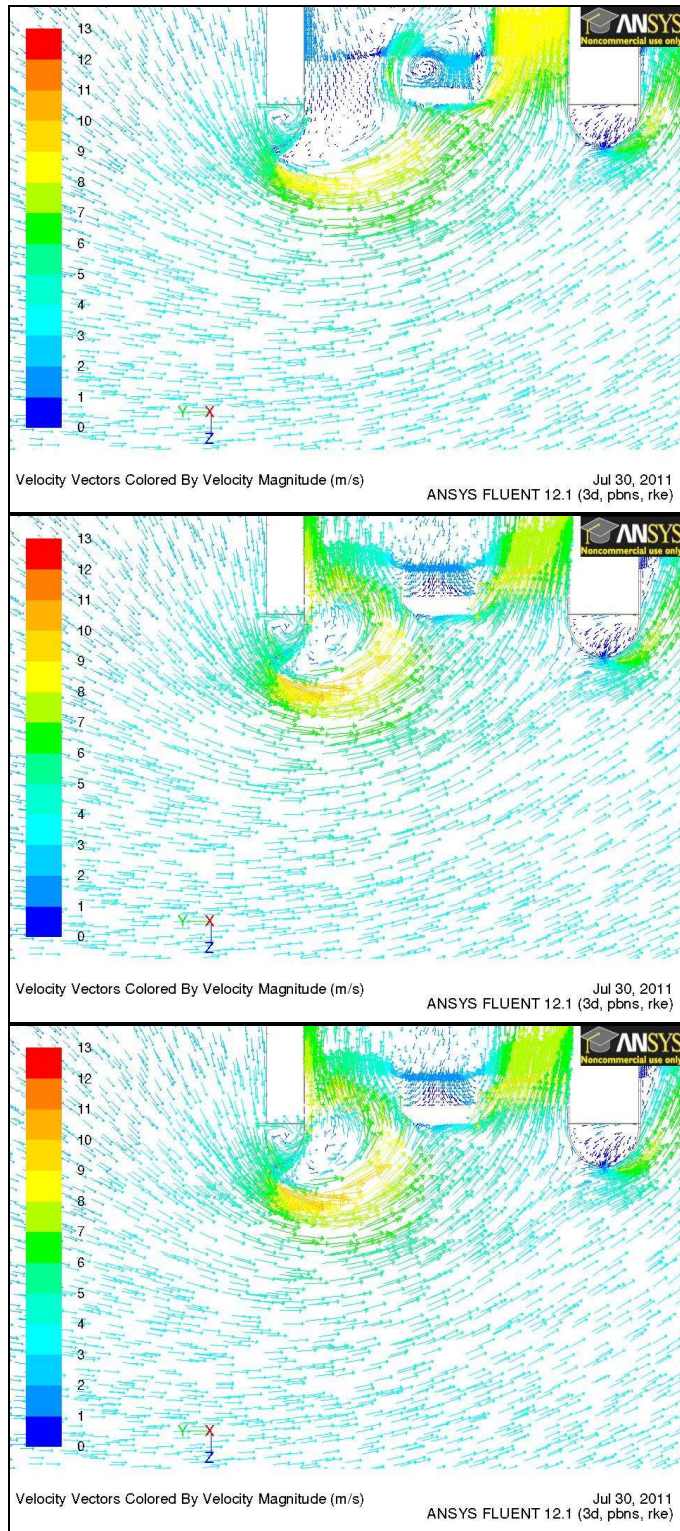


Figure 4.35: Vector plots for (a) PJM, (b) ADM and (c) EADM at 2.5 x fan diameter floor height, H10-fan.

Figure 4.36 shows the velocity profiles along a horizontal line drawn from the edge of the edge fan bell mouth for a 1.0 x fan diameter floor height. At this floor height the numerical results correlate well with the experimental values on the inner half of the edge fan only.

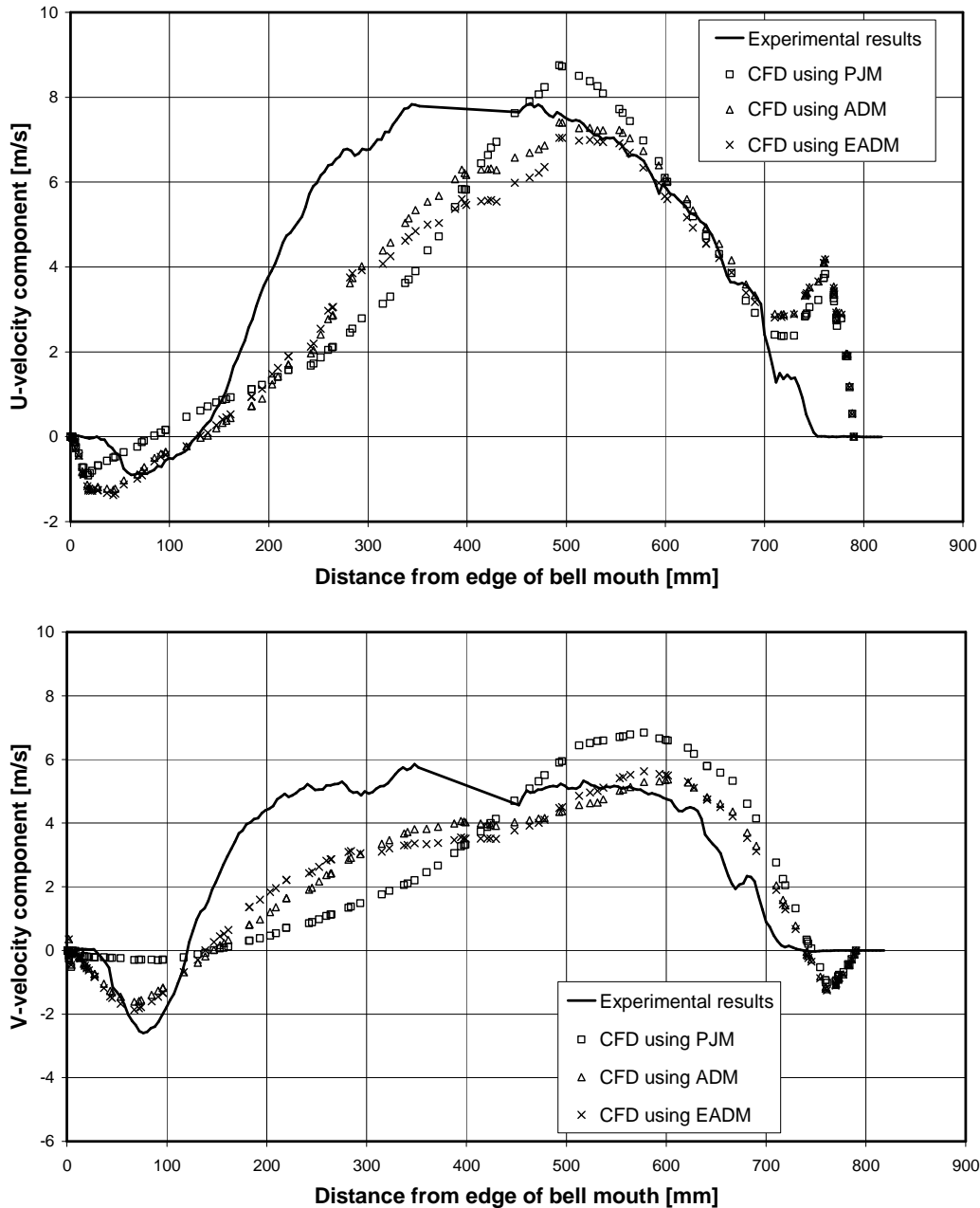


Figure 4.36: Comparison of U- and V-velocity profiles for H10-fan at horizontal line from edge of bell mouth for 1.0 x fan diameter floor height.

Figure 4.37 shows a vector plot of results obtained using the PJM, ADM and EADM (seen from top to bottom) at 1.0 x fan diameter floor height.

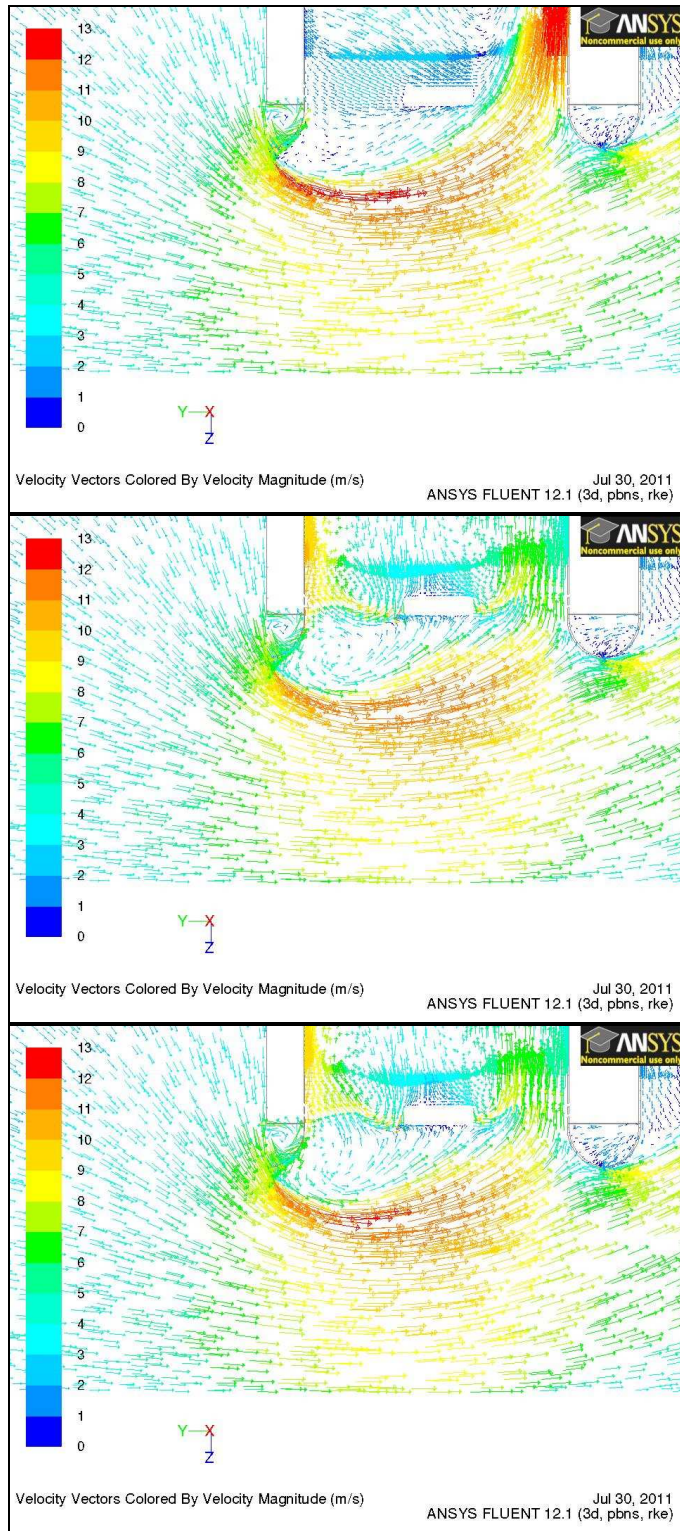


Figure 4.37: Vector plots for (a) PJM, (b) ADM and (c) EADM at 1.0 x fan diameter floor height, H10-fan.

4.8 Summary

4.8.1 Single fan simulations

Three methods were used to simulate the performance of three different experimental fans in CFD. The simplest of these three methods is the pressure jump method (PJM). Although the availability of fan performance information makes the use of this method attractive it also holds disadvantages. The biggest disadvantage associated with the PJM is its inability to take the local fan blade properties into account when predicting the flow distribution over the face of the fan rotor. This disadvantage is however not present when modelling the fan in a single fan environment where the flow distribution over the face of the fan is uniform.

The actuator disc method (ADM) separates the fan rotor into discrete blade elements that incorporate the local geometric properties of the fan blades. The ADM predicts the performance of the fan accurately over its normal operating range. However, the ADM assumes that the flow passes over the fan blades on a cylindrical surface that is aligned with the fan's axis of rotation. It does not take the effect of radial flow through the fan rotor into account and consequently under-predicts the static pressure rise over the fan at low flow rates.

The extended actuator disc method (EADM) was derived to compensate for the ADM's under-prediction of static pressure rise over the fan at low flow rates. Depending on the fan type the EADM still under-predicts the fan's static pressure rise at very low flow rates (although considerably less than is the case for the ADM). This indicates the existence of several pressure increase mechanisms at low flow rates. The difference in prediction accuracy between different fan configurations also indicates that fan configuration influences the mechanisms that cause pressure rise at low flow rates.

4.8.2 Multiple fan simulations

Far upstream of the edge fan (see line 1, 2 and 3 in Figure 3.15) the multiple fan simulations show that the degree of correlation between the experimental and numerical results is largely independent of fan configuration and fan simulation method.

Immediately upstream of the rotor the correlation between the experimental and numerical results is dependent on three factors, namely platform height, fan simulation method and fan configuration. The level of correlation achieved between the experimental and numerical results for these variables are summarised in Tables 4.6, 4.7 and 4.8.

Table 4.6: Summary of error percentages for N- edge fan volumetric effectiveness.

floor height	Experimental	PJM	ADM	EADM
[H/D]		[%]	[%]	[%]
infinite	0.973	-1.70	2.01	2.06
4.5	0.956	-5.88	-1.19	1.42
3.5	0.946	-7.31	-4.40	1.00
2.5	0.922	-10.88	-10.22	-0.42
1.5	0.830	-20.59	-34.13	-15.64
1.0	0.354	5.63	-21.01	5.06

Table 4.7: Summary of error percentages for B- edge fan volumetric effectiveness.

floor height	Experimental	PJM	ADM	EADM
[H/D]		[%]	[%]	[%]
infinite	0.973	-3.54	1.74	1.75
4.5	0.949	-6.44	1.23	1.36
3.5	0.937	-6.65	0.08	0.80
2.5	0.911	-8.07	-4.96	-0.61
1.5	0.824	-12.81	-18.84	-9.10
1.0	0.529	-4.86	-30.25	-14.30

Table 4.8: Summary of error percentages for H10- edge fan volumetric effectiveness.

floor height	Experimental	PJM	ADM	EADM
[H/D]		[%]	[%]	[%]
infinite	0.975	-0.95	0.97	1.10
4.5	0.965	-3.69	0.41	0.55
3.5	0.958	-4.31	0.09	0.22
2.5	0.942	-6.30	-0.71	-0.58
1.5	0.867	-9.42	0.51	0.85
1.0	0.550	11.41	-15.41	-2.97

At an infinite platform height (and no or very little inlet flow distortion) the experimental and numerical results for the edge fan correlate within 3.5% for all fan configurations and simulation methods. This is evident when comparing the edge fan volumetric effectiveness values as well as the velocity components on the centre plane directly upstream of the fan rotor and is valid for all fan configurations as well as the different fan simulation methods.

The level of correlation obtained for the edge fan deteriorates as the platform height is reduced. The accuracy of the PJM varies between a minimum of 3.7%

(H10-fan at 4.5 x fan diameter floor height) and a maximum of 20.6% (N-fan at 1.5 x fan diameter floor height) of the measured values. The ADM predicts the performance of the edge fan between a minimum of 0.41% (H10-fan at 4.5 x fan diameter floor height) and a maximum of 34.13% (N-fan at 1.0 x fan diameter floor height) of the measured values. The EADM predicts edge fan volumetric effectiveness within a minimum of 0.55% (H10-fan at 4.5 x fan diameter floor height) and a maximum of 15.6% (N-fan at 1.5 x fan diameter floor height) of the measured values. The EADM predicts edge fan volumetric effectiveness within 2% of the measured values for any fan configuration at a platform height of 2.5 x fan diameter and higher.

Inspection of the centre plane velocity distribution upstream of the edge fan at the different floor heights shows good correlation at an infinite floor height for all fan configurations and simulation methods and reasonable correlation at 2.5 x fan diameter floor height, depending on fan configuration and simulation method. At 1.0 x fan diameter floor height, reasonable correlation is shown only for the B-fan, specifically using the EADM. Based on the PIV results, it should be concluded that none of the three simplified fan models investigated showed conclusively that it would give reliable results for any fan configuration regardless of the level of inlet flow distortion.

Another interesting aspect of the results is the relative insensitivity of the system volumetric effectiveness towards the different simulation methods and fan configurations, as shown by Figure 4.14, 4.22 and 4.30. This is attributed to the fact that the two inner fans of the multiple fan facility used the N-fan configuration at all times. These fans were also modelled using the PJM in all the simulations.

4.8.3 Advantages and disadvantages of simplified fan models

A number of advantages and disadvantages related to the different simplified fan models were identified during the course of this investigation:

Table 4.9: Summary of advantages and disadvantages of different simplified fan models.

Method	Advantages	Disadvantages
PJM	<ul style="list-style-type: none"> • Only fan static pressure curve required. • Fan section can be modelled with coarse grid. • Correct single fan performance results can be obtained at all flow rates. 	<ul style="list-style-type: none"> • Assumes fan static pressure curve of complete fan is valid at all blade spans. • Fan must be tested under reversed flow conditions to be able to model reversed flow regions. • Does not take the effect of radial flow in the fan rotor into account.
ADM	<ul style="list-style-type: none"> • Sensitive to changing blade properties with span. • Sensitive to local angle of attack variations over complete fan face. • Can handle reversed flow through the rotor. 	<ul style="list-style-type: none"> • Requires detailed information on fan blades. • Requires more detailed mesh than PJM. • Does not take the effect of radial flow in the fan rotor into account. • Does not give accurate single fan performance results at low flow rates.
EADM	<ul style="list-style-type: none"> • Sensitive to changing blade properties with span. • Sensitive to local angle of attack variations over complete fan face. • Can handle reversed flow through the rotor. • Gives an improved estimate of fan performance at low flow rates. 	<ul style="list-style-type: none"> • Requires detailed information on fan blades. • Requires more detailed mesh than PJM. • Does not take the effect of radial flow in the fan rotor into account. • Slightly more complicated than ADM. • Model is empirical and requires additional assumptions.

One of the objectives of this study, as listed in Section 1.4, is to combine the effect of fan configuration and distorted inlet flow conditions with the use of

simplified fan models. The use of simplified models is motivated by the need for reduced computational requirements when analysing a multiple fan installation. The results from this chapter have shown that the EADM gives the most accurate representation of the performance of an axial flow fan that is subjected to distorted inlet flow conditions. Unfortunately the EADM requires a more detailed mesh than the PJM and its practical application when modelling a large ACC consisting of numerous axial flow fans would be limited. In this regard the method applied by van Rooyen (2007) is recommended. Van Rooyen performed an analysis of a 30-fan ACC by iteratively switching between a simplified “boundary condition” method and the ADM for selected critical fans in the ACC.

5 APPLICATION OF THE EXTENDED ACTUATOR DISC METHOD TO ACCs

5.1 Introduction

The purpose of this chapter is to investigate specific applications and results obtained using a simplified numerical model to simulate the performance of an edge fan. For that purpose the extended actuator disc method (EADM) is used to model the operation of the 630 mm diameter B-fan for a number of multiple fan system configurations. The use of the EADM and B-fan combination is motivated by the good results and correlation with the velocity profiles shown in Chapter 4.

5.2 Edge fan installation with bell mouth and no walkway – results and discussion

Figure 5.1 shows a comparison of the numerical and experimental results for the vector field along the centre plane of the multiple fan test facility.

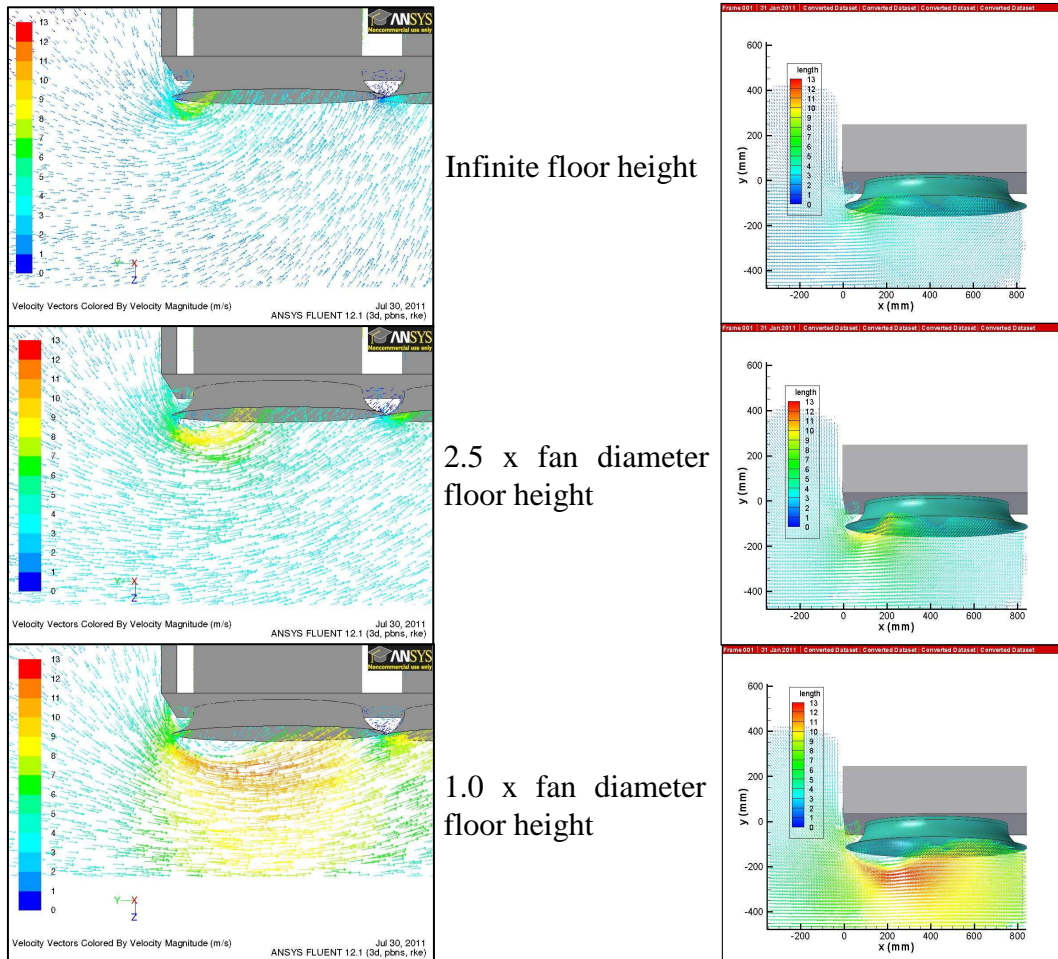
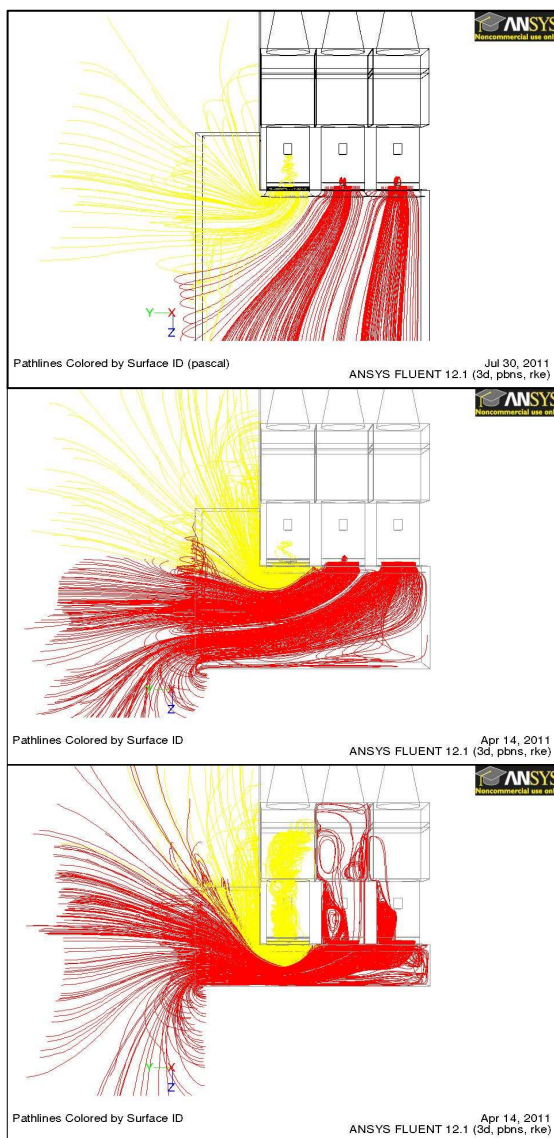


Figure 5.1: Comparison of numerical (left) and experimental (right) results for edge fan.

The simulations were performed at various floor heights and the results show that the EADM gives estimates of the volumetric effectiveness of the edge fan that are within 5% of the experimental values (Figure 4.19). The vector field shown in Figure 5.1 is coloured according to velocity magnitude and shows an increase in the maximum velocity value at the centre plane bell mouth corner upstream of the edge fan from 7 m/s to 13 m/s as the platform height decreases from infinity to 1.0 x fan diameter. The increase in velocity value can be directly attributed to the decrease in flow area as the platform height is reduced.

Figure 5.2 shows the pathlines followed by the air entering the edge fan, relative to the air entering the other two fans, at different floor heights.



Infinite floor height

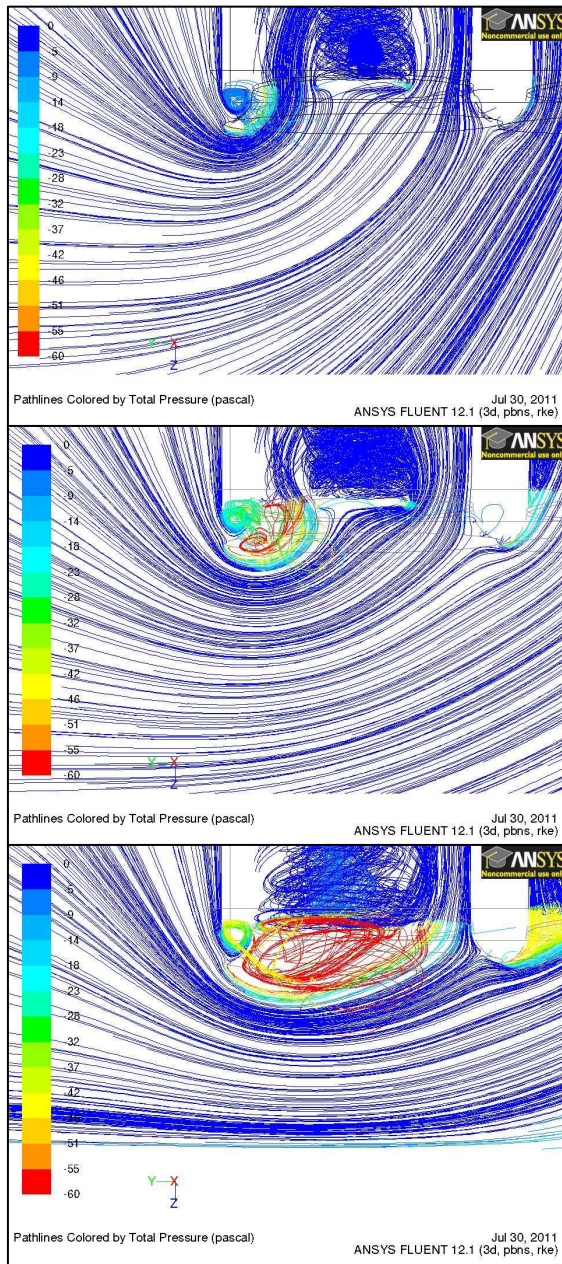
2.5 x fan diameter floor height

1.0 x fan diameter floor height

Figure 5.2: Simulated pathlines at different floor heights.

Of particular interest in Figure 5.2 is how the origin of the air that enters the edge fan changes from an even distribution upstream of the edge fan (at an infinite floor height), to coming exclusively from the air domain that is above the location of the edge fan (at $1.0 \times$ fan diameter floor height). Therefore, at low platform heights the majority of the supply air has to be turned through 180° before it can enter the edge fan. The supply air domain is located next to and above the plenum chamber and in actual plant conditions this may lead to increased plume recirculation. Also important to note is that the pathlines that experience the flow losses caused by the platform and bell mouth edge are all destined for the edge fan. This was also witnessed from the numerical results of the other configurations that were investigated.

Figure 5.3 shows the simulated pathlines followed by the air entering the edge fan at the centre plane. The path lines are coloured according to a total pressure range of 0 to -60 N/m^2 . The large number of blue coloured pathlines (pressure of 0 N/m^2) indicates that a very small total pressure loss occurs along most of the streamlines entering the edge fan at an infinite floor height. The only pathlines that exhibit a significant total pressure loss are the ones entering from the supply air domain above the edge fan. These pathlines try to adhere to an abrupt change in flow direction and display a total pressure loss at the platform corner and another one at the edge of the bell mouth of the edge fan. These pathlines also highlight an area of distorted inlet conditions in front of the fan.



Infinite floor height

2.5 x fan diameter floor height

1.0 x fan diameter floor height

Figure 5.3: Simulated pathlines along centre plane, at different floor heights.

Viewing the pathlines from a slightly different angle, Figure 5.4 shows how the vortices that are shed by the platform corner at a platform height of 2.5 x fan diameter run around the outside of the bell mouth to the side of the fan, from where they are entrained into the low pressure area on the inside of the bell mouth.

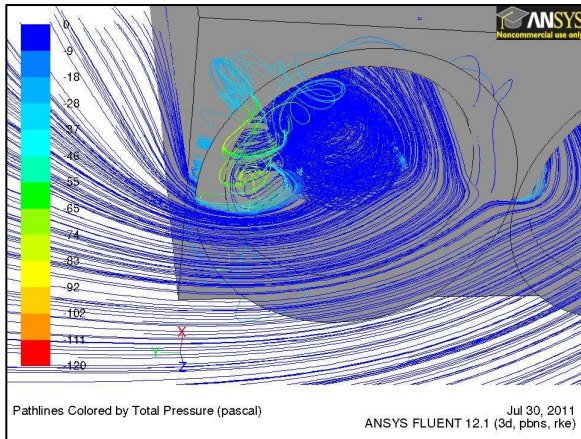


Figure 5.4: Streamline plot at centre plane, 2.5 x fan diameter floor height.

As the floor height is decreased, the number of pathlines entering from the domain above the level of the edge fan increases. A pathline plot of the vortices being shed by the platform corner at a floor height of 1.0 x fan diameter is shown in Figure 5.5. It shows how the number of vortices being shed by the platform corner increases along with increased flow separation at the edge of the bell mouth.

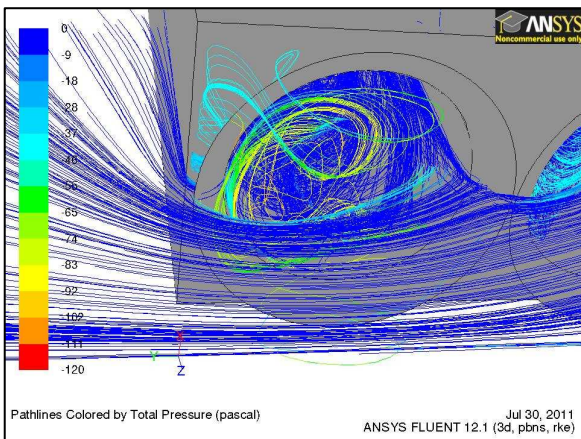
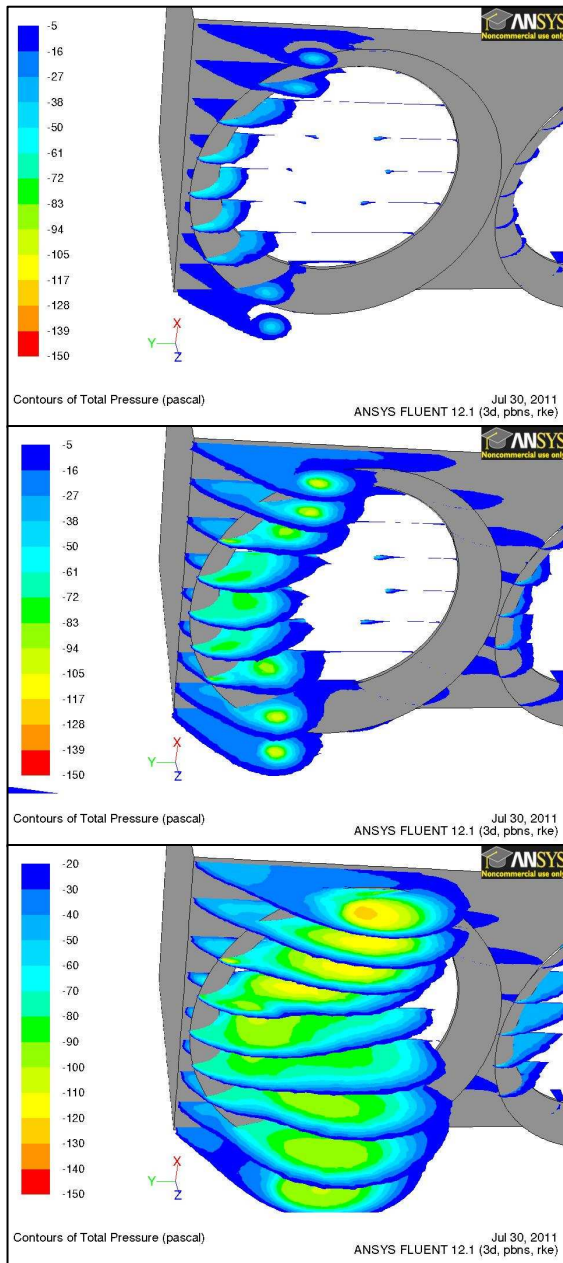


Figure 5.5: Streamline plot at centre plane, 1.0 x fan diameter floor height.

Figure 5.6 shows the total pressure contours at various sections upstream of the edge fan for different platform heights. The contours are shown in a range of -5 to -150 N/m^2 , except at the 1.0 x fan diameter floor height where the maximum pressure shown is -20 N/m^2 for the purpose of visualisation. Figure 5.6 gives an indication of the relative size of the total pressure variation that the flow experiences. It also gives an indication of the 3-dimensional nature of the flow losses. At an infinite floor height the total pressure drop at the edge of the platform is very small (less than 10 N/m^2 - see Figure 5.3). The maximum total pressure drop is 50 N/m^2 located on the centre plane close to the inside surface of the edge fan bell mouth. The total pressure drop increases to a maximum value of

80 N/m² at a floor height of 2.5 x fan diameter. The maximum values are located at the sides of the fan underneath the bell mouth and not along the centre plane. A total pressure value of -60 N/m² is shown on the centre plane on the inside of the bell mouth. At a floor height of 1.0 x fan diameter the total pressure drop increases to a maximum of 140 N/m². The low pressure region extends over most of the bell mouth inlet area and the contour plots are asymmetrical. Air flowing back through the rotor into the upstream region imparts rotation to the reverse flow and causes the flow distribution upstream of the fan to be asymmetrical.



Infinite floor height

2.5 x fan diameter floor height

1.0 x fan diameter floor height

Figure 5.6: Total pressure contours at different floor heights.

5.3 The effect of a walkway on the performance of multiple axial flow fans

The addition of a walkway (or skirt) at the side of a multiple fan installation has been described by a number of authors (Salta and Kröger (1995) and Bredell et al. (2006)). It is shown that the addition of a walkway increases the volumetric effectiveness of a multiple fan system. According to the experimental work of Salta and Kröger (1995) the beneficial effect of a walkway occurs in a range of width to fan diameter ratio of 0.159 to 0.476. This was also confirmed in numerical analyses by Meyer (2005) who showed that a walkway reduces the level of inlet flow distortions. Bredell et al. (2006) simulated an “A-fan” and “B-fan” installation and showed that the volumetric effectiveness of the system increases with the inclusion of a walkway. Bredell et al. (2006) conclude that the inclusion of a walkway reduces the cross flow velocity upstream of the fan and leads to an “abatement” of the separation upstream of the edge fan.

The purpose of this simulation was to evaluate the beneficial effect of a walkway both experimentally and numerically using the same fan configuration. The walkway was added to the side of the existing multiple fan test facility as shown in Figure 5.7. A walkway width of 0.206 m was used based on the numerical work of Bredell (2005).

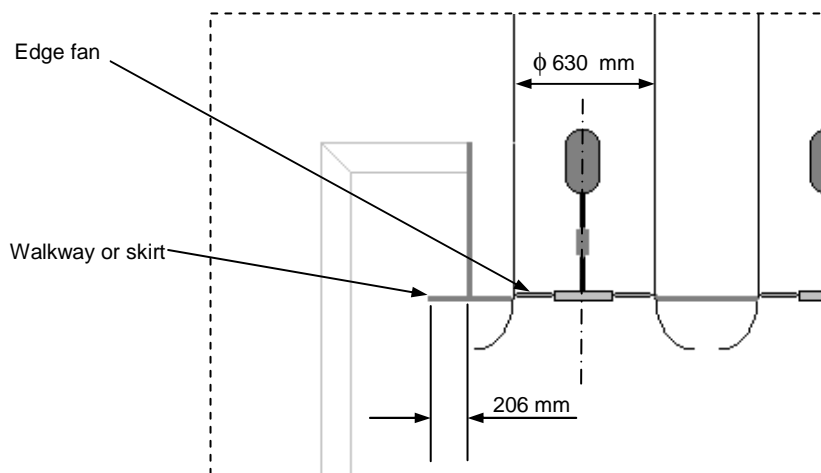


Figure 5.7: Lay-out of multiple fan test facility with walkway added.

The tests were conducted in exactly the same manner as detailed in Chapter 3 and the results are shown in Figure 5.8. The results show an increase in the volumetric effectiveness of the edge fan, ranging from 1% at an infinite fan diameter to 4% at 2.5 x fan diameter and 49% at 1.0 x fan diameter floor height. Tests were also conducted for the N_N_N - and H10_N_N multiple fan configurations and the full set of results are shown in Appendix F.

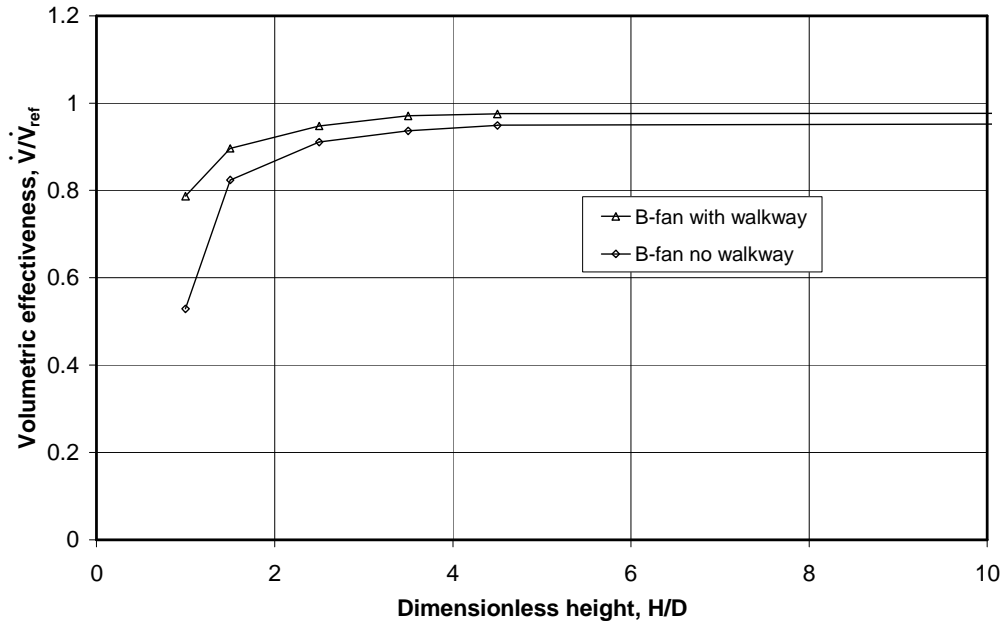


Figure 5.8: Experimental results of tests for B_N_N configuration with and without walkway.

5.3.1 CFD model for edge fan investigation with walkway

The CFD model that was used in this investigation was identical to the model used for the previous investigation without the walkway (see Chapter 4), except for the addition of the walkway. A picture of the geometry surrounding the edge fan, as used in this investigation, is shown in Figure 5.9.

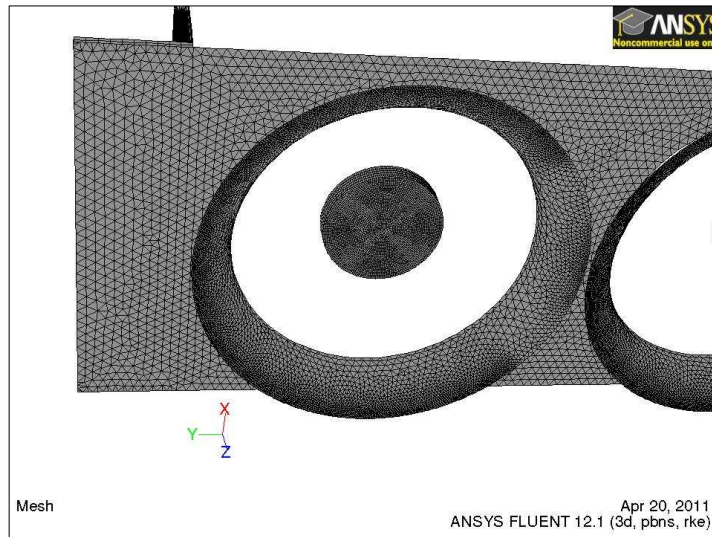


Figure 5.9: Detail of walkway in CFD model.

5.3.2 Results and discussion for walkway investigation

The results of the numerical simulation, showing the volumetric effectiveness of the edge fan, compared to the experimental results are shown in Figure 5.10.

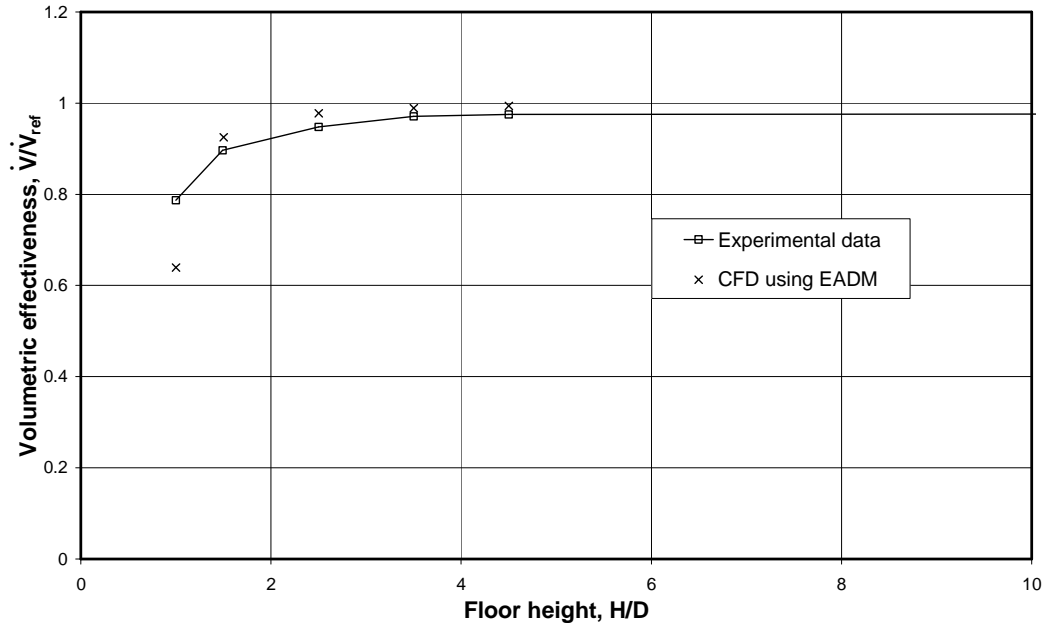


Figure 5.10: Volumetric effectiveness of edge fan for B_N_N configuration with walkway.

Figure 5.10 shows that the numerical simulations over-predict the volumetric effectiveness by 0.025 for the range from infinite fan diameter to 1.5 x fan diameter floor height. At 1.0 x fan diameter floor height the simulated values under-predict the experimental values by 0.15. The measured volumetric effectiveness at a floor height of 1.0 x fan diameter is 0.79. This corresponds with the discrepancy, although somewhat smaller, between the experimental and numerical values noted for the installation without the walkway at a floor height of 1.5 x fan diameter (see Figure 4.40) where the measured volumetric effectiveness is 0.82, compared to a numerical value of 0.75.

A comparison of the numerical and experimental vector field distributions upstream of the edge fan at various floor heights is shown in Figure 5.11.

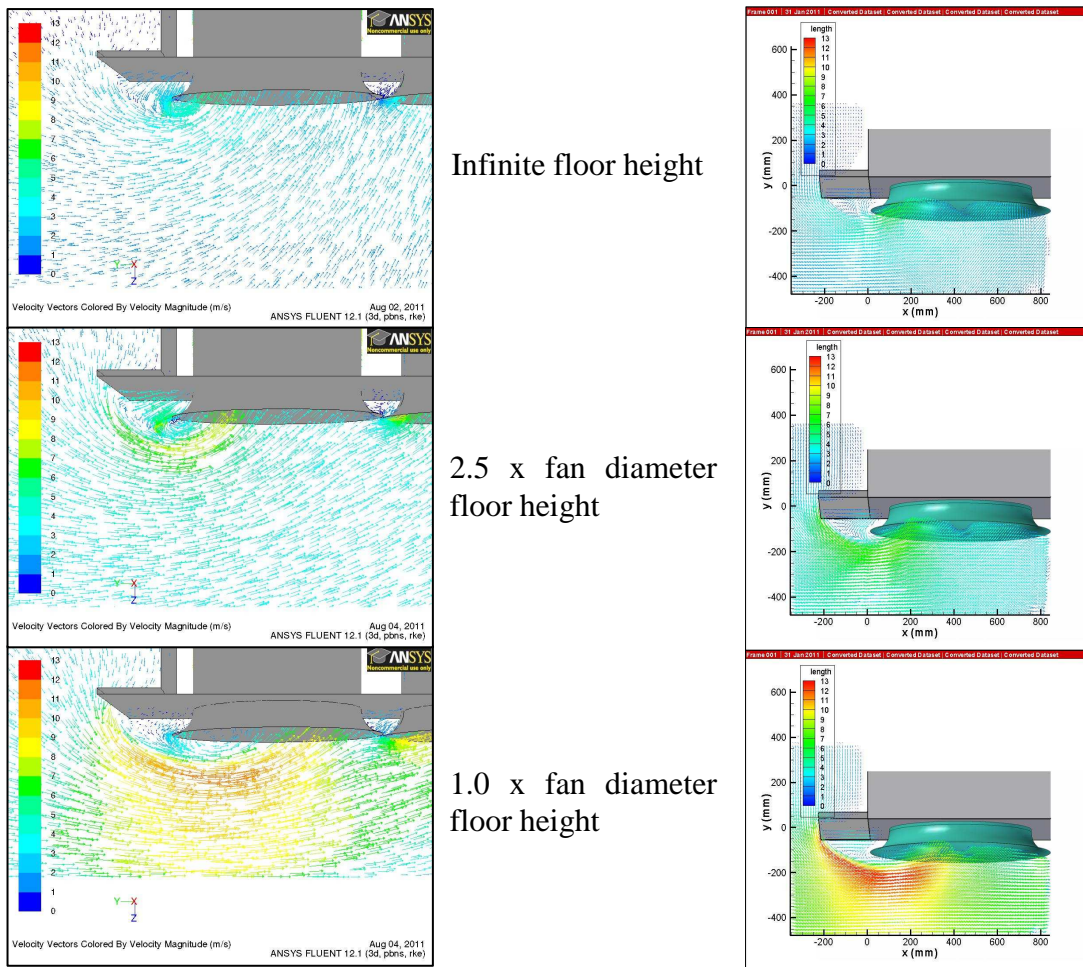
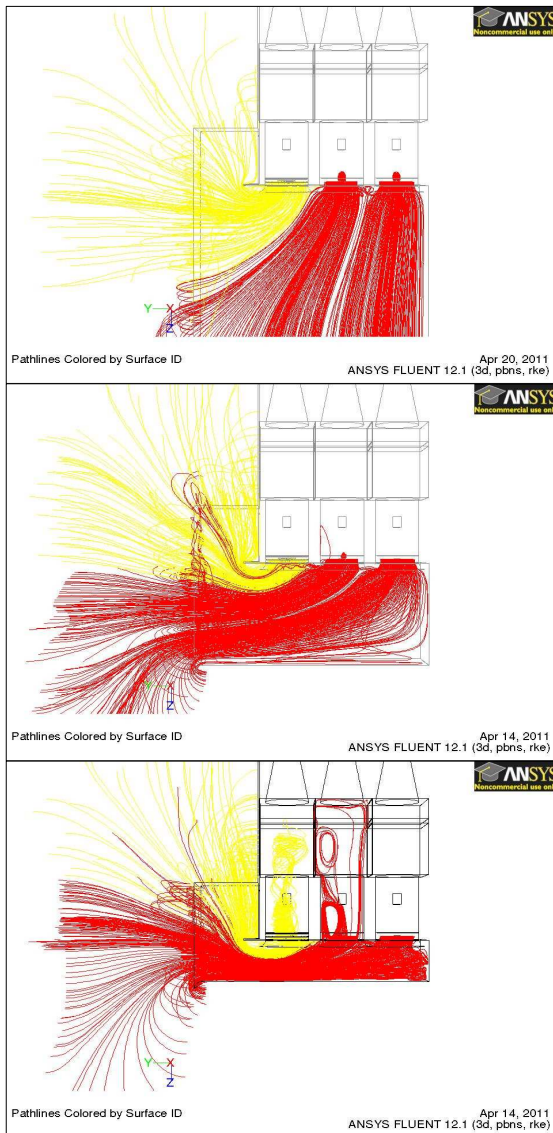


Figure 5.11: Comparison of numerical (left) and experimental (right) results for edge fan with walkway.

Figure 5.11 shows that at an infinite and 2.5 x fan diameter floor height the pictures correlate quite well. At a floor height of 1.0 x fan diameter there is, however, a distinct difference between the two pictures and the high velocity area measured experimentally is larger than that predicted numerically. This is caused by the difference between the measured and simulated volumetric effectiveness of the 2nd fan – the measured value was 0.91, compared to a simulated value of 0.85. The 2nd fan is modelled using the PJM, which was shown to be inaccurate at lower volumetric effectiveness values (see Figure 4.14). The addition of a walkway reduces the volumetric effectiveness of the 2nd fan (without a walkway, the experimentally measured value is 0.94) and also the accuracy with which it is modelled using the PJM.

The vector field distributions in Figure 5.11 show that the flow inside the separation bubble downstream of the walkway gets re-entrained into the centre plane inlet flow at the bell mouth edge. This phenomenon can be observed in both the numerical and experimental flow distributions. The width of the walkway used in this experiment is such that the bell mouth edge at the centre plane sits inside the separation bubble. This means that the pressure drop over the edge of the bell mouth is relatively small and air inside the separation bubble gets entrained into the fan along the centre plane.

Figure 5.12 shows the pathlines entering the edge fan at different floor heights (coloured in yellow). Similar to the installation without a walkway, the supply air that enters the edge fan changes from an even distribution upstream of the edge fan (at an infinite floor height), to coming exclusively from the air domain that is above the location of the edge fan (at a 1 x fan diameter floor height). However, when comparing the installation with a walkway to the installation without a walkway, it is clear that the presence of the walkway reduces the air supply coming from the region directly next to and above the plenum chamber. The walkway forces the location of the air supply to be more spread out, even at a low floor height. Consequently, the angle through which the air that enters the edge fan has to be turned is reduced.



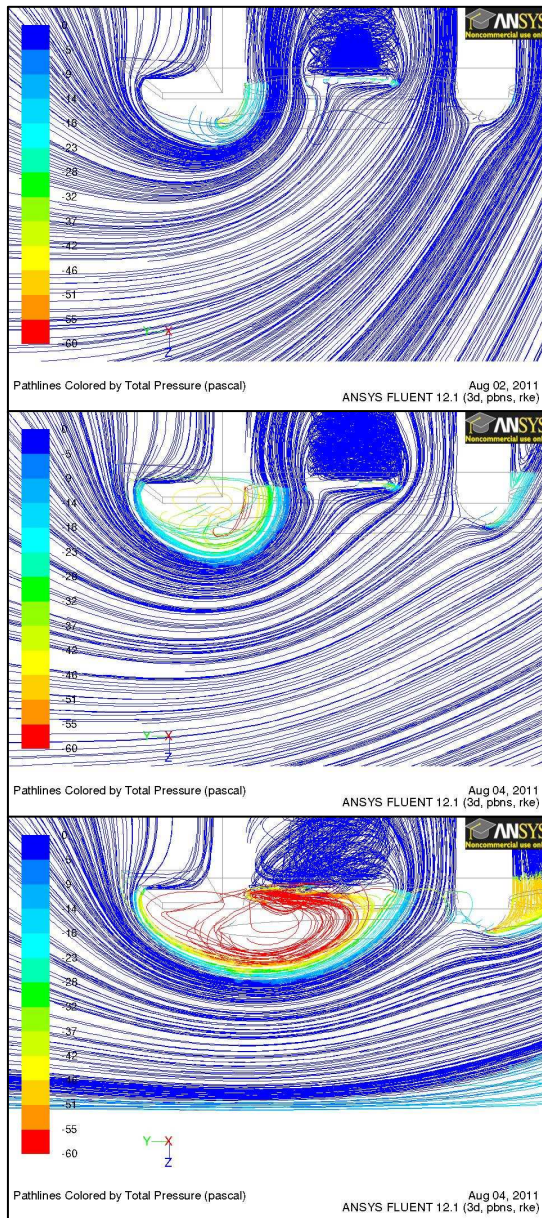
Infinite floor height

2.5 x fan diameter
floor height

1.0 x fan diameter
floor height

Figure 5.12: Simulated pathlines at various floor heights, with walkway.

Figure 5.13 shows the simulated pathlines followed by the air entering the edge fan at the centre plane. The path lines are coloured according to a total pressure range of 0 to -60 N/m^2 . Comparing Figure 5.13 to Figure 5.3 shows the increased radius of curvature of the streamlines entering the edge fan and the lower total pressure drop upstream of the edge fan. Figure 5.13 also shows that, despite the larger separation zone, the addition of the walkway ensures that the area of distorted flow conditions (flow that is not aligned with the designed flow direction) directly upstream of the fan is reduced.



Infinite floor height

2.5 x fan diameter
floor height

1.0 x fan diameter
floor height

Figure 5.13: Simulated pathlines along centre plane, at different floor heights, with walkway.

Viewing the pathlines from a slightly different angle, Figure 5.14 shows the vortices that are shed by the edge of the walkway at a height of 2.5 x fan diameter. The pathline plot shows a different flow pattern from that shown by Figure 5.4. Since the distorted inflow region upstream of the fan is considerably smaller (compared to the set-up without a walkway) the vortices do not run around the outside of the bell mouth to the side of the fan, as shown in the installation without the walkway.

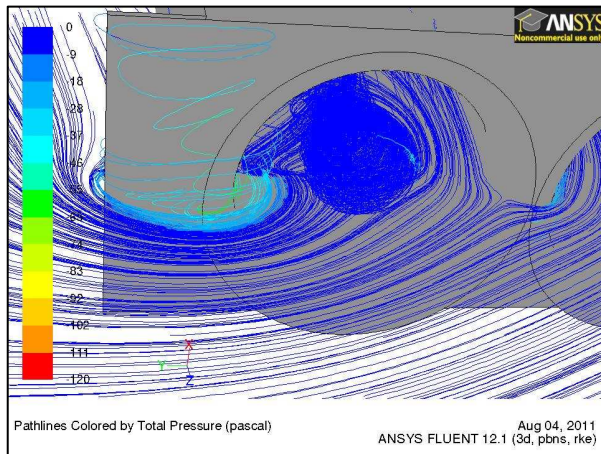
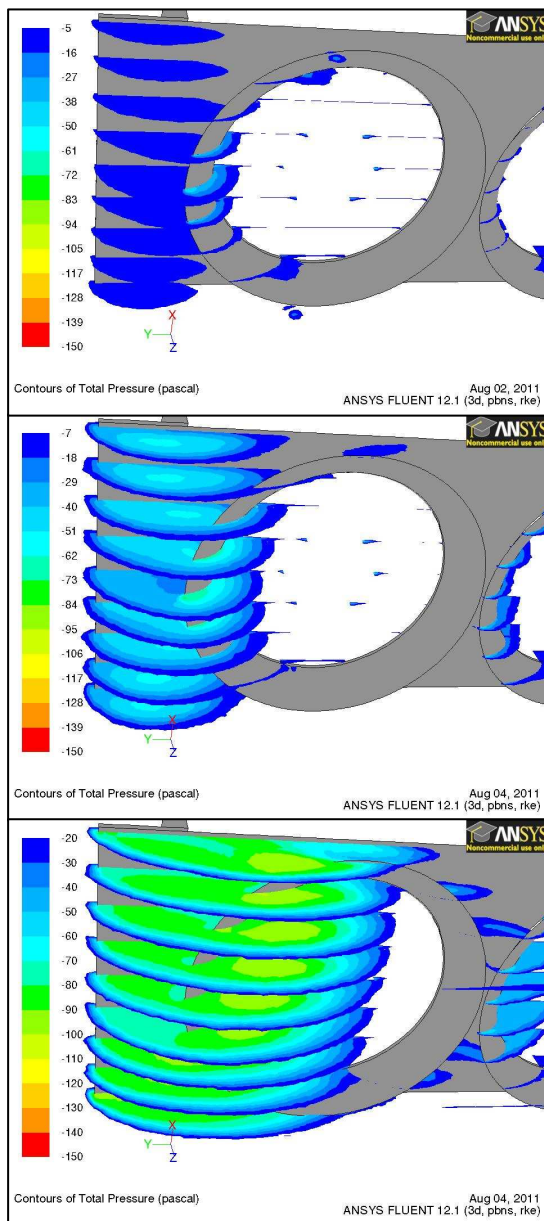


Figure 5.14: Streamline plot at centre plane, 2.5 x fan diameter floor height.

Figure 5.15 shows the total pressure contours at various sections upstream of the edge fan for different platform heights. The contours are shown in a range of -5 to -150 N/m^2 , except at the 1.0 x fan diameter floor height where the maximum pressure shown is -20 N/m^2 for the purpose of visualisation. Figure 5.15 gives an indication of the relative size of the total pressure variation that the flow experiences. At an infinite floor height the total pressure drop downstream of the walkway is 15 N/m^2 . The maximum total pressure drop is 40 N/m^2 and is located on the centre plane close to the inside surface of the edge fan bell mouth. At a floor height of 2.5 x fan diameter the total pressure drop increases to a maximum value of 40 N/m^2 downstream of the walkway and 60 N/m^2 on the centre plane on the inside surface of the edge fan bell mouth. At a floor height of 1.0 x fan diameter the total pressure drop increases to a value of 70 N/m^2 downstream of the walkway and 115 N/m^2 on the centre plane on the inside surface of the edge fan bell mouth. Compared to the installation without the walkway the low pressure region is more uniform and covers a smaller region of the bell mouth inlet area which ensures less inlet flow distortions for the edge fan.



Infinite floor height

2.5 x fan diameter
floor height

1.0 x fan diameter
floor height

Figure 5.15: Total pressure contours at different floor heights, with walkway.

5.4 The performance of an edge fan with no bell mouth inlet

Duvenhage et al. (1995) performed a numerical investigation where they simulated the effect of inlet flow distortions on the performance of forced draught air-cooled heat exchangers by evaluating the performance of a multiple fan system at various floor heights. As part of their investigation they considered the effect of inlet shroud configuration on the volumetric effectiveness of an edge fan. For this purpose they evaluated cylindrical, conical and bell mouth inlets. They found that the variation in volumetric effectiveness with floor height of the fan system follows the general trend of the Salta curve regardless of the inlet shroud configuration. Smaller differences between the results of the different inlet shroud configurations did however exist and Duvenhage et al. (1995) found that the performance of a fan system with cylindrical inlet shrouds was less “dependent” on platform height than a system with bell mouth inlets. They also showed that an optimal length for a cylindrical inlet shroud exists that gives the highest volumetric effectiveness for the system. However they point out that a single, open fan performs better when equipped with a bell mouth than with a cylindrical inlet.

Meyer (2005) simulated various possible fan system configurations. In his simulations he numerically represented the B-fan (see Appendix A) using the ADM. Amongst the system configurations that he investigated was one with no inlet section on the edge fans and a bell mouth inlet on the inner fans. He found that the absence of an inlet section for the edge fan improves the performance of the edge fan at low platform heights. He also found that the presence of a bell mouth upstream of the inner fans is essential to ensure a high value of volumetric effectiveness for these fans. Joubert (2010) simulated the performance of a generic 30-fan air-cooled condenser under windy conditions using the PJM applied to the B-fan. One of the configurations that he evaluated is omitting the bell mouth inlets for the edge fans. He found that the absence of an inlet section for the edge fans did improve the performance of the edge fans but that the 2nd fan row was in turn adversely affected by the absence of a bell mouth in the first fan row. The consequence of this was that the performance of the complete system was affected negatively, although only marginally.

The purpose of this section is therefore to investigate the flow pattern upstream of an edge fan that does not have an inlet section. The flow pattern can then be compared to previous results to explain any possible changes in the performance of the edge fan.

5.4.1 Results and discussion for inlet section investigation

The investigation to determine the performance of an edge fan without an inlet section was conducted only numerically. The simulation was performed using the same geometry and mesh as detailed in Chapter 4 but with the edge fan bell mouth surface changed from a wall to an “interior” boundary condition. Although the facility without the bell mouth was not tested experimentally, a sketch of the lay-out of the multiple fan facility without the edge fan inlet bell mouth is shown in Figure 5.16.

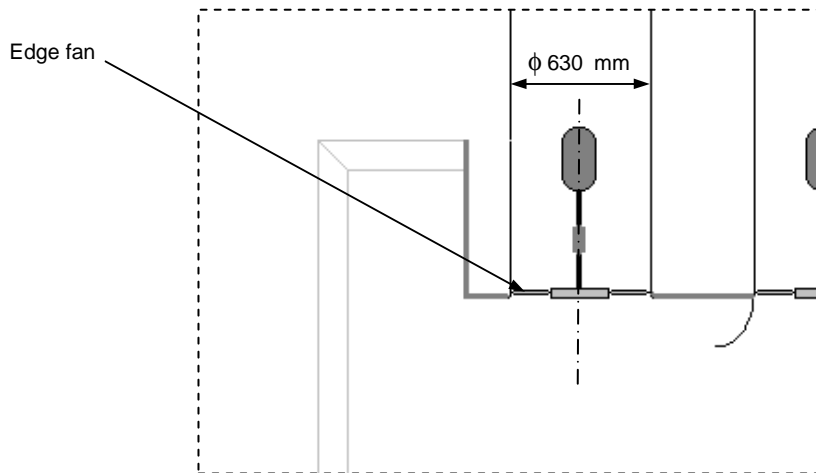


Figure 5.16: Lay-out of multiple fan test facility without edge fan inlet bell mouth.

The results of the numerical simulation, showing the volumetric effectiveness of the edge fan with no inlet section, compared to the numerical and experimental results for the edge fan with a bell mouth inlet section are shown in Figure 5.17.

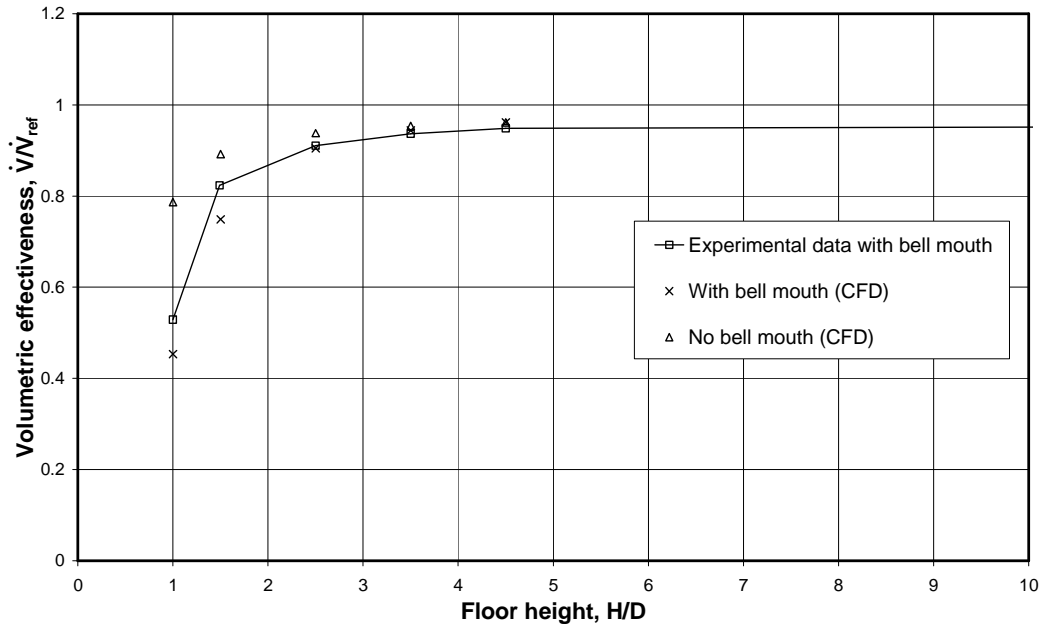
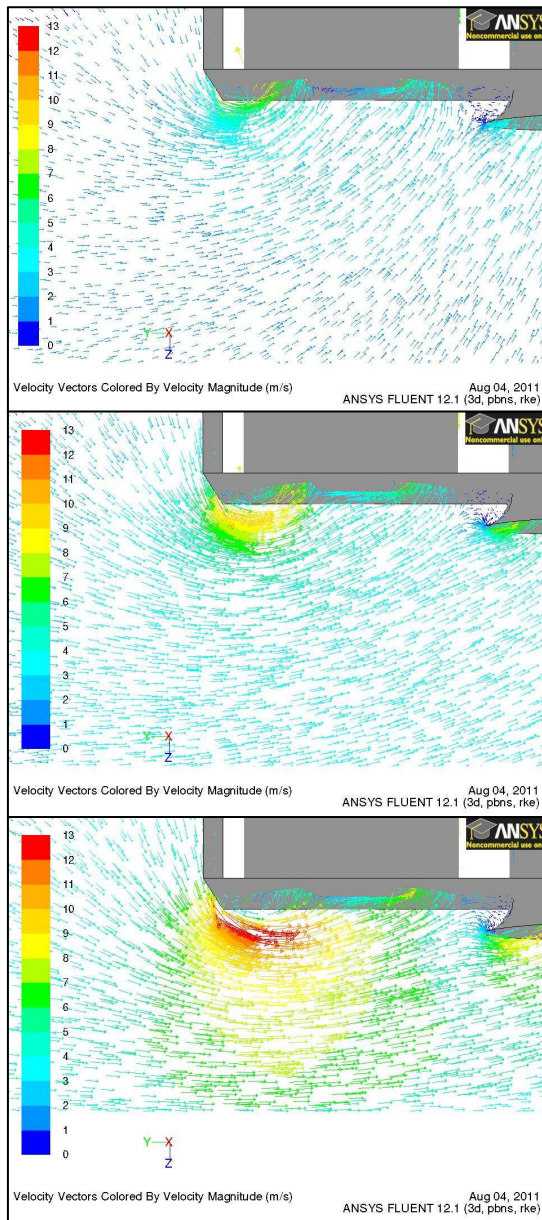


Figure 5.17: Volumetric effectiveness of edge fan for B_N_N configuration with and without bell mouth.

Figure 5.17 shows that at an infinite floor height the volumetric effectiveness of the installation without a bell mouth is slightly lower than that of an installation with a bell mouth (0.981 numerical compared to 0.995 numerical). This can be expected since the effect of distorted inlet flow is not significant at an infinite floor height. For a normal fan inlet (flow equally distributed from all sides) the use of a bell mouth reduces the inlet losses compared to an installation with no bell mouth (Duvenhage et al., 1995). At lower floor heights the volumetric effectiveness of the edge fan without a bell mouth inlet is higher than that of the installation with a bell mouth. The difference in volumetric effectiveness increases from 0.5% at 4.5 x fan diameter floor height to 48% at 1.0 x fan diameter floor height.

The vector field distributions upstream of the edge fan at various floor heights is shown in Figure 5.18. The vector field is coloured according to velocity magnitude and shows an increase in the maximum velocity value at the centre plane bell mouth corner upstream of the edge fan from 6 m/s to 13 m/s as the platform height decreases from infinity to 1.0 x fan diameter. Similar to the other system configurations the increase in velocity value can be directly attributed to the decrease in flow area as the platform height is reduced.



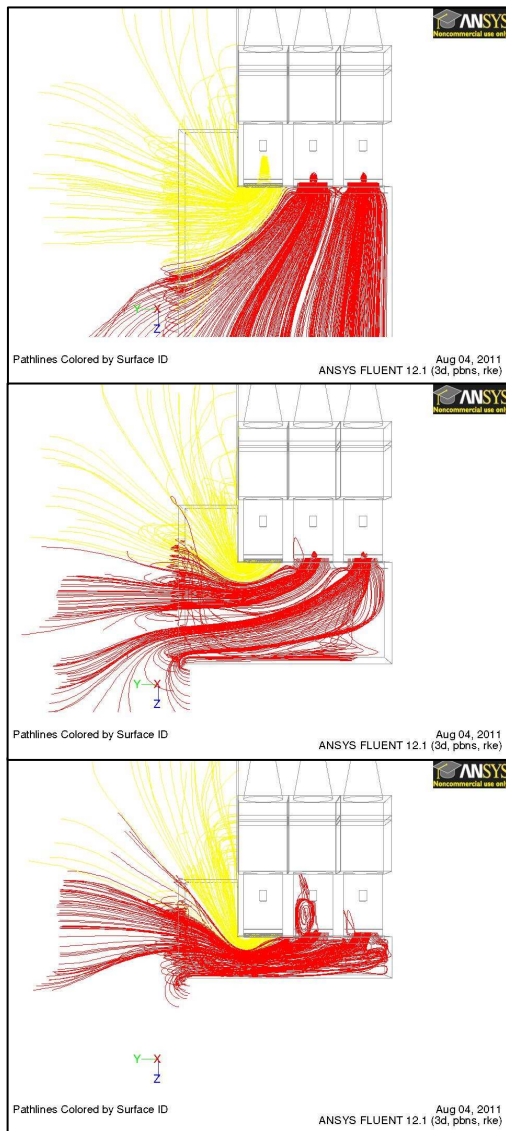
Infinite floor height

2.5 x fan diameter floor height

1.0 x fan diameter floor height

Figure 5.18: Vector field distribution at different floor heights, without bell mouth.

Figure 5.19 shows the pathlines followed by the air entering the edge fan, relative to the air entering the other two fans, at different floor heights. The pathline distribution at different floor heights for the installation without the bell mouth is similar to that of the installation with the bell mouth. At 1.0 x fan diameter height the absence of a bell mouth reduces the radius of curvature of the pathlines considerably.



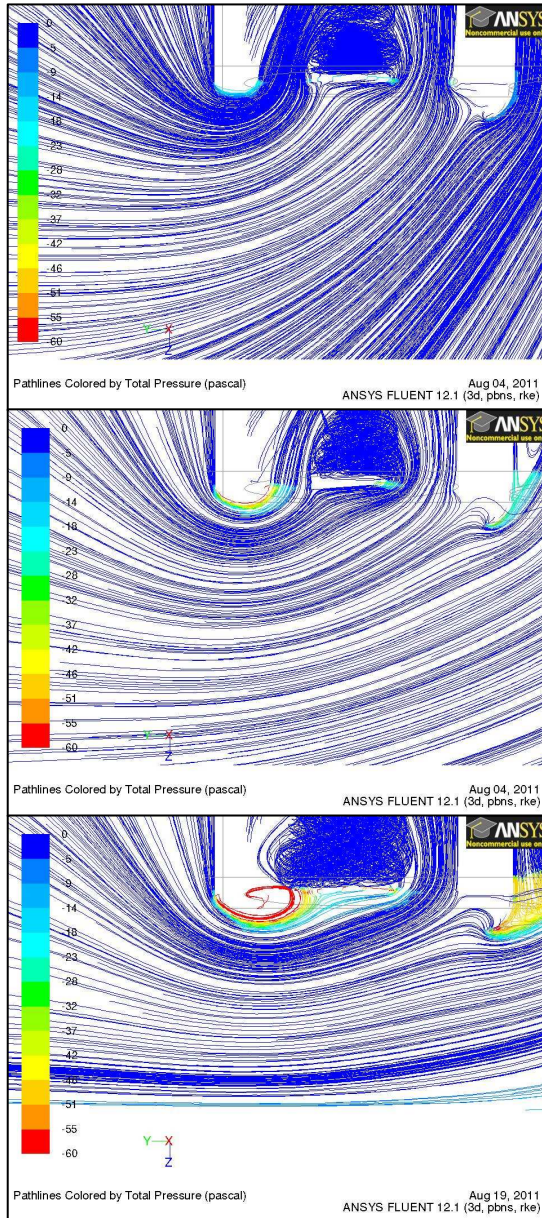
Infinite floor height

2.5 x fan diameter floor height

1.0 x fan diameter floor height

Figure 5.19: Simulated pathlines at various floor heights, without bell mouth.

Figure 5.20 shows the simulated pathlines followed by the air entering the edge fan at the centre plane. The path lines are coloured according to a total pressure range of 0 to -60 N/m^2 . The absence of a bell mouth means that there is only one source of total pressure loss, namely the platform corner. The smaller radius of curvature also means that the size of the distorted region in front of the edge fan is reduced.



Infinite floor height

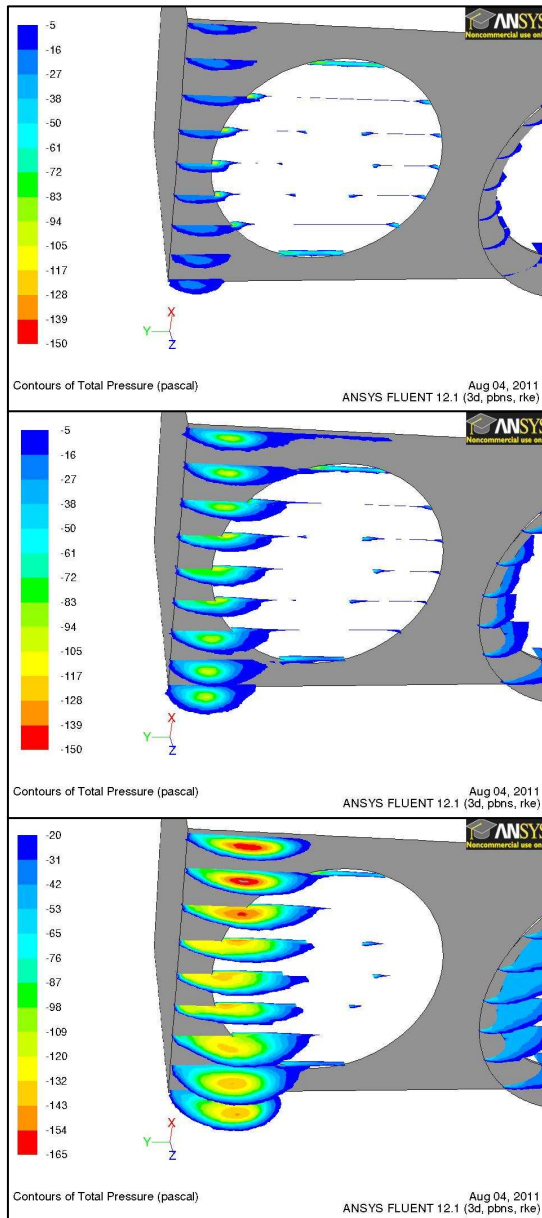
2.5 x fan diameter
floor height

1.0 x fan diameter
floor height

Figure 5.20: Simulated pathlines along centre plane, at different floor heights, without bell mouth.

Figure 5.21 shows the total pressure contours at various sections upstream of the edge fan for different platform heights. The contours are shown in a range of -5 to -150 N/m^2 , except at the $1.0 \text{ x fan diameter}$ floor height where the maximum pressure shown is -20 N/m^2 for the purpose of visualisation. Figure 5.21 gives an indication of the relative size of the total pressure variation that the flow experiences. At an infinite floor height the total pressure drop at the edge of the platform is 20 N/m^2 . The total pressure drop increases to a maximum value of 80 N/m^2 at a floor height of $2.5 \text{ x fan diameter}$, located along the centre plane. At

a floor height of 1.0 x fan diameter, the total pressure drop increases to a maximum value of 115 N/m². The low pressure region only extends over 50% of the bell mouth inlet area. Compared to the installation with a walkway, at a 1.0 x fan diameter floor height the installation without a bell mouth has a similar low pressure region in front of the edge fan.



Infinite floor height

2.5 x fan diameter floor height

1.0 x fan diameter floor height

Figure 5.21: Total pressure contours at different floor heights, without bell mouth.

5.5 Comparison of pressure plots for different inlet configurations

To compare the pressure losses associated with the different inlet configurations the average pressure values along the pathlines crossing through specific surfaces were obtained from the CFD results. The location of these reference surfaces is shown in Figure 5.22. Unfortunately no experimental values were available for comparison to the CFD data, primarily since pressure measurements in these locations would have been very difficult to perform.

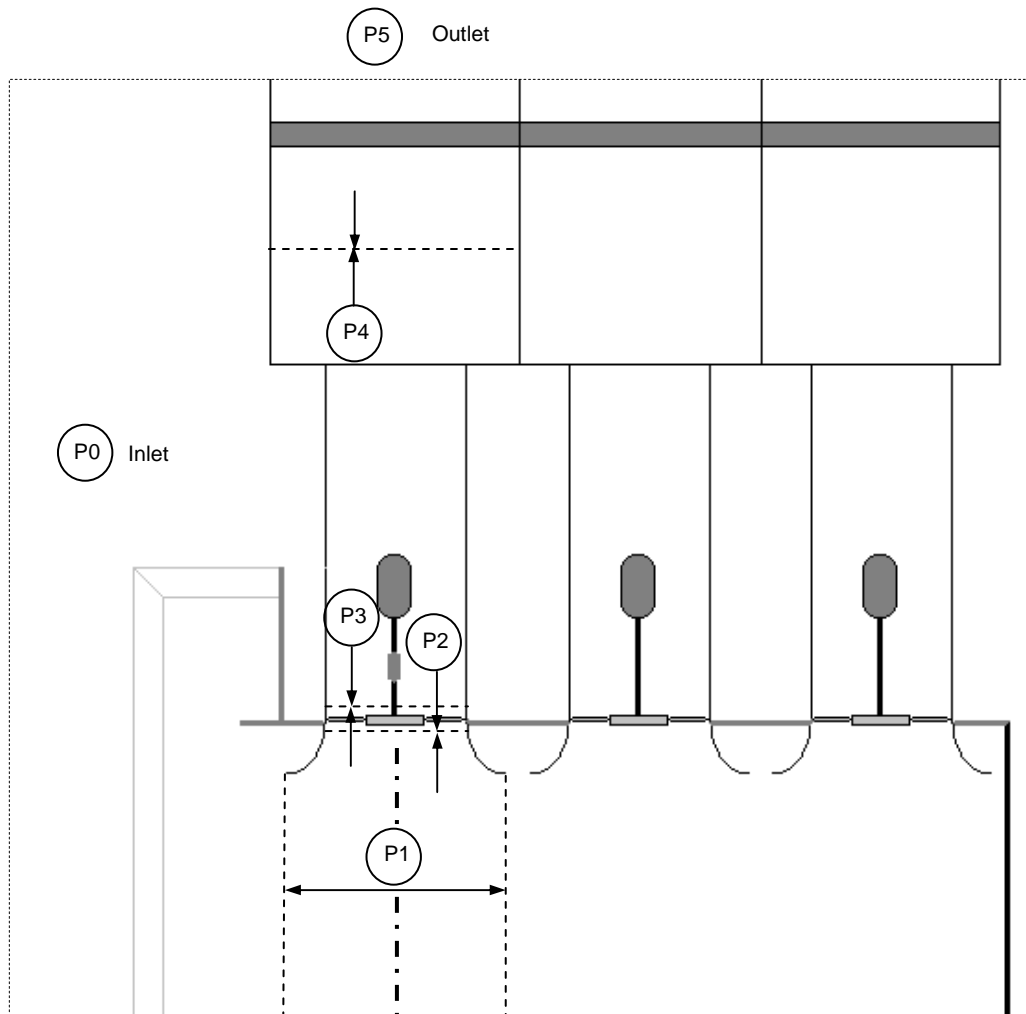


Figure 5.22: Reference surfaces for tracking of pressure values.

As shown in Figure 5.22 P0 is located at the inlet of the test facility. P1 is formed by a cylinder with a radius of 0.395 m that extends downwards from the outer edge of the bell mouth. For the configuration without the bell mouth, P1 had the same radius as before but extended downwards from the bottom edge of the platform. The third surface, P2, is formed by a circular disc with an outer radius of 0.315 m, 55 mm upstream of the plane of rotation of the fan. According to the CFD model, the “z-distance” for the location of P2 was specified to be 0.0625 m.

P3 is formed by a similar circular disc as P2, 100 mm downstream of the plane of rotation of the fan. P4 is located 1200 mm downstream of the plane of rotation of the fan and P5 is located at the outlet of the test facility. The pathlines were traced in reverse from the location of the plane of rotation of the fan. Where the pathlines crossed the reference surfaces, the relevant pressure values were obtained from the CFD results. The pathlines were discretised into 0.01 m sections, so the locating tolerance between the point on the pathline and the reference surface was set to 0.01 m.

Figures 5.23 and 5.24 show the average of the pathline total and static pressure values respectively between P0 and P5 for the edge fan configuration with a bell mouth. The total pressure values are relative to the total pressure at the inlet, which was set to zero, while the static pressure values are relative to the static pressure at the outlet, which was also set to zero (see Chapter 4).

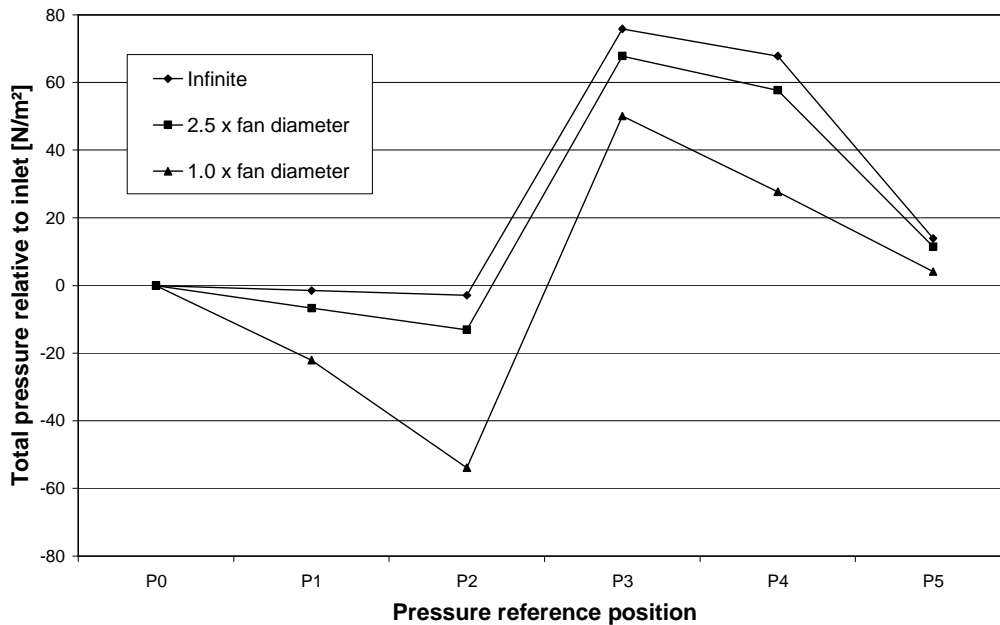


Figure 5.23: Total pressure values for edge fan with bell mouth and no walkway.

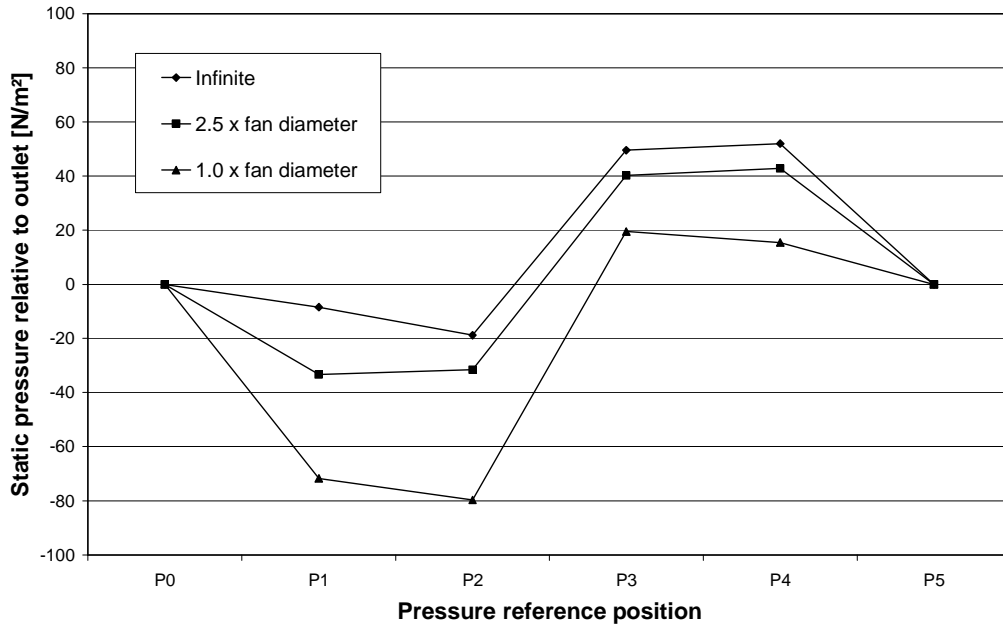


Figure 5.24: Static pressure values for edge fan with bell mouth and no walkway.

Figures 5.25 and 5.26 show the average of the pathline total and static pressure values respectively between P0 and P5 for the edge configuration with a bell mouth and platform extension (walkway).

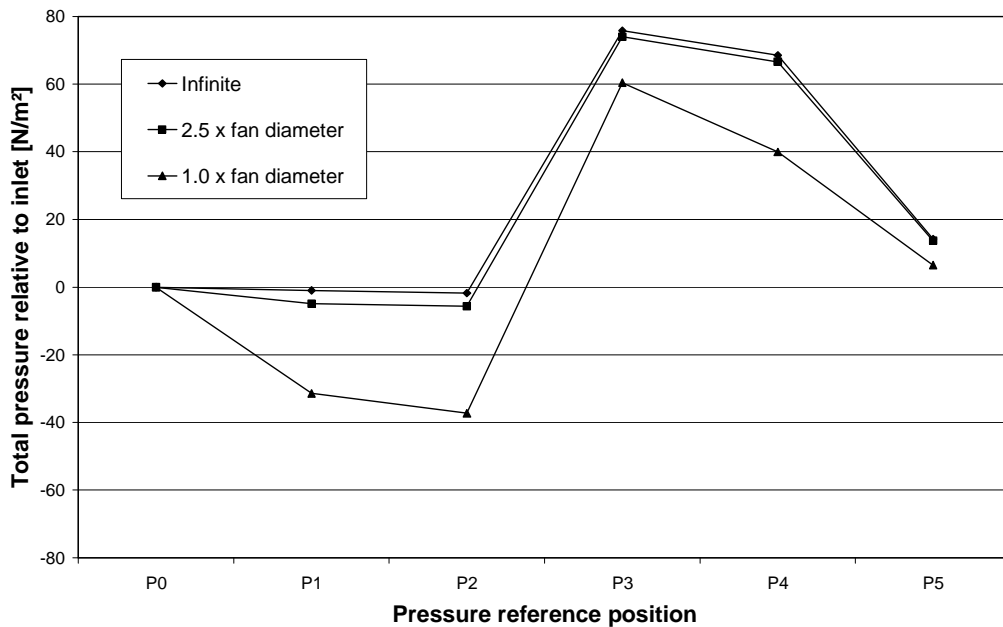


Figure 5.25: Total pressure values for edge fan with bell mouth and walkway.

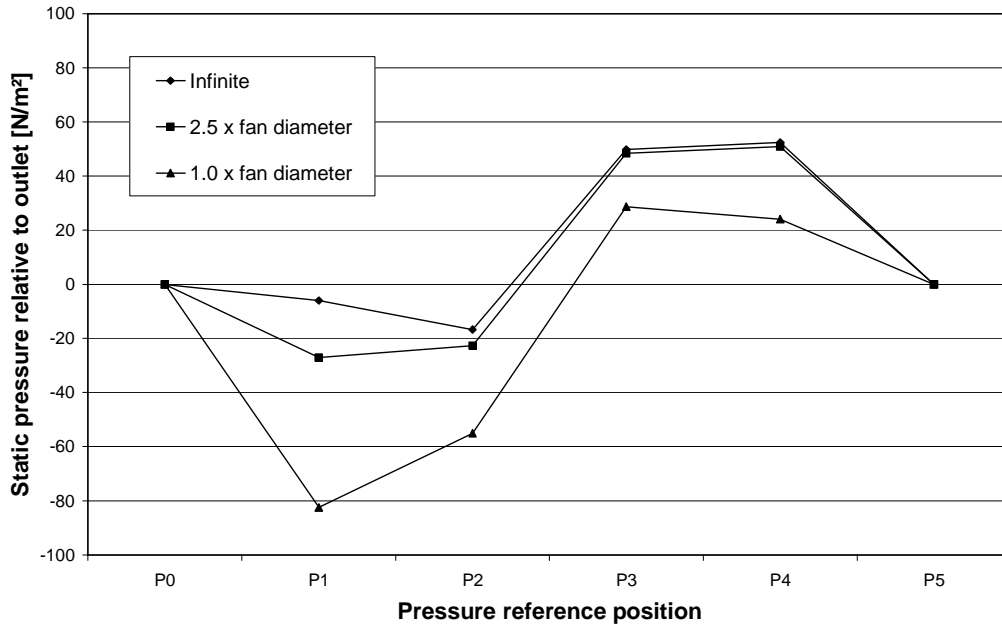


Figure 5.26: Static pressure values for edge fan with bell mouth and walkway.

Figures 5.27 and 5.28 show the average of the pathline total and static pressure values respectively between P0 and P5 for the edge configuration without a bell mouth.

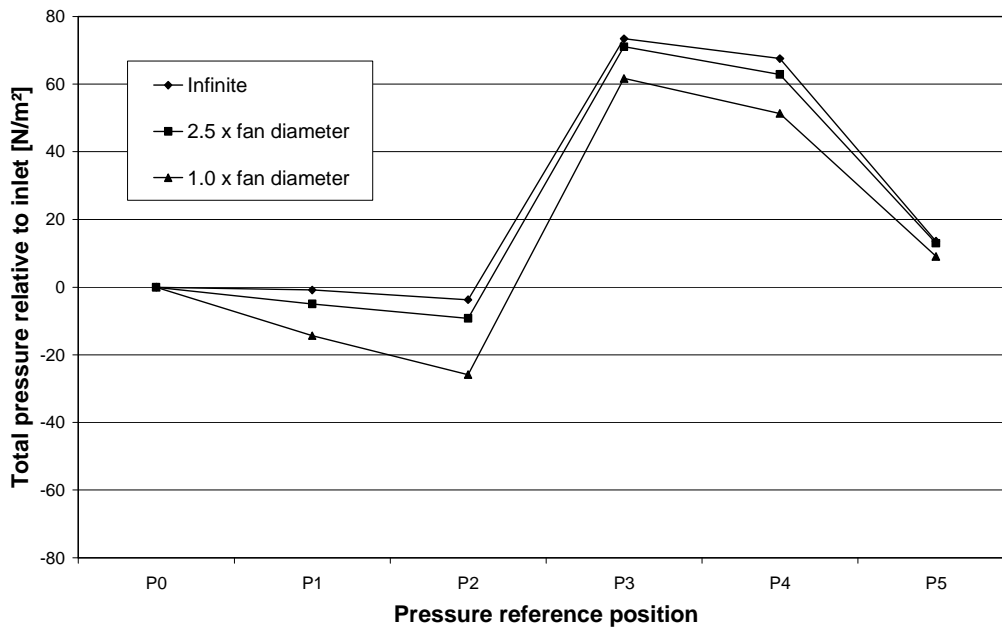


Figure 5.27: Total pressure values for edge fan without bell mouth.

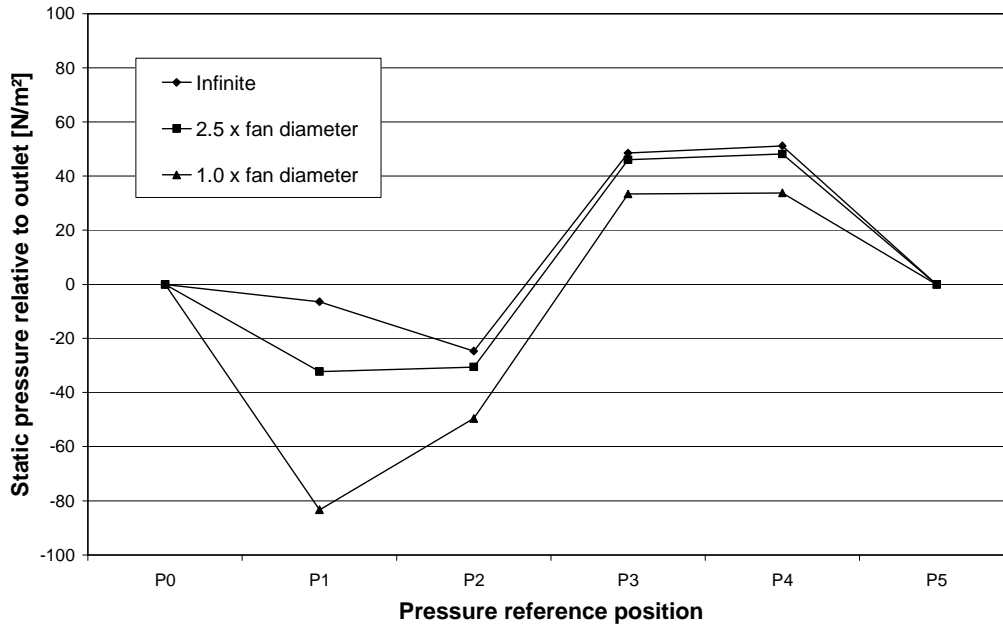


Figure 5.28: Static pressure values for edge fan without bell mouth.

Figure 5.23 shows a steady increase in the total pressure loss upstream of the edge fan (between P0, P1 and P2) with a decrease in platform height. At an infinite and 2.5 x fan diameter platform height the pressure graphs after P2 are very similar and the main difference between the two graphs is the losses upstream of the fan (P0 to P2). At 1.0 x fan diameter platform height there is a distinct total pressure loss between P1 and P2 (between the edge of the bell mouth and the plane upstream of the edge fan) of 32 N/m².

Figure 5.24 shows that the static pressure decreases between P0 and P1 at all platform heights. This is due to flow losses combined with the acceleration of the fluid as it enters the test facility. Between P1 and P2 the static pressure either decrease or increases, depending on the platform height. At an infinite platform height the fluid accelerates as it enters the fan (from P1 to P2), therefore the static pressure decrease exceeds the total pressure decrease shown in Figure 5.23. At 2.5 x fan diameter platform height the fluid accelerates as it enters the test facility (P0 to P1), after which it decelerates as it enters the fan (P1 to P2) therefore the static pressure increases slightly. This static pressure recovery is also present at 1.0 x fan diameter platform height – visible by virtue of the fact that the static pressure decrease is less than the total pressure decrease between P1 and P2.

Figure 5.25 shows the effect of a walkway on the total pressure change through the edge fan inside the test facility. The total pressure graphs at an infinite and 2.5 x fan diameter platform height are almost the same, while the total pressure loss upstream of the fan increases from 2.5 - to 1.0 x fan diameter platform height change. At 1.0 x fan diameter platform height it is interesting to note that the

largest total pressure loss upstream of the edge fan takes place between the inlet and P1 (31.4 N/m^2). Between P1 and P2 the total pressure stays almost constant, compared to the large total pressure drop between these two points shown for the installation without a walkway (Figure 5.23).

Figure 5.26 shows the effect of a walkway on the static pressure change through the edge fan. The general trends of the graphs are the same as those shown for the installation without the walkway, except for three major differences. The first difference is the smaller static pressure loss between P0 and P1 at $2.5 \times$ fan diameter platform height (27.1 N/m^2 compared to 33.4 N/m^2), the second is the larger static pressure drop between P0 and P1 (82 N/m^2 compared to 72 N/m^2) at $1.0 \times$ fan diameter platform height and the third is the significant static pressure increase that takes place between P1 and P2 (27.5 N/m^2) also at $1.0 \times$ fan diameter platform height. The effect of the walkway is therefore to move the large total pressure loss upstream of the edge fan away from the bell mouth edge to the walkway edge and to decelerate the flow as it enters the fan bell mouth.

Figure 5.27 shows that omitting the bell mouth of the edge fan has the same effect as adding a walkway at infinite and $2.5 \times$ fan diameter platform heights. However at $1.0 \times$ fan diameter platform height the pressure losses upstream of the fan are reduced considerably. At this platform height the total pressure upstream of the fan is 25.9 N/m^2 , compared to 53.9 N/m^2 (for an installation with a bell mouth) and 37.3 N/m^2 (for an installation with a walkway). Figure 5.28 shows that the static pressure graphs for the edge fan installation without a bell mouth are similar to the graphs for the installation with the walkway. This indicates that by removing the bell mouth, the total pressure losses upstream of the edge fan moves to the platform edge, similar to the effect of adding a walkway.

5.6 Summary

This section serves as a short summary of the results and discussions contained in Chapter 5. The B_N_N fan configuration was used to investigate the effect of adding a walkway to the side of the fan platform or removing the inlet bell mouth in front of the edge fan. The investigation was performed by means of CFD using the EADM.

The B_N_N configuration, as detailed in Chapter 4, is used to show the increase in distorted edge fan inlet flow with decreasing floor height. It shows that the air entering the edge fan originates from a higher altitude than the fan itself and moves closer to the fan installation as the floor height decreases. The location of two loss mechanisms, namely the platform edge and the inlet bell mouth edge, are also shown. The reduction in flow through the edge fan is due to the existence of distorted inlet flow conditions upstream of the fan which changes the basic functioning of the fan blades, as well as the total pressure loss associated with the platform edge and bell mouth edge that are located upstream of the edge fan.

The addition of a walkway to the side of the existing platform forces the location of the inlet air source to be further from the edge fan. This causes the inlet air to be aligned with the main flow direction through the fan, which improves the operation of the fan, compared to the installation without the walkway. The bell mouth edge at the centre plane sits inside the separation bubble caused by the walkway. Although the addition of a walkway increases the total pressure loss at the new platform edge considerably it reduces the pressure loss experienced at the bell mouth edge. The net effect is an increase in the volumetric effectiveness of the edge fan.

The absence of a bell mouth for the edge fan means that the pressure loss at the edge of the bell mouth is removed completely. This means that there is less distortion of the inlet flow into the edge fan and the volumetric effectiveness of the edge fan is increased. This part of the investigation was performed for one edge fan configuration only and will be expanded to evaluate other configurations as well. The performance of the inner fans should also be investigated. An experimental investigation should also be performed.

6 CONCLUSIONS AND RECOMMENDATIONS

The conclusions mentioned in this chapter are a progression of the summaries and discussions in Chapters 3, 4 and 5. A section containing recommendations for future research is included at the end of this chapter.

6.1 Conclusions

6.1.1 The effect of fan configuration on edge fan performance

The performance of six different 630 mm diameter fan configurations was investigated (see Appendix A for exact details of these fan configurations). The configurations included different blade solidity and hub-to-tip ratios. Blade solidities ranged from 0.33 to 0.85, while hub-to-tip ratios ranged from 0.15 to 0.4.

Each of the fan configurations was tested in a single fan test facility to establish its baseline fan static pressure performance curve. The fan test facility was based on the facility developed by Visser (1990) but included a number of modifications. The most significant modification was removing the “Etoile” flow straightener and replacing it with a plenum chamber and porous mesh sheet. The plenum chamber configuration not only correlated better with actual installations, it also simplified the CFD modelling of the facility considerably. A single reference operating point, based on the design point of Bruneau (1994), was selected and the blade setting angles of all six fan configurations were adjusted so that their performance curves would pass through this reference point.

Operating curves of the different fan configurations were amalgamated into a single operating curve, valid also for very low flow coefficients, by using the curve of the B-fan as a reference and deriving empirical correlations for the effects of blade solidity and hub-to-tip ratio relative to the reference curve. Distorted inlet flow (as experienced by an edge fan) results in a reduced flow rate through the fan. An axial flow fan is designed and tested to operate within its “normal” operating range which is usually limited by a minimum flow rate above which the occurrence of stall over the fan blade is minimal (some fan configurations exhibit stall close to the hub at their design point). Although the average reduction in flow rate through the fan might not necessarily place the fan outside its normal operating range, local reductions in flow rate through the fan might be more severe. Axial flow fan curves that extend outside the normal operating range of a fan are usually not available to the designers of large ACC plants. The advantage of the single operating curve is that, by incorporating the effect of the specific blade solidity and hub-to-tip ratio of a fan, a designer can obtain an indication of fan performance for any fan configuration that falls within the limits of the different fan configurations that were investigated.

The effect of fan configuration on the performance of an edge fan was evaluated by measuring the individual flow rates of the fans in a 3-fan multiple fan test facility. The test facility was configured with the two internal fans being kept the same (representing scaled models of an industrial cooling fan), while different configurations for the edge fan were investigated. Different levels of fan inlet distortion were obtained by varying the platform (floor) height of the test facility. The results showed a decrease in the volumetric effectiveness of the edge fan with decreasing platform height, corresponding to the measurements by Salta and Kröger (1995). Using the single fan performance curve derived previously, another set of empirical correlations were derived that can be used to predict the performance of different fan configurations at different floor heights. This expands the curve published by Salta and Kröger (1995) to include the effect of fan blade solidity and hub-to-tip ratio.

In terms of fan configuration the results showed that the fan with the highest blade solidity and hub-to-tip ratio, namely the H14-fan, had a higher volumetric effectiveness (at all platform heights) than any of the other fans. This correlates with the results of Bredell (2005) and Stinnes and von Backström (2002) who found that a fan with a steep performance curve would be less susceptible to a reduction in volumetric effectiveness when subjected to cross-flow. The N-fan and the H5-fan, with relatively small hub-to-tip ratios and low blade solidities, showed the lowest volumetric effectiveness values. Interestingly, the H10-fan with a solidity twice that of the H5-fan but with the same hub-to-tip ratio, performed the second best of all the configurations (in terms of volumetric effectiveness) slightly outperforming the B-fan which had the same hub-to-tip ratio as the H14-fan. A possible explanation would be that the high blade solidity and small hub size combine to effectively close off the flow area around the hub (forming a pseudo large hub). This is confirmed by the empirical correlation relating blade solidity and hub-to-tip ratio to a reduction in fan performance at different platform heights (see Figures 3.10 and 3.11). While the effect of hub-to-tip ratio seems to be inversely linear (a smaller hub-to-tip ratio has a larger reduction in volumetric effectiveness), the reduction in volumetric effectiveness tapers off as the solidity increases. The practical aspects associated with the use of a large hub (specifically weight and structural integrity) means that the use of a small hub size with high-blade solidity might be preferred by designers of large ACCs. The volumetric effectiveness of an edge fan should however never be viewed in isolation and the efficiency of the individual fan itself should still be considered, as discussed in the next paragraph.

The fan shaft power of the different fan configurations was also measured. The results showed that the B-fan and N-fan had the lowest shaft power consumption (and therefore the highest efficiency), while the H14-fan had the highest shaft power consumption (and therefore the lowest efficiency) at an infinite platform height at the specific operating point. When comparing the heat transfer potential of the edge fan to its shaft power consumption the H5-fan outperforms all the other fan configurations, except at the lowest platform height of $1.0 \times$ fan

diameter. The B-fan shows overall good performance at all platform heights. The H14-fan under performs completely (due to a very high solidity), except at the lowest platform height, where its performance improves but is still lower than that of the B-fan. As mentioned in Section 3.5.2 this indicates the importance of the efficiency of a fan at its specific operating point. It also shows that the efficiency of the fan changes with platform height (and the degree of inlet distortion).

6.1.2 The use of simplified numerical models to simulate edge fan performance

Three fan configurations were investigated, namely the B-, H10- and N-fan. The performance of these configurations were investigated in CFD using three different methods to represent the operation of an axial flow fan, namely the actuator disc method (ADM), pressure jump method (PJM) and extended actuator disc method (EADM).

Each of the three simulation methods were applied to each of the three fan configurations in a single fan test facility format in preparation for use in the multiple fan format. Comparing the simulated fan static pressure curves to their corresponding experimental results the PJM represented single fan operation the best. This can be expected since the PJM is based on a curve fit of the fan static-to-static pressure curve that was originally derived from the fan test results. The ADM assumes that the flow follows the 2-dimensional blade airfoil profiles when passing through the fan rotor. This is the case with limited or no stall occurring over the fan blades and therefore the ADM represents fan operation accurately within the normal operating range of the fan. At low flow rates the ADM under-predicts the fan static pressure rise of an axial flow fan.

The EADM was derived with the purpose of increasing the fan static pressure rise predicted by the ADM at low flow rates. It uses the same equations and calculation methods as the ADM. The EADM differs from the ADM in that it uses an extended 2-dimensional airfoil lift coefficient curve for the blade properties (the drag coefficient is adapted proportionally). The rationale behind the use of the EADM is explained in more detail in Appendix B. Three load mechanisms were identified that exist at low flow rates through an axial flow fan rotor:

1. At low flow rates the early occurrence of stall towards the trailing edge suction side of the blade means that the radial flow of air (caused by centrifugal loads) in the stalled region becomes more prominent. The radial flow sets up a Coriolis force that (if orientated correctly) stabilises the boundary layer at larger radii.
2. As stall at the small hub radii becomes more prominent the flow passes through the rotor while simultaneously moving from a smaller to a larger radius. In the relative rotating coordinate system the radial flow would also be moving in a tangential direction relative to a rotating surface. The pressure side of a rotating fan blade would inhibit this relative tangential

movement and therefore exert a Coriolis force on the flow, which increases the pressure rise through the rotor.

3. The radial flow path followed by the air through the blade passage means that the effective blade chord increases, which also increases the load transferred by the blade to the flow.

Results that were obtained using the EADM show that a higher fan static pressure is predicted compared to using the ADM. The accuracy of the EADM predictions (compared to measured results) varies, which indicates that the method would need further refinement. The fact that the EADM does not take the radial flow through the rotor into account explicitly is one of its major drawbacks.

The results obtained from the single fan simulations provided reference flow rates for use in the simulations of the multiple fan facilities. Each of the three fan configurations, as well as the three simulation methods, was applied to the multiple fan system configuration. The two inner fans, which were N-fans, were simulated using the PJM at all times. The outer fan (or edge fan) was simulated using the three different methods mentioned above, while also investigating the different fan configurations. The results from the simulations were converted to values of volumetric effectiveness using the single fan facility reference values obtained earlier.

The results showed that the values for the 3-fan N_N_N system volumetric effectiveness, for all simulation methods, correlate well with the curve that was derived by Salta and Kröger (1995). The analysis results differ from the experimental results though, specifically at a floor height of 1.5 x fan diameter, with the experimental results being higher than those of the simulation. When comparing the edge fan results only, the simulation results obtained using the EADM correlate well with the experimental results, except a floor height of 1.5 x fan diameter. The results from the ADM and PJM do not correlate well with the experimental results.

The system volumetric effectiveness values for the B_N_N system correlate better with the experimental results, although they fit in-between the experimental results and Salta curve at a floor height of 1.5 x fan diameter. A comparison of the edge fan volumetric effectiveness shows that the results from the EADM and ADM correlate well with the experimental data. The results from the PJM do not correlate well with the experimental results.

The system volumetric effectiveness values for the H10_N_N system correlate well with the experimental results and predict higher volumetric effectiveness values than the Salta curve. A comparison of the edge fan volumetric effectiveness shows that the results from the EADM and ADM correlate well with the experimental data, while the results from the PJM do not correlate well with the experimental results.

Based on the preceding paragraphs it may be concluded that the EADM gives the best estimate of edge fan volumetric effectiveness at all the levels of inlet flow distortion that were investigated. For the fan and system configurations that were investigated the accuracy of the results obtained using the EADM was mostly within 5%, with two of the values within 10%, of the experimental values. The level of correlation achieved between the experimental and numerical results also varied with fan configuration. The worst correlation was obtained for the N-fan (which has the lowest volumetric effectiveness of the three fan configurations), while the best correlation was obtained for the H10-fan (which has the highest volumetric effectiveness of the three fan configurations). Above a floor height of $3.5 \times$ fan diameter, both the EADM and ADM predict the edge fan volumetric effectiveness accurately within 2%, regardless of the fan configuration being simulated.

6.1.3 The format of the inlet flow field of an edge fan

To investigate the inlet flow field for the edge fan installation, particle image velocimetry (PIV) experiments were conducted for the N_N_N, B_N_N and H10_N_N multiple fan configurations at infinite, $2.5 \times$ fan diameter and $1.0 \times$ fan diameter floor heights. The vector field was measured along the centre plane in the vicinity of the edge fan and divided into velocity distributions in the vertical and horizontal directions along lines at specific locations.

The PIV results showed that the velocity distribution upstream of the edge fan, up to a vertical line at the edge of the edge fan bell mouth, can be obtained using any of the three simplified methods for simulating axial flow fans. The different methods also gave acceptable results at these locations for all three floor heights that were investigated regardless of the edge fan configuration that was tested.

A variation in results was however noted when looking at the velocity distributions along a horizontal line drawn in front of the edge fan between the edges of the bell mouth. At an infinite floor height the experimental results showed relatively high velocities in both the horizontal and vertical directions close to the upstream edge of the bell mouth. This was noted for all three fan configurations that were investigated. The EADM and ADM were able to simulate this high velocity region, while the PJM predicted a more even velocity distribution upstream of the fan. At a floor height of $2.5 \times$ fan diameter this high velocity region still existed but the ability of the simplified fan models to simulate the velocity distribution deteriorated, although the EADM and ADM still exhibited the correct tendencies. At a floor height of $1.0 \times$ fan diameter none of the simplified fan models were able to predict the N_N_N or H10_N_N fan configurations correctly. The EADM and ADM (and to a lesser extent the PJM) were, however, able to give a reasonable estimate of the velocity distribution in front of the B_N_N configuration at this floor height.

It can therefore be concluded that the EADM and ADM predict the flow field in front of an edge fan correctly at infinite floor heights, regardless of fan configuration. At a floor height of 2.5 x fan diameter the EADM and ADM still predicts the correct tendencies, although not accurately, while at a floor height of 1.0 x fan diameter the EADM and ADM give reasonable results for one of the configurations only.

6.1.4 A guideline for improved edge fan performance

The fan configuration for which the best numerical results was obtained, namely the B_N_N fan configuration, was used as a reference configuration against which the effect of adding a walkway to the side of the platform or removing the inlet bell mouth in front of the edge fan was investigated using CFD.

Using the B_N_N configuration as a benchmark the increase in distorted edge fan inlet flow was shown with decreasing floor height. It was also shown how the air that enters the edge fan originates from a higher altitude than the fan itself and moves closer to the fan installation as the floor height decreases. The location of two loss mechanisms, namely the platform edge as well as the inlet bell mouth edge, is shown. The reduction in flow through the edge fan is therefore due to:

1. The existence of distorted inlet flow upstream of the fan which changes the basic functioning of the fan blades.
2. The total pressure loss associated with the platform edge and bell mouth edge that are located upstream of the edge fan.

By adding a walkway to the side of the installation the location of the inlet air is forced further away from the fan installation. The result is that the air entering the edge fan has a larger radius of curvature upstream of the fan and is better aligned with the main flow direction through the fan, thereby reducing the level of distorted inlet flow upstream of the fan. The addition of a walkway does however increase the total pressure loss at the platform edge considerably but reduces the pressure loss experienced at the bell mouth edge. The net effect is an increase in the volumetric effectiveness of the edge fan.

Removing the bell mouth of the edge fan reduces the radius of curvature that the flow into the edge fan follows. The pressure loss over the edge of the bell mouth is removed completely. The absence of the bell mouth also leads to less separation and distortion of the inlet flow into the edge fan. Consequently the removal of the inlet bell mouth increases the volumetric effectiveness of the edge fan. It should, however, be noted that this investigation was conducted for one specific installation configuration only.

6.2 Recommendations for future work

Based on the results of this research, a number of recommendations regarding future work can be made. These can be summarised as follows:

1. A single fan test facility specifically suited for the testing of air-cooled heat exchanger fans should be defined. Such a facility should provide for the inclusion of a plenum chamber downstream of the fan as well as the effect of distorted inlet conditions upstream of the fan. The results obtained from experiments on the multiple fan test facility can be used to develop the inlet for such a facility. This may be achieved by partially blocking the single fan inlet to create a disturbance that correlate with the disturbance observed in the multiple fan facility.
2. The possibility of using the multiple fan test facility (and eventually the single fan test facility mentioned in the previous paragraph) to evaluate the effect of the variation in load, experienced by the edge fan, on the structural integrity of the individual fan blades should be investigated. If successful the test facility can be incorporated into a structural development procedure for fan blades.
3. The EADM should be developed further to make specific provision for the effect of radial flow through the fan rotor. For this purpose it is recommended that an attempt be made to measure the vector flow field surrounding the fan blades using PIV.
4. The effect of a bell mouth on the effectiveness of an edge fan should be investigated further. In this regard it is recommended that the effect of different fan configurations as well as the position of the fan rotor be investigated.
5. A detailed CFD analysis of flow through an axial flow fan at low flow rates should be performed. The ability of the analysis to predict the flow field surrounding the individual fan blades should be evaluated.

6.3 Summary

This chapter gave conclusions on the work performed as part of this study. These can be summarised as follows:

- The effect of fan configuration (different hub-to-tip ratios and fan blade solidities) on the performance of fans that are subjected to distorted inlet conditions was investigated. An empirical correlation was derived to show a relationship between edge fan volumetric effectiveness, edge fan hub-to-tip ratio, fan solidity and platform height.
- The use of simplified numerical models when simulating edge fans that experience distorted inlet conditions was investigated. The results show that the level of correlation between the simplified models and the experimental results is influenced by the formulation of the simplified model, the configuration of the edge fan and the level of inlet flow distortion experienced by the edge fan.

- PIV measurements of the flow field upstream of the edge fan were used to visualise the flow field upstream of the edge fan experimentally. These results were also compared to the simulation results and showed that at high levels of inlet flow distortion reasonable correlation could only be obtained when using the EADM to simulate the B- edge fan.
- The EADM was used to investigate the flow field upstream of different edge fan configurations, specifically the use of walkways and inlet bell mouths.

The chapter ended by making recommendations for future work to investigate edge fan performance further.

REFERENCES

Air Moving and Conditioning Association, Laboratory methods of testing axial flow fans for rating purposes, AMCA Standard 210-74, 1974.

Anderson, J.D., Fundamentals of Aerodynamics 2nd Edition, McGraw-Hill, Singapore, 1991.

ANSYS Fluent[®], ANSYS Fluent documentation, ANSYS Inc., 2009.

Balje, O.E., Turbomachines, A Guide to Design, Selection and Theory, John Wiley and Sons, New York, 1981.

Banks, W., Gadd, G., Delaying effect of rotation on laminar separation, AIAA Journal, Vol. 1, no. 4, 1963.

Bredell, J.R., Numerical investigation of fan performance in a forced draft air-cooled steam condenser, M.Sc.Eng. Thesis, Department of Mechanical Engineering, University of Stellenbosch, South Africa, 2005.

Bredell, J.R., Kröger, D.G., Thiart G.D., Numerical Investigation of fan performance in a forced draft air-cooled steam condenser, Applied Thermal Engineering, 26, 2005.

Bredell, J.R., Kröger, D.G., Thiart G.D., Numerical investigation into aerodynamic blade loading in large axial flow fans operating under distorted inflow conditions, R&D Journal, 22 (2), 2006.

British Standards Institution – Part 1: Methods for Testing Performance, Fans for General Purposes, BS 848, 2007.

Bruneau, P.R.P., The Design of a Single Rotor Axial Flow Fan for a Cooling Tower Application, M.Eng. Thesis, Department of Mechanical Engineering, University of Stellenbosch, South Africa, 1994.

Conradie, P.J.F., Edge fan performance in air cooled condensers, M.Sc.Eng. Thesis, Department of Mechanical and Mechatronic Engineering, University of Stellenbosch, South Africa, 2010.

Corrigan, J.J., Schillings, J.J., Empirical model for stall delay due to rotation, American Helicopter Society Aeromechanics Specialists Conference, San Francisco, 1994.

Corten, G.P., Flow Separation on Wind Turbine Blades, Ph.D. Thesis, University of Utrecht, 2001.

- Dantec Dynamics, 2-D PIV Reference manual, Skovlunde, Denmark, 2006.
- Dixon, S.L., Fluid Mechanics, Thermodynamics of Machinery, 3rd Edition, Pergamon Press, Oxford, 1978.
- Drela, M., XFOIL: An Analysis and Design System for Low Reynolds Number Airfoils. Proceedings of the Conference, Notre Dame, Indiana, USA, June 1989.
- Du Toit, C.G., Thiart, G.D., Kröger, D.G., Matimba ACC: Analysis of flow field (phase 3), Report 92/02/3. Department of Mechanical Engineering, University of Stellenbosch, June 1993.
- Duvenhage, K., Vermeulen, J.A., Meyer, C.J., Kröger, D.G., Flow distortions at the fan inlet of forced-draught air-cooled heat exchanger, Applied Thermal Engineering, 16 (8/9), 1995.
- EPRI, Comparison of alternate cooling technologies for U.S. power plants: economic, environmental and other trade-offs, EPRI, Palo Alto, CA: 2004, 1005358.
- Eskom, Progress of construction at Medupi power station, http://www.eskom.co.za/live/content.php?Item_ID=11978, June 2011.
- Gannon, A.J., von Backström, T.W., A comparison of streamline throughflow and streamline curvature methods, International Journal of Turbo and Jet Engines, 17, 2000.
- Gao, X.F., Zhang, C.W., Wei, J.J., Yu, B., Performance prediction of an improved air-cooled steam condenser with deflector under strong wind, Applied Thermal Engineering, 30, 2010.
- Goldschagg, H.B., Vogt, F., du Toit, C.G., Thiart, G.D., Kröger, D.G., Air-cooled steam condenser performance in the presence of crosswinds, Proceedings: Cooling Tower Technology Conference, Electrical Power Research Institute, Palo Alto, California, 1997.
- Gur, O., Rosen, A., Propeller performance at low advance ratio, Journal of Aircraft, 42, no. 2, 2005.
- Hawthorne, W.R., Horlock, C.B.E., Actuator disc theory of the incompressible flow in axial compressors, Proceedings of the Institution of Mechanical Engineers, 176 (30), 1962.
- Himmelskamp, H, Profile investigations on a rotating airscrew, Ph.D. Thesis, Göttingen, 1945 (MAP Volkenrode, Reports and Translations, No. 832, 1947).

Hoerner, S.F., Borst, H.V., Fluid-dynamic lift, Published by L.A. Hoerner, New Jersey, 1975.

Hotchkiss, P.J., Meyer, C.J., von Backström, T.W., Numerical investigation into the effect of cross-flow on the performance of axial flow fans in forced draught air-cooled heat exchangers, Applied Thermal Engineering, 26, 2006.

Houghton, E.L., Carpenter, P.W., Aerodynamics for Engineering Students, 5th Edition, Butterworth-Heinemann, Oxford, 2003.

Hu, D., Hua, O., Du, Z., A study on stall-delay for horizontal axis wind turbine, Renewable Energy, 31, 2006.

Idelchik, I.E., Handbook of Hydraulic Resistance, 3rd Edition, Begell House, 1994.

Jidayi, Y.M., A computational fluid dynamics model of an axial flow fan under cross-flow conditions, M.Eng. Thesis, Department of Mechanical and Mechatronic Engineering, University of Stellenbosch, South Africa, 2008.

Joubert, R., Influence of geometric and environmental parameters on air-cooled steam condenser performance, M.Sc.Eng. Thesis, Department of Mechanical and Mechatronic Engineering, University of Stellenbosch, South Africa, 2010.

Kröger, D.G. Air-cooled Heat Exchangers and Cooling Towers, PennWell Corporation, Tulsa, 2004.

Lauder, B.E., Spalding, D.B., The numerical computation of turbulent flows, Computer Methods in Applied Mechanics and Engineering, 3, 1974.

Le Roux, F.N., The CFD simulation of an axial flow fan, M.Sc.Eng. Thesis, Department of Mechanical and Mechatronic Engineering, University of Stellenbosch, South Africa, 2010.

Leonard, B.P., A stable and accurate convective modelling procedure based on quadratic upstream interpolation, Computer Methods in Applied Mechanics and Engineering, 19, 1978.

Lewis, R.I., Turbomachinery performance analysis, Arnold, London, Great Britain, 1996.

Lindenburg, C., Modelling of rotational augmentation based on engineering considerations and measurements, Proceedings: European Wind Energy Conference, London, 2004.

Louw, F.G., Performance trends of a large air-cooled steam condenser during windy conditions, M.Sc.Eng. Thesis, Department of Mechanical and Mechatronic Engineering, University of Stellenbosch, South Africa, 2011.

McGee, R.J., Beasley, W.D., Low-speed aerodynamic characteristics of a 17-percent-thick airfoil section designed for general aviation applications, NASA Technical Note D-7428, Langley Research Centre, Hampton, Virginia, 1973.

McGee, R.J., Beasley, W.D., Somers, D.M., Low-speed aerodynamic characteristics of a 13-percent-thick airfoil section designed for general aviation applications, NASA Technical Memorandum X-72697, Langley Research Centre, Hampton, Virginia, 1977.

McGee, R.J., Beasley, W.D., Whitcomb, R.T., NASA low and medium-speed airfoil development, NASA Technical Memorandum 78709, Langley Research Centre, Hampton, Virginia, 1979.

McKenzie, A.B., Yu, H., Stall in low hub-tip ratio fans, European conference: Installation effects in fan systems, Proceedings of the Institution of Mechanical Engineers, London, 1990.

McKenzie, A.B., Axial flow fans and compressors: Aerodynamic design and performance, Cranfield series on turbomachinery technology, Hants, England, 1997.

Menter, F.R., Langtry, R.B., Likki, S.R., Suzen, Y.B., Huang, P.G., Völker, S., A Correlation-Based Transition Model Using Local Variables – Part I: Model Formulation, ASME Journal of Turbomachinery, 128, 2006.

Meyer, C.J., Plenum losses in forced draught air-cooled heat exchangers, M.Eng. Thesis, Department of Mechanical Engineering, University of Stellenbosch, South Africa, 1998.

Meyer, C.J., Numerical investigation of the effect of inlet flow distortions on forced draught air-cooled heat exchanger performance, Applied Thermal Engineering, 25, 2005.

Meyer, C.J., Kröger, D.G., Numerical simulation of the flow field in the vicinity of an axial flow fan, International Journal for Numerical Methods in Fluids, 36, 2001.

Meyer, C.J., Kröger, D.G., A numerical investigation of the errors associated with the scaling of axial flow fan performance characteristics, R&D Journal, 20 (2), 2004.

Monroe, R.C., Improving cooling tower fan system efficiencies, *Combustion Magazine*, 50 (11), 1979.

Olivier, K.J., An experimental and numerical investigation of a flat plate blade fan at optimum angles of attack, Final year project, Department of Mechanical and Mechatronic Engineering, University of Stellenbosch, South Africa, 2008.

Pericleous, K.A., Patel, M.K., The modelling of tangential and axial agitators in chemical reactors, *Physico Chemical Hydrodynamics*, 8, 1987.

Rumsey, C.L., Spalart, P.R., Turbulence Behaviour in Low Reynolds Number Regions of Aerodynamic Flowfields, 38th AIAA Fluid Dynamics Conference and Exhibit, June 23-26, Seattle, WA, 2008.

Russel, C.M.B., Peachey, J., Air inflow effect on fan performance in air cooled heat exchangers, International conference on fan design and applications, Guildford, England, 1982.

Salta, C.A., Kröger D.G., Effect of inlet flow distortions on fan performance in forced draft air-cooled heat exchangers, *Heat Recovery Systems and CHP*, 15, 1995.

Schreck, S.J., Sorenson, N.N., Robinson, M.C., Aerodynamic structures and processes in rotationally augmented flow fields, *Wind Energy*, 10, 2007.

Shi, L., Shi, C., Wang, J., Wu, X., Numerical investigation of influence on heat transfer performance of direct air cooled condenser under different wind conditions, International Joint Conference on Computational Sciences and Optimization, 2009.

Shih, T.H., William, W.L., Shabbir, A., Yang, Z., Shu, J., A new K- ϵ eddy viscosity model for high Reynolds number turbulent Flows, *Computers Fluids*, 24 (3), 1995.

Snel, H., Scaling laws for the boundary layer on rotating wind turbine blades, Proceedings of the fourth IEA Symposium on the aerodynamics of wind turbines, ETSU-N-118, Department of Energy, United Kingdom, 1991.

Snel, H., Houwink, R., Bosschers, J., Sectional prediction of lift coefficients on rotating wind turbine blades in stall, ECN-C-93-052, Petten, 1994.

Spalart, P.R., Allmaras, S.R., A one-equation turbulence model for aerodynamic flows, *La Recherche Aérospatiale*, n° 1, 1994.

Stinnes, W.H., The performance of axial fans subjected to forced cross-flow at inlet, M.Eng. Thesis, Department of Mechanical Engineering, University of Stellenbosch, South Africa, 1998.

Stinnes, W.H., von Backström, T.W., Effect of cross-flow on the performance of air-cooled heat exchanger fans, *Applied Thermal Engineering*, 22, 2002.

Tangler, J.L., Insight into wind turbine stall and post-stall aerodynamics, *Wind Energy*, 7, 2004.

Thiart, G.D., A numerical procedure for predicting the effects of distorted inflow conditions on the performance of axial flow fans, Ph.D. Thesis, Department of Mechanical Engineering, University of Stellenbosch, South Africa, 1990.

Thiart, G.D., von Backström, T.W., Numerical simulation of the flow field near an axial fan operating under distorted inflow conditions, *Journal of Wind Engineering and Industrial Aerodynamics*, 45, 1993.

Van der Spuy, S.J., The design of a low-noise rotor-only axial flow fan series, M.Eng. Thesis, Department of Mechanical Engineering, University of Stellenbosch, South Africa, 1997.

Van der Spuy, S.J., von Backström, T.W., Kröger D.G., Performance of low noise fans in power plant air cooled steam condensers, *Noise Control Engineering Journal*, 57 (4), 2009.

Van der Spuy, S.J., von Backström, T.W., Kröger D.G., An evaluation of simplified methods to model the performance of axial flow fan arrays, *R&D Journal*, 26, 2010.

Van Rooyen, J.A., Performance trends of an air-cooled steam condenser under windy conditions, M.Sc.Eng Thesis, Department of Mechanical and Mechatronic Engineering, University of Stellenbosch, 2007.

Van Rooyen, J.A., Kröger, D.G., Performance trends of an air-cooled steam condenser under windy conditions, *Journal of Engineering for Gas Turbines and Power* 130 (2), 0230006-1 to 0230006-7, 2008.

Van Staden, M.P., An integrated approach to transient simulation of large air-cooled condensers using computational fluid dynamics, D.Eng. Thesis, Department of Mechanical Engineering, Rand Afrikaans University, South Africa, 2000.

Van Wylen, G.J., Sonntag, R.E., *Fundamentals of classical thermodynamics*, 3rd Edition, John Wiley and Sons, Singapore, 1985.

Venter, S.J., The Effectiveness of Axial Flow Fans in A-Frame Plenums, Ph.D. Thesis, Department of Mechanical Engineering, University of Stellenbosch, South Africa, 1990.

Venter, S.J., Kröger, D.G., The effect of tip clearance on the performance of an axial flow fan, *Energy Conversion Management*, 33 (2), 1992.

Visser, J.G.J., Die Invloed van Versteurde Inlaatvloeioptrone op Aksiaalwaaiers, M.Eng. Thesis, Department of Mechanical Engineering, University of Stellenbosch, South Africa, 1990.

Von Backström, T.W., Buys, J.D., Stinnes, W.H., Minimisation of the exit losses of a rotor-only axial flow fan, *Engineering Optimisation*, 26, 1996.

Wallis, R.A., *Axial flow fans and ducts*, John Wiley & Sons, New York, 1983.

Wallis, R.A., The F-series airfoils for fan blade sections, *Mechanical Engineering Transactions*, I. E. Aust, ME (2), 1977.

White, F.M., *Fluid Mechanics*, 6th Edition, McGraw-Hill, New York, 2008.

APPENDIX A: AXIAL FLOW FANS

The fans referred to in the main text can be grouped into two different categories according to the role that they played in the investigation. The first group of fans consists of the individual fans that were tested on the large-scale fan test facility (see Appendix B). The second group of fans consists of the 630 mm diameter fans that were used in the multiple fan test facility (see Appendix D).

A.1. Individual fans

A.1.1. B-fan

The B-fan was originally designed for application in ACCs by Bruneau (1994) as the B₂-fan (see Figure A.1). The model B-fan was designed for a volume flow rate of 16 m³/s and fan static pressure rise of 210 N/m² (Bruneau, 1994). The original B₂-fan was irreparably damaged during testing in 2006. A replacement fan was manufactured from the original set of moulds and was extensively tested by le Roux (2010). The overall properties of the B-fan are shown in Table A.1.

Table A.1: B-fan properties.

Fan diameter	1.542 mm
Tip clearance	Variable
Hub-to-tip ratio	0.4
Solidity (at mid-span)	0.4

The B-fan uses the NASA-LS(1) (also referred to as the GAW-2) series profile for its blades (McGee et al., 1977). The blade thickness varies from 13% of the chord length at the hub to 7% of the chord length at the blade tip. The chord length and stagger angle distribution of the B-fan are shown in Figure A.2. The stagger angle of the B-fan is measured at the hub of the blade as the angle between the chord line and the circumferential direction.

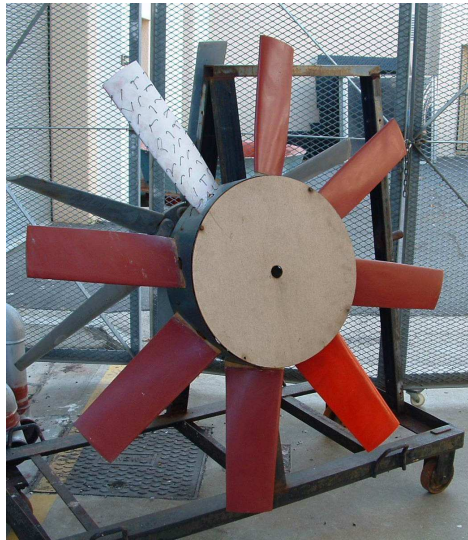


Figure A.1: B-fan, as tested by le Roux (2010).

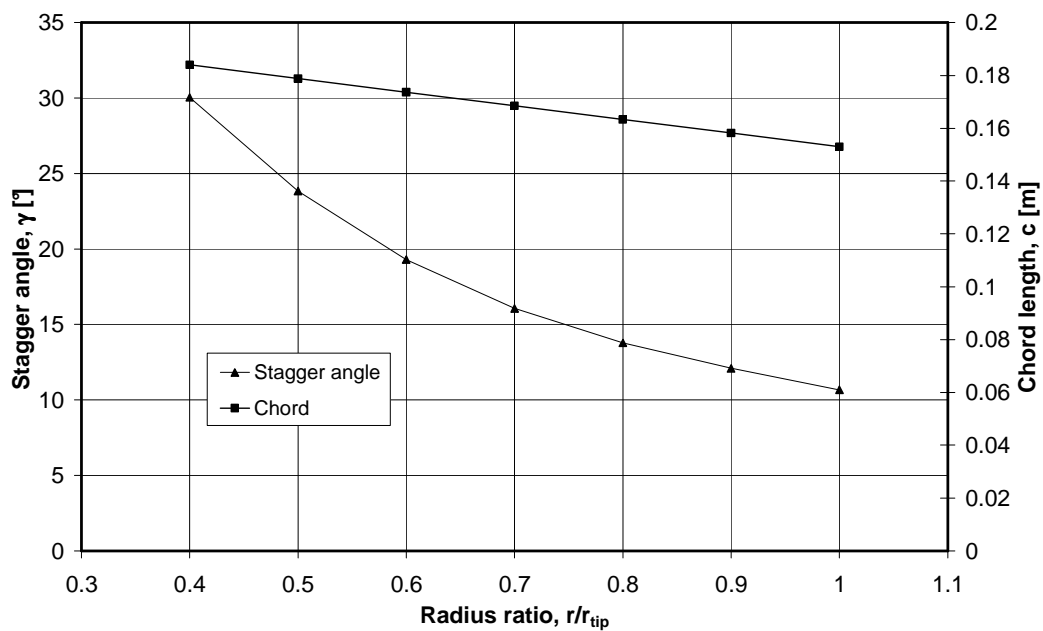


Figure A.2: B-fan blade properties.

A.1.2. V-fan

The V-fan was initially tested by Venter (1990) as a scaled model of an existing industrial cooling fan. The V-fan was re-tested by Stinnes (1998), at which time it was also damaged and replaced by a similar fan, referred to by Stinnes as the S-fan. These two fans had the same diameter, hub-to-tip ratio and blade solidity,

although their blade profiles and stagger distributions were different. A picture of the S-fan is shown in Figure A.3. The overall properties of the V-fan are shown in Table A.2. Since the V-fan was designed and manufactured by an outside company, the designation of the V-fan blade profile is unknown. The information that was required for the modelling of the V-fan was obtained from measurements on a single fan blade, performed using a coordinate measuring machine (Venter, 1990).

Table A.2: V-fan properties.

Fan diameter	1.542 mm
Tip clearance	3 mm
Hub-to-tip ratio	0.15
Solidity (at mid-span)	0.34

The properties of the V-fan blade are shown in Figure A.4. The indicated stagger angle is measured at the tip of the blade, relative to the chord line.



Figure A.3: V-fan replacement fan, referred to as the S-fan.

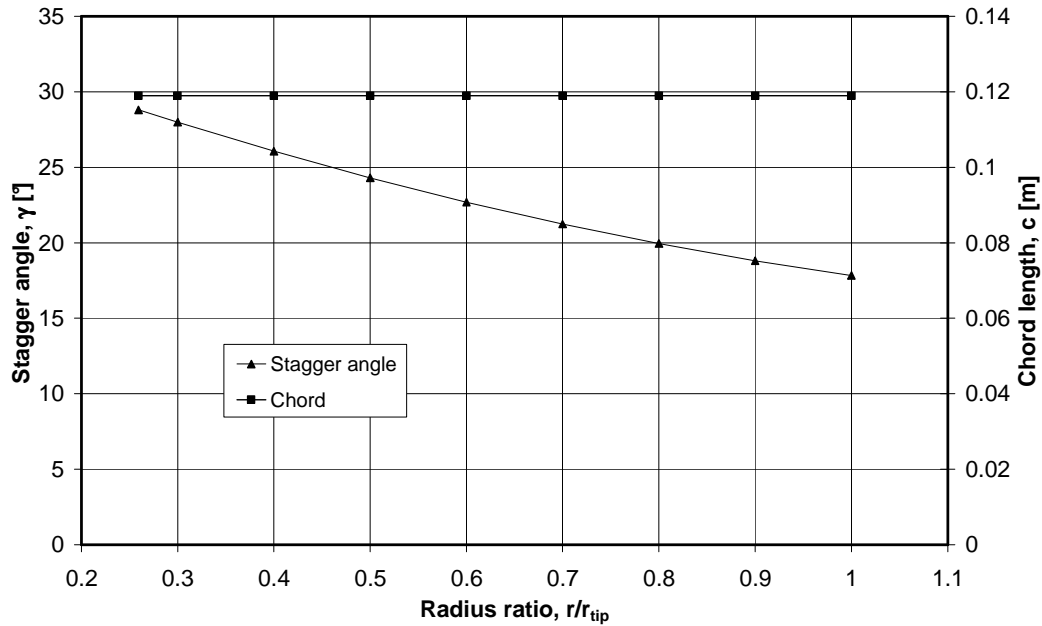


Figure A.4: V-fan blade properties.

A.2. Multiple fans

A.2.1. H-fan

To investigate the effect of fan configuration on edge fan performance a set of variable geometry axial flow fans was purchased. These fans belong to a series of axial flow fans that was developed and tested at Stellenbosch University (van der Spuy, 1997). For the purpose of this project they are referred to as the H-fans. Four different configurations were investigated, namely a 5-bladed fan with a 150 mm diameter hub (H5-fan), a 10-bladed fan with a 150 mm diameter hub (H10-fan), a 7-bladed fan with a 250 mm diameter hub (H7-fan) and a 14-bladed fan with a 250 mm diameter hub (H14-fan). Pictures showing the different H-fan configurations are shown in Figure A.5. The properties of the different configurations are summarised in Table A.3.

Table A.3: H-fan properties.

Fan diameter	630 mm
Tip clearance	1.15 mm
Hub-to-tip ratio: H5- and H10-fan	0.24
Hub-to-tip ratio: H7- and H14-fan	0.39
Solidity: H5-fan (at mid-span)	0.33
Solidity: H10-fan (at mid-span)	0.67
Solidity: H7-fan (at mid-span)	0.42
Solidity: H14-fan (at mid-span)	0.82

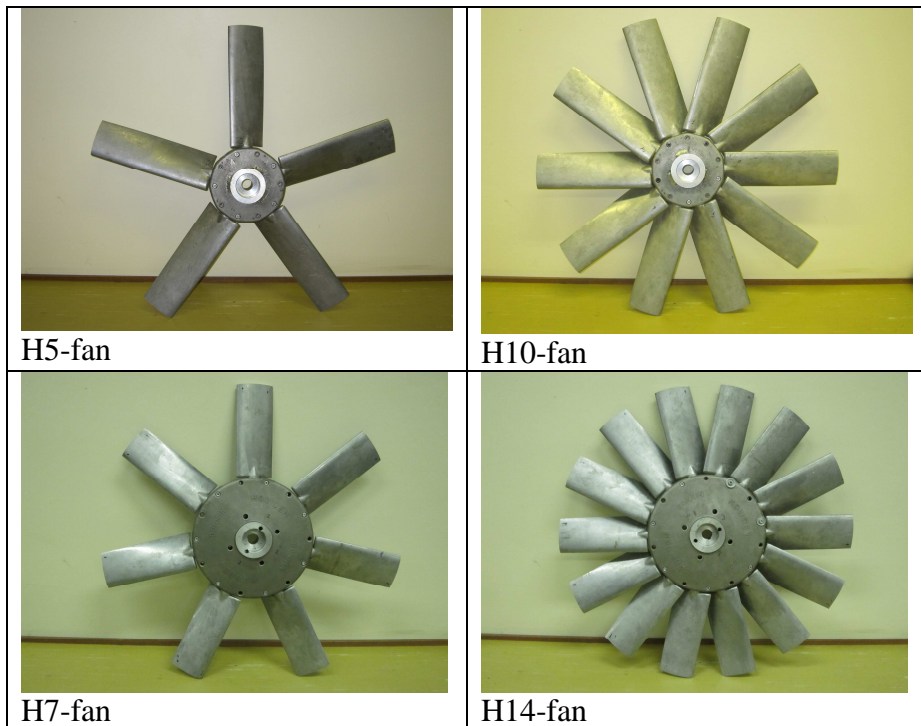


Figure A.5: H-fan configurations.

The H-fan uses the F-series blade profile, described by Wallis (1983). The H-fan was designed to have a fan diameter ranging from 315 mm to 1.2 m with a single blade design. The total length of the blade is 375 mm and the blade is “cropped” to obtain the required fan diameter and hub-to-tip ratio combination. The blade airfoil profile has 3% nose droop, with blade thickness varying from 11% of the chord length at the hub to 7% of the chord length at the blade tip (for the full length blade). The chord length and stagger angle distribution of the H-fan blade is shown in Figure A.6. The stagger angle is measured at the blade hub, relative to the chord line.

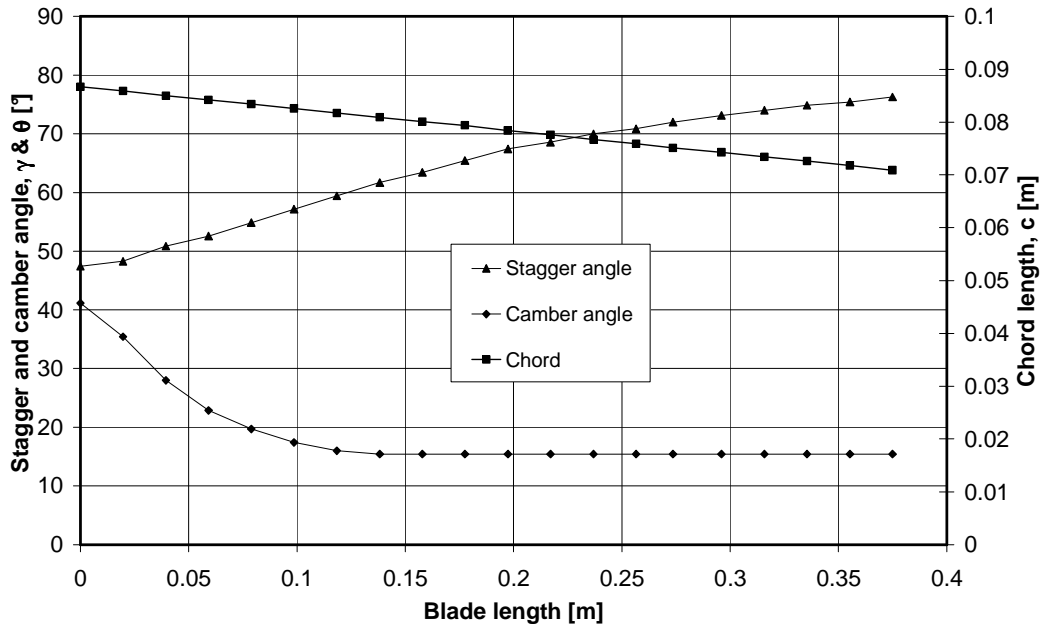


Figure A.6: H-fan blade properties.

A.2.2. N-fan

The N-fan is a 630 mm diameter scaled model of the same 9.216 m diameter general-purpose industrial cooling fan used to model the V-fan. The design and manufacturing of the N-fan is described by Conradie (2010). Since the full-scale version of the N-fan is used in industry it was considered to be the reference fan configuration for the multiple fan tests. A picture of the N-fan is shown in Figure A.7. The overall properties of the N-fan are shown in Table A.4.

Table A.4: N-fan properties.

Nominal diameter	630 mm
Tip clearance	2.45 mm
Hub-to-tip ratio	0.15
Solidity (at mid-span)	0.35

The properties used for the N-fan blade were the same as those of the V-fan and are shown in Figure A.4 with the chord length of the N-fan being scaled by a factor of 0.4086.



Figure A.7: N-fan.

A.2.3. 630 mm diameter B-fan

A 630 mm diameter scaled model of the B-fan was designed and manufactured by Conradie (2010). The fan was manufactured from aluminium and although it was modelled using the design detailed by Bruneau (1994) it incorporated a spherically-shaped hub with the blade profiles correspondingly being projected onto spherically-shaped surfaces. A picture of the B-fan is shown in Figure A.8.



Figure A.8: 630 mm diameter B-fan.

The overall properties of the B-fan are shown in Table A.5. The properties used for the 630 mm diameter B-fan blade were the same as those of the 1.542 m diameter fan and are shown in Figure A.2 with the chord length of the B-fan being scaled by a factor of 0.4086.

Table A.5: 630 mm diameter B-fan properties.

Nominal diameter	630 mm
Tip clearance	0.8 mm
Hub-to-tip ratio	0.4
Solidity	0.4

APPENDIX B: THE ACTUATOR DISC METHOD

B.1. Introduction

Traditionally, “actuator disc analysis” refers to the analysis of a turbomachine using cascade theory (Hawthorne and Horlock, 1962). It represents a step change in the tangential flow through a parallel annulus where the position of the step change coincides with the centre of the plane of rotation of the rotor. Gannon and von Backström (2000) incorporated it into their streamline throughflow method (STFM) code in the form of a prescribed tangential velocity distribution. They were able to model the meridional streamline position to within 0.3% of the analytical solution of Dixon (1978). Thiart and von Backström (1993) defined an actuator disc method that was used to investigate the effect of distorted inlet conditions on the performance of a large-diameter axial flow fan by incorporating it into a computational fluid dynamics (CFD) code. This was based on the work by Pericleous and Patel (1987) who simulated an agitator in a chemical reactor, also using CFD. An axial flow fan actuator disc model has subsequently been used extensively by Meyer and Kröger (2001) and Bredell (2005) to investigate various aspects of the performance of air-cooled heat exchanger systems. The actuator disc method, as applied to axial flow fans, simulates the operation of a fan by calculating the effect of the individual fan blades on the flow through the machine, based on the lift and drag characteristics of the blade elements. Its major perceived advantage lies in the fact that it is able to represent the effect of axial flow fan operation on a system without the need to solve the flow field in the proximity of the fan blade surfaces accurately.

Thiart and von Backström (1993) investigated the effect of inlet flow distortions for a particular “Howden” fan. This fan is generally used for air-cooled heat exchanger installations. They conclude that the actuator disc method is able to predict trends in the operation of a low solidity, low hub-tip ratio fan satisfactorily and mentions accuracy levels in the region of 8% for axisymmetric flow, static pressure comparisons. They further conclude that the performance of the numerical procedure is good but that the computing time required to obtain more accurate results would be excessive.

Meyer and Kröger (2001) provide extensive details of the actuator disc method. Although the exact values are not mentioned the level of correlation achieved between experimental and numerical results is good (see Figure B.1). Thiart and von Backström (1993) made use of empirical correlations to establish the lift and drag characteristics of the blade profiles used in simulations. Meyer and Kröger (2001) on the other hand had extensive development information of a specific fan, referred to as the B-fan (see Appendix A), available. The information included full geometric details of the fan blades, as well as lift - and drag coefficient curves of the blade profiles, as used during the design process. The authors also had access to complete test results for the B-fan that were measured on a BS 848 (2007) part 1, type A fan test facility. The B-fan can be referred to as a medium

hub-to-tip ratio fan and as such the air passing through the fan experiences less radial movement as compared to a fan with a smaller hub-to-tip ratio. Meyer and Kröger (2001) identify the actuator disc method's inability to model radial loads exerted by the fan blades as one of its shortcomings. Looking at Figure B.1, it is apparent that their simulations only considered fan operation within the normal operating range of the specific fan (above $10 \text{ m}^3/\text{s}$ and below $20 \text{ m}^3/\text{s}$).

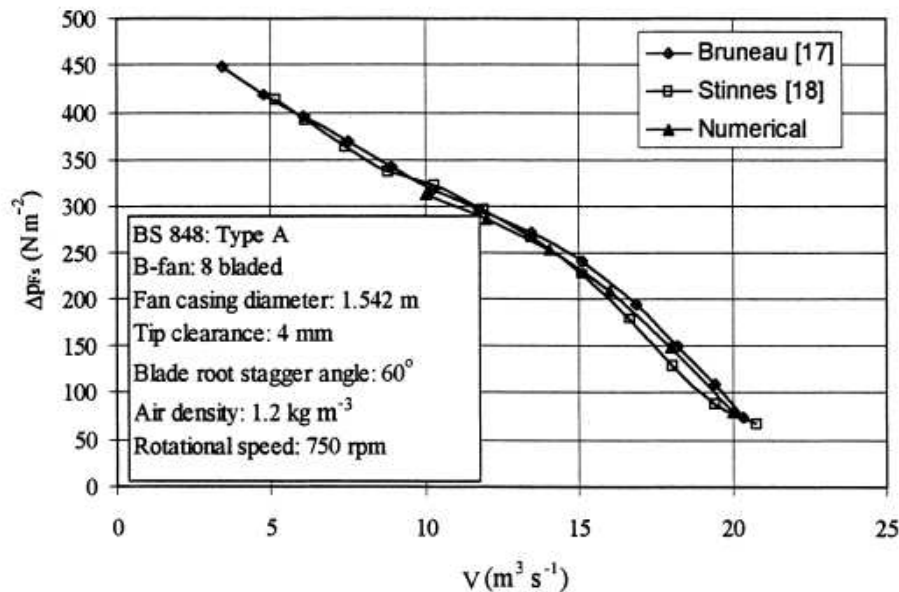


Figure B.1: Fan static pressure vs. volume flow curve, (copied directly from Meyer and Kröger, 2001).

Bredell (2005) continued the work of Thiart and von Backström (1993). Thiart and von Backström investigated the effect of inlet flow distortions on axial fan performance in general, while Bredell focussed on air-cooled heat exchanger installations and considered wind loads, structures and neighbouring fans in his CFD analyses. He compared the full scale performance of a low (0.153) and medium (0.4) hub-to-tip ratio fan installed at the perimeter of an array of cooling fans and found the performance of the medium hub-to-tip ratio fan to be markedly better. Bredell (2005) established a method where he initially “calibrates” the actuator disc model by modelling a typical BS 848 test facility in CFD and compares the results with that of a fan curve for the specific fan being simulated. He found good correlation with the 1.542 m diameter B-fan (see Appendix A) and the 9.145 m diameter A-fan curves (the A-fan is a popular large-diameter cooling fan from industry). He subsequently calculated the normal operating point flow rate for an air-cooled condenser installation by modelling a geometrically scaled B-fan (from 1.542 m to 9.145 m) and A-fan coupled to a generic heat exchanger. Once the normal operating flow rate is known the fan is modelled in its installed condition. By comparing the flow rate of a fan in its installed condition to its normal value an estimate of its installed performance can be made.

A paper published by Hotchkiss et. al (2006) compares the experimental results measured for the B-fan subjected to set angular off-axis inflow values to the numerical results simulated for this fan. He found that agreement between the various data sets was “good”. Of significant importance is his ability to extract data from the simulations that enabled him to quantify the azimuthal variation in thrust and torque loading on the fan rotor due to the effect of the off-axis inflow. Bredell et. al (2006) reported on a similar investigation where they calculated the variation in peripheral fan rotor load in its “installed” position and found that the blade flapping moment can vary by as much as 70% above its average steady state load condition. These calculations highlighted the ability of the actuator disc method to quantify and compare possible improvements in air-cooled heat exchanger system operation by lowering the variation in axial fan rotor load.

B.2. Application of the actuator disc method to calculate fan performance curves

B.2.1. Basic method

Considering the curved flow element shown in Figure B.2, Lewis (1996) lists the three per-unit-mass momentum equations for flow through such an element in cylindrical coordinates as follows (assuming axisymmetric inviscid flow as a simplification):

$$F_z - \frac{1}{\rho} \frac{\partial p}{\partial z} = C_z \frac{\partial C_z}{\partial z} + C_r \frac{\partial C_z}{\partial r} \quad (\text{B.1})$$

$$F_r - \frac{1}{\rho} \frac{\partial p}{\partial r} = C_r \frac{\partial C_r}{\partial z} + C_r \frac{\partial C_r}{\partial r} - \frac{C_\theta^2}{r} \quad (\text{B.2})$$

$$F_\theta = C_z \frac{\partial C_\theta}{\partial z} + C_r \frac{\partial C_\theta}{\partial r} + \frac{C_\theta C_r}{r} \quad (\text{B.3})$$

These three equations can be written relative to a rotating blade as follows:

$$F_z - \frac{1}{\rho} \frac{\partial p}{\partial z} = W_z \frac{\partial W_z}{\partial z} + W_r \frac{\partial W_z}{\partial r} \quad (\text{B.4})$$

$$F_r - \frac{1}{\rho} \frac{\partial p}{\partial r} = W_r \frac{\partial W_r}{\partial z} + W_r \frac{\partial W_r}{\partial r} - \frac{W_\theta^2}{r} - 2W_\theta \Omega - r\Omega^2 \quad (\text{B.5})$$

$$F_\theta = W_z \frac{\partial W_\theta}{\partial z} + W_r \frac{\partial W_\theta}{\partial r} + \frac{W_\theta W_r}{r} + 2W_r \Omega \quad (\text{B.6})$$

where

$$W_r = C_r ; W_\theta = C_\theta - r\Omega ; W_z = C_z$$

The right-hand side of these equations represents the momentum change experienced by the fluid in the curved control volume (see Figure B.2). It is interesting to note that the last two terms of equation B.5 and the last term of equation B.6 represent the centrifugal and Coriolis terms introduced into the flow by virtue of the use of a relative rotating coordinate scheme. If the momentum equations were applied in a relative rotating coordinate system, provision would have to be made for the inclusion of these terms into the momentum equations (Corten, 2001). However, if these equations are solved in an absolute stationary coordinate system (as is the case for the actuator disc method) these terms are inherently part of the momentum equations.

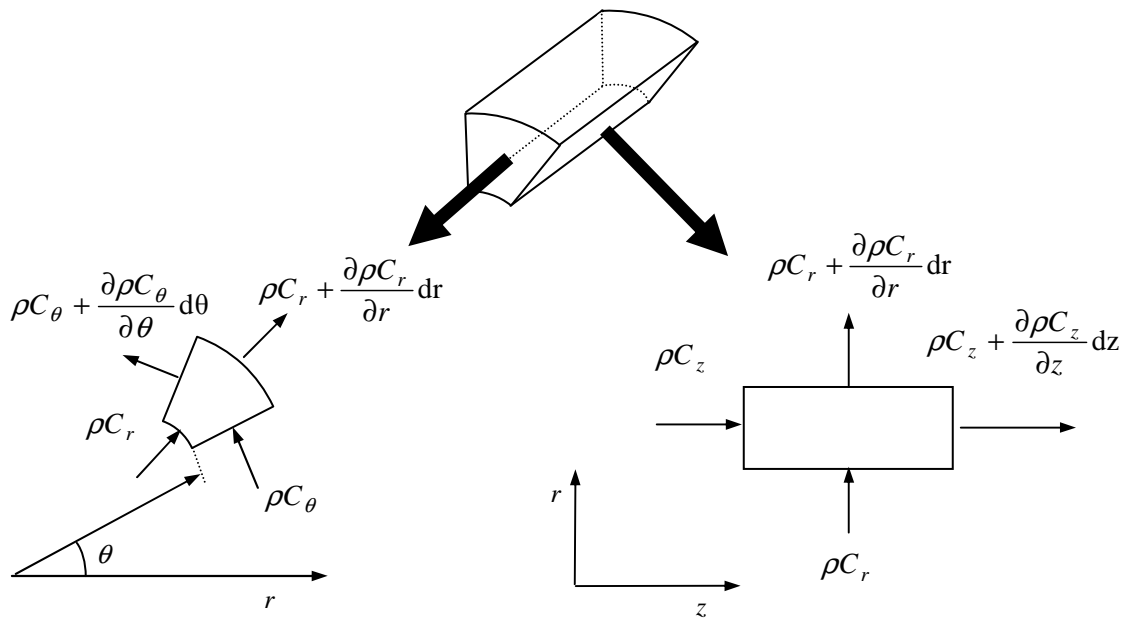


Figure B.2: Curved control volume.

The calculations used to determine the effect of the axial flow fan rotor on the flow field rely on the assumption that the blades of a low solidity fan can be considered as individual airfoils acting on the air stream. This isolated airfoil approach is considered valid for solidity values less than 0.7 (Bruneau, 1994). Figure B.3 shows the lay-out and definitions of flow angles and forces related to a blade segment.

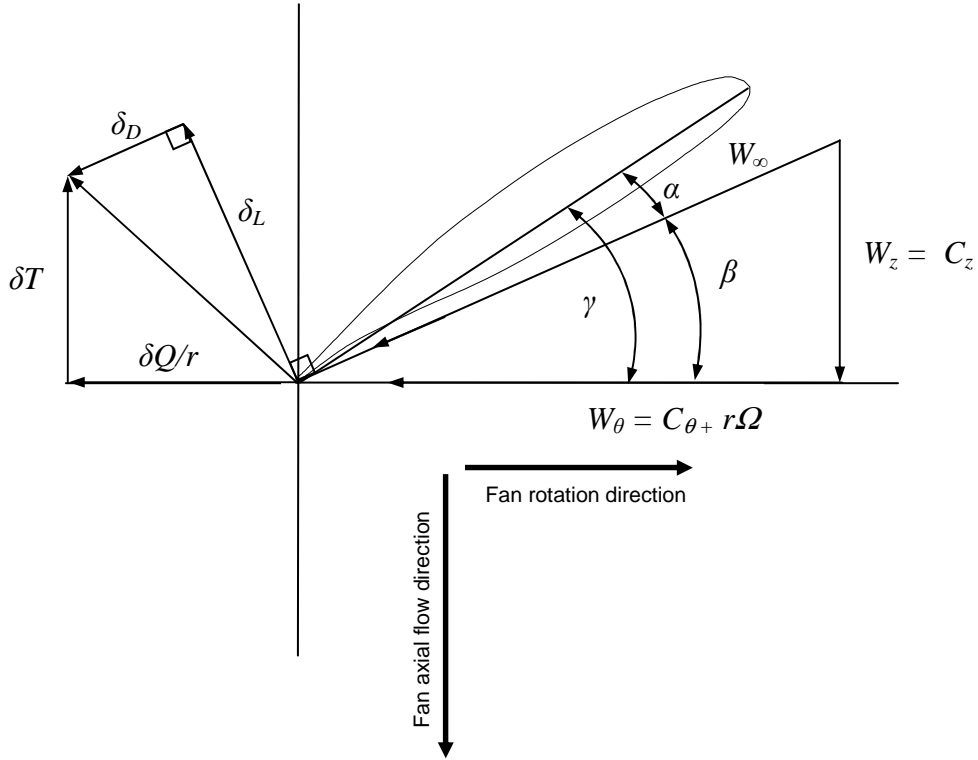


Figure B.3: Lay-out of blade element.

Each fan blade is represented by discrete radial elements corresponding to the computational mesh seeding specified for the annular space of the fan in the radial direction. The lift and drag forces for the blade elements are incorporated into the Navier-Stokes equations of the CFD model as momentum sources. For a typical blade element, the values for the lift and drag forces are calculated as follows:

$$\delta_L = \frac{1}{2} \rho W_\infty^2 C_L c \delta r \quad (\text{B.7})$$

$$\delta_D = \frac{1}{2} \rho W_\infty^2 C_D c \delta r \quad (\text{B.8})$$

It should be noted that for the actuator disc used in this study, W_∞ is the average relative velocity vector, consisting of components in the axial and circumferential directions over the blade element. The values for the lift and drag coefficients, C_L and C_D , are obtained from 2-dimensional airfoil data, based on the angle of attack, α . Airfoil data is based on flow in a plane perpendicular to the span-wise direction of the airfoil. Since the blade element is assumed to represent an airfoil flow in a radial direction is not considered in the actuator disc calculations.

Once the forces acting on the air stream are calculated they are transformed into per unit-mass source terms. The effect of a discrete radial blade element is

multiplied by the number of individual blades and then distributed equally along the circumference at a specific radius, once again according to the mesh seeding in the circumferential direction:

$$F_z = -\frac{1}{2}W_\infty^2\sigma(C_L \cos \beta - C_D \sin \beta) / \Delta z \quad (\text{B.9})$$

$$F_\theta = \frac{1}{2}W_\infty^2\sigma(C_L \sin \beta + C_D \cos \beta) / \Delta z \quad (\text{B.10})$$

The source terms (equations B.9 and B.10) are then inserted into the linear momentum equations B.1 to B.3 (or B.4 to B.6 if working in a relative coordinate system) for a specific control volume.

The actuator disc model is incorporated into CFD by means of a user subroutine (Bredell, 2005). The user subroutine calculates the source terms to be added to the momentum equation of the elements that coincide with the centre of the fan rotation plane. The subroutine enables the user to set the blade number, fan rotational speed, reference fan blade setting angle, fan shroud radius and fan hub radius. The user is however required to ensure that the shroud and hub radii of the fan being simulated (and set in the user subroutine) correspond to the actual values used in the fan geometry.

B.2.2. Geometry

All simulations were performed on the ANSYS Fluent[®], versions 6.3.26 and 12.1, finite volume CFD code. The geometry that was modelled represented a standard BS 848 part 1 (2007), type A (free inlet and outlet) test facility (see Figure B.4) in the laboratories of the Department of Mechanical and Mechatronic Engineering at Stellenbosch University. The facility has a fan shroud (bell mouth) diameter of 1.542 m.

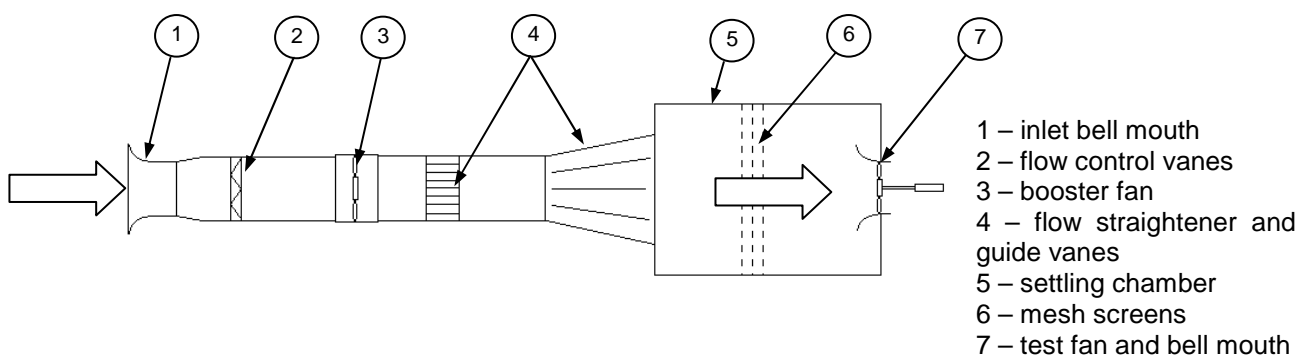


Figure B.4: Schematic representation of BS 848 (2007) fan test facility.

The test facility was represented in the CFD simulation by modelling the settling chamber, the bell mouth (with an actuator disc representation of the test fan) and a

free atmospheric volume at the outlet-side of the fan. The model corresponded to the “fan test models” of Bredell (2005) and Meyer and Kröger (2001) (see Figure B.5). For these models the fan test facility geometry was represented in cylindrical format. The bell mouth was modelled as an attachment onto the settling chamber and the free atmosphere excluded any provision for solid wall surfaces. Although a number of CFD simulations were completed where the actual test facility (rectangular settling chamber and solid structures in the outlet volume) were modelled, only results obtained for the generic format of the CFD model will be discussed in this document.

Bredell (2005) showed that this generic format model gave accurate results for the B-fan. The cross-sectional dimension of the modelled settling chamber corresponded to $2\frac{1}{2}$ fan diameters. The axial length of the modelled settling chamber was selected to correspond to the actual distance from the fan inlet to the settling chamber pressure tap points (2.0 m). A comparative analysis where the axial length of the modelled settling chamber was the same as the length of the actual settling chamber (7.0 m) showed minimal differences in fan static pressure values (less than 4%), compared to the shorter settling chamber length. The axial length of the outlet-side free atmosphere was selected as 8 fan diameters. A comparative analysis evaluated the length of the free atmosphere behind the fan, where it was varied between 12 m, 24 m and 36 m. It was found that the fan static pressure results between the longest and shortest domain varied by less than 2%. The cross-sectional dimension of the modelled free atmospheric volume was 6 fan diameters. A graphic representation of the modelled geometry is shown in Figure B.5.

The actuator disc method is implemented by using three pre-defined annular disc fluid zones. These three zones are arranged sequentially in an axial direction and are modelled to have exactly the same radial and circumferential mesh distribution as well as only one cell thickness in the axial direction. The first and third zones are used to calculate the direction and size of the average velocity vector over the fan blade. As such, they are modelled to be located approximately at the leading and trailing edges of the fan blades (in this instance a value of 60 mm was used). The central (second) zone is located at the centre of the fan rotation plane and is the zone where the source terms, mentioned in the previous section, are added. The axial thickness of the three zones was modelled to be 10 mm. The hub geometry of the fan was modelled as wall boundaries with an axial length that corresponds to the actual hub length of the fan being simulated. The discs were connected to the rest of the model using unmatched boundaries.

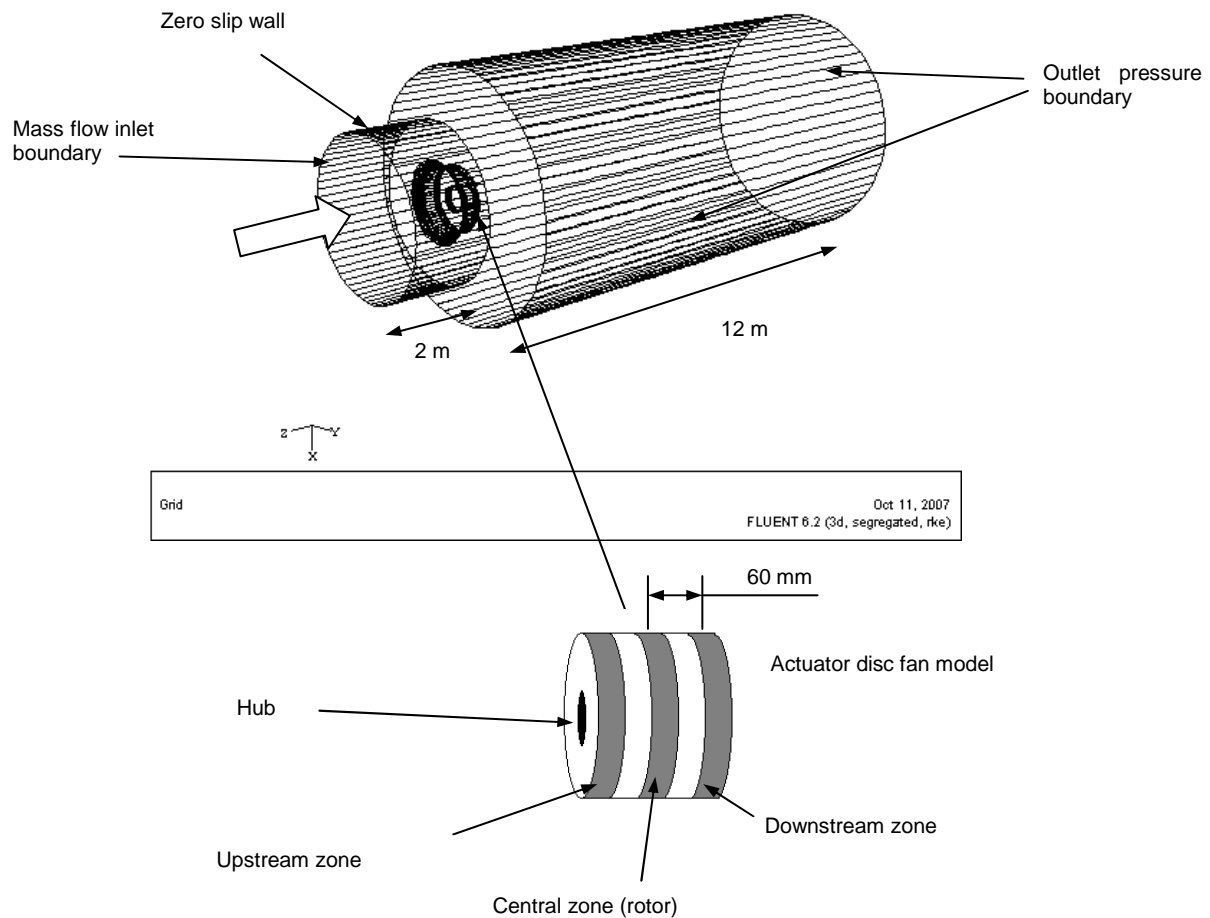


Figure B.5: Lay-out of CFD geometry.

The fan performance curve of the B-fan was modelled. The B-fan was designed by Bruneau (1994) and was previously modelled successfully by Meyer and Kröger (2001). The B-fan is discussed in more detail in Appendix A.

B.2.3. Mesh

To facilitate the structured requirements of the actuator disc (shown in Figure B.5), the mesh containing the discs was constructed using hexahedral elements. The annulus of the B-fan was meshed with a hexahedral mesh of 200 circumferential elements. The annulus of the B-fan model had 50 radial elements.

A mesh investigation was conducted on the B-fan model. Figure B.6 shows the fan static pressure vs. volume flow rate curve for an actuator disc simulation of the B-fan using hexahedral elements. The first model has 3.5 million mesh elements, while the second model has 5.5 million mesh elements. The mesh refinement was applied to the outlet section of the model by decreasing the

minimum cell side length downstream of the fan from 30 mm to 10 mm. The results show that the two performance curves are almost identical. A relatively coarse mesh size (in the order of 700 000 mesh elements) was investigated initially and gave good results within the normal operating range of the fan (specifically the B-fan). It was however found that the mesh density directly up- and downstream of the fan becomes important when simulating the fan at low flow rates where reverse flow starts to occur through the fan. At these low flow rates, the format of the outlet volume (which represents an open atmosphere in the case of a Type A test facility) also plays a role. The outlet volume was therefore modelled much larger than would have been required to model the fan accurately when only considering the normal operating range of the fan (see Meyer and Kröger, 2000). The consequence of these factors was that the number of mesh elements in the entire model increased significantly.

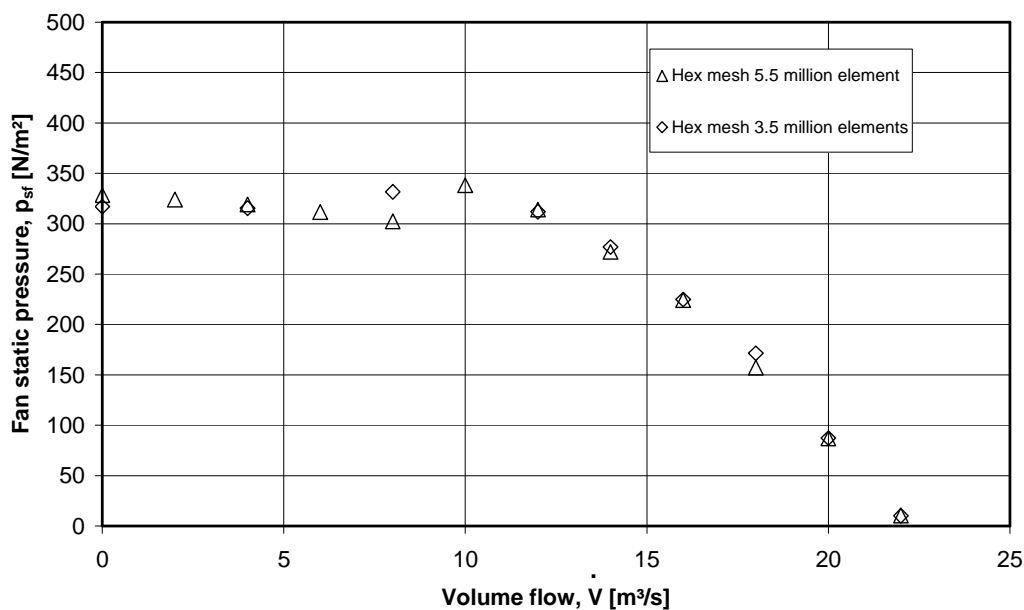


Figure B.6: Mesh size investigation for B-fan.

The use of a simplified fan model means that the effect of boundary layer modelling on the results becomes much less than would be the case when modelling all the fan blades in detail. For the above simulation, a boundary layer existed on the fan bell mouth and the fan hub. As before, the use of a single model to simulate a fan's performance over its entire operating range meant that obtaining a suitable mesh for all flow conditions becomes a challenge. The y^+ -values on the bell mouth inside surface was however checked and verified to be within the acceptable range of the realizable k - ϵ model (between 20 and 100) at a flow rate of 16 m³/s. To verify the influence of the boundary layers on the results, the bell mouth surface was modelled with and without boundary mesh elements and the maximum difference between the two sets of results over the entire flow range of the fan was less than 1%.

Figure B.7 shows the fan static pressure vs. volume flow rate curve for an actuator disc simulation of the B-fan containing 5.5 million structured hexahedral mesh elements, compared to the same type of curve obtained from a simulation containing 5 million unstructured tetrahedral mesh elements. The results show that the two performance curves are very similar with the biggest differences occurring at flow rates between 0 and 10 m³/s. At these flow rates the exhaust jet coming from the axial flow fan expands from a predominantly axial direction (at higher flow rates) towards the radial direction (at lower flow rates). Since simultaneous expansion of an unstructured tetrahedral mesh in two directions can be controlled more accurately than with a structured hexahedral mesh, it was decided to preferably use a tetrahedral mesh when simulating a complete fan performance curve over a range of flow rates.

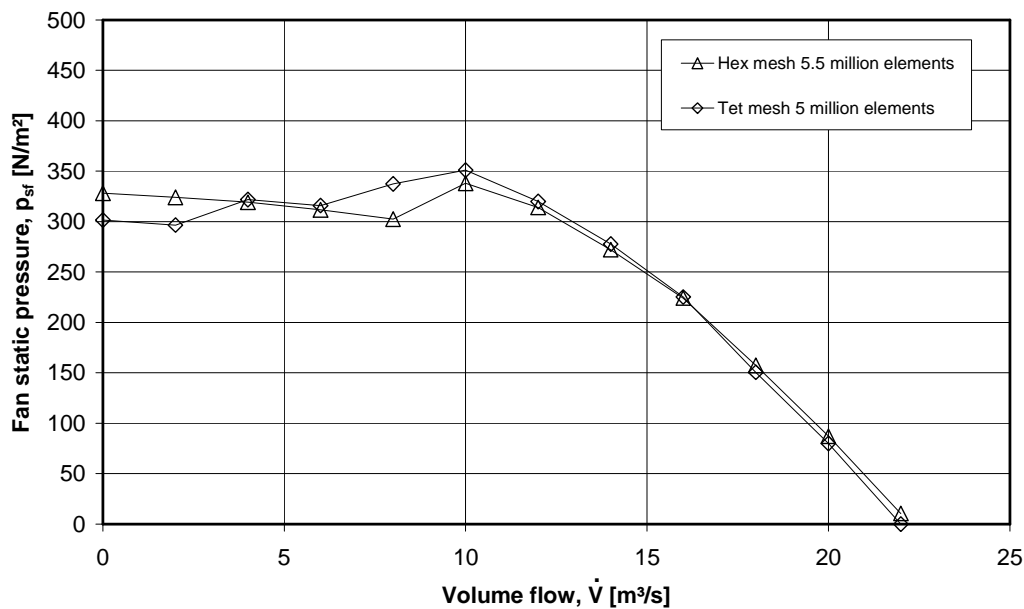


Figure B.7: Mesh type investigation for B-fan.

B.2.4. Boundary conditions

To calculate a fan static pressure performance curve the relevant output data would be the total-to-static pressure rise and volume flow characteristics of the fan. To simulate this, the mass flow inlet boundary condition should consist of a uniformly distributed axial velocity (derived from the specified mass flow, inlet area and inlet density), along with values of turbulent kinetic energy, k , and dissipation rate, ε . Normally the jet exit condition specifies that the static pressure at a jet outlet would be atmospheric. Strictly speaking, this is not the case where rotation exists in the flow. The outlet boundary was initially modelled as a static pressure boundary with provision for the rotation of the flow by incorporating

radial equilibrium into calculating the pressure distribution at the exit boundary. The radial equilibrium equation is given in cylindrical coordinates by Lewis (1996) as:

$$\frac{1}{\rho} \frac{\partial p}{\partial r} = \frac{C_{\theta}^2}{r} \quad (\text{B.11})$$

The radial equilibrium equation assumes the reference pressure (in this case atmospheric pressure) to exist at the zero radius. It was, however, found that the radial equilibrium equation at the outlet boundary caused fluctuation of the continuity residuals at operating conditions where stable flow conditions were known to exist. It was therefore decided to waive the radial equilibrium condition in favour of more stable solutions and to apply only a fixed static outlet pressure condition. This was considered valid based on the fact that the outlet pressure boundary was far enough from the fan to ensure very small circumferential velocities (in the order of 0.1 m/s to 0.5 m/s).

The static pressure boundary value automatically becomes a total pressure value when back flow into the domain occurs as would typically be the case when flow entrainment by the exhaust jet takes place. A reference static pressure value of “0” (corresponding to atmospheric pressure) was used. Instead of defining a static pressure boundary, modelling the outlet boundary as a total pressure boundary was considered, but it was found that the results differed by less than 1% for fan static pressure calculated using the static pressure boundary with radial equilibrium. The use of zero shear walls at the sides of the outlet boundary was also investigated but it was shown to hold very little advantage in terms of stability of the simulations and accuracy of the results.

The containing walls of the settling chamber, as well as the walls of the bell mouth, were all modelled as standard zero slip walls. Due to the dominating large scale of the effect generated by the source terms representing the rotating fan blades no provision was made for the modelling of blade tip leakage. The mesh height perpendicular to the inside surface of the bell mouth was modelled as such that the y^+ -values in this region were below 100 at the design flow rate of the fan.

B.2.5. Turbulence modelling

Meyer and Kröger (2001) used the standard k - ε turbulence model for their actuator disc simulations. It was found that this turbulence model works well when simulating the B-fan where little to no back flow through the fan occurs. The Fluent software manual (ANSYS Fluent[®], 2009), however, proposes the use of the realizable k - ε model for rotating flows.

The nature of turbulent flow is such that the flow field exhibits rapid, small, time-dependant fluctuations. The fluctuating component of the velocity vector results in the addition of a second order tensor to the momentum equation as follows:

$$\rho F_i - \frac{\partial \bar{p}}{\partial x_i} + \frac{\partial}{\partial x_j} (\bar{\tau}_{ij} - \rho \overline{u_i u_j}) = \frac{\partial}{\partial t} (\rho \overline{U_i}) + \frac{\partial}{\partial x_j} (\rho \overline{U_i U_j}) \quad (\text{B.12})$$

where the actual velocity consists of an average value, plus a fluctuating value:

$$U = \bar{U} + u \quad (\text{B.13})$$

The second order tensor is referred to as the Reynolds or turbulent stresses. Launder and Spalding (1974) defined the “standard” k - ε model for turbulent flow to model the effect that turbulence has on the flow. For the standard k - ε model, the Reynolds stresses for incompressible flow are expressed as:

$$-\rho \overline{u_i u_j} = \mu_t \left[\frac{\partial U_i}{\partial x_j} + \frac{\partial U_j}{\partial x_i} \right] - \frac{2}{3} \rho \delta_{ij} k \quad (\text{B.14})$$

where k is the turbulent energy:

$$k = \frac{1}{2} \overline{u_i u_i} \quad (\text{B.15})$$

and μ_t is the turbulent viscosity:

$$\mu_t = C_\mu \frac{\rho k^2}{\varepsilon} \quad (\text{B.16})$$

where C_μ is a model constant (equal to 0.9) and ε represents the dissipation rate of turbulent energy. The conservation equations for turbulent kinetic energy and dissipation rate are given by Launder and Spalding (1974) as:

$$\rho \frac{\partial k}{\partial t} + \rho \frac{\partial (U_i k)}{\partial x_i} = \frac{\partial}{\partial x_i} \left[\left(\mu + \frac{\mu_t}{\sigma_k} \right) \frac{\partial k}{\partial x_i} \right] - \rho \overline{u_i u_j} \frac{\partial U_i}{\partial x_j} - \rho \varepsilon \quad (\text{B.17})$$

$$\rho \frac{\partial \varepsilon}{\partial t} + \rho \frac{\partial (U_i \varepsilon)}{\partial x_i} = \frac{\partial}{\partial x_i} \left[\left(\mu + \frac{\mu_t}{\sigma_\varepsilon} \right) \frac{\partial \varepsilon}{\partial x_i} \right] - C_{\varepsilon 1} \overline{\rho u_i u_j} \frac{\partial U_i}{\partial x_j} \frac{\varepsilon}{k} - \rho C_{\varepsilon 2} \frac{\varepsilon^2}{k} \quad (\text{B.18})$$

where σ_k , σ_ε , $C_{\varepsilon 1}$ and $C_{\varepsilon 2}$ are model constants (equal to 1.0, 1.3, 1.44 and 1.92 respectively). Considering equation (B.14), it would be possible to have a result

where the normal stress becomes negative, or “non-realizable”. From equation (B.14), consider the following term (Shih et al., 1995):

$$\overline{u_i u_i} = -2 \frac{\mu_t}{\rho} \left[\frac{\partial U_i}{\partial x_i} \right] + \frac{2}{3} k \quad (\text{B.19})$$

The term on the left-hand side of equation (B.19) is, by mathematical definition, always positive. However, if the flow-field strain is large, the situation may occur where:

$$\frac{k}{\varepsilon} \frac{\partial U_i}{\partial x_i} > \frac{1}{3C_\mu} \approx 3.7 \quad (\text{B.20})$$

and the term on the left-hand side of equation (B.19) would become negative. It can be similarly shown that for large strain rates, the Schwarz inequality (Shih et al., 1995):

$$\overline{u_i u_j}^2 \leq \overline{u_i^2 u_j^2} \quad (\text{B.21})$$

can be violated. Shih et al. (1995) proposes the use of a realisable k - ε turbulence model where the C_μ variable in equation (B.16) depends on the mean flow and turbulent field as follows:

$$C_\mu = \frac{1}{A_0 + A_S U^{(*)} (k/\varepsilon)} \quad (\text{B.22})$$

where A_0 and A_S are constants and

$$U^{(*)} = \sqrt{S_{ij} S_{ij} + \tilde{Q}_{ij} \tilde{Q}_{ij}} \quad (\text{B.23})$$

These relations enable the realizable model to simulate rotating homogeneous shear flows. The realizable k - ε model also overcomes the “round-jet anomaly” of the standard k - ε model (the spreading rate of plane jets is predicted very well, while the prediction for an axisymmetric jet is poor) by using a different conservation equation for dissipation rate (Shih et al., 1995):

$$\rho \frac{\partial \varepsilon}{\partial t} + \rho \frac{\partial (U_i \varepsilon)}{\partial x_i} = \frac{\partial}{\partial x_i} \left[\left(\mu + \frac{\mu_t}{\sigma_\varepsilon} \right) \frac{\partial \varepsilon}{\partial x_i} \right] - \rho C_1 S \varepsilon - \rho C_2 \frac{\varepsilon^2}{k + \sqrt{\frac{\mu \varepsilon}{\rho}}} \quad (\text{B.24})$$

where C_1 and S are determined using the equations shown in Shih et al. (1995). Model constants also include σ_k , σ_ϵ , C_2 and A_0 (equal to 1.0, 1.2, 1.9 and 4.0 respectively). Shih et. al (1995) concludes that the realizable $k-\epsilon$ model outperforms the standard $k-\epsilon$ model in all test cases (including rotating homogeneous shear flows) and enhances numerical stability. Based on these observations it was decided to use the realizable $k-\epsilon$ model when applying the actuator disc method.

B.2.6. Discretization model

To apply the partial differential conservation equations over a finite region these equations are transformed (discretized) into algebraic equations which approximate the conservation equations as close as possible. The finite volume nature of the CFD code requires the flux terms of the conservation equations to be integrated over the faces of individual cells in order to calculate the values of the different variables at the cell centres. These face values have to be interpolated from known cell centre values (see Figure B.8).

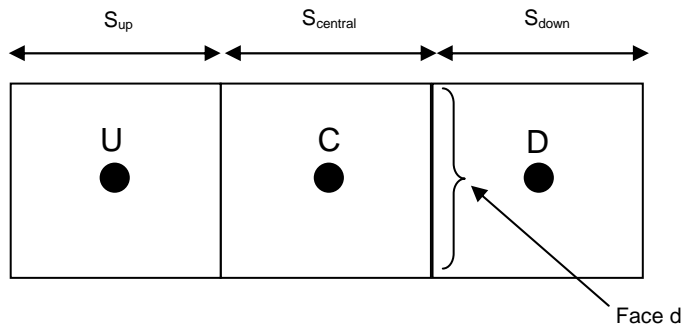


Figure B.8: One-dimensional control volume (redrawn from ANSYS Fluent[®], 2009).

Different interpolation schemes exist, with the most prominent distinction being between first order and second order schemes. A first order scheme bases the inter-cell face value on the single cell centre value upstream of the specific face (first order upwind or central differencing). A second order scheme bases the inter-cell face value on a weighted average of, for instance the two cell centre values upstream of the face (second order upwind differencing), or the two cell centre values on either side of the face (second order central differencing). Leonard (1978) proposes the use of the QUICK interpolation scheme, which is based on a combination of the second order upwind and the second order central differencing schemes as follows (for a variable ϕ at a face d):

$$\phi_d = \theta \left[\frac{S_{down}}{S_{central} + S_{down}} \phi_C + \frac{S_{central}}{S_{central} + S_{down}} \phi_D \right] + (1 - \theta) \left[\frac{S_{up} + 2S_{central}}{S_{up} + S_{central}} \phi_C - \frac{S_{central}}{S_{up} + S_{central}} \phi_U \right] \quad (B.25)$$

ANSYS Fluent[®] implements the QUICK-type scheme, where the combination of the upwind and central schemes is controlled by a weighting factor, θ (as shown in equation (B.27)) that is adjusted along with the solution to ensure stability. The QUICK scheme avoids the stability problems associated with central differencing and the inaccuracies of an upwind differencing scheme. The traditional QUICK scheme has a θ value of 1/8. However, on faces of non-hexahedral cells, θ is set to 0 to allow the use of a second order upwind scheme.

Meyer and Kröger (2001) mention the use of the QUICK scheme for the discretization of the momentum and turbulence transport equations. Although Bredell (2005) acknowledges the advantages associated with the use of a second order differencing scheme he resorts to using a first order upwind differencing scheme in order to maintain stability. The simulations referred to in this document made use of the QUICK differencing scheme for the momentum and turbulence transport equations.

The pressure gradient term that forms part of the momentum equation requires special treatment. Although the pressure value is stored at cell centres its influence on the momentum equation is accounted for at the cell faces and therefore the pressure values at the cell faces also need to be interpolated. ANSYS Fluent[®] recommends the use of the PRESTO! interpolation scheme for rotating flow simulations (2009). After numerous simulations it was concluded that the PRESTO! interpolation scheme inhibits the convergence of the simulations and it was decided to rather use a more simple linear interpolation scheme. Although this improved the stability of the simulation the convergence was still not satisfactory and it was only after the radial equilibrium requirement for the outlet boundary was removed that the convergence improved.

The convergence of the simulations was judged according to a number of criteria:

1. The normalised residual values from the major governing equations were expected to be less than 10^{-4} (in other words four orders of magnitude smaller than the initial values). The residual value represents the sum over all the cells of the difference between the current cell centre value and the “new” value calculated using the discretized conservation equation (which is based on the cell face values and source terms). This value is normalised with respect to the current cell centre value.
2. The conservation of mass (calculated as the difference between the mass flux specified at the inlet boundary, minus the mass flux calculated at the outlet boundary) had to be maintained. Experience has shown that for

simulations where good correlation with experimental results was obtained this difference was less than 0.5% of the specified inlet flux.

3. The graph plot of the normalised residual values had to show a steady trend, free of erratic behaviour (regularly repeating fluctuations of residual values were considered to represent a “steady” flow condition).

All simulations were set to run a maximum of 2000 iterations or to a residual value of 10^{-4} on all governing equations. The following relaxation factors were used:

Table B.1: Relaxation factors

Pressure	0.3
Momentum	0.7
Turbulence kinetic energy	0.8
Turbulent dissipation rate	0.8

Since the modelling of a fan curve consists of a number of different simulations at different flow rates, it should be expected that the level of convergence, as defined above, varied.

B.2.7. Results

A comparison of the actuator disc simulation and test results for the B-fan is shown in Figures B.9, B.10 and B.11. Two sets of simulation results (fan static pressure) are shown for the B-fan. The first simulation was modelled using the realizable $k-\varepsilon$ turbulence model, while the second used the standard $k-\varepsilon$ model. Both simulation models consisted of 5.5 million hexahedral elements. The simulation results are compared to B-fan test results from both Stinnes (1998) and le Roux (2010). Figure B.9 shows very good correlation between the measured values of le Roux and the simulated values within the normal operating range of the fan. There is however a distinct offset between the values of le Roux and Stinnes (presumably both measured at the same angle). Figure B.9 also shows the small difference in results given by the standard and realizable $k-\varepsilon$ turbulence models.

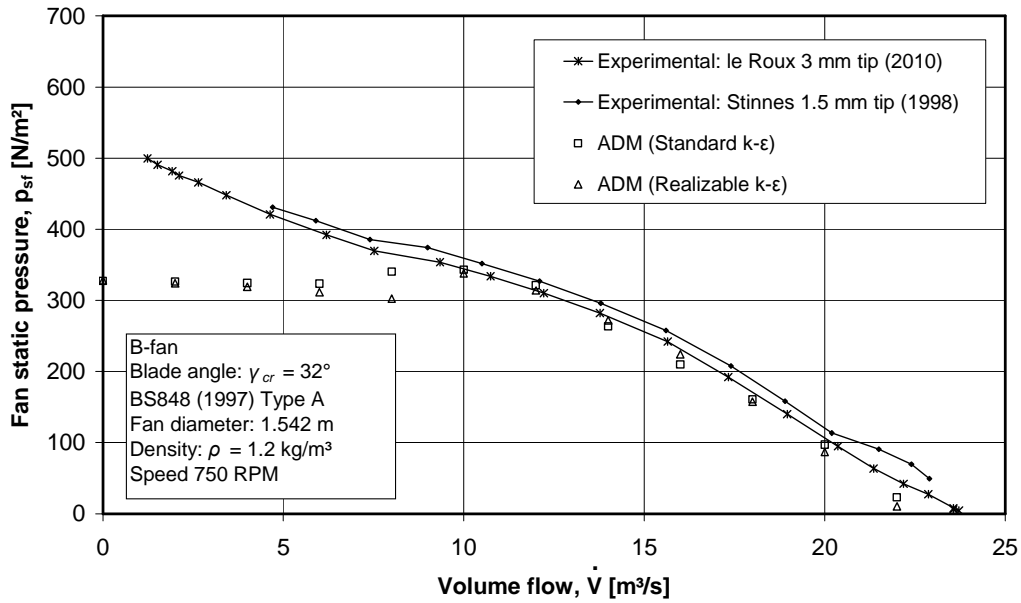


Figure B.9: Fan static pressure, B-fan.

Figure B.10 shows a large difference in results between the experimental and simulated values for fan shaft power vs. volume flow rate. Although it is expected that the predicted shaft power consumption would be lower than the experimental values, primarily due to the exclusion of tip leakage flow losses from the CFD model and possible discrepancies in the prediction of flow turbulence levels, the difference in results seems excessive. The good correlation between the experimental fan static efficiency of Stinnes (1998) and the simulated fan static efficiency (see Figure B.11) however, indicates that a possible cause of the difference in results might be an offset in the blade setting angle, as applied by le Roux (2010).

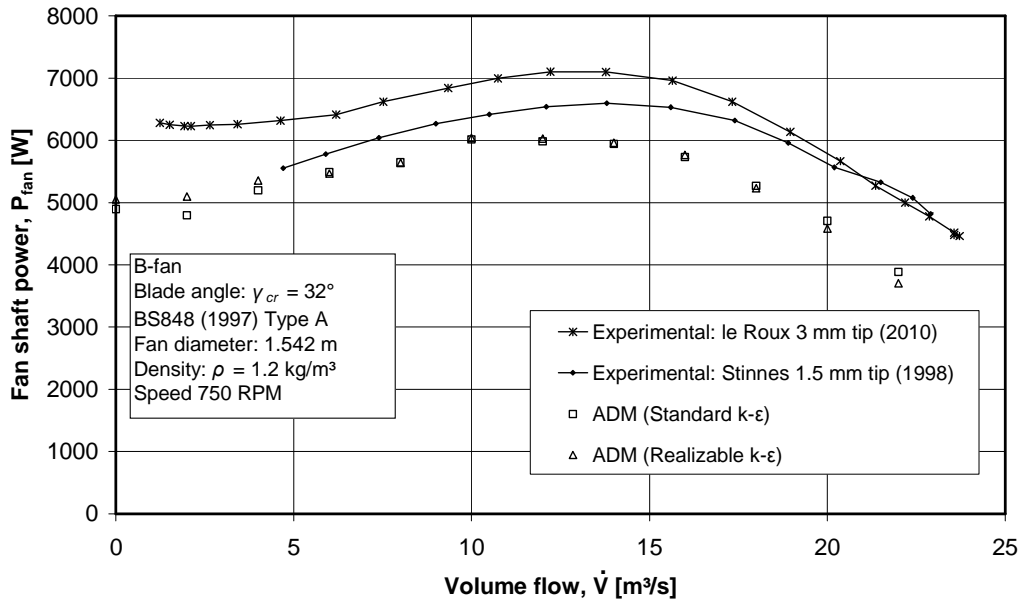


Figure B.10: Fan shaft power, B-fan.

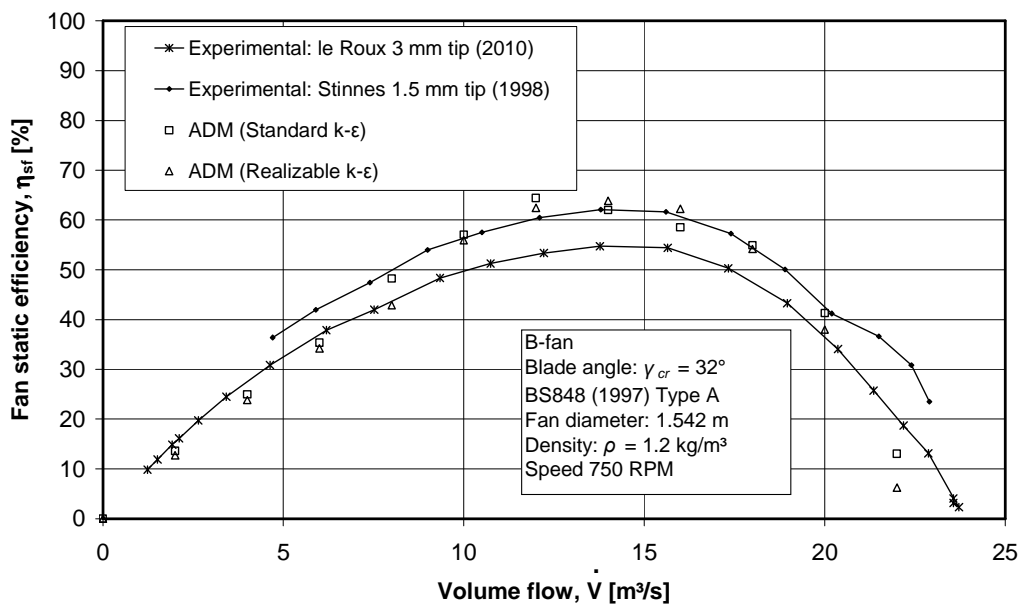


Figure B.11: Fan static efficiency, B-fan.

Figures B.12 and B.13 show the fan static pressure and fan shaft power simulated using the ADM for a blade setting angle of 33° . The correlation between the numerical results and the results of Stinnes (1998) is excellent. This seems to indicate a problem with the setting of the blade angle. Since the equipment used by Stinnes to set the blade angles is no longer available this problem could not be resolved by le Roux.

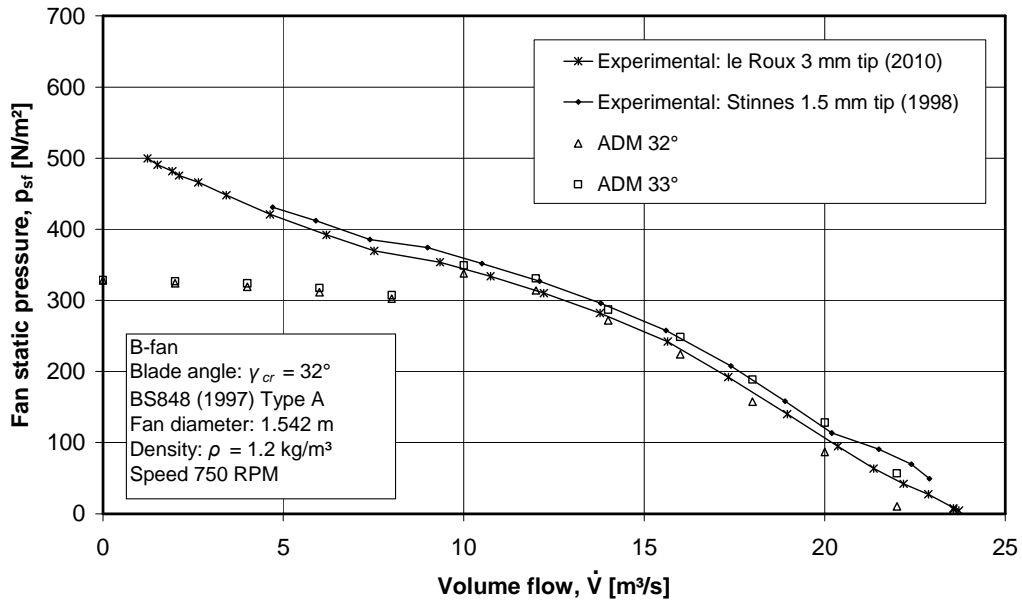


Figure B.12: Fan static pressure at different blade angles, B-fan.

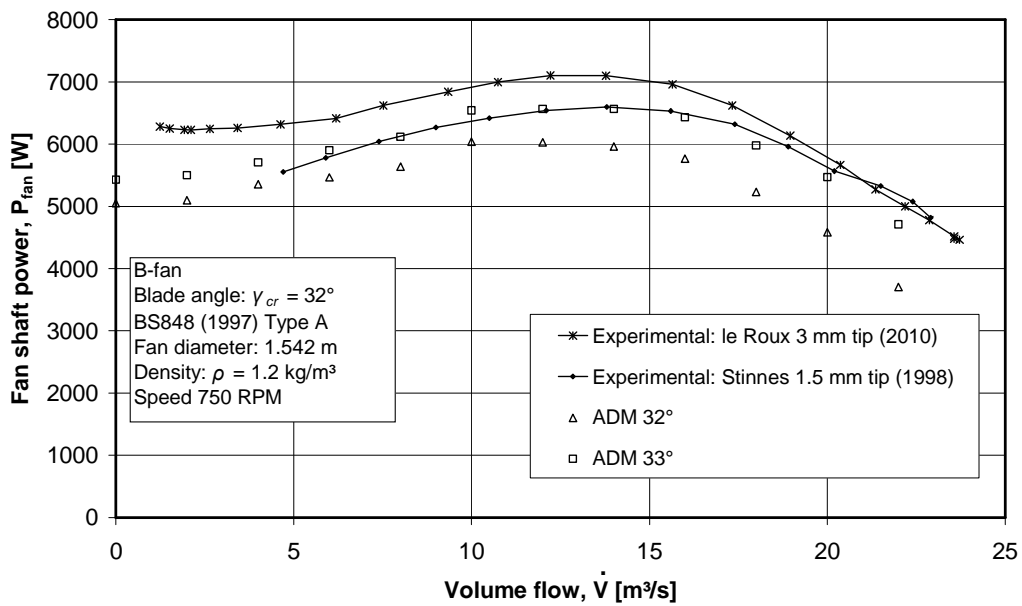


Figure B.13: Fan shaft power at different blade angles, B-fan.

B.3. Modelling 3-dimensional effects in actuator discs

The actuator disc method, as detailed and used by Thiart (1990), Meyer and Kröger (2001) and Bredell (2005) assumes that the flow enters and exits the fan blade rotation plane in “separate” annular rings and that there is no radial flow between the annular rings. It has, however, been noted (in particular by Meyer and Kröger (2001)) that this assumption is not always valid. The circumferential velocity of an axial flow fan blade rotating around a central axis is a linear function of radius:

$$U = r\Omega \quad (\text{B.26})$$

If an absolute velocity field with velocity components on an annular surface plane only is superimposed on the circumferential velocity of the blade, the velocity vector relative to the blade would be as follows (see Figure B.3):

$$W_\infty = \sqrt{C_z^2 + (C_\theta + r\Omega)^2} \quad (\text{B.27})$$

The angle of attack between the direction of the relative velocity vector and the direction of the blade chord is given by:

$$\alpha = \gamma - \arctan\left(\frac{C_z}{C_\theta + r\Omega}\right) \quad (\text{B.28})$$

From the above equations it can be concluded that, for a general axial flow fan inlet condition with zero swirl ($C_\theta = 0$) and a uniform axial velocity distribution ($C_z = \text{constant}$), the inner section (close to the hub) of the blade would be more sensitive to a change in the value of axial velocity than the outer section of the blade where the circumferential velocity of the blade is higher. At low flow rates an axial flow fan would typically see a sharp decrease in relative velocity and an increase in angle of attack. The actuator disc method shows the inner section of the blade to experience stall and, in severe cases, reverse flow at low flow rates. This forces the incoming flow to deflect outwards toward the outer radius of the fan (see Figure B.14).

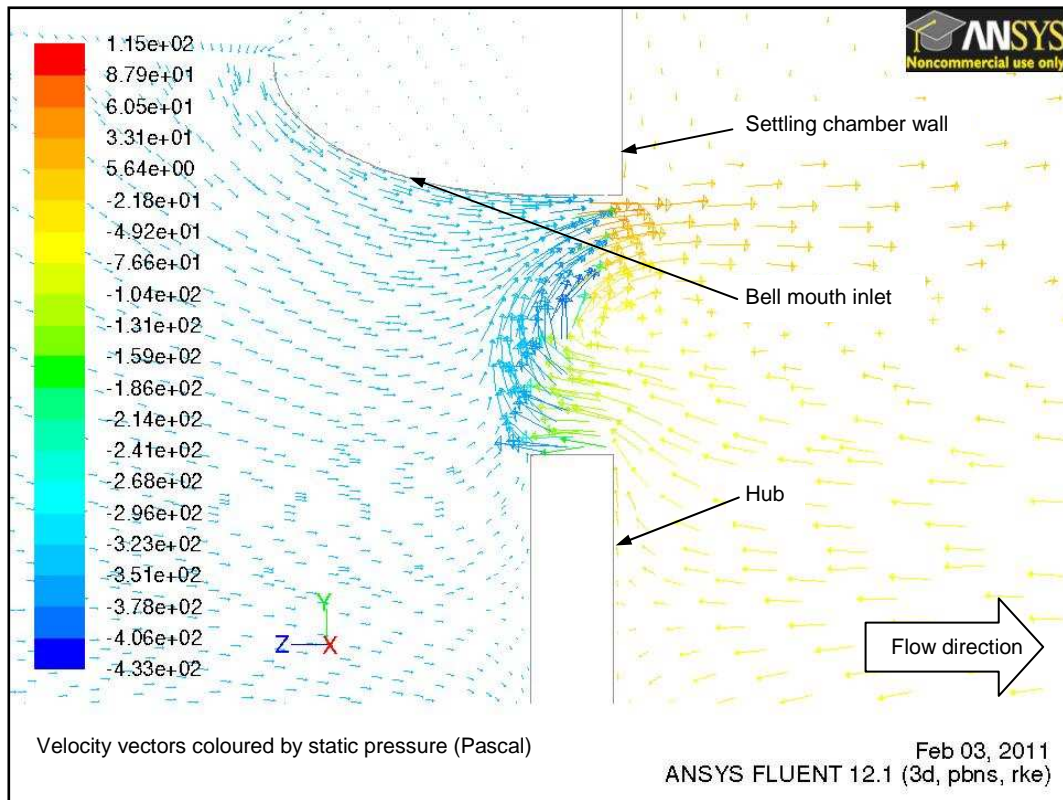


Figure B.14: Vector plot for B-fan in wind tunnel test facility at 6 m³/s, simulated using the actuator disc method.

Although the actuator disc method ignores the existence of any radial velocity components its basic formulation causes flow to occur in all three main directions (r , θ , z) at low flow rates. Radial flow also occurs in a fan rotor due to the existence of obstructions in the vicinity of the rotor (for instance a flat hub nose plate), the radial variation of rotor blade properties and centrifugal loads due to the helical flow path of the air through the fan rotor.

In the traditional actuator disc model the forces that are applied to the flow originate from 2-dimensional airfoil profile tests performed in a wind tunnel. These are a force in the axial direction of the flow, F_z , and a force in the circumferential direction of fan rotation, F_θ , both which are derived from the airfoil drag and lift characteristics. No radial force is exerted on the flow.

An axial flow fan that experiences radial flow can be regarded as a mixed flow fan. Lewis (1996) identifies two types of forces that are transferred onto the flow in a mixed flow fan, namely aerodynamic forces and Coriolis forces. He concludes that the aerodynamic forces can be defined as the forces that result in a change of angular momentum of the flow, while the Coriolis force is exerted on the flow based on its radial velocity component. It should be noted that, in the

case of a mixed flow fan, the aerodynamic force exists along a flow path that runs diagonally across the blade.

Besides the abovementioned two mixed flow fan effects, Himmelskamp (1945) describes the augmentation of the 2-dimensional blade profile lift coefficients due to the effect of rotation on the boundary layer that exists over the fan blade suction surface. In the following paragraphs the different 3-dimensional flow effects are discussed in greater detail.

B.3.1. Coriolis force

If one were to consider an absolute radial flow path to exist in the rotating blade row of a fan, it would mean that an observer locked to the suction side of one of the rotating blades would witness the Coriolis effect of the flow curving away in a tangential direction relative to the observer while moving radially outwards in absolute terms. On the pressure side of the blade, the presence of the blade would inhibit the relative tangential movement of the radial flow and the blade would exert a circumferential force, equal but opposite in direction to the circumferential Coriolis term of equation B.6. This circumferential force is therefore termed the Coriolis force exerted by the blade on the flow field. The Coriolis force, expressed as a force per unit-mass, is written as follows (note that $W_r = C_r$):

$$F_{\theta c} = \frac{2W_r \Omega \times c}{\Delta z \sin \gamma} \quad (\text{B.29})$$

The fact that the blade chord direction is not perpendicular to the tangential direction means that the Coriolis force also has a force in the axial direction, given by:

$$F_{zc} = F_{\theta c} / \tan \gamma \quad (\text{B.30})$$

B.3.2. Blade cross-flow

In the event of radial flow occurring through a blade row, the effective blade section over which the aerodynamic loading occurs does not lie perpendicular to the fan blade axis (as assumed for the actuator disc method (see Figure B.15)).

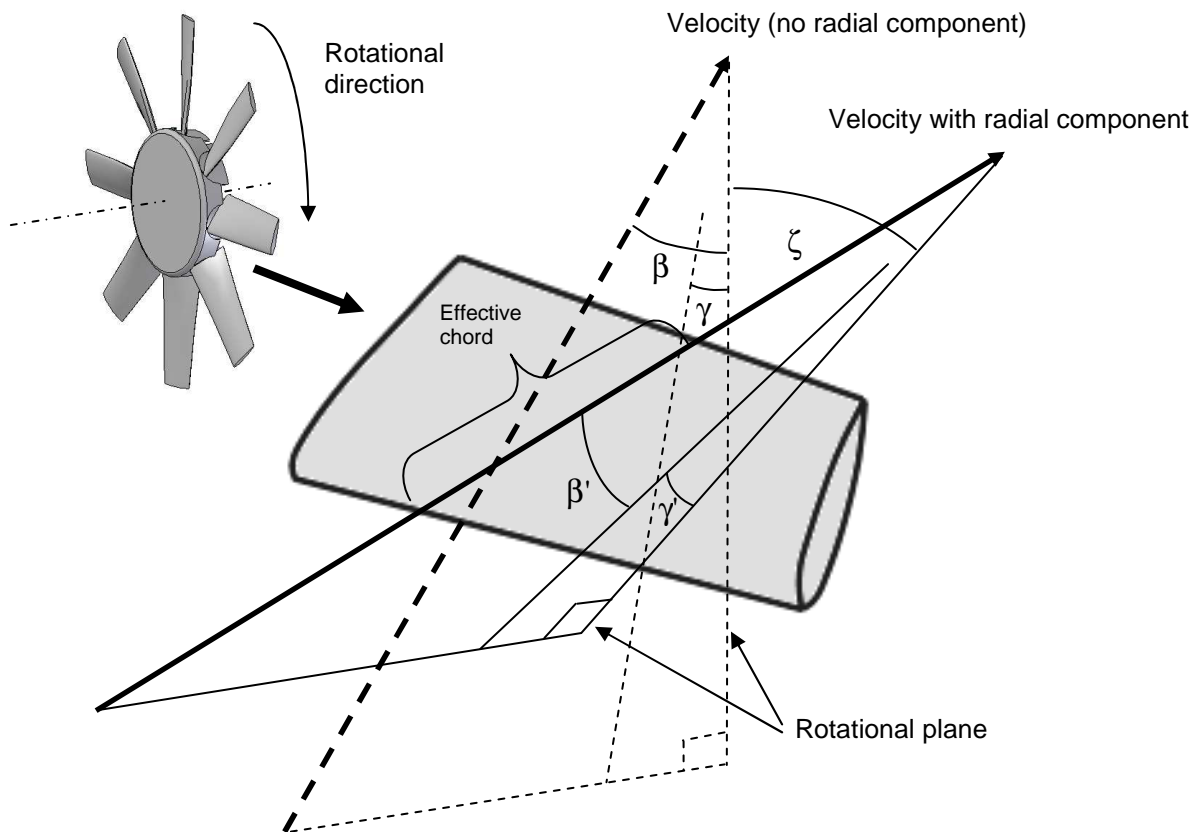


Figure B.15: Blade cross-flow.

If the cross-flow that occurs at a specific radial location across the blade is assumed to be uniform over the entire effective chord of the blade, the velocity is given by:

$$W_{\infty}' = \sqrt{W_z^2 + W_{\theta}^2 + W_r^2} \quad (\text{B.31})$$

The cross-flow angle is calculated as follows:

$$\zeta = \arctan(W_r/W_z) \quad (\text{B.32})$$

If the flow crosses the blade at an angle ζ , as shown, the relative flow and blade stagger angle would be transformed to:

$$\beta' = \arctan\left(\frac{\tan \beta}{\cos \zeta}\right) \quad (\text{B.33})$$

$$\gamma' = \arctan\left(\frac{\tan \gamma}{\cos \zeta}\right) \quad (\text{B.34})$$

The new value for angle of attack would then be:

$$\alpha' = \gamma' - \beta' \quad (\text{B.35})$$

While the effective chord length would then be calculated as:

$$c' = \frac{c \cos \gamma}{\cos \gamma'} \quad (\text{B.36})$$

Increasing the chord length of a specific blade profile, while keeping the thickness constant, would effectively alter the camber and therefore the lift characteristics of the blade profile. Based on thin-foil theory, as described in Houghton and Carpenter (2003), an airfoil's camber affects the value for lift coefficient at zero incidence angle. Consequently, a change in camber due to a change in chord length would change the value for the zero-lift angle of attack, α_0 , as follows:

$$\alpha_0' = \frac{\alpha_0 c}{c'} \quad (\text{B.37})$$

The angle of attack, calculated using equation (B.35), would then be adjusted by this change in α_0 as follows:

$$\alpha'' = \alpha' - (\alpha_0' - \alpha_0) \quad (\text{B.38})$$

The transformed angle of attack, α'' , is then used to get the lift and drag coefficients of the corresponding airfoil, based on its 2-dimensional properties, as detailed in Appendix C. These lift and drag coefficients, along with the relative velocity value (equation (B.31)) and chord (equation (B.36)) can then be used to express the equation for force per unit-mass as follows:

$$F_z' = -\frac{1}{2} W_\infty'^2 \sigma (C_L \cos \beta' - C_D \sin \beta') \cos \zeta / \Delta z \quad (\text{B.39})$$

$$F_\theta' = \frac{1}{2} W_\infty'^2 \sigma (C_L \sin \beta' + C_D \cos \beta') / \Delta z \quad (\text{B.40})$$

$$F_r' = \frac{1}{2} W_\infty'^2 \sigma (C_L \cos \beta' - C_D \sin \beta') \sin \zeta / \Delta z \quad (\text{B.41})$$

The cross flow and Coriolis terms were applied to the momentum equations in the ADM. The calculated fan static pressure curve is shown in Figure B.16.

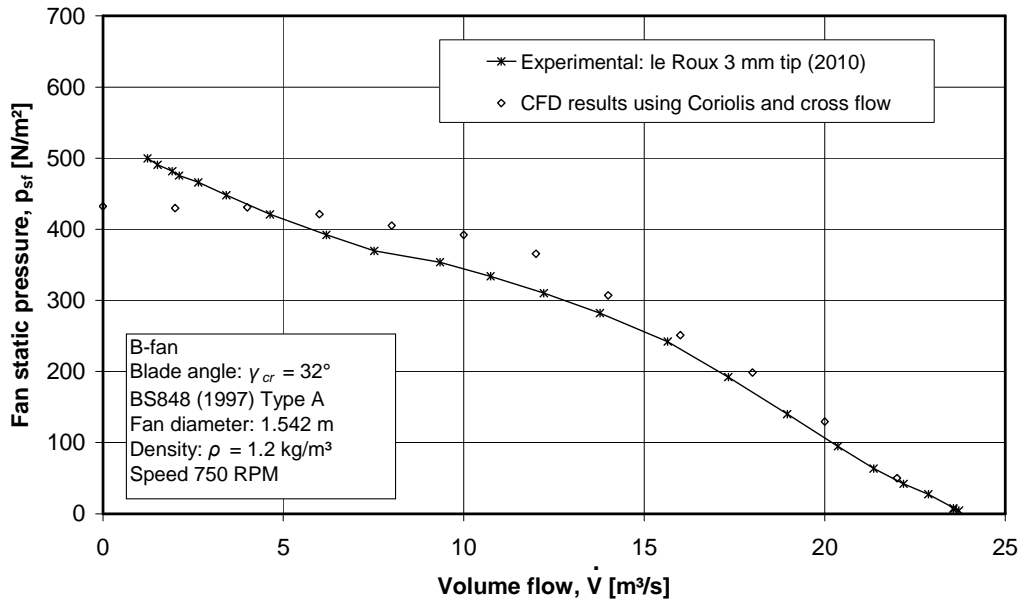


Figure B.16: Fan static pressure simulated using Coriolis and cross flow terms (B-fan).

B.3.3. Rotational augmentation of aerodynamic loads

As mentioned in Chapter 2, augmentation of the 2-dimensional blade profile lift capabilities on a rotating blade was first described by Himmelskamp (1945). He found that:

1. The maximum lift coefficient of a rotating blade increased in the presence of radial flow.
2. The increase in lift coefficient was the strongest at the smaller radii where the rotating blade is more susceptible to stall.
3. Stall occurs at a larger angle of attack when a blade is rotating than when it is stationary.

The measured airfoil data from the publication of Himmelskamp (1945) is given in Figure B.17.

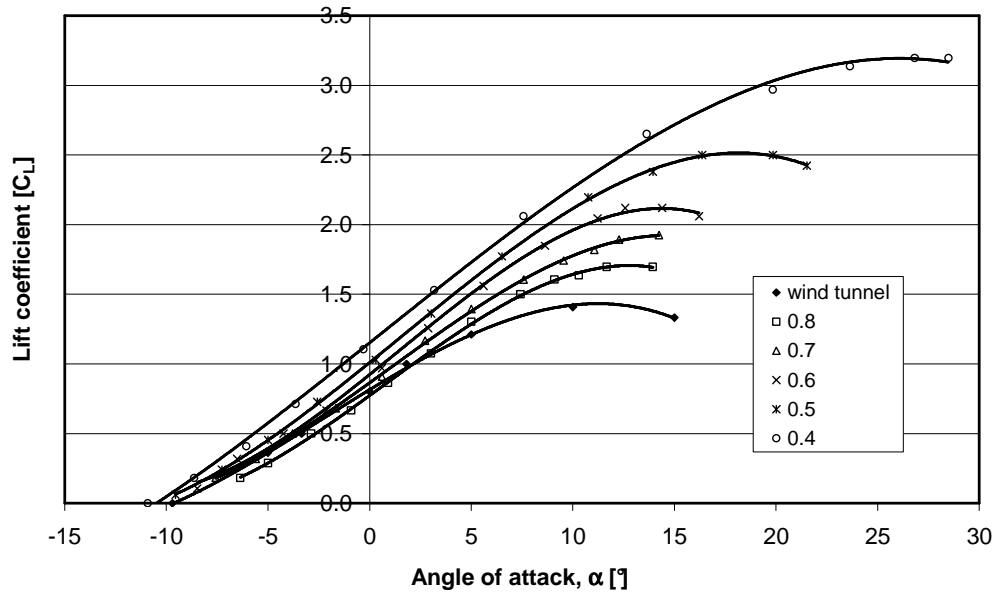


Figure B.17: Measured lift coefficients for rotating wing, plotted for various values of r/R (Himmelskamp, 1945)

The following aspects should be noted when considering the results of Himmelskamp:

1. Himmelskamp questions the accuracy of his own velocity measurements downstream of the fan rotor. He conducted these velocity measurements using a 3-hole velocity probe that was connected to a multiple-tube manometer. The probe was arranged to measure the axial and tangential velocities at different radii upstream and downstream of the rotor. Himmelskamp acknowledges that the velocity distribution downstream of the rotor is highly unsteady in the circumferential direction and that the visual pressure readings used to determine the average velocity profile would not have been accurate. The downstream velocity profile is used to calculate the average relative velocity over the fan blade, W_∞ , the angle of attack over the blade, and also to calculate the lift and drag components of the effective blade load.
2. The Himmelskamp experiments were conducted at various flow rates with the minimum flow rate being the point where reverse flow at the hub started occurring (in other words where the axial velocity downstream of the rotor was measured to be close to zero).
3. The measurements from Himmelskamp's experiments were processed in a manner similar to the implementation of the actuator disc method. The calculations (see equations (B.7) and (B.8)) use a reference velocity, W_∞ , that is based on the average values of axial and tangential velocities up and downstream of the rotor. The possible radial shift of streamlines through the rotor is ignored and it is assumed that the flow conditions at

the same radius ratio up- and downstream of the rotor occur along the same streamline.

4. Himmelskamp does not refer to the Coriolis and cross-flow effects and attributes the augmentation of the 2-dimensional blade profile lift coefficients to the stabilisation of the boundary layer on the suction side of the blade surface.

More recently Gur and Rosen (2005) derived a correlation which implied that the true value for the lift coefficient of a rotating airfoil section would lie between the 2-dimensional, non-rotating value and the inviscid flow solution. To achieve this they used a hyperbolic tangent function based on the value of chord length divided by radius to interpolate between these two extremes.

A number of other correlations for rotational augmentation of blade properties, particularly for wind turbines, are mentioned in Section 2.4.3. However, it is important to distinguish between wind turbines and axial flow fans when considering the “Himmelskamp effect”. A number of correlations for the Himmelskamp effect assume the rotating blade profile chord to be located in the plane of rotation (or very close to the plane of rotation). The consequence of this assumption is that the Coriolis effect would be entirely beneficial to the boundary layer on the blade. If however the blade setting angle is considered, the Coriolis effect is split into two components. The one component is aligned with the blade profile chord and is beneficial to the stability of the boundary layer profile by increasing the velocity inside the boundary layer and consequently decreasing the boundary layer thickness. The second component is however acting perpendicular to the blade profile chord. In the case of wind turbines, where the topic of 3D-augmentation is often encountered, the second component acts perpendicularly inward to the suction-side surface of the blade profile and further enhances the stability of the boundary layer and delays stall. In the case of axial flow fans, this second component acts perpendicularly outward from the suction-side surface of the blade profile and may destabilize the boundary layer to assist the occurrence of stall (see Figure B.18).

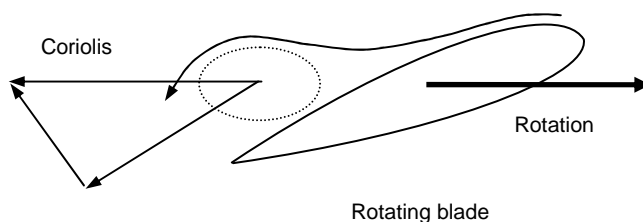


Figure B.18: Illustration of Coriolis force effect on boundary layer stability.

It can be concluded that for an axial flow fan the extent of the Himmelskamp effect in the boundary layer of the fan blade would be determined by the direction

of the Coriolis force relative to the blade chord, which varies radially according to the blade setting angle.

B.3.4. Integration of rotational augmentation into the actuator disc method

The actuator disc method as described by Bredell (2005) and Meyer and Kröger (2001) is based on the 2-dimensional airfoil profile characteristics at an average blade Reynolds number. Rotational augmentation is based on a radial variation in blade properties and therefore, to account for the 3-dimensional flow over a rotating blade, the spanwise (radial) variation in blade properties has to be taken into account. A linear relationship between the lift and drag coefficient properties of the hub and tip section of a specific fan blade was used, based on the angle of attack of the flow and the radial location of the specific point in the flow being investigated. The lift and drag coefficients were obtained as described in Appendix C. The relevant 2-dimensional lift or drag force coefficient at a specific radius was obtained as follows:

$$C_f = C_{fhub} - \frac{(r - r_{hub})}{(r_{tip} - r_{hub})} (C_{fhub} - C_{ftip}) \quad (\text{B.42})$$

Based on the procedure followed by Gur and Rosen, rotational augmentation is implemented into the actuator disc as follows (this proposed new method is referred to as the “extended actuator disc method” (EADM)):

1. Ignoring tip losses, it is assumed that the effective angle of attack of air at the tip of a shrouded rotating fan blade would always be within the linear range of the lift coefficient vs. angle of attack curve. This is due to the high circumferential speed of the blade tip, as well as the fact that the flow through the rotor is displaced towards the blade tip and the effective throughflow area decreases as the volume flow rate through the fan decreases. Moving away from the blade tip (to smaller radii) the effective angle of attack and the extent of radial flow over the blade increases. The increase in radial flow over the blade leads to increased augmentation of the effective lift force over the blade. To account for this effect the lift coefficient values of the particular blade profile used in the fan is increased by extending the linear section of the lift coefficient vs. angle of attack curve irrespective of its value for radius ratio (see Figure B.19).

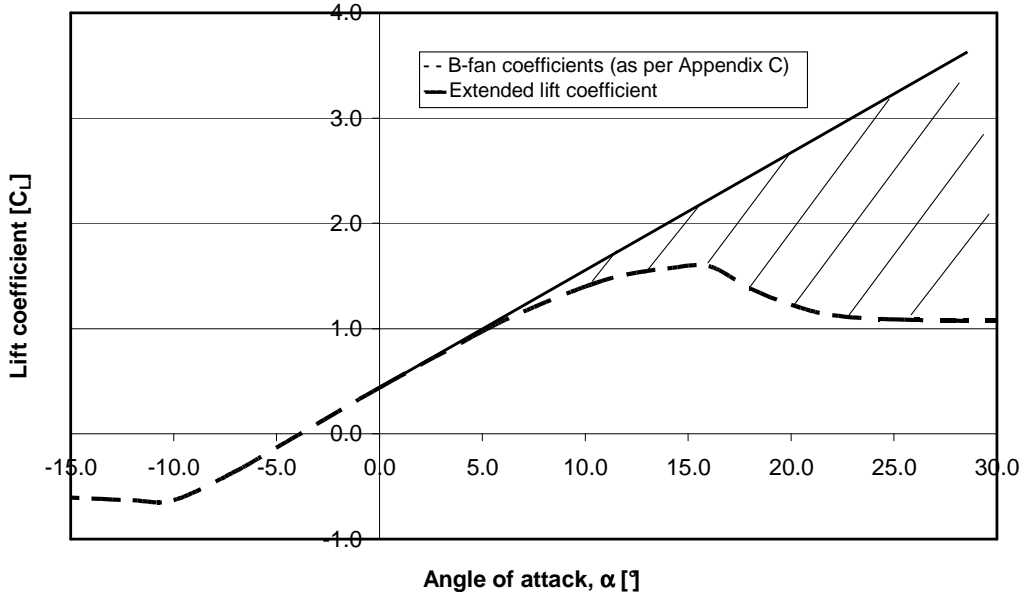


Figure B.19: Illustration of extended lift coefficient curve for B-fan blade profile.

2. At the other extreme the effective angle of attack of a rotating fan blade close to the hub becomes large at low flow rates (primarily due to the lower rotational speed at smaller radii). The suction side of the fan blade would be experiencing stall and reverse flow would be occurring at the hub. The occurrence of augmentation of the blade lift force is therefore not possible and it was decided to specify a limiting radius ratio below which the extended coefficient values would not be used and the model uses the original 2-dimensional profile values for the lift and drag coefficients. Although this may seem to counter the results of Himmelskamp, it should be noted that Himmelskamp only conducted his experiments at decreasing flow rates up to a point where reverse flow was observed in the outlet velocity profile at the hub of the experimental fan.
3. An appropriate value for the limiting radius ratio was determined by iteratively comparing the simulation results to the experimental results for the static pressure vs. volume flow rate curve (see Figure B.20) and in this instance it was found that a value of 0.5 gave satisfactory results.
4. The value of the 2-dimensional drag coefficients (used in the actuator disc method) is adjusted proportionally according to the increase in the 3-dimensional lift coefficient, as proposed by Gur and Rosen (2005):

$$C_{D3D} = C_{L3D} \times (C_{D2D} / C_{L2D}) \tag{B.43}$$

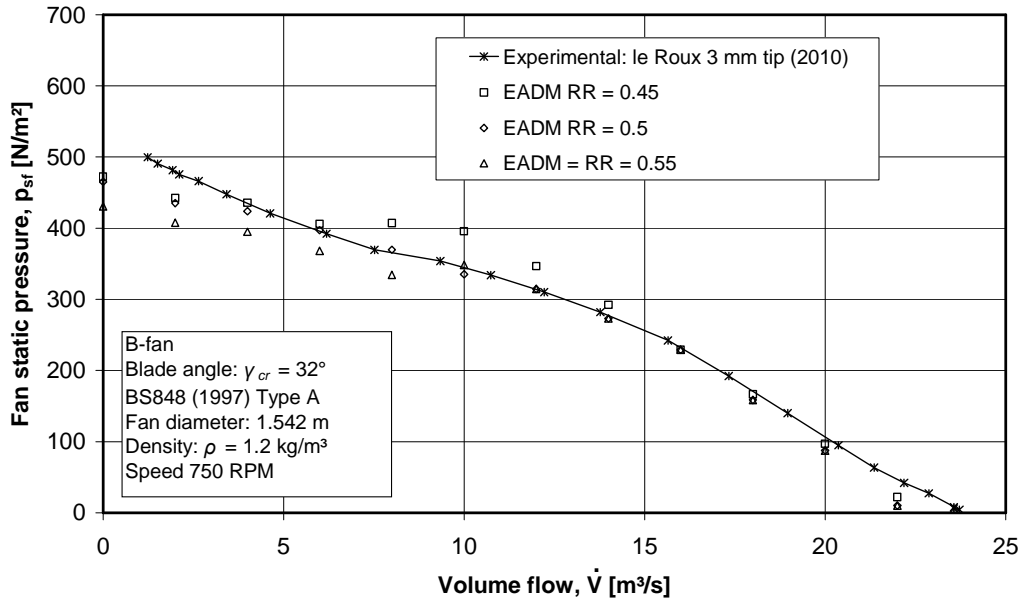


Figure B.20: Effect of different limiting ratios on fan static pressure curve using the EADM.

B.3.5. Results for extended actuator disc method (EADM)

A comparison of the simulation and test results for the B-fan is shown in Figures B.21, B.22 and B.23.

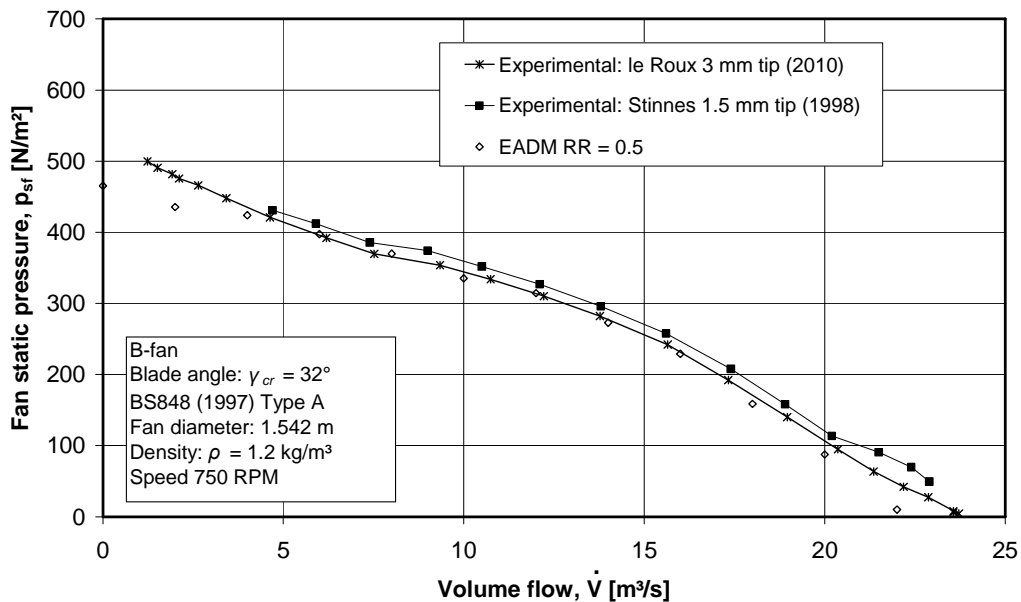


Figure B.21: Fan static pressure obtained using EADM, B-fan.

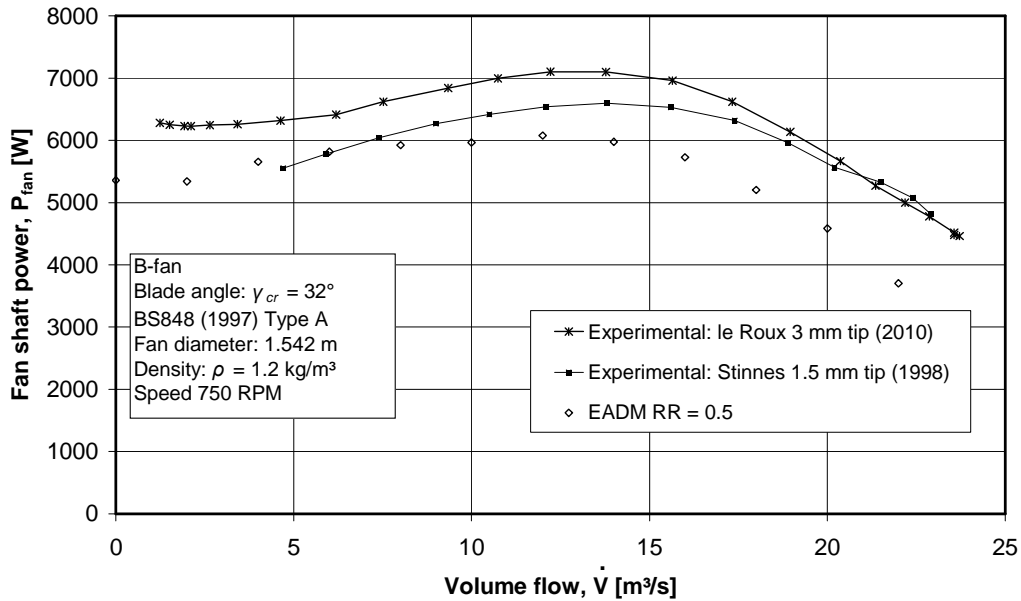


Figure B.22: Fan shaft power obtained using EADM, B-fan.

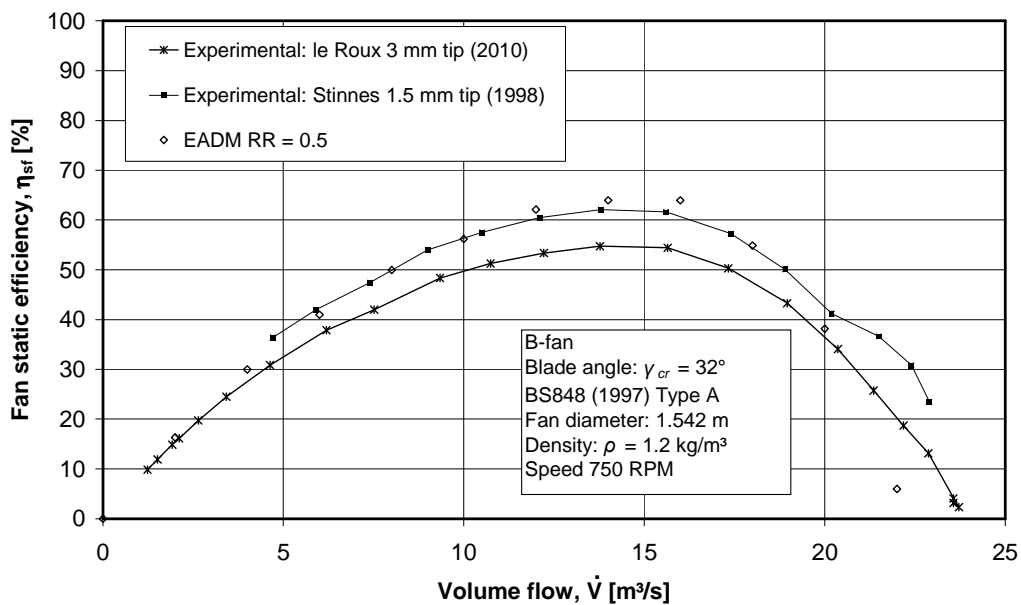


Figure B.23: Fan static efficiency obtained using EADM, B-fan.

B.4. Summary

The actuator disc method (as used by previous authors) was implemented on the B-fan, that was previously tested in a standard BS 848 type A test facility. A number of points should be noted regarding the implementation of the standard actuator disc method as part of this investigation:

1. The realizable $k-\varepsilon$ turbulence model is recommended for use with the actuator disc method. This is based on specific advantages that this turbulence model holds, as detailed in Section B.2.4.
2. The actuator disc method shows good correlation with experimental results for fan static pressure vs. volume flow rate within the normal operating range of both fan geometries.
3. The actuator disc method deviates from the measured fan shaft power values, as shown in Figure B.10. This can be attributed to the fact that the effect of fan tip clearance is not included in the actuator disc method (Meyer and Kröger, 2001) and a possible offset in the blade setting angle used by le Roux (2010).

The extended actuator disc method was implemented on the CFD simulation of the B-fan. The simulations using the extended actuator disc method show an increase in fan static pressure at lower flow rates that correspond well with the experimental results. Although the results obtained were very promising, the following should be noted as far as the extended actuator disc model is concerned:

1. To investigate the augmentation of the lift coefficients further, the CFD results from the analysis using the extended actuator disc model were used to calculate the lift coefficient vs. angle of attack values at $16 \text{ m}^3/\text{s}$ and $6 \text{ m}^3/\text{s}$ and these values were compared to the values for the NASA LS(1)-0413 profile originally published by McGee et al. (1977) (see Figure B.24). Figure B.24 shows that the majority of the lift coefficient values used by the extended actuator disc method correlate with the original profile coefficients published by McGee et al. It also shows that the extended lift coefficient values have very little effect on the results simulated using this model at $16 \text{ m}^3/\text{s}$. The effect of limiting the radius ratio is more clearly evident at the last point (at 41° angle of attack) shown for the analysis at $6 \text{ m}^3/\text{s}$.

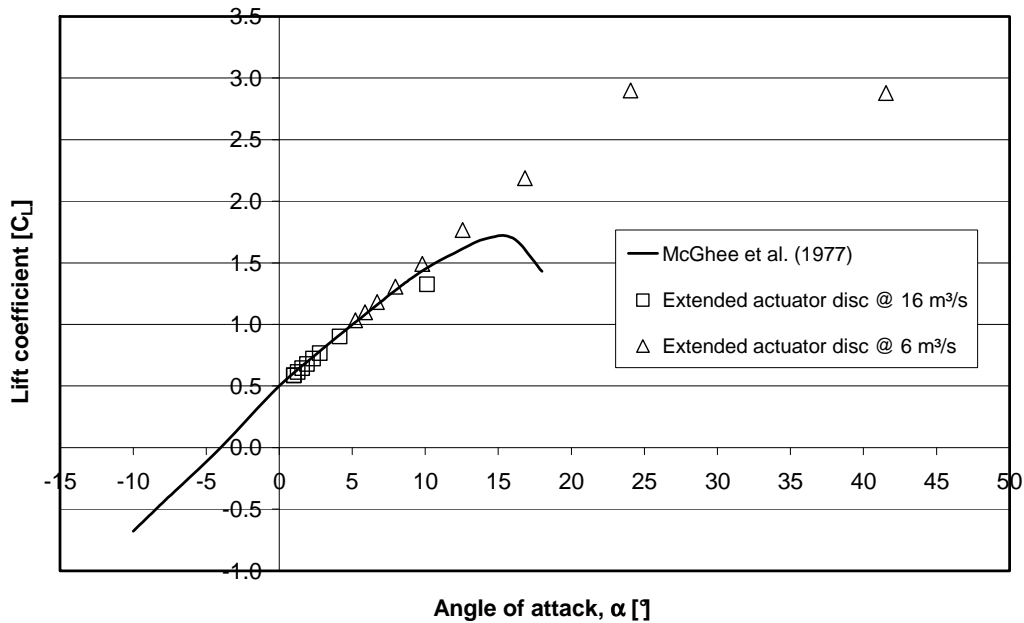


Figure B.24: Post processed lift coefficients at different radius ratios for B-fan at 16 m³/s and 6 m³/s, compared to published airfoil data.

2. The proposed extended actuator disc method represents all the different augmentation effects (Coriolis force, blade cross-flow and stall delay) in a single model. In practice the extent to which these different effects play a role in a specific fan may vary, based on factors like the blade setting angle, blade hub-to-tip ratio and blade solidity.
3. The augmentation of a blade's airfoil properties is caused by the occurrence of radial flow over the blade. The proposed model assumes that the occurrence of radial flow over the blade would coincide with a reduced flow rate through the fan and subsequently augments the blade profile coefficients using the axial and tangential velocity values.
4. Considering the relationship between boundary layer stability and Coriolis force on the blade suction side (see Figure B.15) the use of a limiting radius ratio below which the extended actuator disc method does not apply, is feasible (at a smaller radius ratio, an axial flow fan blade usually has a larger blade setting angle).
5. The extended actuator disc method is purely empirical and its use should be investigated further, possibly by means of detailed velocity measurements up- and downstream of a rotating fan blade.

APPENDIX C: MODELLING 2D AIRFOIL PROFILES

C.1. Introduction

For airfoils used in the aeronautical industry the lift and drag coefficients are typically restricted to values corresponding to angles of attack ranging from -10° to $+20^\circ$ (the angle of attack is defined as the angle between the main flow direction and the chord line of the airfoil profile). To take into account the varying flow conditions that might exist (depending on flow rate, rotational speed, blade twist and blade setting angle) in an axial flow fan, the angular range of the lift and drag coefficients needs to be extended to consider possible stall and flow reversal over different sections of the fan blade. Meyer and Kröger (2001) extended the measured airfoil data for the B-fan blade profile (McGee et. al, 1977) by matching it to the lift and drag coefficients for a flat plate obtained from Hoerner and Borst (1975) (see Figure C.1) and using extrapolation to account for the effect of Reynolds number on these coefficients (McGee et. al, 1979, Meyer and Kröger, 2004).

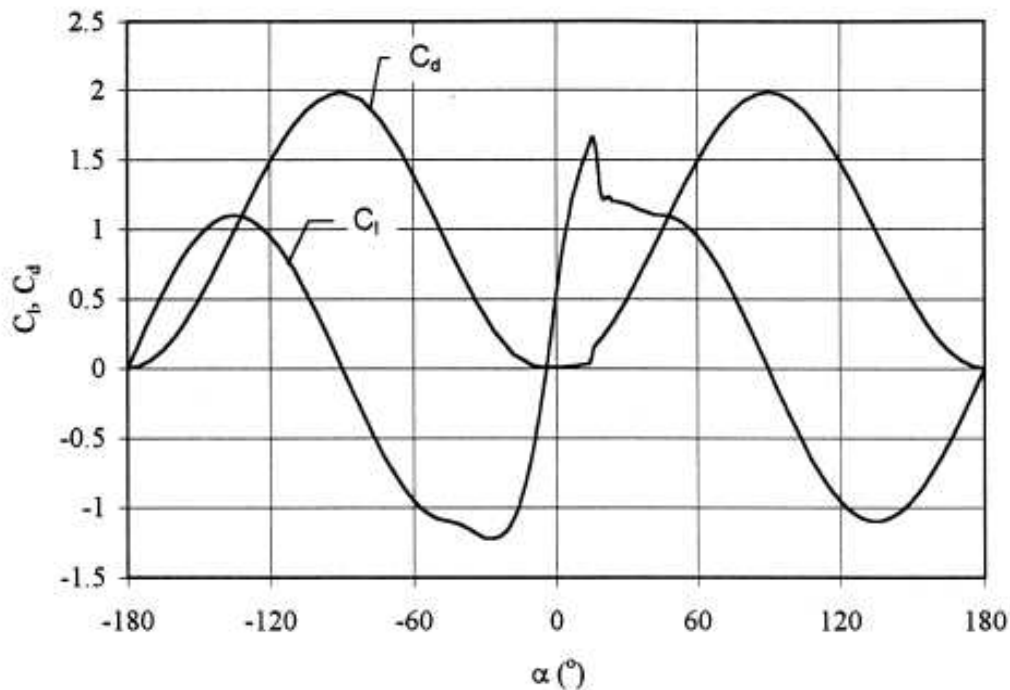


Figure C.1: Example of a composite blade profile characteristic at $Re = 1.9 \times 10^6$ (Copied from Meyer and Kröger, 2001).

If measured lift and drag data of a specific airfoil is available it is often at Reynolds numbers suited for aviation purposes and usually not for the specific axial flow fan blade being investigated. When striving to obtain the 2D lift and

drag coefficients of a specific airfoil profile at a specific Reynolds number, the following has to be considered:

1. A fan blade is designed so that its airfoil profile operates at an effective angle of attack between 0° and 10° (bear in mind that the angle of attack may vary with radial location along the blade span). Therefore, in order to obtain good correlation between standard axial flow fan test results and the results from the actuator disc method for the normal fan operating range, accurate airfoil data within a band of about -10° to 20° is required.
2. Large, 9 m diameter axial flow fans, operating at 125 rpm with a chord length of 1 m at standard atmospheric conditions would have a maximum rotational Reynolds number in the order of 4×10^6 . At this Reynolds number, the use of CFD turbulence models to simulate the flow characteristics around an airfoil would be appropriate.
3. A 1.5 m diameter axial flow fan operating at 750 rpm with a chord length of 150 mm at standard atmospheric conditions has a maximum rotational Reynolds number of 7.8×10^5 . According to White (2008) transition from laminar to turbulent flow for typical surfaces and free streams would occur in the region of 5×10^5 . The flow over the blades of a fan operating under these conditions can therefore be classified as low Reynolds number flow. Rumsey and Spalart (2008) evaluated the behaviour of two well-known turbulence models (Spalart-Allmaras and Menter shear stress transport) at low Reynolds numbers and found that using these models in transitional flows is not appropriate.
4. The use of a transitional turbulence model (Menter et al., 2006) was also considered. This model requires y^+ values in the order of 1, as well as a large number of iterations for its residuals to converge. The main advantage of the transitional turbulence model is reported to be its ability to predict laminar separation and subsequent re-attachment. However, Lindenburg (2004) states that one of the effects of 3-dimensional boundary layer augmentation (as discussed elsewhere) is to suppress the formation of laminar separation completely.
5. It was therefore decided to use a combination of panel methods and viscous/inviscid interaction methods to solve the flow around the airfoil at low Reynolds numbers for angles of attack between -10° and 16° . For this purpose a software programme referred to as Xfoil (Drela, 1989) was used. An Xfoil analysis at a specific angle of attack takes about 2 seconds to execute, compared to a CFD analysis taking between 30 minutes and an hour (depending on the mesh density and turbulence model being used).
6. If the Xfoil programme was unable to analyse the airfoil geometry, the transitional turbulence model of Menter et al. (2006) was used. This was found to be the case for airfoil profiles with large camber values and subsequent separation on the pressure side of the airfoil profile.
7. When considering 3-dimensional effects in the actuator disc, the span-wise variation of the blade airfoil properties has to be taken into account. For this purpose the hub and tip profiles of a specific blade was simulated at their respective rotational Reynolds numbers over the complete -180° to

+180° angles of attack. The relevant blade properties at a specific radial location were then obtained by linear interpolation between the hub and tip profile properties (see equation B.42).

C.2. Standard CFD analysis

C.2.1. Airfoil profile

The published experimental results for a known airfoil profile (in this case the LS(1)-0413 profile (McGhee et. al, 1973, 1977 and 1979) which was used in the B-fan (Bruneau, 1994) were compared to the results from a 2-dimensional CFD simulation of the same profile for a specific Reynolds number of 2.1×10^6 (this is the lowest Reynolds number for which experimental data is available).

The LS(1)-0413 airfoil belongs to a family of “low-speed” (LS) airfoils developed in the 1970s. The first airfoil in this family was a 17% thick profile, referred to as GA(W)-1 (later referred to as LS(1)-0417). The LS(1)-0413 is a 13% thick profile that was obtained from the GA(W)-1 by simply scaling the thickness around the mean camber line. The LS(1)-0413 was originally referred to as the GA(W)-2 airfoil. According to McGhee et al. (1979) the LS airfoils exhibit superior maximum lift coefficients when compared to older NACA airfoil profiles.

The B-fan incorporates an LS(1)-0413 profile at the hub (at a Reynolds number of 2.97×10^5) and an LS(1)-0409 profile at the tip (at a Reynolds number of 6.19×10^5). The initial CFD analysis at a Reynolds number of 2.1×10^6 was therefore followed by analyses of the hub and tip profiles at their appropriate, lower Reynolds numbers.

C.2.2. Solver

ANSYS Fluent® versions 6.3.26 and 12.1 CFD software was used for these simulations. It was decided to use the Spalart Allmaras turbulence model for all 2D airfoil simulations (Spalart and Allmaras, 1994). The Spalart Allmaras turbulence model is a one-equation model that solves the transport equation for turbulent viscosity. It is considered to be well-suited for use in aerodynamic applications with adverse pressure gradients at high Reynolds numbers (Spalart and Allmaras, 1994). However, the Spalart Allmaras turbulence model can not predict the location of the transition point and, as mentioned before, Rumsey and Spalart (2008), found that using the Spalart Allmaras turbulence model in transitional flows is not appropriate.

All analyses were performed using a second order upwind differencing scheme and the default relaxation factors as prescribed by the software. Although the eventual purpose of the analysis was to compare lift and drag coefficients which are essentially non-dimensional (meaning that densities and sizes do not necessarily have to be the same) a standard density of 1.2 kg/m^3 and a chord length of 1 m was used.

C.2.3. Geometry and mesh

The geometry of the airfoil shape was imported into Gambit[®] 2.4.6 as vertex data. As mentioned before, the airfoil profile was modelled with a chord length of 1 m. A single B-spline was fitted through the vertices, except for the blunt trailing edge which was modelled as a separate straight curve.

The lay-out of the analysis domain was based on the same format used by Bredell (2005). The nature of the airfoil analyses meant variously shaped profiles had to be modelled at a full range of angles of attack (-180° to $+180^{\circ}$). Usually the author would propose the use of hexahedral elements when modelling the flow over an airfoil. However, where an airfoil profile might be meshed appropriately using a hexahedral mesh for a variation in angle of attack from -10° to $+10^{\circ}$, that same mesh may not be suitable for an angle of attack of 180° and a complete re-mesh of the model would be required. It was therefore decided to model the airfoil profile using triangular elements in an elliptically shaped domain within a maximum distance of one chord length around the profile.

The elliptically shaped domain with the triangular elements was surrounded by a circular domain with a radius of 20 chord lengths using hexahedral elements. A total of about 35000 triangular elements and 13000 hexahedral elements were used. Size functions were used to specify the cell length on the airfoil surface (2 mm) and the outer boundary of the domain (500 mm). This resulted in about 750 elements (depending on the exact shape of the particular profile used) being generated around the circumference of the airfoil profile. The author of this thesis refrained from using mesh seeding around the profile because of the need to alter the angle of attack through such a wide range. It was therefore decided to rather use a size function with a generally overall small element length. The blunt rear end of the profile was modelled as a separate part of the foil profile using five elements. The author considered the use of a larger outer domain to verify the influence of domain size on the results at larger angles of attack. The domain was extended to a radius of 100 chord lengths but no significant change in the results could be observed.

The boundary layer around the profile was modelled sufficiently fine to obtain a y^+ -value of one at the airfoil surface. The height of the first cell row was modelled as 0.05 mm. The boundary layer contained 10 cell elements perpendicular to the airfoil surface. To ensure accuracy when using triangular meshes, the Green-Gauss node-based gradient evaluation option is used. This option means that the face values, used to calculate the gradient of a specific scalar at a cell centre, is calculated as the arithmetic average of the nodal values on a specific face. A lay-out of the CFD model is shown in Figure C.2.

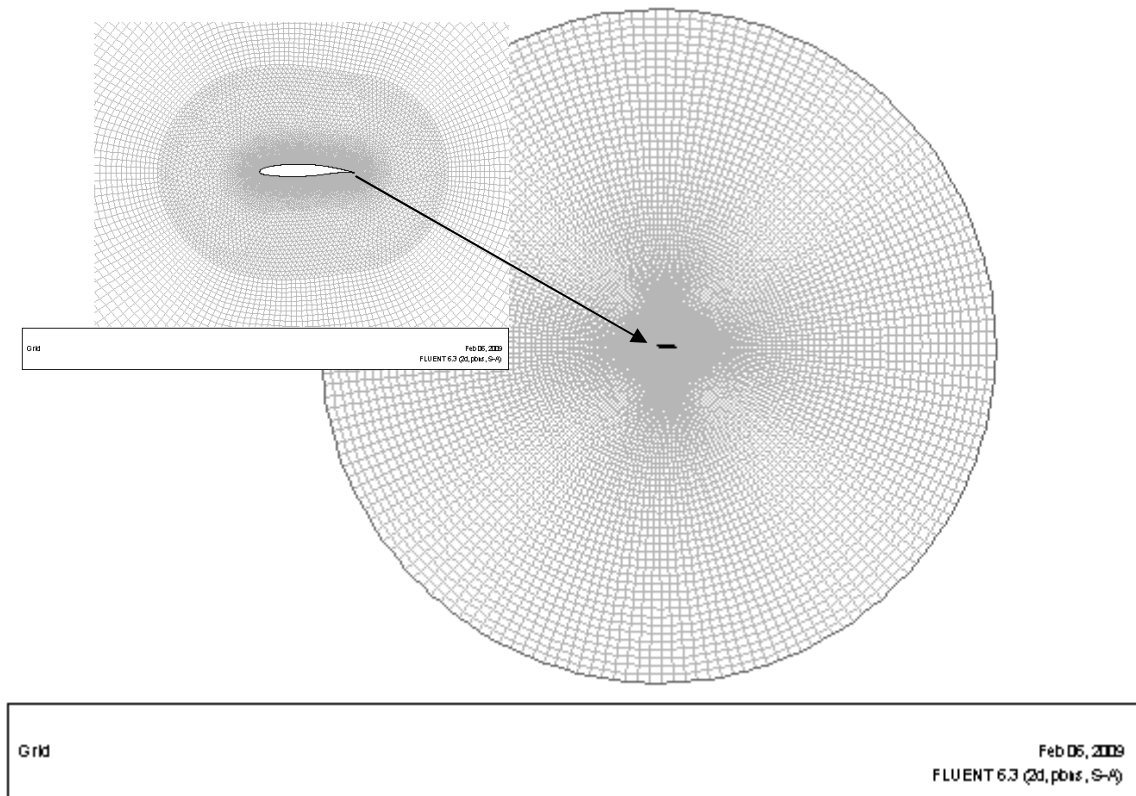


Figure C.2: Lay-out of CFD-model for airfoil analyses.

C.2.4. Boundary conditions

The boundary conditions were also specified in the same format used by Bredell (2005). The airfoil profile was modelled in the centre of a circular domain with a prescribed velocity value and direction (depending on the angle of attack being investigated) around the perimeter of the domain. Turbulence intensity and dissipation length scales were set to the same order of magnitude as that of the facility being emulated. For instance, the turbulence intensity in the large fan test tunnel was measured to be between 1% and 2% (Olivier, 2008). This facility also has a 10 mm x 10 mm wire mesh located upstream of the fan and therefore a length scale value of 0.01 m was used.

C.3. Low Reynolds number analyses

C.3.1. Xfoil solver

Xfoil was developed by Drela (1989) and first released in 1986. Xfoil uses a viscous/inviscid analysis to solve flow around airfoils and is considered particularly effective at low Reynolds numbers. The inviscid linear-vorticity panel analysis is constructed from a general two-dimensional flow field which

superimposes a free stream flow, vortex sheet with strength γ on the airfoil surface and a source sheet of strength σ on the airfoil surface and wake. The stream function is then given as (Drela, 1989):

$$\Psi(x, y) = u_\infty y - v_\infty x + \frac{1}{2\pi} \int \gamma(s) \ln r(s, x, y) ds + \frac{1}{2\pi} \int \sigma(s) \theta(s, x, y) ds \quad (\text{C.1})$$

The source distribution permits modelling of the viscous layer influence on the inviscid flow by setting the source strength equal to the gradient of the mass defect:

$$\sigma_i = \frac{dm}{d\xi} \quad (\text{C.2})$$

where

$$m = u_e \delta^* \quad (\text{C.3})$$

The viscous flow is solved by using the following standard integral momentum and kinetic energy shape parameter equations:

$$\frac{d\theta}{d\xi} + (2 + H - M_e^2) \frac{\theta}{u_e} \frac{du_e}{d\xi} = \frac{C_f}{2} \quad (\text{C.4})$$

$$\theta \frac{dH^*}{d\xi} + (2H^{**} + H^*(1 - H)) \frac{\theta}{u_e} \frac{du_e}{d\xi} = 2C_D - H^* \frac{C_f}{2} \quad (\text{C.5})$$

Under turbulent flow conditions Xfoil uses a rate equation for the maximum shear stress coefficient, C_τ , to account for deviations of the outer layer dissipation coefficient, C_D , from the local equilibrium value:

$$\frac{\delta}{C_\tau} \frac{dC_\tau}{d\xi} = 5.6 \left(C_{\tau_{EQ}}^{1/2} - C_\tau^{1/2} \right) + 2\delta \left\{ \frac{4}{3\delta^*} \left[\frac{C_f}{2} - \left(\frac{H_k - 1}{6.7H_k} \right)^2 \right] - \frac{1}{u_e} \frac{du_e}{d\xi} \right\} \quad (\text{C.6})$$

In laminar regions this equation is replaced by a rate equation which models the growth of the amplitude \tilde{n} of the most-amplified Tollmien-Schlichting wave:

$$\frac{d\tilde{n}}{d\xi} = \frac{d\tilde{n}}{d\text{Re}_\theta} (H_k) \frac{d\text{Re}_\theta}{d\xi} (H_k, \theta) \quad (\text{C.7})$$

The transition point is defined by the location where \tilde{n} reaches a user-specified critical value \tilde{n}_{crit} . This user-specified value represents the background disturbance level and is set during execution of the analysis.

The Xfoil analyses were repeated for the same LS(1)-0413 profile mentioned in Section 2 but at lower Reynolds numbers. Since Xfoil can not solve separated flows the analyses were only done for angles of attack between -10° and $+16^\circ$.

C.3.2. Transitional CFD-modelling

To investigate the behaviour of the LS(1)-0413 airfoil profile further, a CFD analysis was done using the transitional turbulence model of Menter et al. (2006). This transitional model is based on a coupling of the traditional SST $k-\omega$ transport equations with a transport equation for intermittency (the fraction of time that the flow at a given position is turbulent) and one for the transition onset criteria (in terms of momentum thickness Reynolds number). The model does not solve the physics of the transition process but is based on empirical correlations derived from experimental results (Menter et al., 2006).

The transitional CFD analysis used the exact same geometry and mesh detailed in section C.2.3. The analysis was only done for angles of attack ranging between -10° and $+16^\circ$.

C.4. Results

C.4.1. Verification of CFD model

A comparison of CFD-simulated (using the Spalart Allmaras turbulence model) and experimental results for the lift and drag coefficient of the LS(1)-0413 profile at a Reynolds number of 2.1×10^6 is shown in Figures C.3 and C.4. Figure C.4 is specifically given as lift coefficient vs. drag coefficient to correlate with the format of the published data of McGhee et al. (1977).

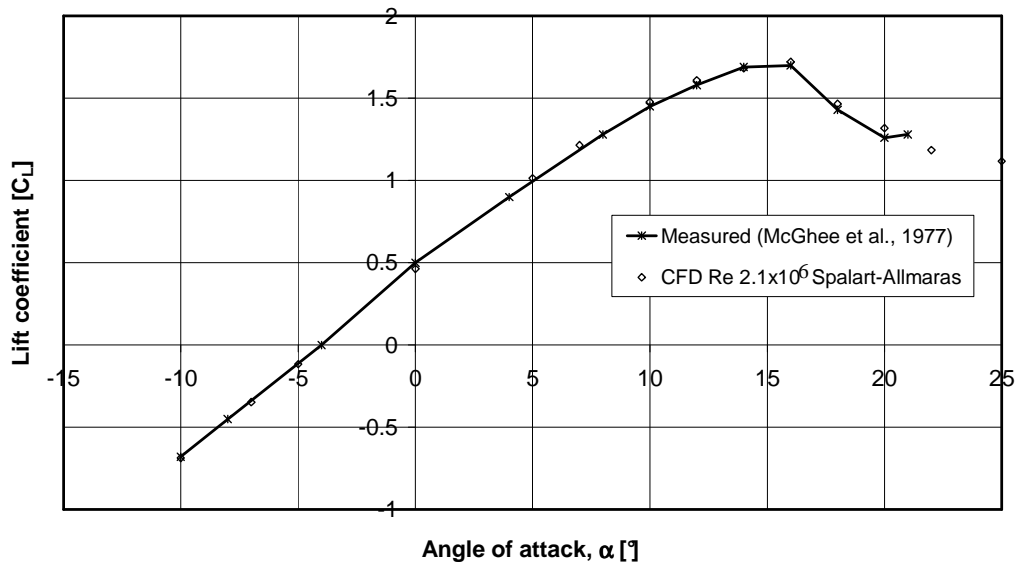


Figure C.3: Comparison of lift coefficient for CFD-simulation and experimental results (LS(1)-0413, $Re = 2.1 \times 10^6$).

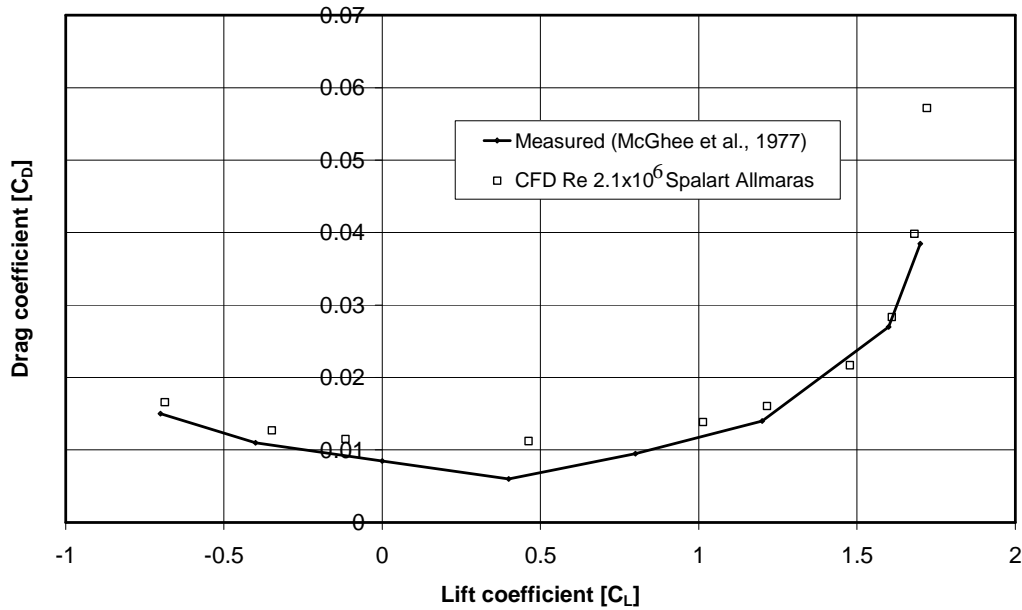


Figure C.4: Comparison of drag coefficient for CFD-simulation and experimental results (LS(1)-0413, $Re = 2.1 \times 10^6$).

Figures C.5 and C.6 show a comparison of lift and drag coefficients using the CFD-Spalart Allmaras turbulence model, compared to using Xfoil and the CFD-transitional turbulence model for the LS(1)-0413 profile at a Reynolds number of 2.97×10^5 .

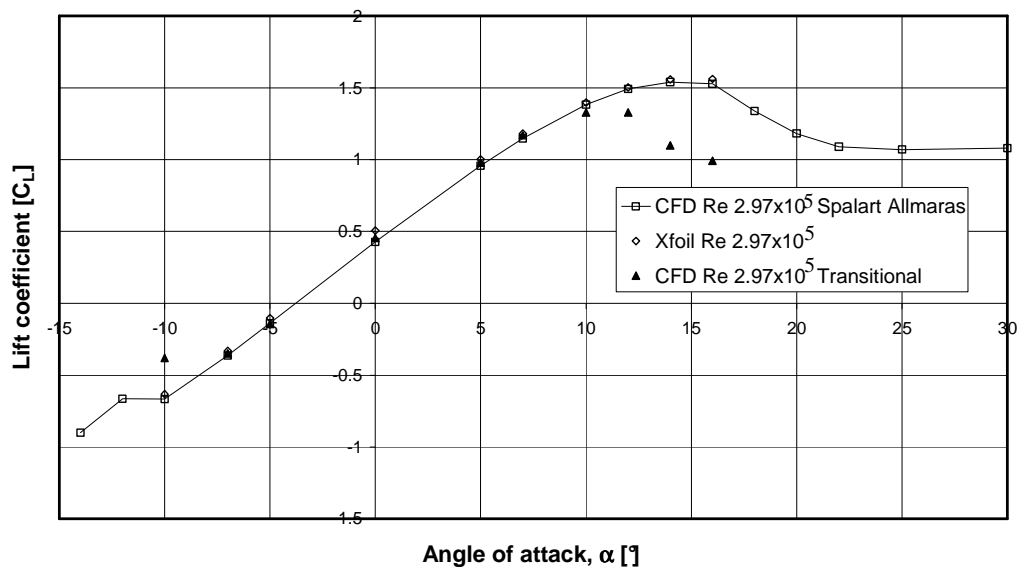


Figure C.5: Comparison of lift coefficients using the Spalart Allmaras, Xfoil and transitional model (LS(1)-0413, $Re = 2.97 \times 10^5$).

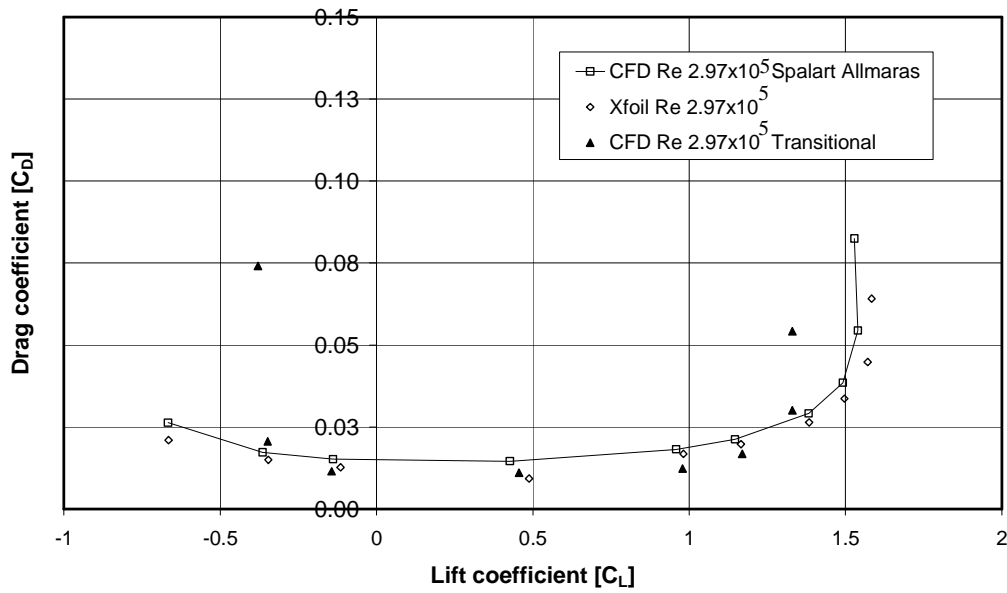


Figure C.6: Comparison of drag coefficients using the Spalart Allmaras, Xfoil and transitional model (LS(1)-0413, $Re = 2.97 \times 10^5$).

C.4.2. Blade profile modelling

The hub and tip profiles of the B-fan blade were analysed at their appropriate Reynolds numbers using Xfoil for angles of attack between -10° and $+16^\circ$ and the Spalart Allmaras turbulence model for all other angles of attack. Figure C.7 shows the complete -180° to $+180^\circ$ lift coefficient curve for the hub blade profile of the B-fan (LS(1)-0413, $Re 2.97 \times 10^5$).

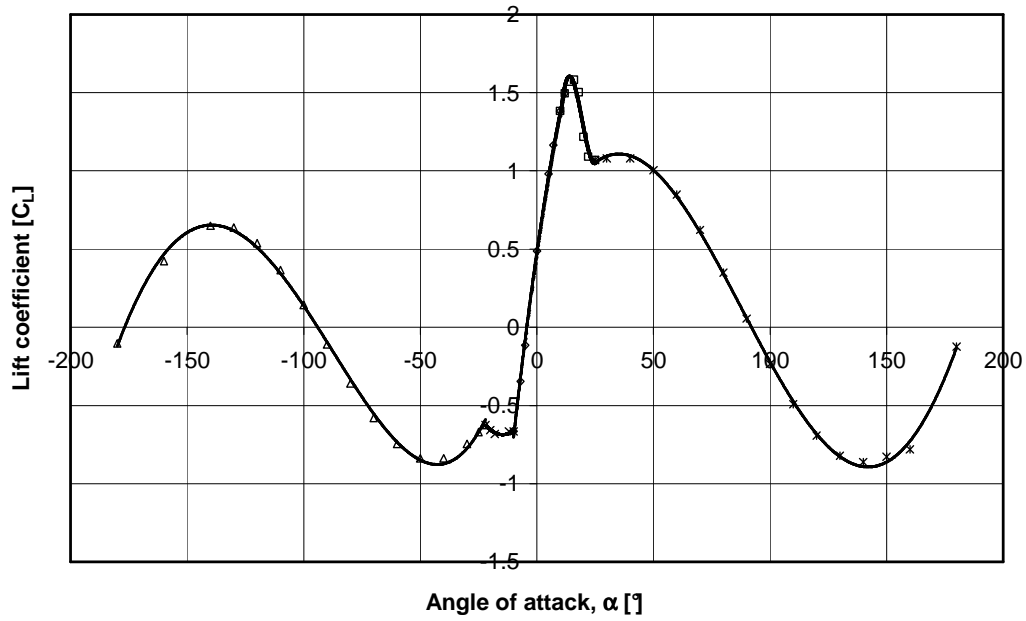


Figure C.7: Complete lift coefficient curve for B-fan hub blade profile (LS(1)-0413, $Re = 2.97 \times 10^5$).

Figure C.8 shows the complete -180° to $+180^\circ$ drag coefficient curve for the hub blade profile of the B-fan (LS(1)-0413, $Re 2.97 \times 10^5$).

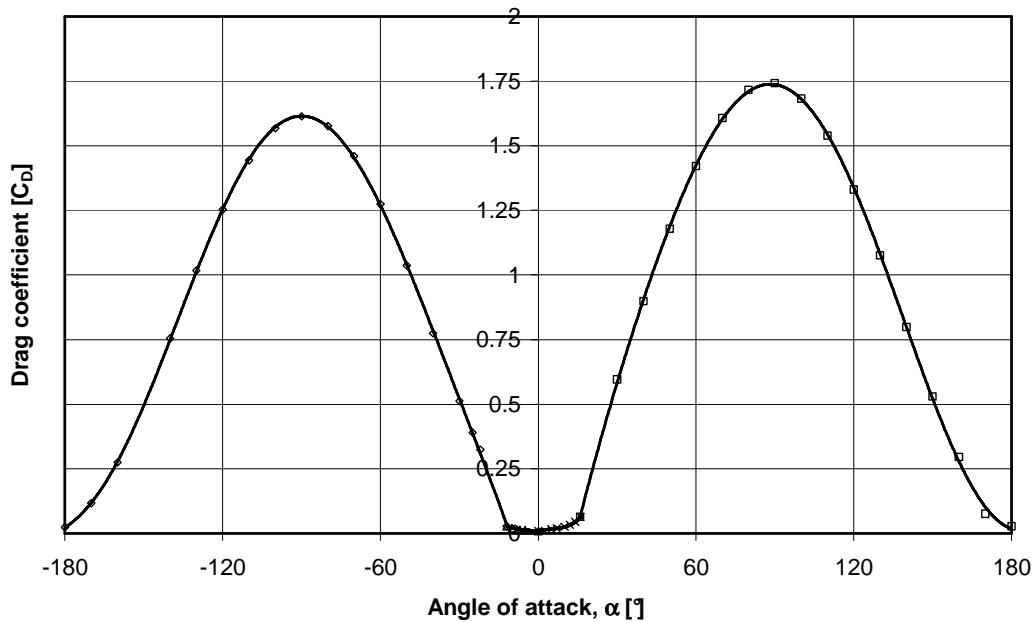


Figure C.8: Complete drag coefficient curve for B-fan hub blade profile (LS(1)-0413, $Re = 2.97 \times 10^5$).

Figure C.9 shows the complete -180° to $+180^\circ$ lift coefficient curve for the tip blade profile of the B-fan (LS(1)-0409, $Re\ 6.19 \times 10^5$).

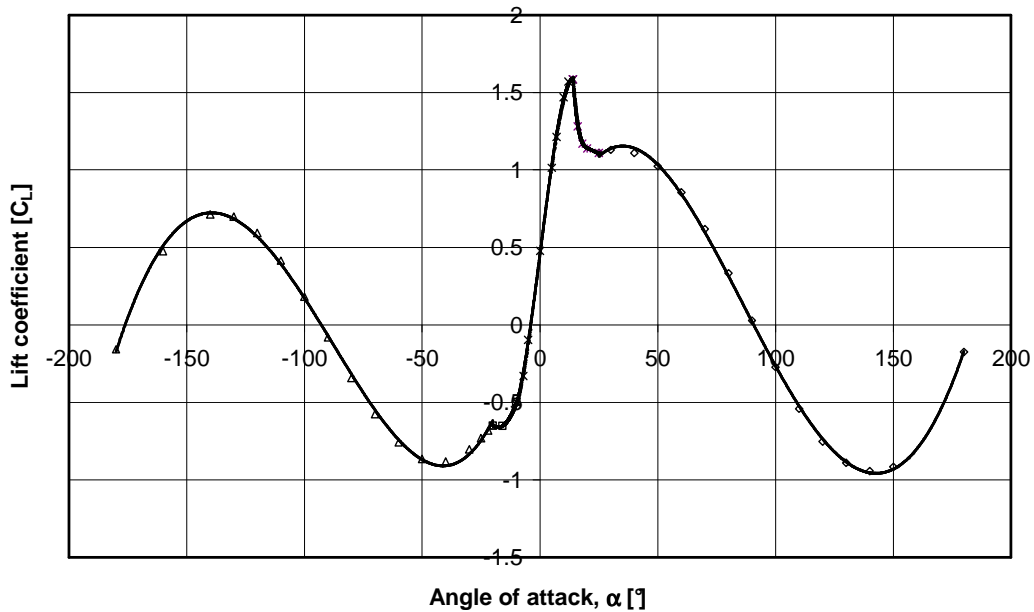


Figure C.9: Complete lift coefficient curve for B-fan tip blade profile (LS(1)-0409, $Re = 6.19 \times 10^5$).

Figure C.10 shows the complete -180° to $+180^\circ$ drag coefficient curve for the tip blade profile of the B-fan (LS(1)-0409, $Re\ 6.19 \times 10^5$).

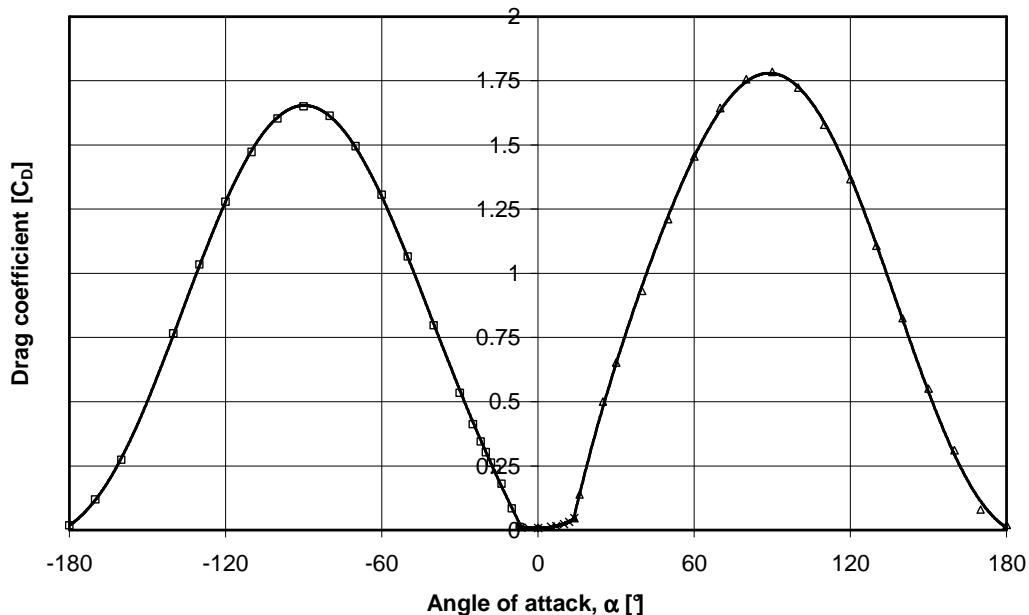


Figure C.10: Complete drag coefficient curve for B-fan tip blade profile (LS(1)-0409, $Re = 6.19 \times 10^5$).

C.5. Discussion

C.5.1. Verification results

Figure C.3 shows excellent correlation between the experimental lift coefficient results of McGhee et al. (1977) and those obtained from the CFD simulation using the Spalart Allmaras turbulence model at the same Reynolds number. This excellent level of correlation is, however, not evident when comparing the drag coefficient values shown in Figure C.4. The drag coefficient comparison shows quite a significant deviation at a lift coefficient of 0.5 where the simulated drag coefficient is 0.0115 and the measured value is in the order of 0.006. However, the measured values shown are for a smooth surface and measurements performed by McGhee et al. (1977) with an added surface roughness showed a drag coefficient of 0.011 at the same point. It would therefore seem that the inability of the Spalart Allmaras turbulence model to simulate the laminar flow region accurately has a definite effect on the simulated drag coefficient values.

The presence of the laminar flow region once again becomes apparent when comparing the low Reynolds number results for lift and drag coefficients (Figures C.5 and C.6). The CFD simulation using the transitional turbulence model predicts a maximum lift coefficient of 1.3 at an angle of 12° , compared to the CFD simulation using the Spalart Allmaras model which predicts a maximum lift coefficient of 1.55 at an angle of 15° . The Xfoil results for lift coefficient correspond very closely to the CFD simulation results using the Spalart Allmaras model. Neither of these (Xfoil or Spalart Allmaras) can handle laminar flow separation and re-attachment. As mentioned before, one of the main advantages of the transitional turbulence model is its ability to model the laminar separation, transition and re-attachment of the turbulent flow. The author spent many hours investigating the effect of boundary conditions (grid refinement, domain size, inlet turbulence conditions, intermittency) on the CFD results when using the transitional turbulence model but no alteration of boundary conditions could affect the CFD results in such a way that the predicted lift coefficient value was closer to the predicted value obtained when using either the Spalart Allmaras model or Xfoil.

When comparing the drag coefficients it is interesting to note that Xfoil predicts lower drag coefficients than the CFD simulation with Spalart Allmaras, which can most probably be attributed to Xfoil predicting the existence of a laminar flow region on the blade. The CFD simulation with transitional modelling also predicts lower drag coefficients but these become quite large once stall occurs.

C.5.2. Blade profile results

As mentioned before, the blade profile results were obtained by combining the results from Xfoil (-10° to $+16^\circ$) and Spalart Allmaras. There are only small differences between the results for the LS(1)-0413 and LS(1)-0409 blade profiles (for both lift and drag coefficients, see Figures C.7 to C.8). It should be noted that

most of the modelling effort went into simulation of the blade profiles at angles of attack between -10° and $+30^\circ$ because these values fall within the normal operating range of the fan. It is also interesting to note the difference between the maximum lift coefficient measured by McGhee et al. (1.7 at $Re = 2.1 \times 10^6$) and the simulated maximum lift coefficient at the lower Reynolds number (1.55 at $Re = 2.97 \times 10^5$).

C.6. Summary

A number of distinct conclusions could be drawn from these simulations:

1. The principle of simulating a blade hub and tip profile for a particular fan blade means that the effect of Reynolds number can be taken into account, as well as any difference in blade profile shape. In this instance the difference between the blade tip and hub profile was merely a blade thickness value and this seemed to have a small influence on the results. The accuracy of the simulation can be improved by adding another blade profile (for instance at mid radius) from which linear radial changes can be applied between the profiles.
2. Based on the good correlation between the measured and simulated results shown in Figure C.3 it can be concluded that the geometry and mesh used currently is sufficiently accurate.
3. The large difference between results for Xfoil and CFD using the transitional turbulence model indicates the presence of laminar separation and flow re-attachment on the blade surface. Ideally the transitional turbulence model should be used to model the flow over the blade profiles. However, as mentioned before, one of the effects of 3-dimensional boundary layer augmentation is to suppress the formation of laminar separation completely (Lindenburg 2004). The use of the much simpler and easier Xfoil is therefore justified.
4. The difference in measured and simulated drag coefficients for the Spalart Allmaras model (at $Re = 2.1 \times 10^6$) makes the author suspicious of the Spalart Allmaras model's ability to handle laminar flow regions and seems to confirm the conclusions of Rumsey and Spalart (2008) that this turbulence model should not be used in transitional flow.
5. Very little attention was paid to results obtained outside the "normal" angle of attack range of -10° and $+30^\circ$. Investigating the accuracy of results in these ranges further would be something to consider for the future.

APPENDIX D: THE PRESSURE JUMP METHOD

D.1. Introduction

The pressure jump method utilises a static-to-static pressure increase that occurs at the location of the fan rotation plane. The value of the static pressure increase is based on the value of the volume flow rate through the fan rotation plane. In his thesis on the simulation of large ACCs, van Staden (2000) describes the use of a particular fan's static pressure vs. volume flow rate curve to derive momentum source terms in the axial flow direction. Van Staden inserted the fan static pressure value as a force per area source term into the momentum equation and then proceeded to adjust the source term to obtain the desired flow rate through a single fan unit. Once the correct value of the source term had been established the fan model was applied to the simulation of a multiple fan installation.

Van der Spuy et al. (2009) explains the use of the pressure jump method (PJM) and points out that the fan static pressure values obtained from a standard BS 848 test, and often quoted by a supplier, are actually fan total-to-static pressure values and therefore require conversion to fan static-to-static pressure values. In essence the format of the fan test facility has to be considered to convert the values measured at their specific locations, regardless of whether these are total or static pressure, to static pressure values on either side of the fan's plane of rotation. The effect of the fan is added to the axial flow direction momentum equation of the rotor cell by converting the static-to-static pressure value to a momentum source term. The use of a static-to-static pressure jump to represent an axial flow fan in a multiple fan arrangement is based on the findings of Stinnes and von Backström (2002). Stinnes and von Backström tested the 1.542 m diameter B-fan at various off-axis inlet flow angles and concluded that the static-to-static pressure increase through the rotor of an axial flow fan is independent of the angle at which the flow enters the fan.

The two most notable differences between the ADM and the PJM is the fact that the PJM ignores the relationship between the fan rotor design and the distribution of the flow field that enters the fan (meaning that the axial momentum source terms predicted for the different cells would be incorrect) and the absence of any tangential momentum source terms when using the PJM. The flow field predicted by the PJM downstream of the fan rotor would therefore be incorrect. This would also be the case for reverse flow occurring through the fan rotor. This investigation is particularly concerned with the effect of inlet flow distortion on fan performance and only considers the flow rate through the test system predicted by the PJM when calculating the flow losses. In this instance in particular (and when considering flow through air-cooled heat exchangers) the absence of tangential flow components is considered negligible since the tangential velocity components are removed by the porous sheet downstream of the fan.

The PJM was used by Joubert (2010) to investigate the effect of various geometry changes on the performance of a generic 30-fan air-cooled condenser (ACC). Based on his results he was able to make various suggestions for improved performance of the generic ACC. Joubert used the same generic ACC model as used by van Rooyen (2007). Van Rooyen used the ADM to investigate individual fan performance but, due to limited computational resources, had to implement an iterative dual-model system. In the first model he solved the ACC inlet flow field using a prescribed outlet velocity distribution for the ACC after which he used this inlet flow field to solve the flow through individual fans in the ACC in his second model. A new outlet velocity distribution was therefore obtained which he used to update the first model. The availability of more computational resources meant that Joubert could model the generic ACC using a single model. Joubert includes a comparison to the results of van Rooyen in his thesis and shows that his results for overall system volumetric effectiveness correlate with those of van Rooyen to within 3%. However, Joubert indicates a 60% difference in volumetric effectiveness, calculated for specific individual fans at high wind speeds, between his results and those of van Rooyen. It is not clear whether this difference in specific fan performance should be attributed to the solution approach (the dual-model or single model) or the fan model (ADM or PJM) since the CFD models were not verified against experimental results.

D.2. Application of the Pressure Jump Model to calculate fan performance curves

D.2.1. Description

The application of the PJM is illustrated using the B-fan (see Appendix A). The basic equations used for the PJM analysis remain the same as for the ADM (see Equations B.1 to B.3). However, as mentioned in Section D.1, the PJM only makes use of an axial momentum source term (F_z). This means that the tangential and radial momentum source terms (F_θ and F_r) remain zero. To apply the PJM to a specific fan the objective is to convert the fan static pressure curve obtained in a test facility to a fan static-to-static pressure value that can be used in a CFD simulation. The pressure measurements, on which the fan static pressure curve is based, are performed using static pressure taps at the walls of the settling chamber shown in Figure B.2 while the static-to-static pressure increase in the CFD simulation occurs at the fan's plane of rotation (see Figure D.1).

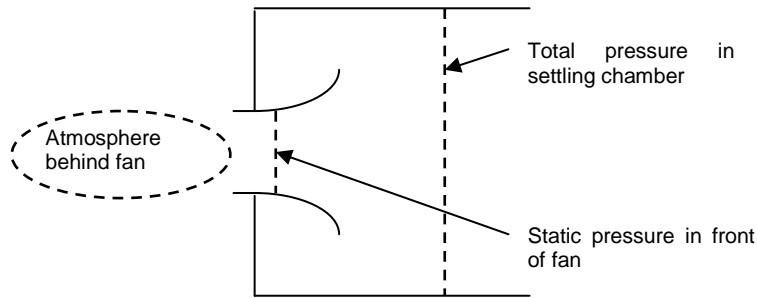


Figure D.1: Conversion between measured and simulated pressure value.

A 3rd order polynomial equation is fitted to the fan static pressure curve, as shown in Figure D.2. This equation is written as:

$$p_{sf} = -32.572V^3 + 85.114V^2 - 119.07V + 148.23 \quad (D.1)$$

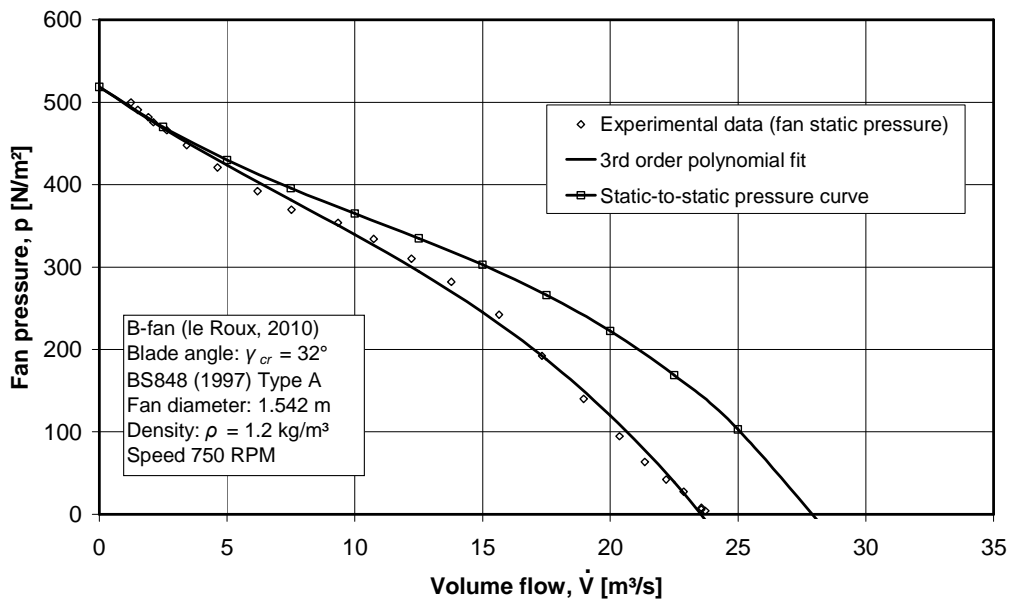


Figure D.2: Fan static pressure curve with polynomial curve fit.

For a fan tested on a BS 848 type A test facility the fan static pressure curve is actually a fan total-to-static pressure curve. However, the velocity distribution forms an integral part of the CFD solution, and as such should be excluded from the applied momentum source term. To convert the fan total-to-static pressure value to a static-to-static pressure value, the dynamic pressure component of the fan total-to-static pressure value (based on the measured volume flow rate and fan annular area) should be added to the polynomial equation, Equation D.1, as follows:

$$P_{static-to-static} = -32.572\dot{V}^3 + 85.114\dot{V}^2 - 119.07\dot{V} + 148.23 + \frac{1}{2}\rho v^2 \quad (D.2)$$

where

$$v = \frac{\dot{V}}{\pi(r_{shroud}^2 - r_{hub}^2)} \quad (D.3)$$

The static-to-static pressure value can be refined further by accounting for the bell mouth inlet losses that occur between the pressure measurement location in the inlet settling chamber and the fan rotation plane. The loss term is relatively small and may also be neglected (Joubert, 2010).

$$P_{static-to-static} = -32.572\dot{V}^3 + 85.114\dot{V}^2 - 119.07\dot{V} + 148.23 + \frac{1}{2}\rho v^2 + \frac{1}{2}\rho K_{inlet} v^2 \quad (D.4)$$

The value for K_{inlet} is obtained using Idelchik (1994). The inlet loss is given in terms of the area defined by the shroud diameter as:

$$K_{inletOD} = 0.06$$

This value is converted to reference the actual flow area as follows:

$$K_{inlet} = K_{inletOD} \frac{\pi(r_{shroud}^2 - r_{hub}^2)}{\pi r_{shroud}^2} \quad (D.5)$$

All simulations were performed using ANSYS Fluent[®], version 6.3.26 and version 12.1, finite volume CFD code. Fluent's standard "fan" boundary is applied at an inter-cell face upstream of the cell row that represents the centre of the fan plane of rotation (see Figure D.3).

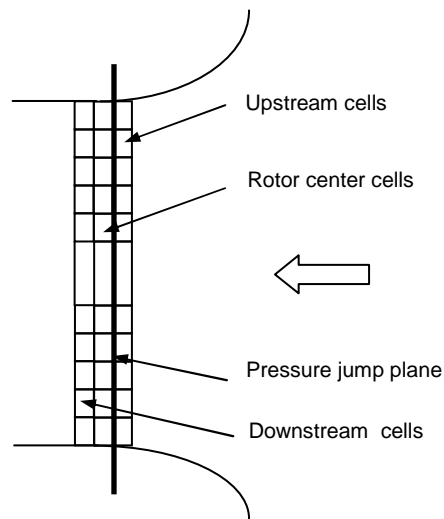


Figure D.3: Application of PJM in Fluent®.

The fan boundary condition requires the coefficients of the static-to-static pressure vs. axial velocity curve to be specified. Equation D.4 is therefore converted to a static-to-static pressure vs. velocity curve by separating the original polynomial coefficients into a velocity and flow area term as follows:

$$\begin{aligned}
 P_{static-to-static} = & -32.572A^3v^3 + 85.114A^2v^2 - 119.07Av \\
 & + 148.23 + \frac{1}{2}\rho v^2 + \frac{1}{2}\rho K_{inlet}v^2
 \end{aligned}
 \tag{D.6}$$

where the flow area is given by:

$$\begin{aligned}
 A = \pi(r_{shroud}^2 - r_{hub}^2) &= \pi(0.771^2 - 0.308^2) \\
 &= 1.569 \text{ m}^2
 \end{aligned}
 \tag{D.7}$$

Using a density of 1.2 kg/m^3 , this gives:

$$\begin{aligned}
 P_{static-to-static} = & -0.59v^3 + 6.501v^2 \\
 & - 31.272v + 148.23
 \end{aligned}
 \tag{D.8}$$

Equation D.8 is also shown in Figure D.2.

The static-to-static pressure increase in the pressure jump plane (see Figure D.3) is incorporated into the CFD simulation as a per unit-mass axial momentum source term in the cells immediately downstream of the pressure jump plane as follows:

$$F_z = \frac{P_{static-to-static} A_{cellface}}{\rho V_{cell}} \quad (D.9)$$

D.2.2. Geometry

The same geometry and mesh was used for both the PJM and the ADM simulations shown in Appendix B. The geometry that was modelled represented a standard BS 848 part 1 (2007), type A (free inlet and outlet) test facility (see Figure B.4). The lay-out of the CFD model was also the same as described in Appendix B (Figure B.5), with the only difference being that the actuator disc regions were left unspecified. Instead, the cell face upstream of the centre cell zone was specified as a fan boundary.

The same mesh used for the ADM in Appendix B was also used for the PJM.

D.2.3. Boundary conditions

The PJM was simulated using the same boundary conditions as used for the ADM in Appendix B, namely a mass flow inlet boundary and pressure outlet boundary, with zero slip walls representing the sides of the settling chamber. As mentioned in Section D.2.2 the PJM simulation required a fan boundary condition to be specified on the cell faces upstream of the cell zone that represented the rotor centre plane.

D.2.4. Solver settings

The realizable $k-\varepsilon$ turbulence model and Quick interpolation scheme were used for all simulations. The simulations were set to run a maximum of 2000 iterations or to a residual value of 10^{-4} on all governing equations. The default relaxation factors were used for all simulations (see Table B.1).

D.2.5. Results

A comparison of the simulation and test results for the B-fan is shown in Figure D.4. The simulation results are compared to B-fan test results from both le Roux (2010) and Stinnes (1998). Since the pressure jump model does not include tangential momentum source terms the torque exerted on the blade rotor and consequently the fan shaft power and static efficiency can not be calculated.

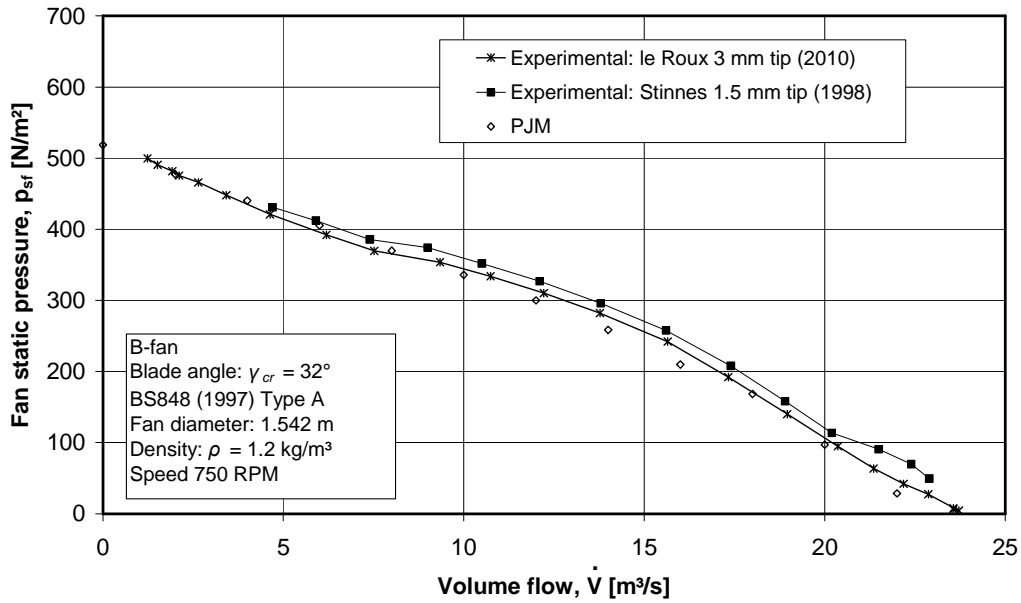


Figure D.4: Fan static pressure, B-fan

D.3. Summary

The two most notable differences between the ADM and the PJM is the fact that the PJM ignores the relationship between the fan rotor design and the distribution of the flow field that enters the fan (meaning that the axial momentum source terms predicted for the different cells would be incorrect) and the absence of any tangential momentum source terms when using the PJM. The flow field predicted by the PJM downstream of the fan rotor would therefore be incorrect. This would also be the case for reverse flow occurring through the fan rotor. The fact that no tangential momentum source terms are included in the PJM means that no estimate of fan shaft power can be obtained from simulations using this simplified model.

APPENDIX E: MULTIPLE FAN TEST FACILITY

E.1. Facility configuration

E.1.1. Layout

The facility used for this research consisted of a three fan system, as used by Conradie (2010). During individual testing of fans with a high solidity ratio (typically a ten-bladed 630 mm diameter fan), it was found that the characteristics of the flow straightener section (see Figure 3.1) would vary according to the volume flow rate at which the fan was operating. It prompted a decision to replace the straightener section with a plenum chamber incorporating a porous sheet resistance section. The dimensions of the plenum chamber (790 mm x 790 mm x 800 mm) corresponded in scale with the dimensions of the plenum chamber used by Bredell (2005), van Rooyen (2007) and Joubert (2010). The use of a plenum chamber had the following advantages:

1. Testing with a plenum chamber means that the test facility is a more realistic representation of an ACC fan installation, which also incorporates a plenum chamber.
2. The plenum chamber configuration should make a comparison with fan performance obtained from a fan tested on a BS 848 type A facility possible.
3. A numerical simulation of flow through a large area plenum chamber with a porous resistance section is more robust than a simulation of flow over the vane sections of the flow straightener. The vaned flow straightener consists of long flat plate sheets and a numerical simulation of these plates would require an accurate representation of the state of the boundary layer on both sides of these plates.

A lay-out of the facility is shown in Figure E.1. The facility included an extended pipe section between the fan rotor and the plenum chamber to accommodate the torque transducer that was installed on tunnel 3. The adjustable platform height values are shown in Figure E.1.

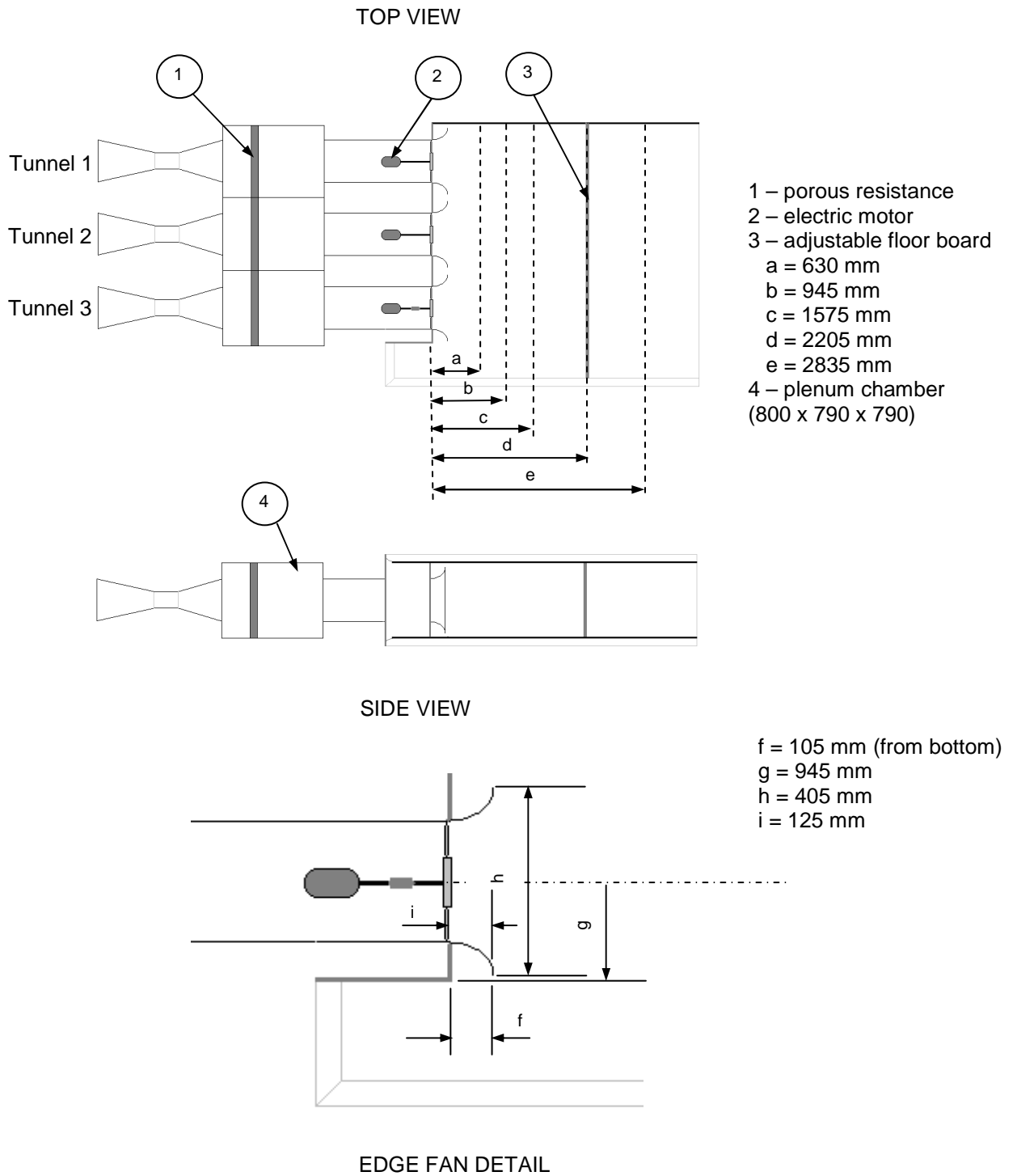


Figure E.1: Lay-out of multiple fan test facility used in this investigation.

The original facility used 200 W electric motors to drive the fans at 740 rpm (Visser, 1990), resulting in small flow rate and pressure values (0.7 m³/s and 20 Pa). To achieve higher pressure readings in the facility the running speed of the fans had to be increased and it was decided to install 4-pole, 750 W electric motors in each of the tunnels. The drive shaft of the edge fan (referred to as tunnel 3 or fan 3) was adapted to install a torque transducer between the fan rotor and the motor. This meant that the position of the electric motor was moved further downstream. Although only tunnel 3 was equipped with a torque transducer the relative motor position in each of the other two tunnels was adjusted to be identical to that of tunnel 3. The increased capacity of the new motors also meant that their diameters were slightly larger than those of the old motors. Moving the motors sufficiently downstream ensured that the size of the motors did not affect the possible occurrence of backflow in small hub diameter fans. Each of the individual fan rotors were tested in tunnel 3 with a full open inlet (excluding the inlet chamber). The flow through the test tunnel was varied using a flow throttle installed at the diffuser-end of the tunnel (see Figure E.2).

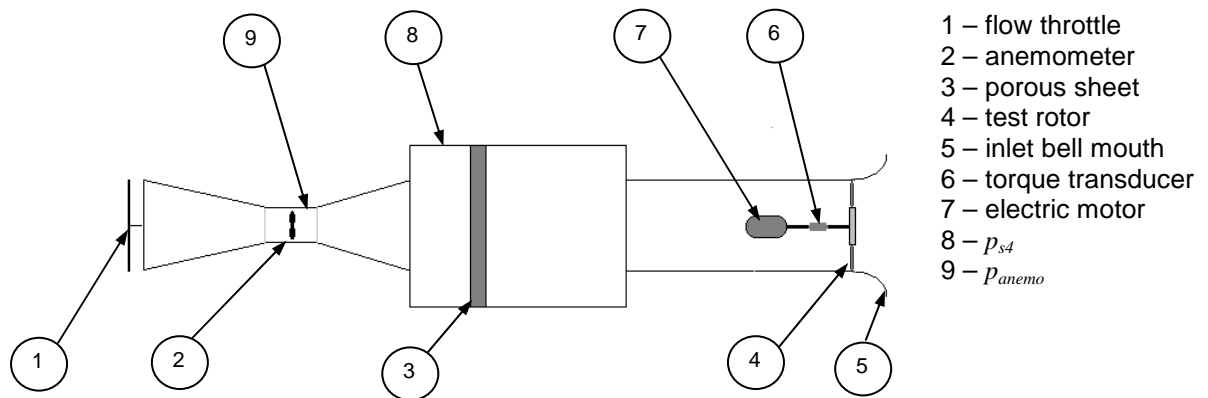


Figure E.2: Single fan test facility (including instrumentation lay-out).

The porous resistance sheets used in the plenum chambers consisted of aluminium hexcore mesh with an axial thickness of 76 mm. The hexahedral apertures were 6.35 mm across flats. To determine the flow resistance characteristics of the hexcore sheet a series of pressure loss tests were conducted inside the small wind tunnel facility of the Department of Mechanical and Mechatronic Engineering at Stellenbosch University. The resulting flow characteristic curve is shown in Figure E.3.

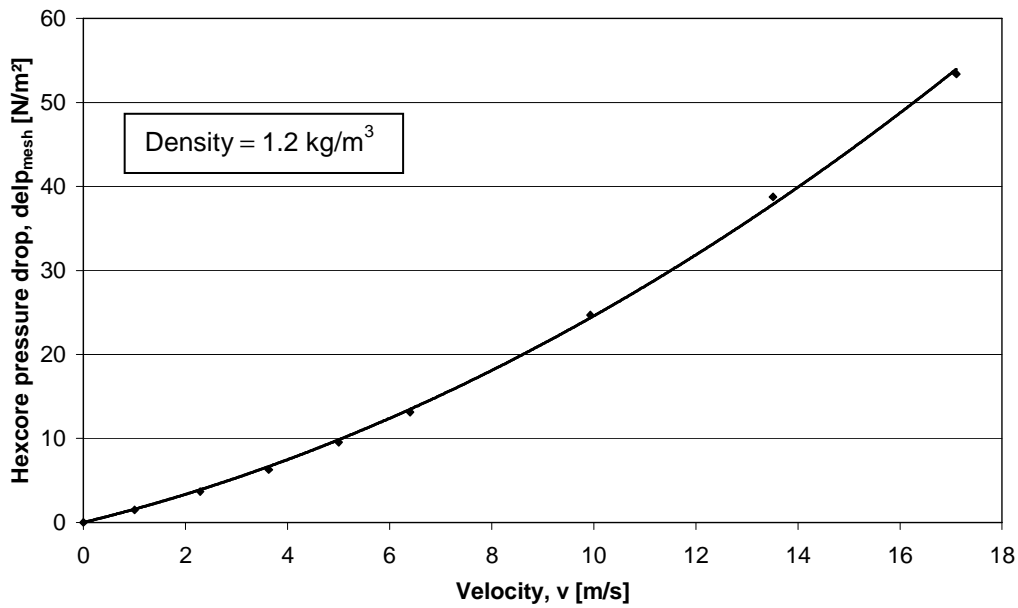


Figure E.3: Hexcore mesh flow resistance characteristic curve

The equation for mesh resistance pressure loss in terms of throughflow velocity was derived as:

$$delp_{mesh} = 0.0981v^2 + 1.4782v \quad (\text{E.1})$$

E.1.2. Instrumentation

The test facility used a rotating vane anemometer, installed in the throat of the venturi section of the tunnel, to measure the volume flow rate through the tunnel. Although Visser (1990) originally calibrated and used the venturi sections of each of the tunnels to measure the flow rate, Salta and Kröger (1995), used rotating anemometers to measure the flow rate in these tunnels. The rotating vane anemometers are small DC generators with a 0 to 10 V output.

The pressure after the porous sheet, p_{s4} , and the pressure in the venturi throat, p_{anemo} , was measured using a set of Autotran 860D pressure transducers. These transducers have a range of 0 to 1000 Pa and an output of 1 to 10 V. The pressure transducers were arranged into two banks of 5 identical transducers, each with their own 24 V / 300 mA power supply. The pressure measurement after the porous sheet was required to determine the main pressure characteristic of the fan, while the pressure in the venturi throat was measured to correlate the change in air density in the tunnel during the calibration of the anemometer. Subsequent tests

showed that the change in density due to pressure variation through the tunnel was negligible and these readings were therefore ignored.

The shaft torque between the electric motor and fan of tunnel 3 was measured using a HBM T22WN torque transducer. The torque transducer has a range of +/- 100 Nm and an output of +/- 5 V. The torque transducer has its own 12 V / 300 mA power supply.

Each of the test tunnels was equipped with a toothed wheel and 5 to 15 V magnetic pick-up to measure the rotational speed of the fans. Each of the pick-ups was connected to a Brodersen PXF-20 frequency-to-analogue converter with a 0 to 10 V output. The three frequency converters were jointly supplied by a 12 V / 1 A power supply.

All the measured signals were relayed to a National Instruments NI-6218 USB data acquisition card. The capturing of the data was controlled from a personal computer using a Labview 8.5 interface which automatically averages each channel and outputs the data in a comma separated value (CSV) format text file.

E.1.3. Calibration

A reference anemometer, along with its own bell mouth section, was calibrated on the test wind tunnel located in the laboratories of the Department of Mechanical and Mechatronic Engineering, Stellenbosch University, as detailed in Figure 5.2.1 of Kröger (2004). The calibration produced a curve showing volumetric flow rate through the anemometer vs. voltage output as follows (Conradie, 2010):

$$\dot{V} = 1.1678V_{ref\ anemo} + 3.10^{-5} \quad (E.2)$$

The reference anemometer was subsequently clamped to the diffuser-end of each of the test tunnels, along with a throttle-controlled booster fan at the outlet. The tunnel anemometers were calibrated individually while running both the test fan and the booster fan. The resulting calibration equations for the tunnel anemometers were as follows (Conradie, 2010):

$$\dot{V}_{tunnel1} = 1.3594V_{tunnelanemo1} + 0.004798 \quad (E.3)$$

$$\dot{V}_{tunnel2} = 1.3832V_{tunnelanemo2} + 0.005684 \quad (E.4)$$

$$\dot{V}_{tunnel3} = 1.3983V_{tunnelanemo3} + 0.005008 \quad (E.5)$$

The pressure transducers were calibrated using a Betz manometer. The resulting calibration equations for the pressure transducers were as follows (Conradie, 2010):

$$p_{s4tunnel1} = 111.4921V_{p1} - 99.8966 \quad (E.6)$$

$$P_{anemotunnel1} = 111.8529V_{p2} - 118.7924 \quad (E.7)$$

$$P_{s4tunnel2} = 111.2938V_{p3} - 113.4987 \quad (E.8)$$

$$P_{anemotunnel2} = 111.7340V_{p4} - 112.8226 \quad (E.9)$$

$$P_{s4tunnel3} = 111.2243V_{p5} - 114.1828 \quad (E.10)$$

$$P_{anemotunnel3} = 111.3758V_{p6} - 109.6832 \quad (E.11)$$

Each transducer is supplied with a zero offset adjustment screw so that the transducer zero offset value can be adjusted between tests without affecting the slope value. To accommodate any changes in offset value zero readings were taken before the start of any tests. The zero readings were then subtracted from all subsequent readings, taking into account any variation in offset value.

The torque transducer was calibrated using a torque calibration arm that was clamped to the front end of the drive shaft. Calibration weights were suspended from the end of the arm at a known distance from the centre of the drive shaft. The resultant torque value was then compared to the voltage read-out to obtain an equation for torque-based transducer voltage. The following equation was obtained (Conradie, 2010):

$$T_{tunnel3} = 19.9326V_{torque} + 0.790974 \quad (E.12)$$

The magnetic pick-up speed measurement devices were calibrated using a handheld tachometer. The following equations were obtained:

$$N_{tunnel1} = 246.4559V_{tunnelspeed1} - 6.3659 \quad (E.13)$$

$$N_{tunnel2} = 250.1809V_{tunnelspeed2} - 3.5475 \quad (E.14)$$

$$N_{tunnel3} = 250.9742V_{tunnelspeed3} - 1.6962 \quad (E.15)$$

E.2. Fan testing

To quantify the operation of a fan that forms part of a matrix configuration its individual, free inlet performance needs to be specified. This was determined by testing each of the fan rotors (detailed in Appendix A) using tunnel 3, as detailed in Figure E.2. The fans were tested using the same tunnel format as used in the multiple test arrangement.

E.2.1. Individual fan performance calculations

The measured data was processed using the equations detailed by the BS 848 part 1 standard (British Standard Institution, 2007), as applied by Visser (1990). Provision was made in the calculations for the use of the hexcore mesh instead of the Etoile flow straightener used by Visser.

The calibration equations detailed in Section E.2 were used to obtain values for the different performance variables as follows (showing values measured while testing the 630 mm B-fan):

Table E.1: Measured performance values for B-fan (tested on tunnel 3).

\dot{V}	[m ³ /s]	0.944
p_{s4}	[N/m ²]	98.623
p_{anemo}	[N/m ²]	34.248
N	[rpm]	1053.44
T	[Nm]	1.962

The measured ambient conditions were as follows (measured inside the laboratory where the test facility is located):

$$p_{amb} = 100500 \text{ N/m}^2$$

$$T_{amb} = 295.75 \text{ K}$$

giving:

$$\rho_{amb} = \frac{p_{amb}}{RT_{amb}} = \frac{100500}{287.08 \times 295.75} \quad (\text{E.16})$$

$$= 1.184 \text{ kg/m}^3$$

The flow rate is used to determine the average velocity inside the outlet pipe section directly after the fan (with diameter equal to 0.63 m) as follows:

$$v_2 = \frac{\dot{V}}{A_2} = \frac{0.944}{\pi \times 0.315^2} \quad (\text{E.17})$$

$$= 3.029 \text{ m/s}$$

The dynamic pressure based on the average velocity inside the outlet pipe section is calculated as follows:

$$\begin{aligned} p_{d2} &= \frac{1}{2} \rho_{amb} v_2^2 = \frac{1}{2} \times 1.184 \times 3.029^2 \\ &= 5.433 \text{ N/m}^2 \end{aligned} \quad (\text{E.18})$$

Using a viscosity of $1.78e^{-5}$ Ns/m for air at 20 °C (White, 2008), the Reynolds number for the flow in this section of pipe is given as:

$$\begin{aligned} \text{Re}_2 &= \frac{\rho_{amb} v_2 D_2}{\mu} = \frac{1.184 \times 3.029 \times 0.63}{1.78e^{-5}} \\ &= 126951 \end{aligned} \quad (\text{E.19})$$

The average velocity inside the plenum chamber section (with hydraulic diameter equal to 0.79 m) is calculated as:

$$\begin{aligned} v_3 &= \frac{\dot{V}}{A_3} = \frac{0.944}{0.79 \times 0.79} \\ &= 1.513 \text{ m/s} \end{aligned} \quad (\text{E.20})$$

The dynamic pressure inside the plenum chamber section is calculated as:

$$\begin{aligned} p_{d4} &= \frac{1}{2} \rho_{amb} v_4^2 = \frac{1}{2} \times 1.184 \times 1.513^2 \\ &= 1.355 \text{ N/m}^2 \end{aligned} \quad (\text{E.21})$$

The corresponding Reynolds number is calculated as:

$$\begin{aligned} \text{Re}_4 &= \frac{\rho_{amb} v_4 D_{h4}}{\mu} = \frac{1.184 \times 1.513 \times 0.79}{1.78e^{-5}} \\ &= 79513 \end{aligned} \quad (\text{E.22})$$

Using the correlations given in the BS 848 standards, the pressure loss in the pipe sections between the fan exit plane and the pressure measuring plane, p_{s4} , are calculated as:

$$\begin{aligned} p_{pipe} &= \left(0.1 + 0.005 + 0.42 \text{Re}_2^{-0.3}\right) p_{d2} + \left(0.005 + 0.42 \text{Re}_4^{-0.3}\right) p_{d4} \\ &= \left(0.105 + 0.42 \times 126951^{-0.3}\right) \times 5.433 + \left(0.005 + 0.42 \times 79513^{-0.3}\right) \times 1.355 \\ &= 0.664 \text{ N/m}^2 \end{aligned} \quad (\text{E.23})$$

Provision is made in the first part of equation E.23 for a sudden expansion loss factor of 0.1 (White, 2008). Using the curve shown in Figure E.3, as well as the average plenum chamber velocity calculated in equation E.21, the pressure loss over the porous sheet is given as:

$$p_{hex} = 2.439 \text{ N/m}^2$$

The fan static pressure rise is defined by BS 848 (2007) as the difference between the outlet static pressure and the inlet total pressure. Since the inlet total pressure is atmospheric, the fan static pressure can be calculated as:

$$\begin{aligned} p_{sf} &= p_{s4} + p_{pipe} + p_{hex} + p_{d3} - p_{d2} \\ &= 98.623 + 0.664 + 2.439 + 1.355 - 5.433 \\ &= 97.648 \text{ N/m}^2 \end{aligned} \quad (\text{E.24})$$

The fan shaft power is calculated using the measured rotational speed and the measured shaft torque as:

$$\begin{aligned} P_{fan} &= \frac{2\pi NT}{60} = \frac{2\pi \times 1.962 \times 1053.44}{60} \\ &= 170.816 \text{ W} \end{aligned} \quad (\text{E.25})$$

The fan scaling laws described in BS 848 (2007) were used to adjust the measured values to fixed reference values of 1000 RPM and 1.2 kg/m^3 .

$$\begin{aligned} \dot{V}' &= \dot{V} \left(\frac{N'}{N}\right) = 0.944 \left(\frac{1000}{1053.44}\right) \\ &= 0.896 \text{ m}^3/\text{s} \end{aligned} \quad (\text{E.26})$$

$$\begin{aligned} p_{sf}' &= p_{sf} \left(\frac{N'}{N}\right)^2 \left(\frac{\rho'}{\rho_{amb}}\right) = 97.648 \left(\frac{1000}{1053.44}\right)^2 \left(\frac{1.2}{1.184}\right) \\ &= 89.181 \text{ N/m}^2 \end{aligned} \quad (\text{E.27})$$

$$P_{fan}' = P_{fan} \left(\frac{N'}{N} \right)^3 \left(\frac{\rho'}{\rho_{amb}} \right) = 170.816 \left(\frac{1000}{1053.44} \right)^3 \left(\frac{1.2}{1.184} \right) \quad (\text{E.28})$$

$$= 148.089 \text{ W}$$

E.2.2. Individual fan performance curves

Individual fan performance curves showing fan static pressure rise vs. volume flow rate were compiled for each of the test fans (see Appendix A). The inherent system resistance that existed due to the configuration of the test facility, and the absence of a booster fan, meant that measurements could not be conducted down to the zero pressure rise point of the fan. However, to investigate the applicability of the performance curves of the 630 mm diameter axial flow fans, tested on the test facility described in Figure E.3, the fan performance curves of the applicable fans were compared to those of the 1.542 m diameter V-fan and B-fan described in Appendix A by scaling the results of the larger diameter fans (1.542 m, 750 RPM, 1.2 kg/m³) down to the size and speeds of the smaller fans (630 mm, 1000 RPM, 1.2 kg/m³). Both the 1.542 mm diameter fans' test results were determined on a BS 848 type A test facility. The results of these comparisons are shown in Figures E.4 and E.5.

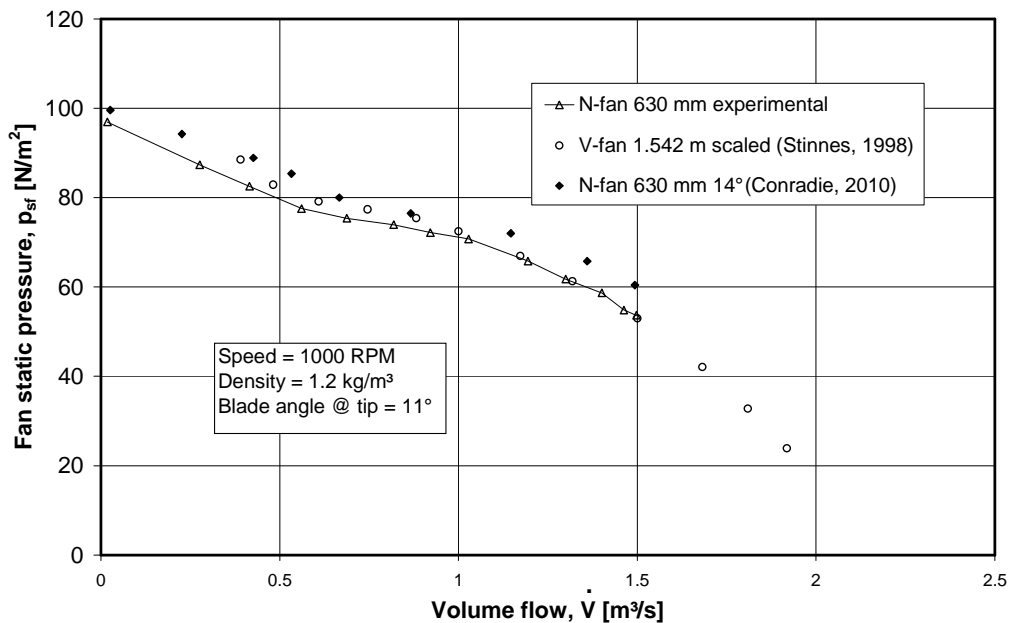


Figure E.4: Comparison of the 1.542 m diameter V-fan results to that of the 630 mm diameter N-fan.

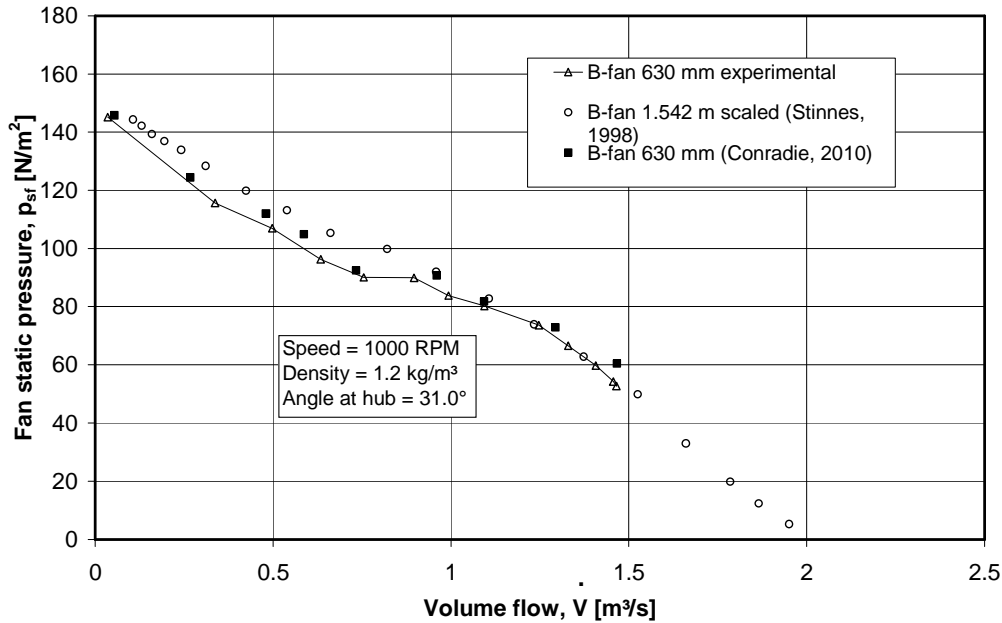


Figure E.5: Comparison of the 1.542 m diameter B-fan results to that of the 630 mm diameter B-fan.

The results show that the 630 mm diameter fans follow the curves of the larger diameter fans well at the mid flow rates (1 to 1.5 m³/s). For both fans there is a distinct difference between the larger and smaller diameter fans at lower flow rates (below 1 m³/s), with the smaller diameter fans having a fan static pressure value that is a maximum of 10% lower than the value for the larger diameter fan. The results also show good correlation with the measurements of Conradie (2010) for the B-fan which were conducted on the original tunnel format. The measurements for the N-fan were conducted at a different blade setting angle (11° compared to 14° by Conradie).

E.2.3. Multiple fan performance curves

The performance of a fan system in a multiple fan arrangement is quantified according to the volume flow rate of air being consumed by the fans, divided by the volume flow rate of air that would be consumed by the exact same fan if installed in an individual fan system arrangement with no inlet flow distortion. This quantity is referred to as the volumetric effectiveness of the fan system (Salta and Kröger, 1995). The system configuration of both the individual and multiple fan test facility has to be identical. The individual fan operating point was set according to the ACC axial flow fan design point specified by Bruneau (1994). The design point of Bruneau was specified for a density of 1.2 kg/m³, rotational speed of 750 rpm and diameter of 1.542 m and had to be scaled to a diameter of 630 mm and speed of 1000 rpm using the fan scaling laws. The individual fan operating point was therefore calculated as:

Table E.2: Fan operating point.

	Bruneau (1994)	630 mm scaled operating point	Final operating point
\dot{V} [m ³ /s]	16	1.45	1.45
p_{sf} [N/m ²]	210	62.32	56.38

The system configuration was fixed at the above flow rate of 1.45 m³/s by removing the throttle plate mentioned in Figure E.2 and installing a fixed system resistance at the tunnel outlet instead of the throttle plate (see Figure E.6). Once all the multiple fan experiments were completed, it was observed that the operating point of the fans on their fan curves was actually closer to 56.5 N/m², which would translate to 190 N/m² for a 1.542 m diameter fan. This difference was however considered negligible for the purposes of this investigation.

Two N-fans were used for the inner fans, while the edge fan was replaced with different fan configurations. The N-N-N configuration was regarded as the reference set-up, based on the fact that the N-fan is modelled from an existing large diameter ACC cooling fan (see Appendix A).

**Figure E.6: Fan test tunnel with fixed resistance at tunnel outlet.**

The fixed system performance of each of the different test fans was confirmed to be within 2% of the final operating point specified in Table E.2. The multiple fan performance of various fan configurations was tested by adjusting the platform height of the test facility and thereby increasing the level of inlet flow disturbance observed by the fan at the edge of the multiple fan arrangement. The platform heights used in the tests are shown in Figure E.1 and corresponded to those used by Visser (1990).

To obtain an indication of the performance of the 3-fan system as a whole, the results were processed and compared to the empirical correlation derived by Salta and Kröger (1995). Salta and Kröger expressed the volumetric effectiveness of the installation as a function of dimensionless platform height as follows:

$$\left(\dot{V} / \dot{V}_{ref} \right)_{system} = 0.985 - \exp(-X) \quad (E.29)$$

where X is the dimensionless platform height:

$$X = \frac{(1 + 45/n)H}{6.35D_F} \quad (E.30)$$

In the above equation, H is the platform height, n is the total number of fans per row (in other words 6 for the described 3-fan unit) and D_F is the fan shroud diameter. The reference flow rate when determining the volumetric effectiveness of the multiple fan test system was specified according to Table E.2. A comparison of the test results for the N-N-N fan configuration to the empirical correlation is shown in Figure E.7.

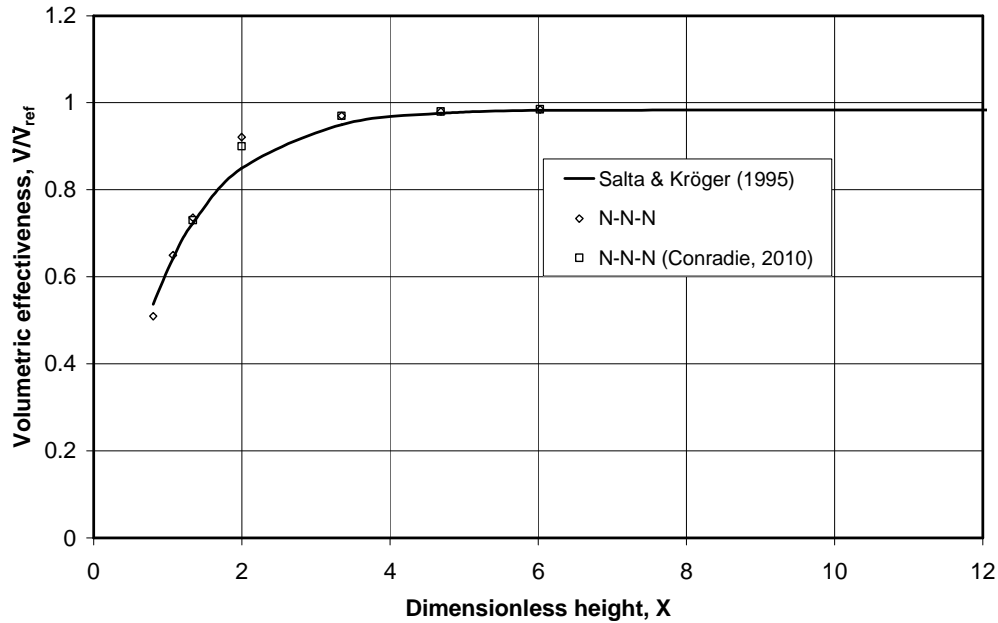


Figure E.7: Comparison of measured (N-N-N configuration) volumetric effectiveness to predicted effectiveness.

The measured system volumetric effectiveness for the N-N-N configuration corresponds well to the values predicted by the equation of Salta and Kröger, except at a dimensionless platform height of 2 (which corresponds to one fan diameter). It should be noted though that the equation of Salta and Kröger does not take fan configuration into account. The above results correlate well with the results of Conradie (2010), which were obtained on the original tunnel format.

E.3. Particle image velocimetry (PIV)

The particle image velocimetry (PIV) tests formed an integral part of the fan test sequence. The unique nature of the test equipment and - execution required it to be discussed in a separate section of this appendix. This section describes the PIV test equipment and how it was configured to suit the multiple fan test facility. The description focuses on the work that is relevant to this project. More information and background on PIV measurements may be found in the PIV manual obtained from Dantec Dynamics (2006).

E.3.1. PIV test equipment

Particle image velocimetry is used to measure the vector field of a flow stream. This is accomplished by seeding the flow with very fine particles which are then illuminated by a laser light sheet. The illumination of the particles is photographed using a high-speed digital camera. By taking two photos of the flow field in quick succession (the timing between the two photos would depend on the

prevalent velocity in the flow field) the direction and speed of change in the flow field can be observed and used to obtain the vector field. The timing of the high-speed camera coincides with the pulsing of the laser sheet and is controlled from a synchroniser unit. The processing and correlation of the photographs is a mathematically intensive software process performed on a personal computer.

A 2-dimensional flow field can be interrogated by using a single camera with its axis orientated perpendicular to the laser light sheet. By adding a second camera that is orientated at an angle to the first camera, a third dimension can be added to the vectors of the 2-dimensional flow field that is observed when using only one camera. This is referred to as stereoscopic PIV.

The PIV system used by Stellenbosch University was manufactured and distributed by Dantec Dynamics in Denmark. The system consists of the following:

- A Dual-power 200-15 double-cavity Q-switched Nd:YAG laser source. The 200 mJ laser light is passed through a filter that compresses it into a light sheet.
- Two Flowsense 4M CCD (charge coupled device), 2048 x 2048 pixel cameras, each equipped with a Nikon 60 mm lens.
- An 80N77 synchroniser unit (also referred to as the timer box) that correlates the timing of the high speed camera to the pulsing of the laser sheet.
- A personal computer, equipped with Dantec Dynamics' software suite, Dynamic Studio version 3.0, as well as three National Instruments cards. The NI PCI-6602 card is used to control the synchroniser unit, while the two NI PCIe-1427 cards are used to control the two cameras.
- A 10F03, 3 μm , seeding generator.
- A Dantec 3-axis traverse system with controller that is used to position the laser source accurately relative to the interrogation area.

The laser, cameras and traverse are all managed through the Dynamic Studio software.

E.3.2. PIV test lay-out

The PIV measurements were performed on the multiple fan test facility shown in Figure E.1. A sketch detailing the lay-out of the PIV apparatus is shown in Figure E.8.

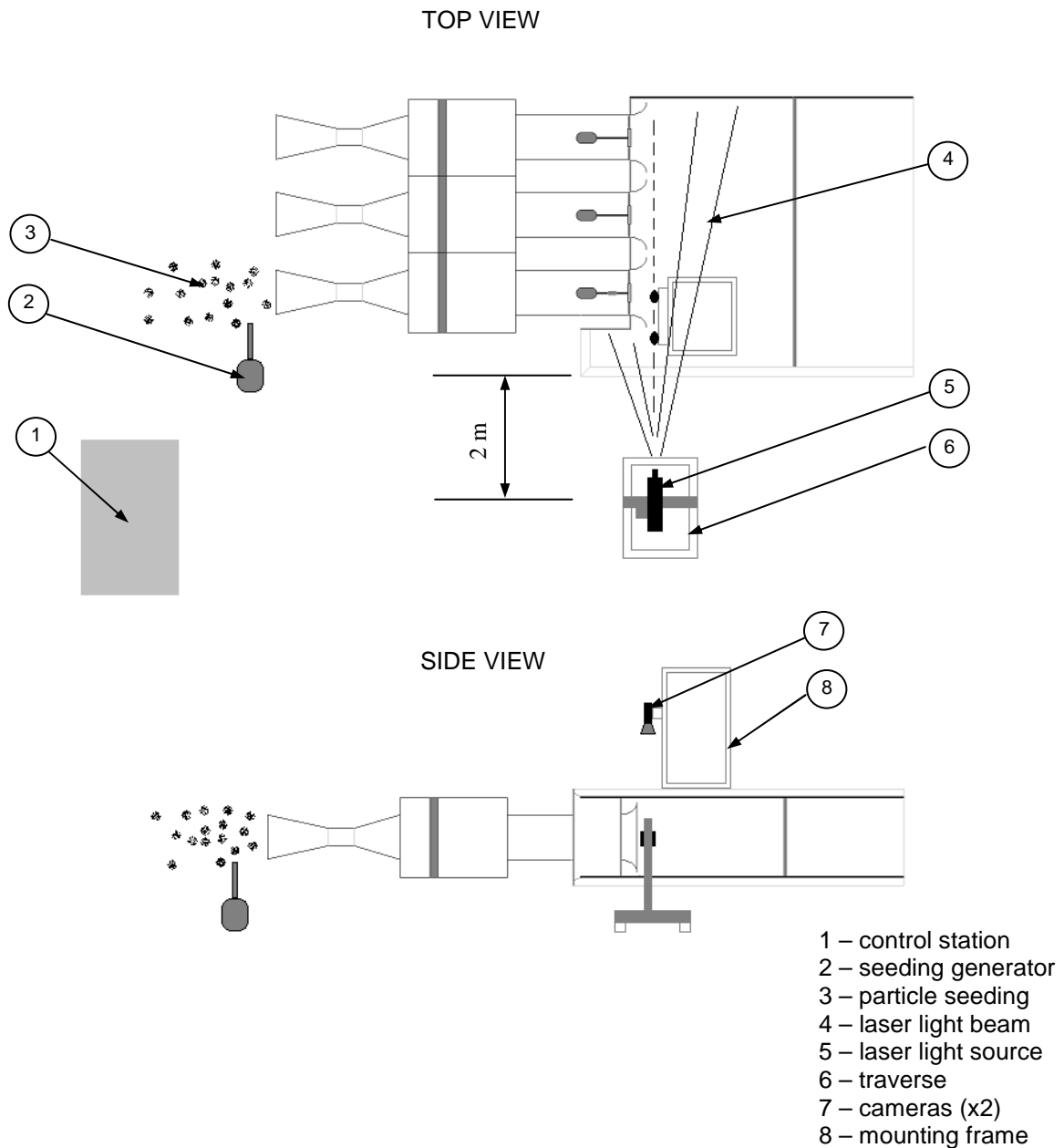


Figure E.8: PIV test lay-out.

The plane of measurement was selected to be halfway between the upper and lower sidewalls of the inlet chamber. The air was seeded by placing the seeding generator at the outlet of the edge fan tunnel. The seeding particles would

therefore circulate back through the fans and thereby seed the region upstream of the edge fan. The laser light source was placed a distance of 2 m from the side of the test facility to minimise interference with the inlet flow. The test operator was seated at the control station, along with the personal computer, synchroniser unit and data cards. The control station was placed at a distance of 6 m from the fan inlets. The following modifications of the original test facility were required to perform the PIV measurements:

1. The inclusion of a glass window through which the laser sheet could be photographed. The glass window was installed into the upper floor of the inlet chamber, viewing the inlet corner of the edge fan (see Figure E.9). The existing wooden beam structure of the test facility partially obstructed the view of the cameras on the laser sheet and after careful consideration these were removed.
2. All surfaces on the inside of the inlet chamber within a distance of 0.6 m from the fan inlets were given a coat of black paint to limit reflection of the laser light.
3. The two Flowsense cameras were installed onto a frame structure that was mounted on top of the inlet chamber in such a way that the cameras could view the interrogation area through the glass window (see Figure E.10). The position of the cameras relative to the laser light sheet meant that reflection barriers had to be installed on some parts of the facility.



Figure E.9: Glass window in upper floor of inlet chamber.



Figure E.10: PIV camera frame structure.

The proximity of the existing upper floor support beams, as well as the limited height of the camera support structure meant that the maximum area that could be photographed during one test was 400 mm x 400 mm in size. This meant that the experiment had to be subdivided into three sub-tests. For each of these sub-tests the experiment had to be set up and calibrated. The PIV calibration process requires both cameras to be focussed on a standard target (see Figure E.11). Photos of the target taken by each of the cameras are interpreted using the Dynamic Studio software to establish a matrix onto which the photos of the flow field can be fitted. The software will not interpret the photos correctly if the cameras are not focussed on the target. Since the size of the target area is known the software is able to quantify the distances that particles move once photo sequences of the flow field have been fitted onto the target. The layout of the targets used in this experiment is shown in Figure E.12.

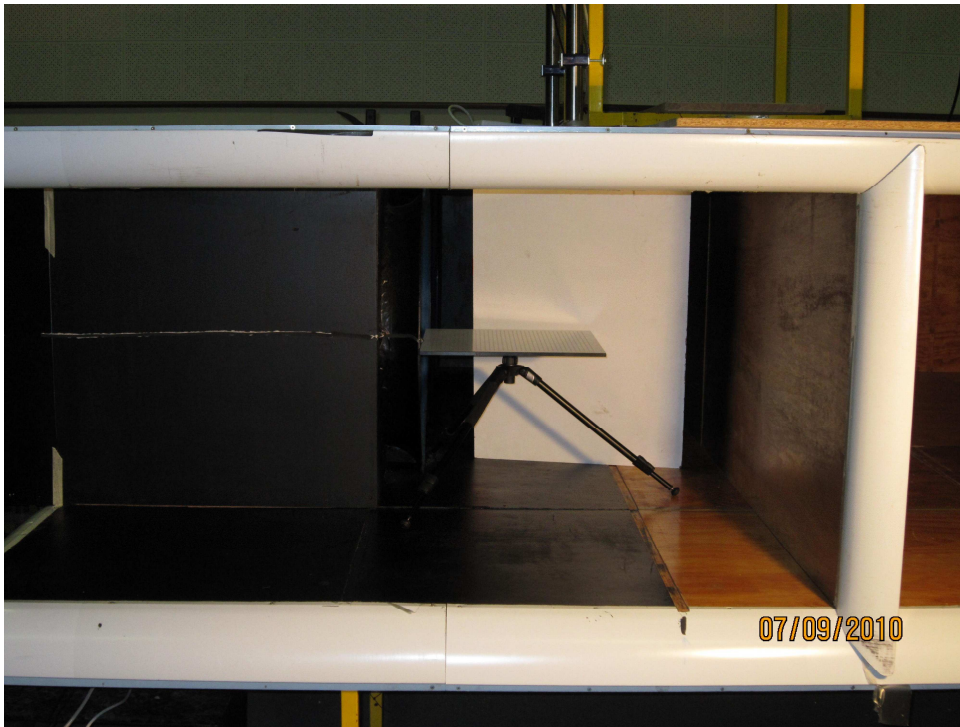


Figure E.11: PIV calibration target positioned inside facility.

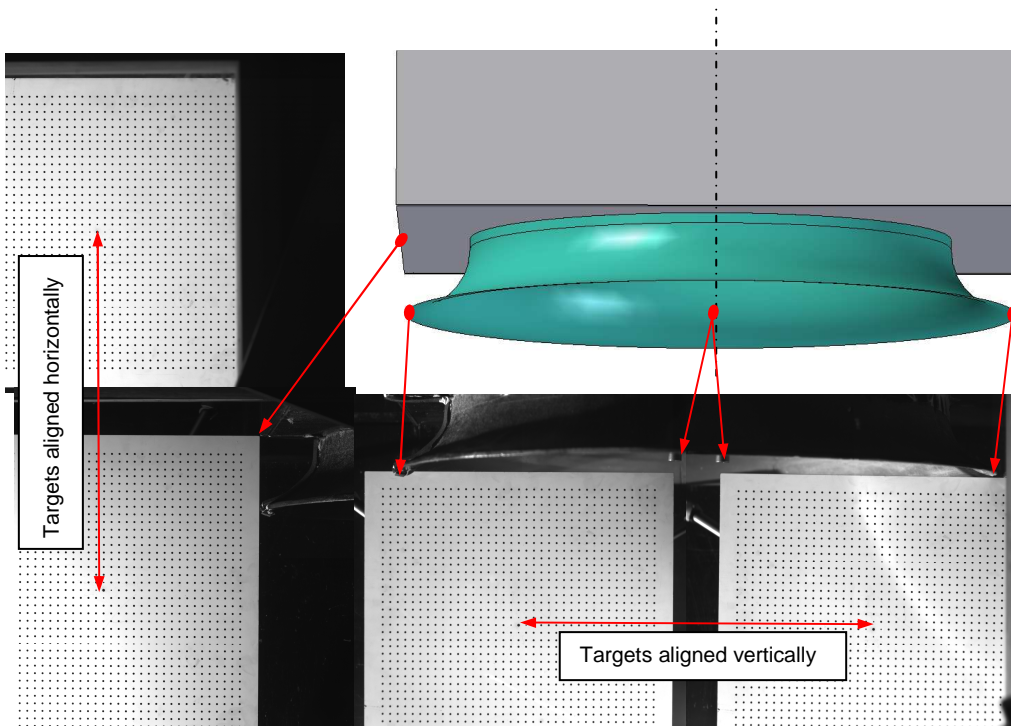


Figure E.12: Lay-out of calibration targets relative to test facility.

E.3.3. Preliminary PIV test results

A photo detailing the particle seeding in front of the edge fan is shown in Figure E.13. The photo shows two of the main problems encountered, namely the reflection of laser light onto the camera and obstruction of the view by the support beams in the facility.

The PIV images from the different sub-tests were exported into TECPLOT as *.dat files. The datasets were aligned relative to each other and then amalgamated into one image using the TECPLOT “interpolate” function. The interpolate function determines the velocity distribution at a point by interpolating the values from the 8 closest points available in the image datasets.

To illustrate the applicability of the PIV measurements a visual comparison of the inlet flow field of an edge fan is shown between 2-dimensional PIV flow field results and results from a CFD analysis using the pressure jump method (PJM) at an infinite platform height (see Figure E.14).

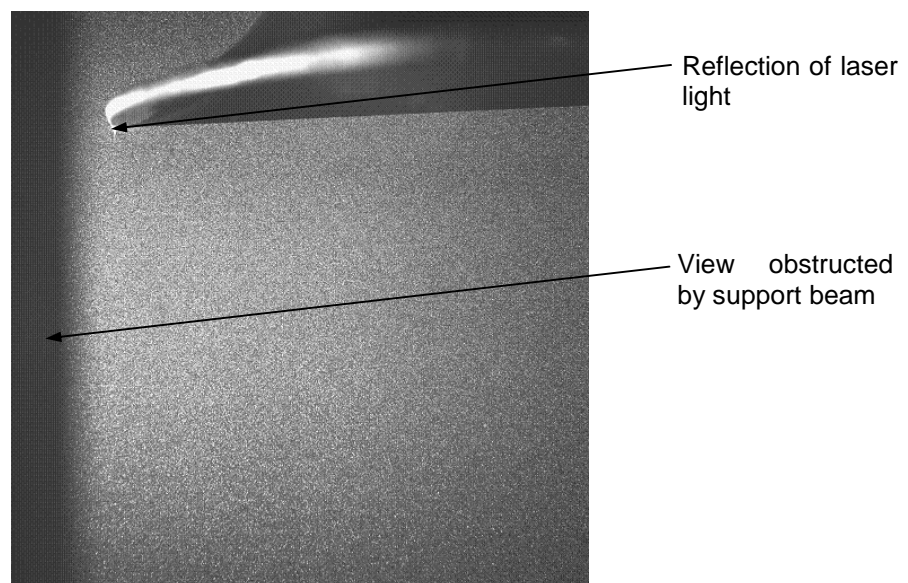


Figure E.13: Photo showing particle seeding upstream of edge fan.

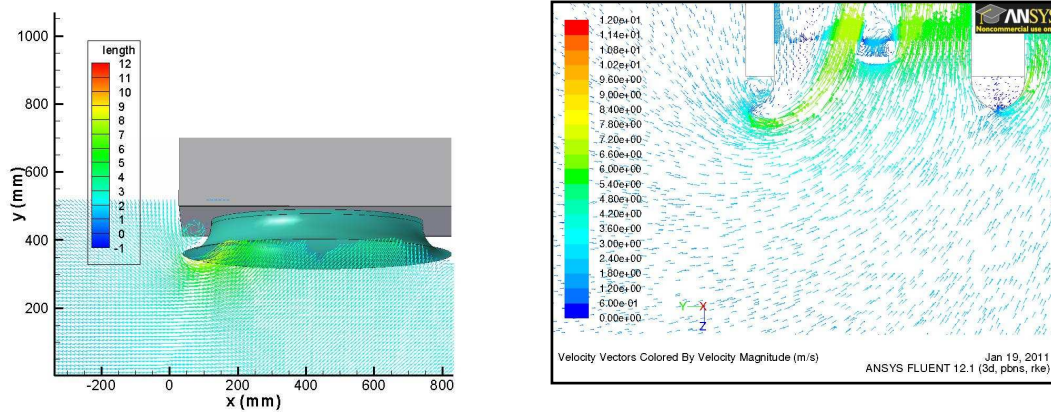


Figure E.14: 2D PIV and PJM results for inlet flow field of edge fan (N-fan configuration) with infinite floor height.

Figure E.14 shows good correlation between the PIV and CFD results.

E.3.4. Hot-film measurement comparison with PIV test results

A set of hot-film velocity measurements were performed at four specific locations to confirm the measurements of the PIV-system. The hot-film measurements were performed adjacent to the edge fan, horizontally in line with the edge of the “platform” and in line with the edge of the bell mouth, as shown in Figure E.15. The measurements were performed using a TSI IFA 100 flow analyser with a Model 1240-20 hot-film cross-probe.

All measurements were performed in the centre plane of the multiple fan test facility, as shown in Figure E.16. The measurements were performed with the B-fan in the edge fan position and with the floor at 1.0 x fan diameter and infinite fan diameter heights. Two sets of measurements were taken at all points. The atmospheric pressure and temperature during the measurements were 100 000 N/m² and 292 K respectively. The fan speed (of all 3 fans) was kept constant at 1000 RPM.

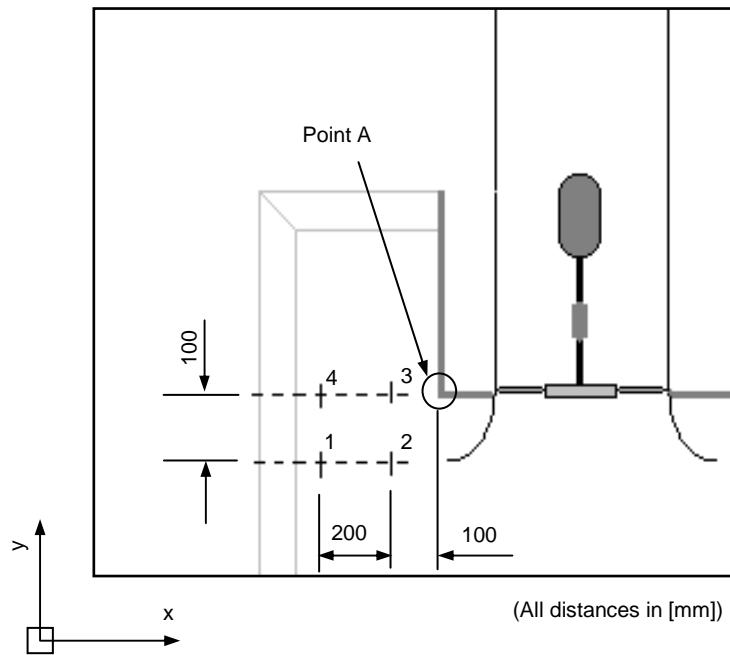


Figure E.15: Location of measuring points for hot-film measurements.



Figure E.16: Hot-film probe installed at position 4.

The hot-film results were analysed by comparing them with the 2-dimensional PIV results at the indicated measurement locations. The results are compared with velocities given according to the 2-dimensional axis system shown in Figure E.18. The location of the measurement points are referenced according to the horizontal distance from point A (see Figure E.15). Figure E.17 shows the velocity results

for points 1 and 2 at 1.0 x fan diameter platform height in the x- and y-directions respectively.

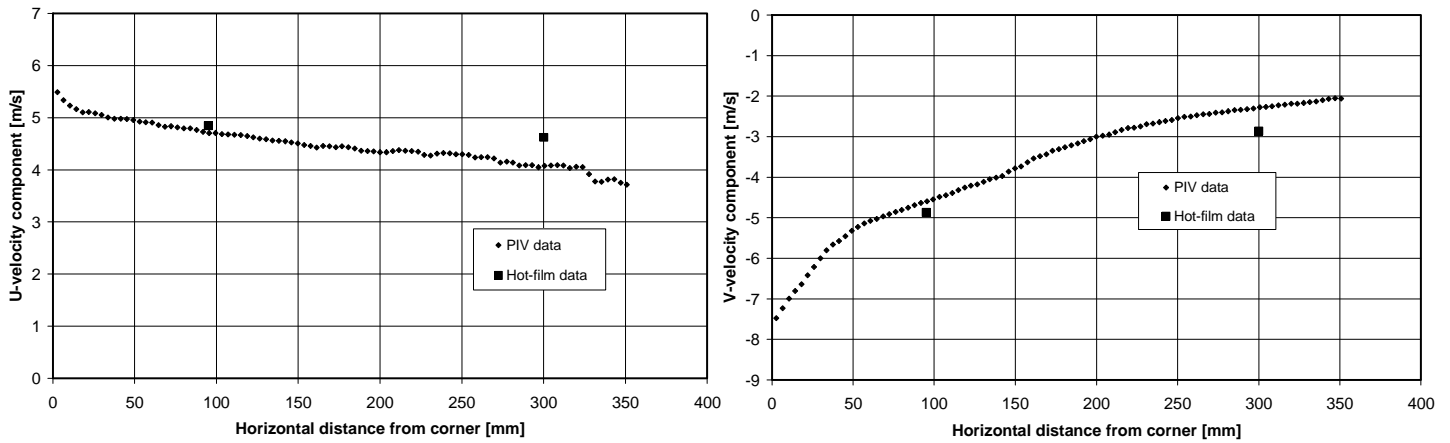


Figure E.17: Comparison of velocities for points 1 and 2 at platform height of 1.0 x fan diameter.

Figure E.18 shows the velocity results for points 3 and 4 at 1.0 x fan diameter platform height in the x- and y-directions respectively.

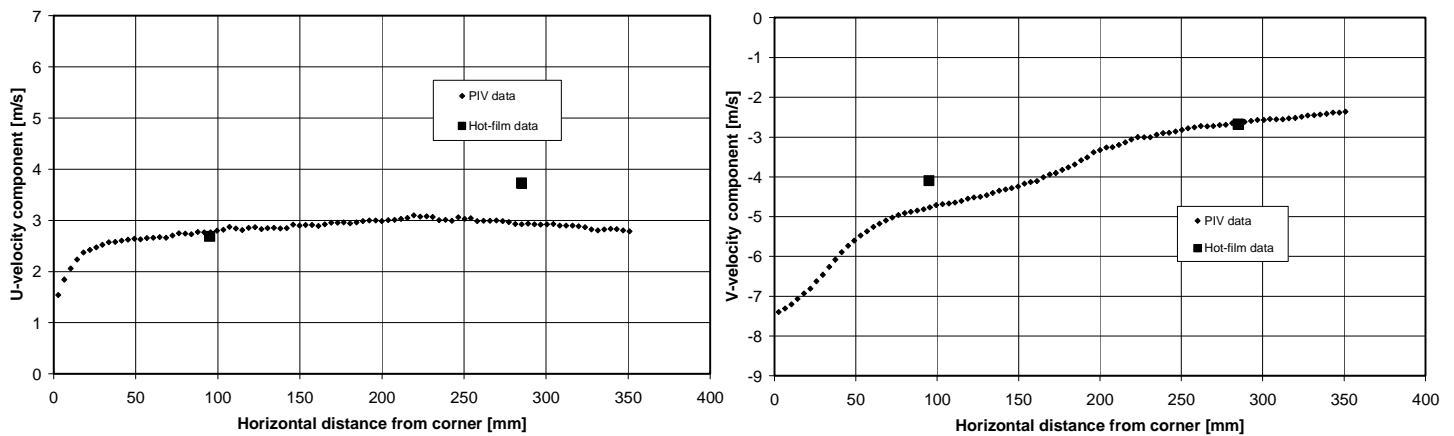


Figure E.18: Comparison of velocities for points 3 and 4 at platform height of 1.0 x fan diameter.

Figures E.19 shows the velocity results for points 1 and 2 at infinite fan diameter platform height in the x- and y-directions respectively.

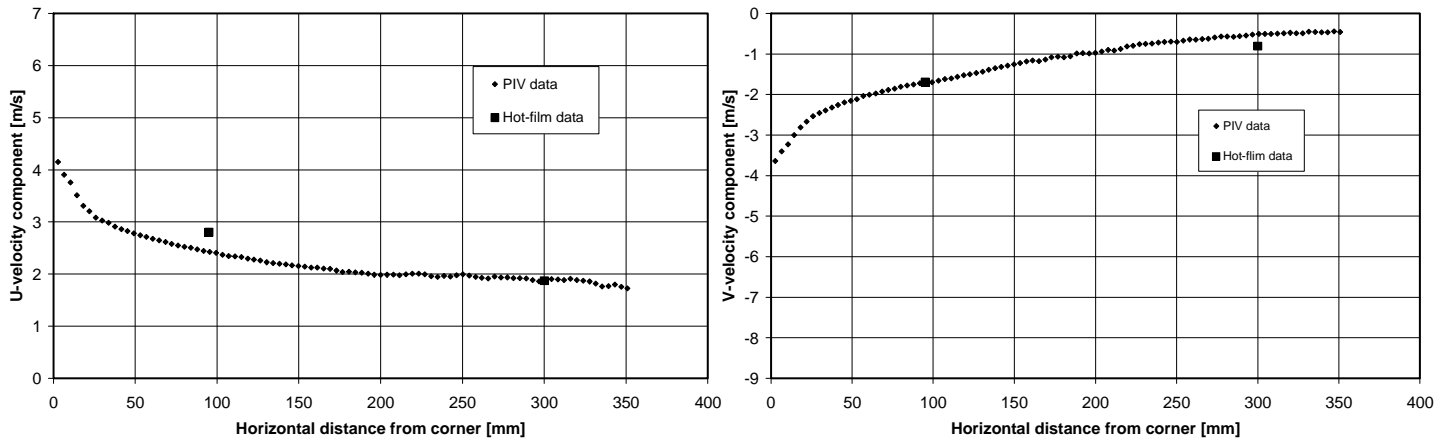


Figure E.19: Comparison of velocities for points 1 and 2 at infinite platform height.

Figures E.20 shows the velocity results for points 3 and 4 at infinite fan diameter platform height in the x- and y-directions respectively.

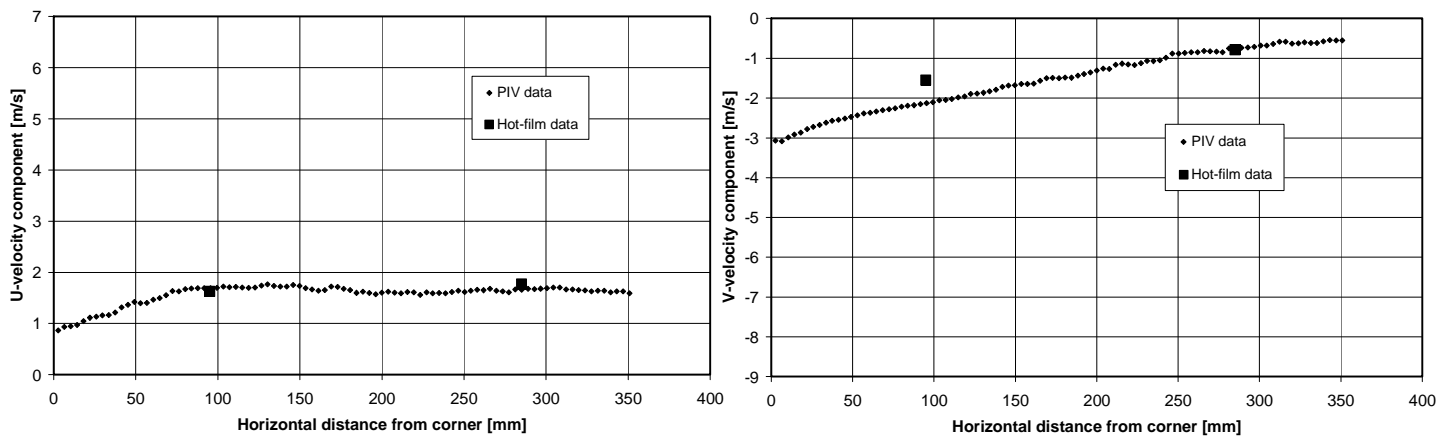


Figure E.20: Comparison of velocities for points 3 and 4 at infinite platform height.

In general the results show good correlation between the PIV and hot-film measurements. The largest difference is in the x-direction at point 4 (1.0 x fan diameter platform height) where the PIV measurements indicate a value of 3 m/s, compared to 3.8 m/s indicated by the hot-film measurement. Considering the purpose of the investigation, namely to confirm the PIV-measurements, this difference was considered negligible.

APPENDIX F: EXPERIMENTAL RESULTS

The individual and multiple fan test results are included in this appendix.

F.1. Individual fans

The data shown below for the various axial flow fans represent an average value of two sets of readings. Each reading contained in these two sets is in itself the average of five sequential readings taken at each of the throttle settings.

F.1.1. N-fan

The measured results for the N-fan are included in Table F.1 and the processed results in Table F.2.

Table F.1: Measured data for single N-fan test.

Atmospheric temperature		294.5 K	
Atmospheric pressure		100200 Pa	
\dot{V}	P_{s4}	Speed	Torque
[m ³ /s]	[Pa]	[RPM]	[Nm]
1.566	61.468	1048.846	2.152
1.545	62.634	1048.785	2.130
1.455	66.275	1048.742	2.134
1.355	69.609	1049.127	2.114
1.243	73.325	1049.193	2.063
1.076	78.041	1049.835	2.021
0.962	79.260	1050.572	1.987
0.846	80.929	1051.508	1.907
0.715	82.625	1052.406	1.819
0.581	85.210	1052.672	1.798
0.432	90.132	1052.469	1.801
0.282	95.458	1052.450	1.803
0.021	106.057	1051.558	1.847

Table F.2: Processed data for single N-fan test.

Reference speed		1000 RPM							
Reference density		1.2 kg/m ³							
Measured density		1.186 kg/m ³							
P_{d2}	P_{d4}	P_{minor}	P_{hex}	P_{t2}	P_{fs}	Shaft power	\dot{V}	P_{fs}'	Shaft power'
[Pa]	[Pa]	[Pa]	[Pa]	[Pa]	[Pa]	[W]	[m ³ /s]	[Pa]	[W]
14.963	3.733	4.039	4.249	73.490	58.526	190.929	1.493	53.844	167.468
14.558	3.632	3.930	4.184	74.380	59.822	188.517	1.473	55.043	165.403
12.926	3.225	3.493	3.912	76.905	63.980	188.965	1.388	58.873	165.805
11.208	2.796	3.032	3.614	79.051	67.843	186.851	1.292	62.383	163.761
9.428	2.352	2.554	3.285	81.516	72.088	181.285	1.185	66.278	158.858
7.060	1.761	1.917	2.808	84.527	77.467	176.739	1.025	71.136	154.591
5.647	1.409	1.536	2.491	84.696	79.050	173.146	0.916	72.487	151.131
4.364	1.089	1.190	2.173	85.380	81.017	164.494	0.804	74.159	143.187
3.119	0.778	0.853	1.823	86.079	82.960	154.924	0.679	75.808	134.529
2.059	0.514	0.566	1.470	87.760	85.701	152.657	0.552	78.274	132.459
1.141	0.285	0.315	1.087	91.819	90.678	152.863	0.411	82.851	132.725
0.487	0.122	0.136	0.706	96.422	95.934	153.191	0.268	87.657	132.997
0.003	0.001	0.001	0.051	106.109	106.106	157.836	0.020	97.115	137.361

The fan static pressure and shaft power vs. volume flow rate curves are shown in Figures F.1 and F.2.

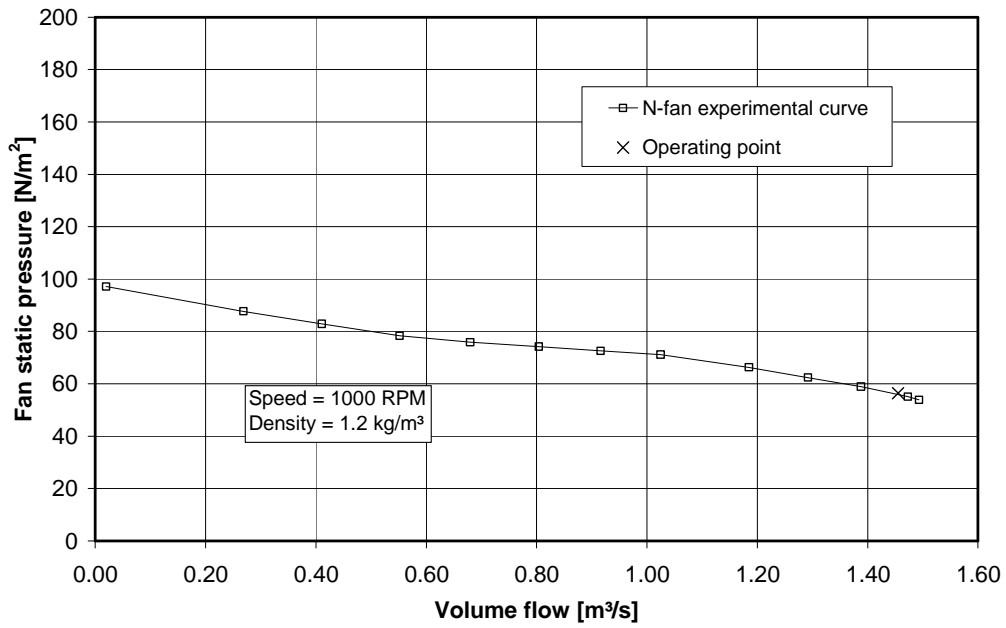


Figure F.1: N-fan fan static pressure curve.

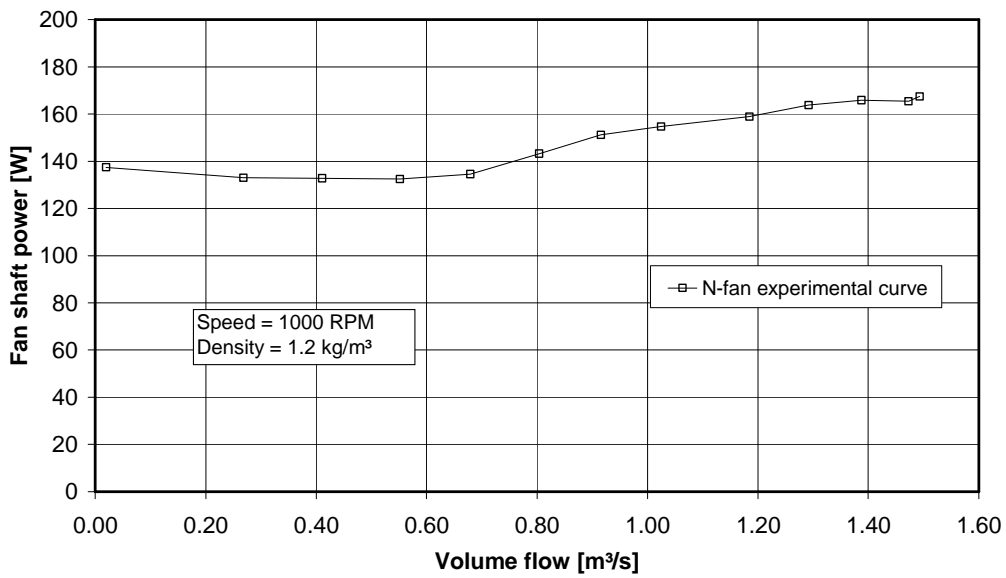


Figure F.2: N-fan fan shaft power curve.

F.1.2. 630 mm diameter B-fan

The measured results for the 630 mm diameter B-fan are included in Table F.3 and the processed results in Table F.4.

Table F.3: Measured data for single B-fan test.

Atmospheric temperature		295.8 K	
Atmospheric pressure		99950 Pa	
\dot{V}	P_{s4}	Speed	Torque
[m ³ /s]	[Pa]	[RPM]	[Nm]
1.551	60.286	1053.689	1.940
1.537	62.721	1053.617	1.854
1.481	68.635	1053.057	1.964
1.404	73.797	1052.851	1.959
1.305	80.397	1052.696	2.011
1.155	88.434	1052.628	1.954
1.047	92.011	1053.057	1.974
0.939	97.563	1053.294	1.927
0.800	98.023	1054.301	1.884
0.659	105.151	1053.851	1.909
0.519	116.945	1053.295	1.897
0.342	125.873	1053.302	1.959
0.035	156.172	1047.769	2.247

Table F.4: Processed data for single B-fan test.

Reference speed		1000 RPM							
Reference density		1.2 kg/m ³							
Measured density		1.178 kg/m ³							
P_{d2}	P_{d4}	P_{minor}	P_{hex}	P_{r2}	P_{fs}	Shaft power	\dot{V}'	P_{fs}'	Shaft power'
[Pa]	[Pa]	[Pa]	[Pa]	[Pa]	[Pa]	[W]	[m ³ /s]	[Pa]	[W]
14.584	3.638	3.937	4.172	72.034	57.449	168.485	1.472	52.730	146.757
14.317	3.572	3.866	4.128	74.287	59.970	158.984	1.459	55.052	138.509
13.288	3.315	3.590	3.959	79.499	66.211	171.007	1.406	60.845	149.233
11.944	2.980	3.230	3.729	83.736	71.792	170.412	1.334	66.001	148.805
10.318	2.574	2.793	3.439	89.204	78.885	176.103	1.240	72.541	153.832
8.079	2.016	2.192	3.009	95.649	87.570	169.783	1.097	80.540	148.348
6.639	1.656	1.804	2.706	98.177	91.538	172.086	0.994	84.121	150.168
5.343	1.333	1.454	2.410	102.760	97.418	166.990	0.891	89.482	145.625
3.875	0.967	1.058	2.035	102.083	98.207	162.395	0.759	90.035	141.217
2.629	0.656	0.720	1.662	108.189	105.560	165.077	0.625	96.860	143.728
1.632	0.407	0.449	1.301	119.102	117.470	163.592	0.493	107.900	142.668
0.709	0.177	0.197	0.851	127.098	126.389	170.429	0.325	116.092	148.631
0.008	0.002	0.002	0.087	156.264	156.256	201.139	0.034	145.049	178.198

The fan static pressure and shaft power vs. volume flow rate curves are shown in Figures F.3 and F.4.

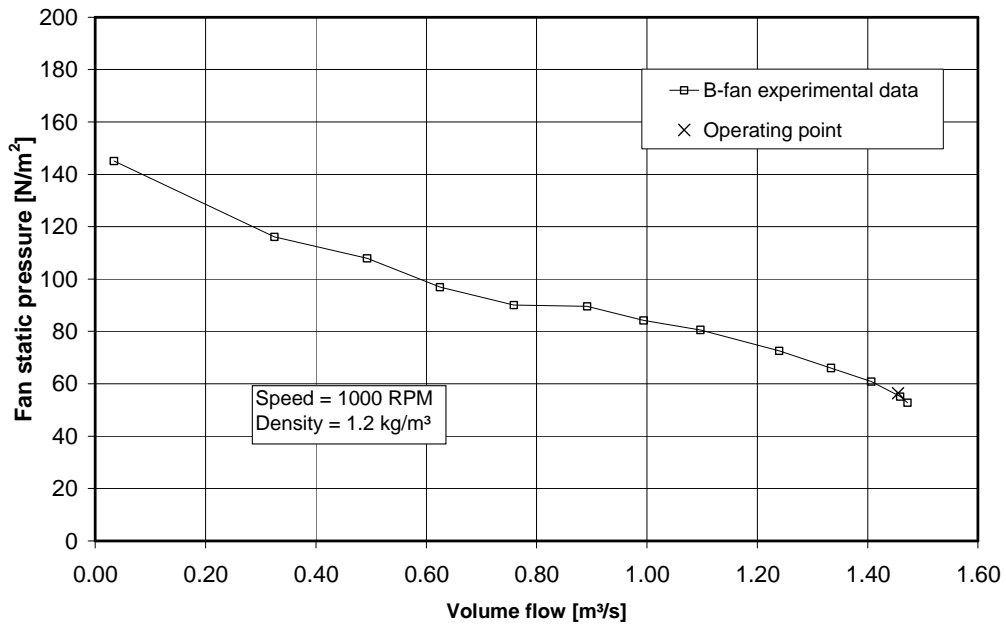


Figure F.3: B-fan fan static pressure curve.

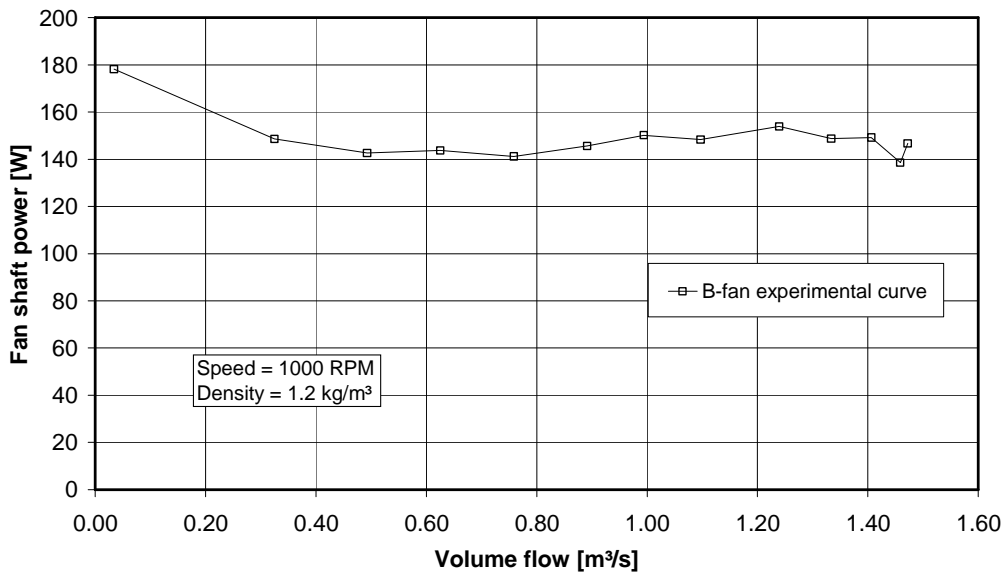


Figure F.4: B-fan fan shaft power curve.

F.1.3. H5-fan

The measured results for the 5-bladed H-fan are included in Table F.5 and the processed results in Table F.6.

Table F.5: Measured data for H5-fan test.

Atmospheric temperature		296.6 K	
Atmospheric pressure		99900 Pa	
\dot{V}	P_{s4}	Speed	Torque
[m ³ /s]	[Pa]	[RPM]	[Nm]
1.570	60.868	1054.417	1.962
1.542	63.290	1054.265	1.971
1.468	67.277	1054.262	1.952
1.370	71.505	1054.614	1.978
1.262	75.253	1054.971	1.961
1.101	81.923	1055.370	1.874
0.997	85.058	1056.056	1.813
0.876	86.918	1057.189	1.723
0.753	90.329	1058.293	1.621
0.617	95.133	1058.774	1.584
0.474	102.585	1058.838	1.635
0.313	108.792	1059.120	1.604
0.032	128.086	1056.717	1.820

Table F.6: Processed data for H5-fan test.

Reference speed		1000 RPM							
Reference density		1.2 kg/m ³							
Measured density		1.174 kg/m ³							
P_{d2}	P_{d4}	P_{minor}	P_{hex}	P_{l2}	P_{fs}	Shaft power	\dot{V}	P_{fs}'	Shaft power'
[Pa]	[Pa]	[Pa]	[Pa]	[Pa]	[Pa]	[W]	[m ³ /s]	[Pa]	[W]
14.897	3.716	4.021	4.214	72.820	57.923	170.992	1.489	53.263	149.119
14.358	3.582	3.877	4.127	74.876	60.519	171.924	1.462	55.666	149.997
13.012	3.246	3.516	3.905	77.944	64.933	169.868	1.392	59.726	148.202
11.342	2.830	3.068	3.617	81.020	69.678	172.837	1.299	64.048	150.647
9.621	2.400	2.606	3.304	83.563	73.942	170.967	1.196	67.922	148.867
7.320	1.826	1.987	2.847	88.584	81.264	161.397	1.043	74.591	140.372
6.002	1.497	1.632	2.560	90.747	84.745	154.773	0.944	77.685	134.342
4.630	1.155	1.262	2.231	91.565	86.935	144.986	0.828	79.522	125.443
3.426	0.855	0.936	1.905	94.025	90.599	133.820	0.712	82.700	115.415
2.298	0.573	0.631	1.548	97.885	95.587	129.754	0.583	87.174	111.762
1.356	0.338	0.374	1.181	104.478	103.122	135.394	0.447	94.035	116.604
0.592	0.148	0.165	0.775	109.880	109.288	132.029	0.296	99.604	113.610
0.006	0.002	0.002	0.077	128.167	128.161	155.681	0.030	117.337	134.901

The fan static pressure and shaft power vs. volume flow rate curves are shown in Figures F.5 and F.6.

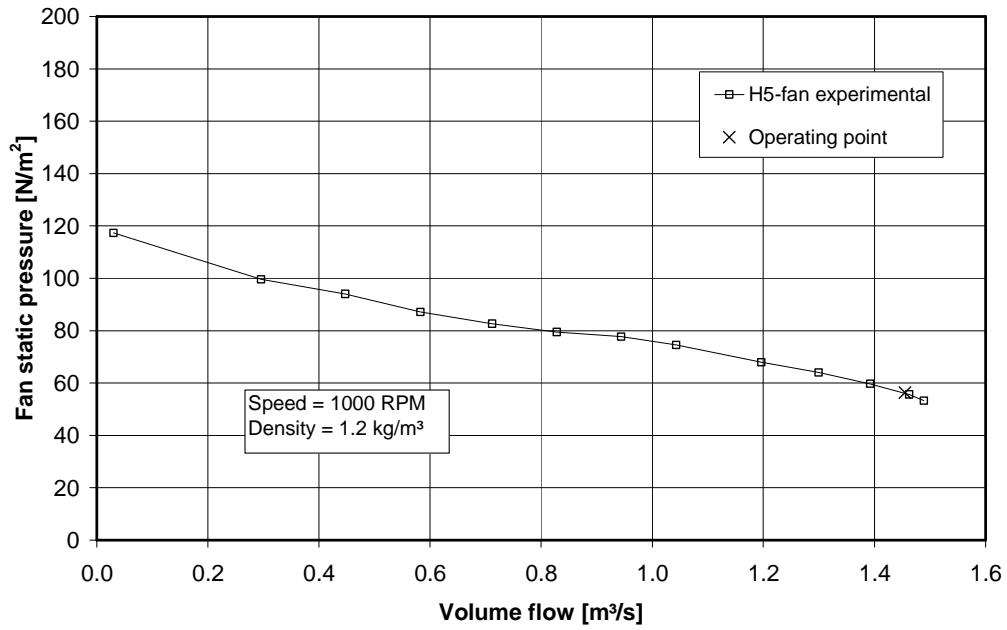


Figure F.5: H5-fan fan static pressure curve.

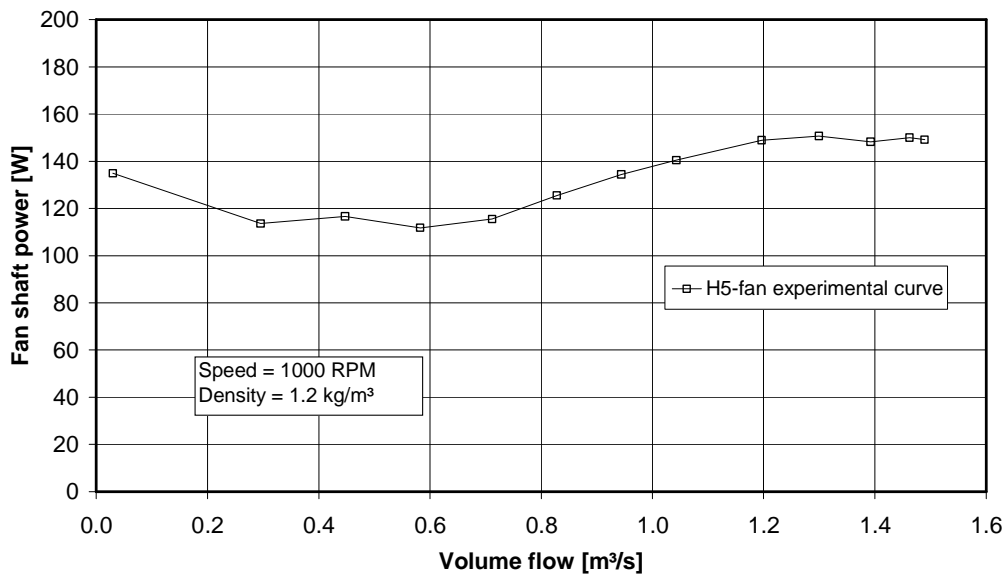


Figure F.6: H5-fan fan shaft power curve.

F.1.4. H10-fan

The measured results for the 10-bladed H-fan are included in Table F.7 and the processed results in Table F.8.

Table F.7: Measured data for H10-fan test.

Atmospheric temperature		294.5 K	
Atmospheric pressure		99900 Pa	
\dot{V}	P_{s4}	Speed	Torque
[m ³ /s]	[Pa]	[RPM]	[Nm]
1.550	58.382	1051.510	2.054
1.533	61.131	1050.962	2.060
1.488	67.947	1050.115	2.102
1.413	75.148	1049.415	2.136
1.320	82.967	1048.805	2.169
1.197	95.251	1048.314	2.203
1.100	101.404	1048.499	2.158
0.991	108.481	1048.711	2.144
0.866	116.709	1049.387	2.125
0.714	124.504	1051.011	2.003
0.551	137.153	1051.610	1.937
0.376	153.943	1052.061	1.955
0.048	182.484	1054.051	1.855

Table F.8: Processed data for H10-fan test.

Reference speed		1000 RPM							
Reference density		1.2 kg/m ³							
Measured density		1.186 kg/m ³							
P_{d2}	P_{d4}	P_{minor}	P_{hex}	P_{t2}	P_{fs}	Shaft power	\dot{V}	P_{fs}'	Shaft power'
[Pa]	[Pa]	[Pa]	[Pa]	[Pa]	[Pa]	[W]	[m ³ /s]	[Pa]	[W]
14.486	3.614	2.173	4.144	68.313	53.827	180.677	1.474	49.854	159.144
14.162	3.533	2.125	4.092	70.880	56.718	181.239	1.458	52.587	159.890
13.357	3.332	2.006	3.959	77.245	63.888	185.664	1.417	59.330	164.189
12.044	3.005	1.811	3.737	83.700	71.656	189.341	1.347	66.633	167.776
10.504	2.621	1.583	3.464	90.634	80.130	192.800	1.258	74.599	171.140
8.635	2.154	1.305	3.111	101.822	93.187	196.452	1.142	86.836	174.627
7.297	1.820	1.105	2.840	107.170	99.873	191.550	1.049	93.034	170.179
5.928	1.479	0.901	2.540	113.401	107.473	190.101	0.945	100.073	168.789
4.519	1.127	0.690	2.200	120.726	116.207	188.131	0.825	108.066	166.717
3.077	0.768	0.473	1.799	127.543	124.466	174.975	0.680	115.389	154.341
1.832	0.457	0.284	1.376	139.270	137.438	167.764	0.524	127.270	147.729
0.853	0.213	0.134	0.932	155.222	154.368	169.824	0.358	142.825	149.349
0.014	0.004	0.002	0.118	182.608	182.594	159.099	0.046	168.303	139.128

The fan static pressure and shaft power vs. volume flow rate curves are shown in Figures F.7 and F.8.

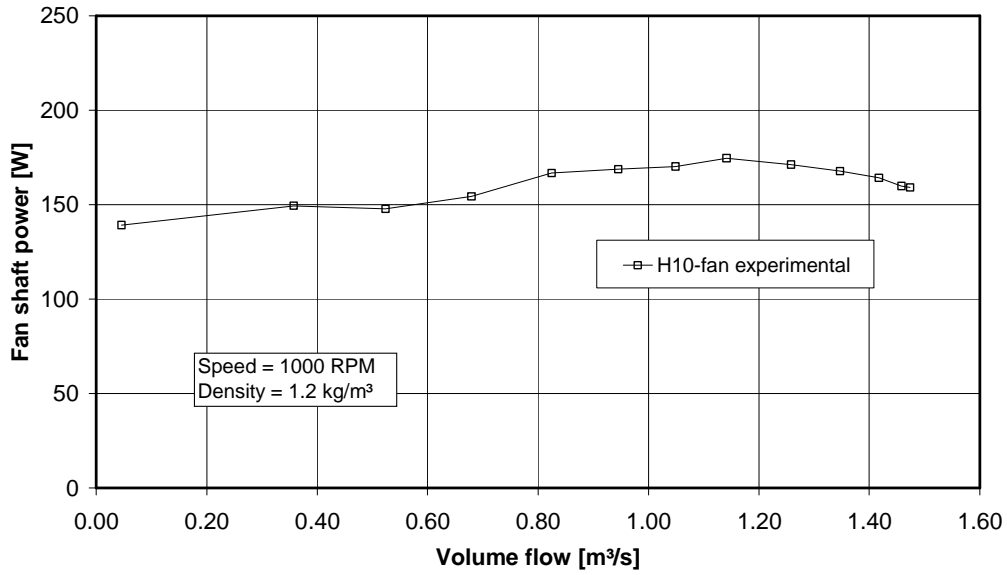


Figure F.7: H10-fan fan static pressure curve.

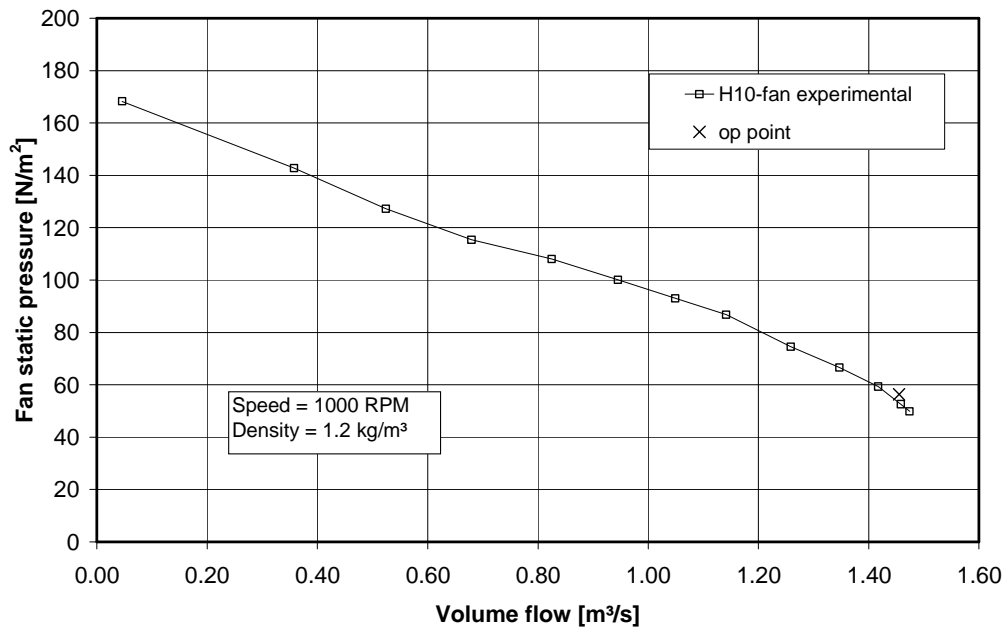


Figure F.8: H10-fan fan shaft power curve.

F.1.5. H7-fan

The measured results for the 7-bladed H-fan are included in Table F.9 and the processed results in Table F.10.

Table F.9: Measured data for H7-fan test.

Atmospheric temperature		294.5 K	
Atmospheric pressure		100200 Pa	
\dot{V}	P_{s4}	Speed	Torque
[m ³ /s]	[Pa]	[RPM]	[Nm]
1.574	60.095	1051.509	2.118
1.554	62.105	1051.108	2.124
1.482	67.968	1050.567	2.152
1.394	73.953	1050.193	2.174
1.302	80.994	1049.853	2.112
1.165	90.555	1049.854	2.126
1.065	96.091	1050.263	2.074
0.950	101.544	1051.031	2.028
0.816	106.367	1052.477	1.980
0.670	111.752	1054.255	1.831
0.527	125.426	1054.373	1.851
0.362	139.620	1055.359	1.723
0.044	170.206	1058.121	1.681

Table F.10: Processed data for H7-fan test.

Reference speed		1000 RPM							
Reference density		1.2 kg/m ³							
Measured density		1.186 kg/m ³							
P_{d2}	P_{d4}	P_{minor}	P_{hex}	P_{I2}	P_{fs}	Shaft power	\dot{V}	P_{fs}'	Shaft power'
[Pa]	[Pa]	[Pa]	[Pa]	[Pa]	[Pa]	[W]	[m ³ /s]	[Pa]	[W]
14.794	3.691	3.994	4.172	71.951	57.158	187.677	1.497	53.438	166.871
14.422	3.598	3.895	4.112	73.710	59.287	188.254	1.478	55.472	167.572
13.123	3.274	3.546	3.900	78.688	65.565	191.293	1.411	61.408	170.541
11.599	2.894	3.138	3.640	83.624	72.025	193.669	1.327	67.507	172.843
10.128	2.527	2.743	3.377	89.641	79.512	186.769	1.240	74.573	166.849
8.110	2.023	2.200	2.992	97.771	89.660	188.270	1.110	84.090	168.189
6.779	1.691	1.842	2.716	102.339	95.561	182.589	1.014	89.555	162.924
5.390	1.345	1.467	2.403	106.759	101.369	177.754	0.904	94.859	158.260
3.980	0.993	1.086	2.048	110.494	106.514	172.637	0.776	99.400	153.074
2.681	0.669	0.734	1.667	114.822	112.142	156.458	0.635	104.299	138.026
1.660	0.414	0.457	1.302	127.599	125.939	158.753	0.500	117.105	140.005
0.783	0.195	0.217	0.888	140.920	140.138	144.682	0.343	130.064	127.238
0.012	0.003	0.003	0.108	170.320	170.308	140.500	0.042	157.242	122.595

The fan static pressure and shaft power vs. volume flow rate curves are shown in Figures F.9 and F.10.

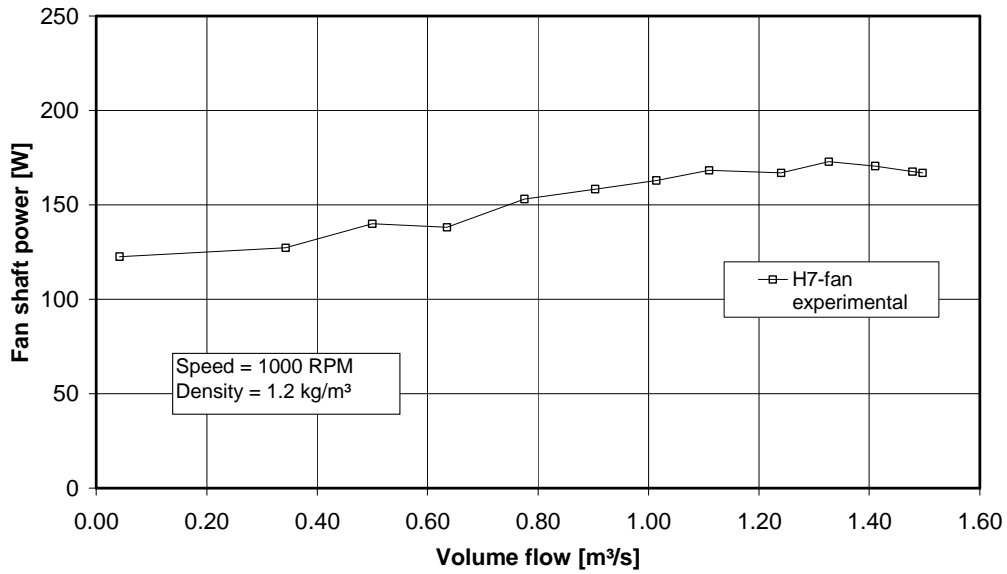


Figure F.9: H7-fan fan static pressure curve.

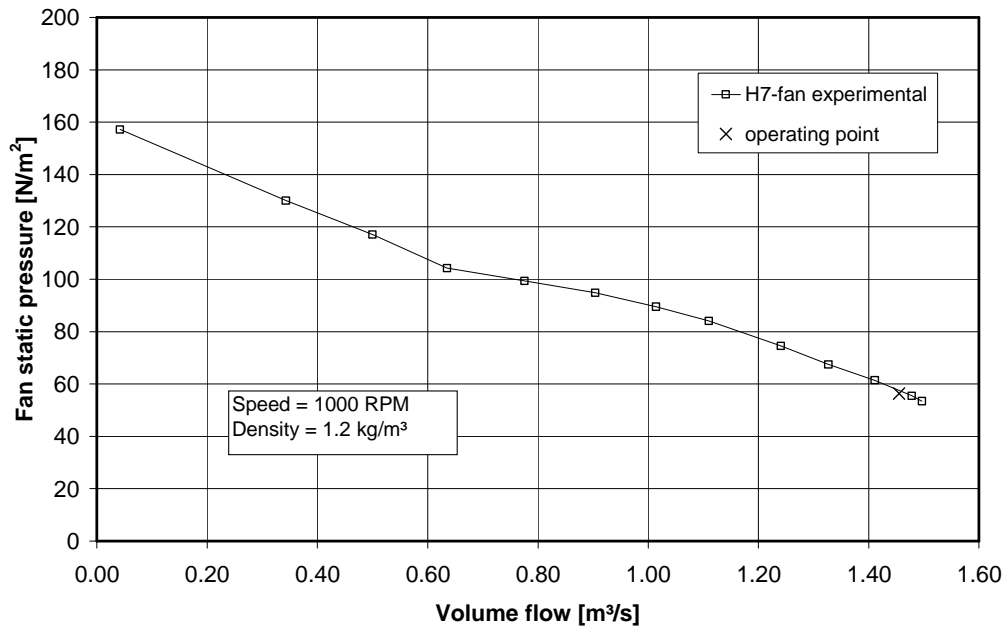


Figure F.10: H7-fan fan shaft power curve.

F.1.6. H14-fan

The measured results for the 14-bladed H-fan are included in Table F.11 and the processed results in Table F.12.

Table F.11: Measured data for H14-fan test.

Atmospheric temperature		294.5 K	
Atmospheric pressure		100200 Pa	
\dot{V}	P_{s4}	Speed	Torque
[m ³ /s]	[Pa]	[RPM]	[Nm]
1.526	58.924	1044.616	2.334
1.513	61.775	1044.043	2.496
1.477	69.013	1043.218	2.489
1.421	76.215	1042.204	2.572
1.355	86.444	1041.051	2.294
1.254	103.366	1039.042	2.678
1.171	113.142	1038.427	2.764
1.062	122.829	1038.117	2.734
0.938	133.962	1038.886	2.835
0.781	144.559	1040.230	2.630
0.616	158.087	1041.136	2.574
0.444	184.918	1040.137	2.535
0.060	241.884	1043.871	2.308

Table F.12: Processed data for H14-fan test.

Reference speed		1000 RPM							
Reference density		1.2 kg/m ³							
Measured density		1.186 kg/m ³							
P_{d2}	P_{d4}	P_{minor}	P_{hex}	P_{t2}	P_{fs}	Shaft power	\dot{V}'	P_{fs}'	Shaft power'
[Pa]	[Pa]	[Pa]	[Pa]	[Pa]	[Pa]	[W]	[m ³ /s]	[Pa]	[W]
13.970	3.485	3.773	4.048	70.230	56.260	210.047	1.461	53.084	189.694
13.735	3.427	3.710	4.010	72.921	59.187	227.724	1.449	55.902	206.031
13.090	3.266	3.537	3.903	79.719	66.629	226.749	1.416	63.032	205.632
12.106	3.020	3.273	3.736	86.245	74.138	235.546	1.363	70.274	214.240
11.008	2.746	2.979	3.544	95.713	84.705	205.051	1.301	80.470	187.053
9.437	2.354	2.557	3.256	111.533	102.096	246.457	1.207	97.366	226.194
8.221	2.051	2.230	3.020	120.443	112.223	255.576	1.127	107.150	235.011
6.769	1.689	1.839	2.720	129.077	122.308	252.272	1.023	116.849	232.166
5.273	1.316	1.436	2.381	139.094	133.821	263.431	0.903	127.658	241.966
3.662	0.914	1.000	1.965	148.438	144.776	241.462	0.751	137.753	220.864
2.273	0.567	0.624	1.534	160.812	158.539	235.533	0.591	150.587	214.871
1.180	0.294	0.326	1.096	186.634	185.455	231.073	0.426	176.487	211.434
0.022	0.005	0.006	0.146	242.042	242.020	207.128	0.057	228.667	187.524

The fan static pressure and shaft power vs. volume flow rate curves are shown in Figures F.11 and F.12.

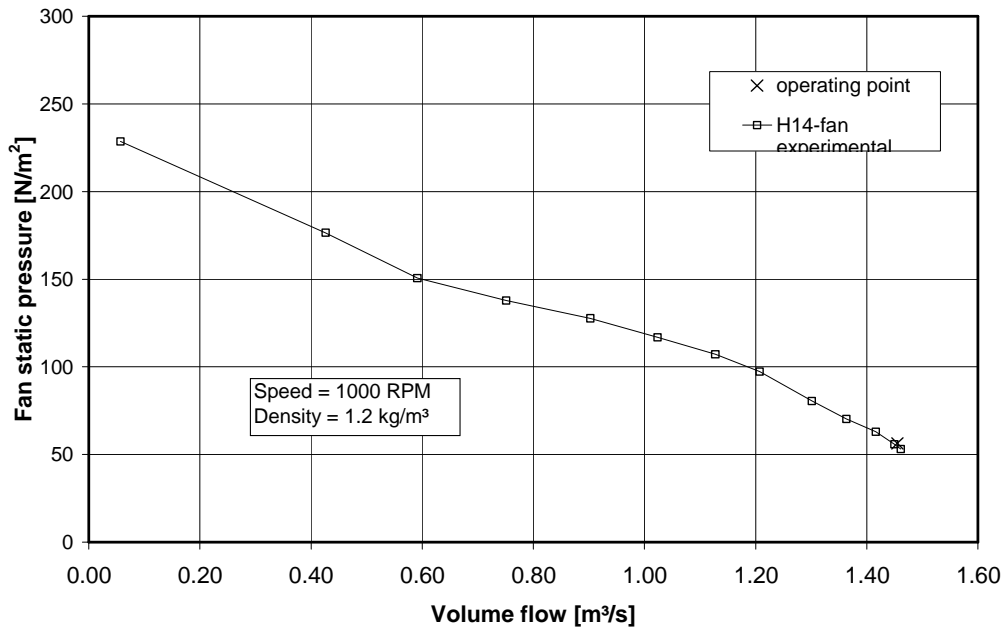


Figure F.11: H14-fan fan static pressure curve.

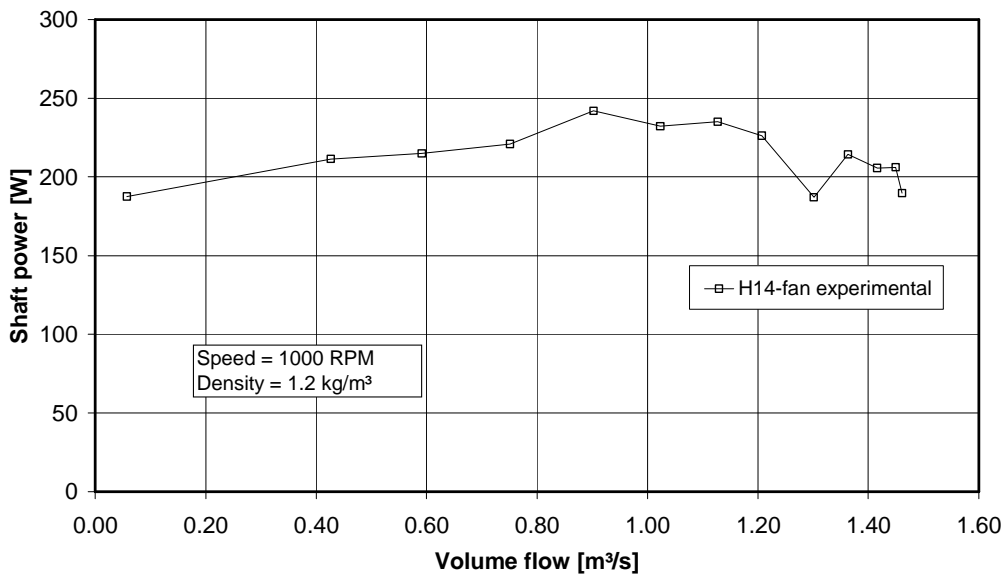


Figure F.12: H14-fan fan shaft power curve.

F.2. Multiple fans

The data shown below for the various multiple fan configurations represent an average value of two sets of readings. Each reading contained in these two sets is in itself the average of five sequential readings taken at each of the platform heights.

F.2.1. N_N_N configuration

The values for the N_N_N configuration without the walkway extension are included in Table F.13 and the values for the N_N_N configuration with the walkway extension are included in Table F.14.

Table F.13: Test data for N_N_N configuration without walkway.

Reference speed		1000 RPM							
Reference density		1.2 kg/m ³							
Measured density		1.164 kg/m ³							
		Tunnel 1		Tunnel 2		Tunnel 3		3-fan system	
		Ref. flow rate [m ³ /s]	1.458	Ref. flow rate [m ³ /s]	1.453	Ref. flow rate [m ³ /s]	1.462		
Height	H/D	\dot{V}'	Vol. eff.	\dot{V}'	Vol. eff.	\dot{V}'	Vol. eff.	Shaft Power	Vol. eff.
[m]		[m ³ /s]		[m ³ /s]		[m ³ /s]		[W]	
no floor	infinite	1.468	1.007	1.459	1.005	1.422	0.973	159.993	0.995
2.835	4.5	1.459	1.001	1.449	0.997	1.398	0.956	162.158	0.985
2.205	3.5	1.453	0.996	1.448	0.997	1.383	0.946	161.863	0.980
1.575	2.5	1.443	0.989	1.451	0.999	1.347	0.922	162.824	0.970
0.940	1.5	1.393	0.955	1.419	0.977	1.214	0.830	166.061	0.921
0.630	1.0	1.341	0.920	1.351	0.930	0.518	0.354	149.818	0.735

Table F.14: Test data for N_N_N configuration with walkway.

Reference speed		1000 RPM							
Reference density		1.2 kg/m ³							
Measured density		1.200 kg/m ³							
		Tunnel 1		Tunnel 2		Tunnel 3		3-fan system	
		Ref. flow rate [m ³ /s]	1.458	Ref. flow rate [m ³ /s]	1.453	Ref. flow rate [m ³ /s]	1.462		
Height	H/D	\dot{V}'	Vol. eff.	\dot{V}'	Vol. eff.	\dot{V}'	Vol. eff.	Shaft Power	Vol. eff.
[m]		[m ³ /s]		[m ³ /s]		[m ³ /s]		[W]	
no floor	infinite	1.468	1.007	1.463	1.007	1.446	0.989	161.369	1.001
2.835	4.5	1.462	1.002	1.449	0.998	1.424	0.974	158.440	0.991
2.205	3.5	1.458	1.000	1.440	0.991	1.411	0.965	157.218	0.986
1.575	2.5	1.447	0.992	1.439	0.991	1.382	0.945	157.328	0.976
0.940	1.5	1.388	0.952	1.407	0.969	1.302	0.890	157.574	0.937
0.630	1.0	1.316	0.902	1.354	0.932	0.930	0.636	135.444	0.823

Graphs showing the experimentally determined volumetric effectiveness for the edge fan, as well as 3-fan system for the N_N_N configuration are shown in Figures F.13 and F.14. Figure F.15 shows the variation in the power consumption of the edge fan with a variation in platform height.

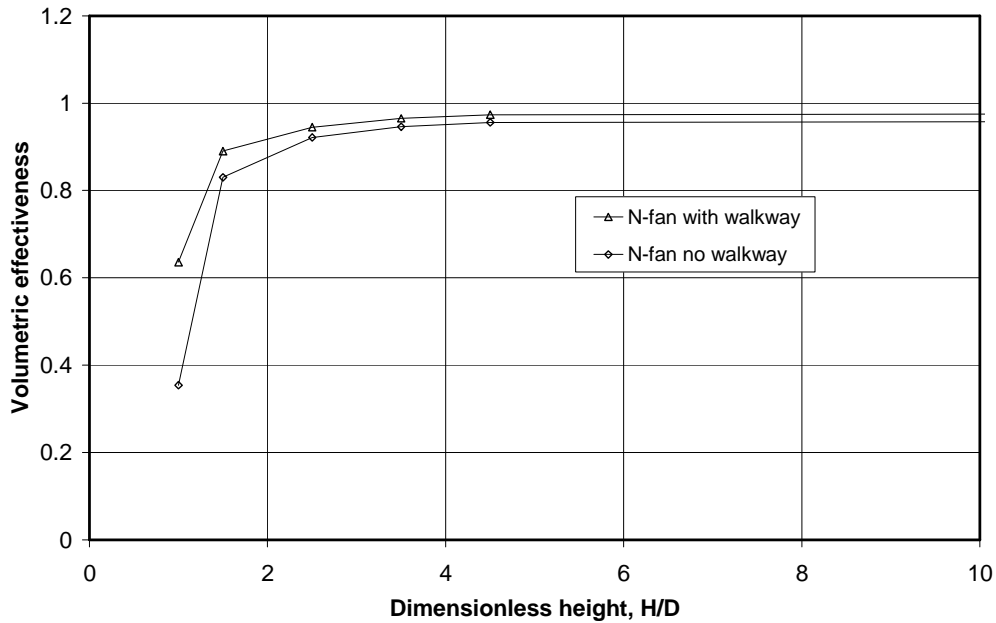


Figure F.13: Volumetric effectiveness vs. platform height of edge fan for N_N_N configuration.

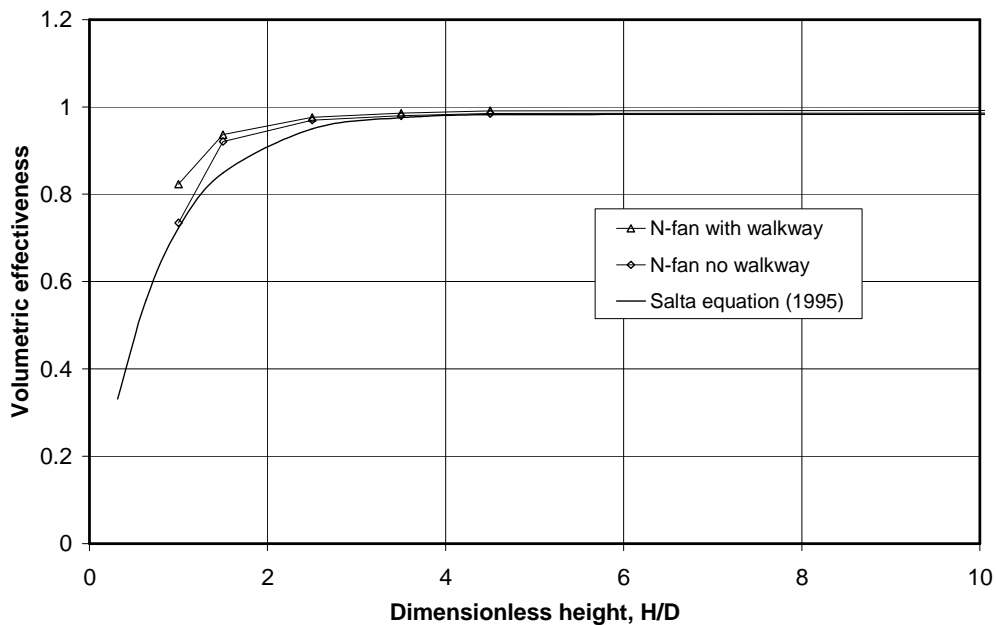


Figure F.14: Volumetric effectiveness vs. platform height of 3-fan system for N_N_N configuration.

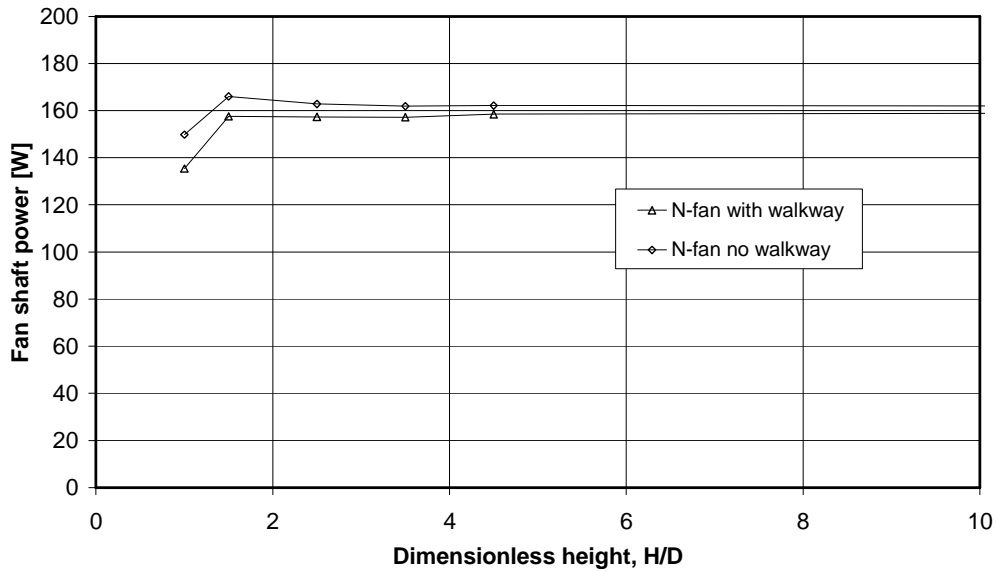


Figure F.15: Edge fan shaft power vs. platform height for N_N_N configuration.

F.2.2. B_N_N configuration

The values for the B_N_N configuration without the walkway extension are included in Table F.15 and the values for the B_N_N configuration with the walkway extension are included in Table F.16.

Table F.15: Test data for B_N_N configuration without walkway.

Reference speed		1000 RPM							
Reference density		1.2 kg/m ³							
Measured density		1.164 kg/m ³							
		Tunnel 1		Tunnel 2		Tunnel 3		3-fan system	
		Ref. flow rate	1.458	Ref. flow rate	1.453	Ref. flow rate	1.458		
		[m ³ /s]		[m ³ /s]		[m ³ /s]			
Height	H/D	\dot{V}'	Vol. eff.	\dot{V}'	Vol. eff.	\dot{V}'	Vol. eff.	Shaft Power	Vol. eff.
[m]		[m ³ /s]		[m ³ /s]		[m ³ /s]		[W]	
no floor	infinite	1.461	1.002	1.453	1.000	1.418	0.973	150.459	0.992
2.835	4.5	1.465	1.005	1.445	0.995	1.383	0.949	150.973	0.983
2.205	3.5	1.452	0.996	1.442	0.992	1.365	0.937	148.551	0.975
1.575	2.5	1.449	0.993	1.444	0.994	1.328	0.911	153.057	0.966
0.940	1.5	1.383	0.949	1.419	0.977	1.201	0.824	154.041	0.916
0.630	1.0	1.308	0.897	1.364	0.939	0.771	0.529	164.032	0.788

Table F.16: Test data for B_N_N configuration with walkway.

Reference speed		1000 RPM							
Reference density		1.2 kg/m ³							
Measured density		1.195 kg/m ³							
		Tunnel 1		Tunnel 2		Tunnel 3		3-fan system	
		Ref. flow rate [m ³ /s]	1.458	Ref. flow rate [m ³ /s]	1.453	Ref. flow rate [m ³ /s]	1.458		
Height	H/D	\dot{V}	Vol. eff.	\dot{V}	Vol. eff.	\dot{V}	Vol. eff.	Shaft Power	Vol. eff.
[m]		[m ³ /s]		[m ³ /s]		[m ³ /s]		[W]	
no floor	infinite	1.459	1.000	1.459	1.004	1.431	0.982	144.344	0.996
2.835	4.5	1.463	1.003	1.451	0.999	1.422	0.975	137.392	0.992
2.205	3.5	1.454	0.997	1.439	0.991	1.416	0.971	144.141	0.986
1.575	2.5	1.457	0.999	1.438	0.990	1.382	0.948	142.850	0.979
0.940	1.5	1.388	0.952	1.413	0.973	1.307	0.896	137.621	0.940
0.630	1.0	1.305	0.895	1.321	0.909	1.147	0.787	149.090	0.864

Graphs showing the experimentally determined volumetric effectiveness for the edge fan, as well as 3-fan system for the B_N_N configuration are shown in Figures F.16 and F.17. Figure F.18 shows the variation in the power consumption of the edge fan with a variation in platform height.

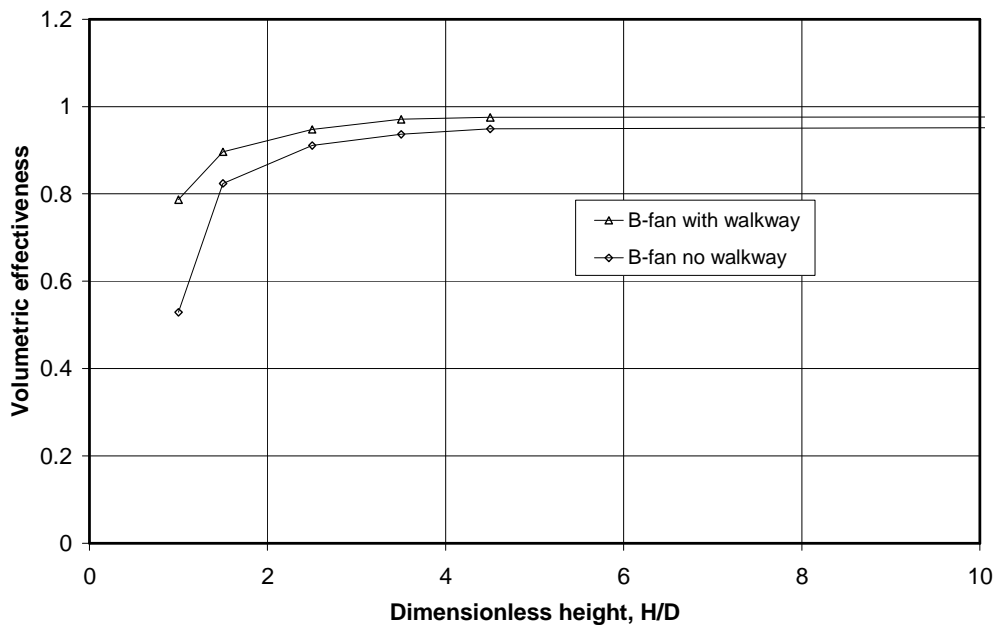


Figure F.16: Volumetric effectiveness vs. platform height of edge fan for B_N_N configuration.

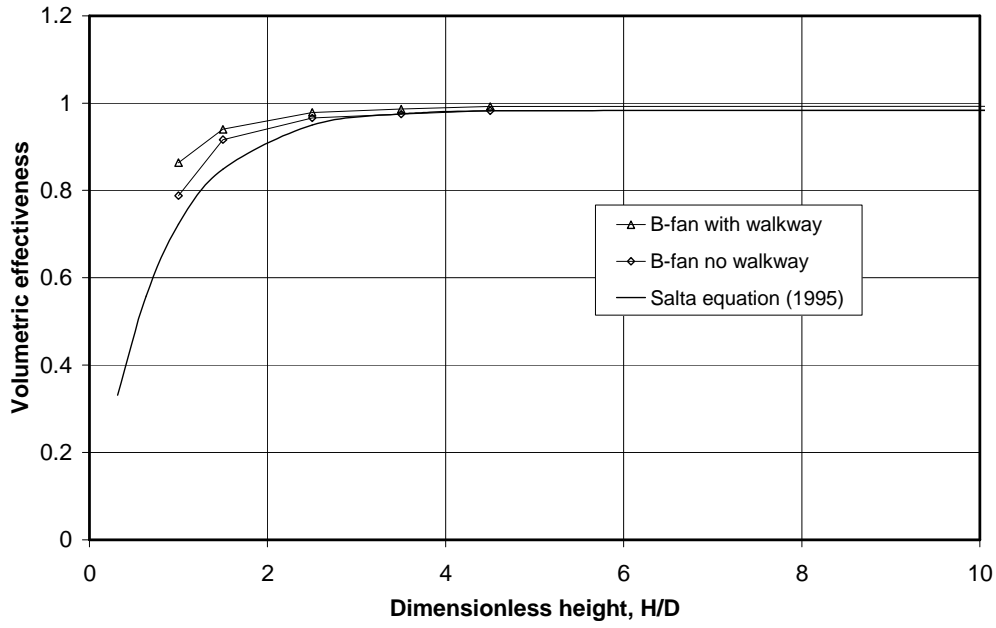


Figure F.17: Volumetric effectiveness vs. platform height of 3-fan system for B_N_N configuration.

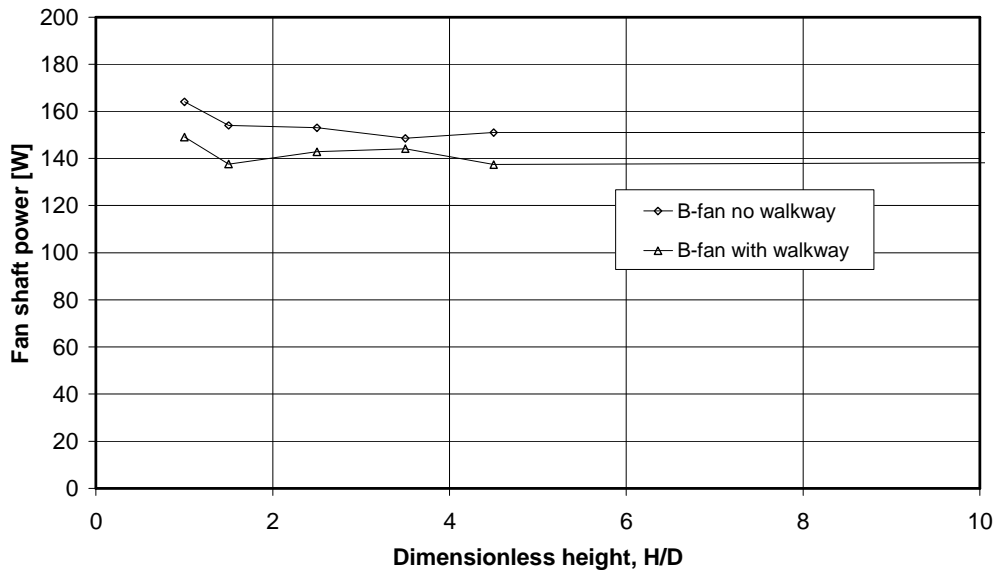


Figure F.18: Edge fan shaft power vs. platform height for B_N_N configuration.

F.2.3. H10_N_N configuration

The values for the H10_N_N configuration without the walkway extension are included in Table F.17 and the values for the H10_N_N configuration with the walkway extension are included in Table F.18.

Table F.17: Test data for H10_N_N configuration without walkway.

Reference speed		1000 RPM							
Reference density		1.2 kg/m ³							
Measured density		1.165 kg/m ³							
		Tunnel 1		Tunnel 2		Tunnel 3		3-fan system	
		Ref. flow rate [m ³ /s]	1.458	Ref. flow rate [m ³ /s]	1.453	Ref. flow rate [m ³ /s]	1.458		
Height	H/D	\dot{V}'	Vol. eff.	\dot{V}'	Vol. eff.	\dot{V}'	Vol. eff.	Shaft Power	Vol. eff.
[m]		[m ³ /s]		[m ³ /s]		[m ³ /s]		[W]	
no floor	infinite	1.469	1.007	1.465	1.008	1.415	0.975	159.946	0.997
2.835	4.5	1.459	1.001	1.455	1.002	1.399	0.965	164.019	0.989
2.205	3.5	1.455	0.998	1.450	0.998	1.389	0.958	164.107	0.985
1.575	2.5	1.442	0.989	1.450	0.998	1.367	0.942	166.024	0.976
0.940	1.5	1.428	0.980	1.419	0.977	1.257	0.867	162.393	0.941
0.630	1.0	1.274	0.874	1.362	0.938	0.833	0.575	154.807	0.795

Table F.18: Test data for H10_N_N configuration with walkway.

Reference speed		1000 RPM							
Reference density		1.2 kg/m ³							
Measured density		1.200 kg/m ³							
		Tunnel 1		Tunnel 2		Tunnel 3		3-fan system	
		Ref. flow rate [m ³ /s]	1.458	Ref. flow rate [m ³ /s]	1.453	Ref. flow rate [m ³ /s]	1.462		
Height	H/D	\dot{V}'	Vol. eff.	\dot{V}'	Vol. eff.	\dot{V}'	Vol. eff.	Shaft Power	Vol. eff.
[m]		[m ³ /s]		[m ³ /s]		[m ³ /s]		[W]	
no floor	infinite	1.466	1.005	1.464	1.008	1.436	0.990	161.084	1.001
2.835	4.5	1.465	1.005	1.447	0.996	1.424	0.982	154.590	0.994
2.205	3.5	1.454	0.997	1.447	0.996	1.419	0.979	155.738	0.991
1.575	2.5	1.454	0.997	1.443	0.994	1.406	0.969	158.998	0.987
0.940	1.5	1.380	0.946	1.410	0.971	1.346	0.928	155.443	0.948
0.630	1.0	1.319	0.904	1.328	0.914	1.233	0.850	121.805	0.890

Graphs showing the experimentally determined volumetric effectiveness for the edge fan, as well as 3-fan system for the H10_N_N configuration are shown in Figures F.19 and F.20. Figure F.21 shows the variation in the power consumption of the edge fan with a variation in platform height.

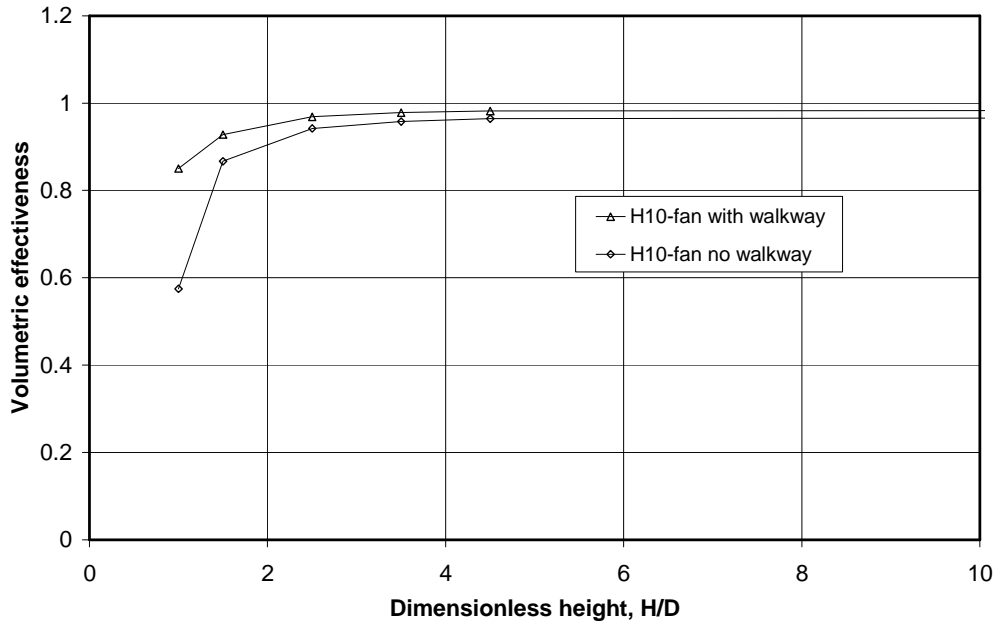


Figure F.19: Volumetric effectiveness vs. platform height of edge fan for H10_N_N configuration.

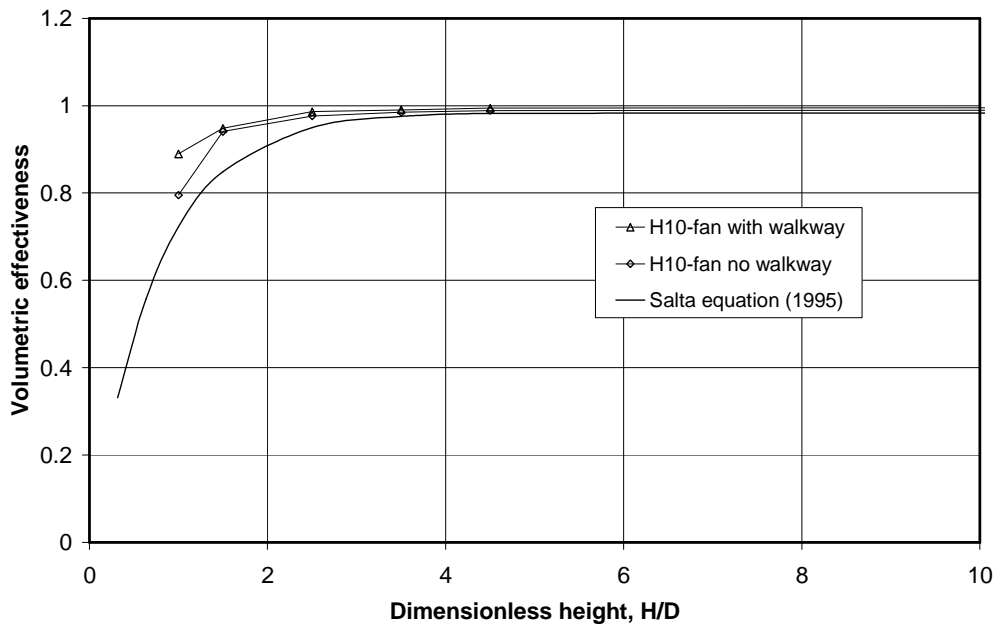


Figure F.20: Volumetric effectiveness vs. platform height of 3-fan system for H10_N_N configuration.

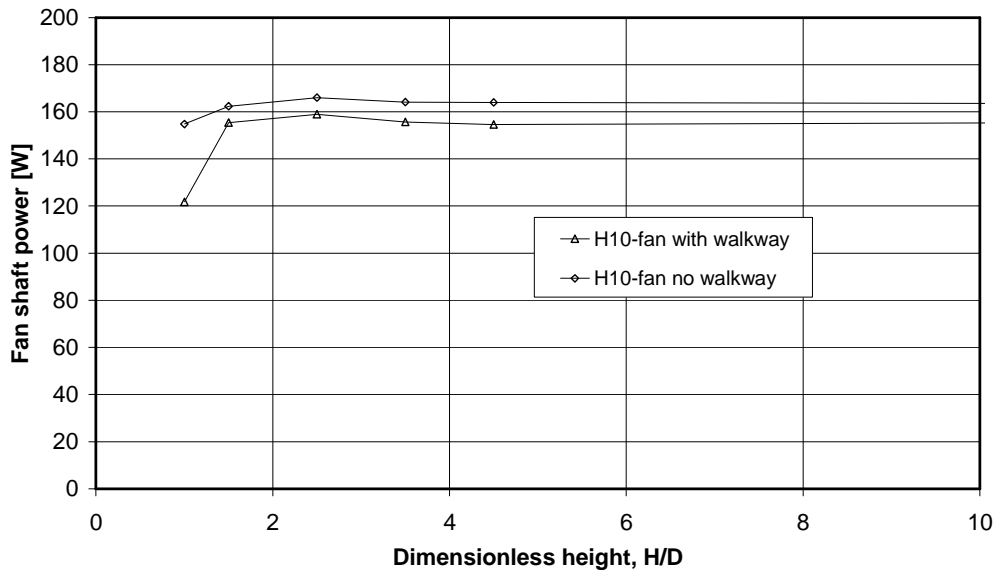


Figure F.21: Edge fan shaft power vs. platform height for H10_N_N configuration.

F.3. PIV data for multiple fans

Two sets of PIV measurements were performed. Only results from the second set of measurements are reflected in this document.

F.3.1. N_N_N configuration

Figure F.22 shows the PIV measurements for the N_N_N configuration at three different fan platform heights.

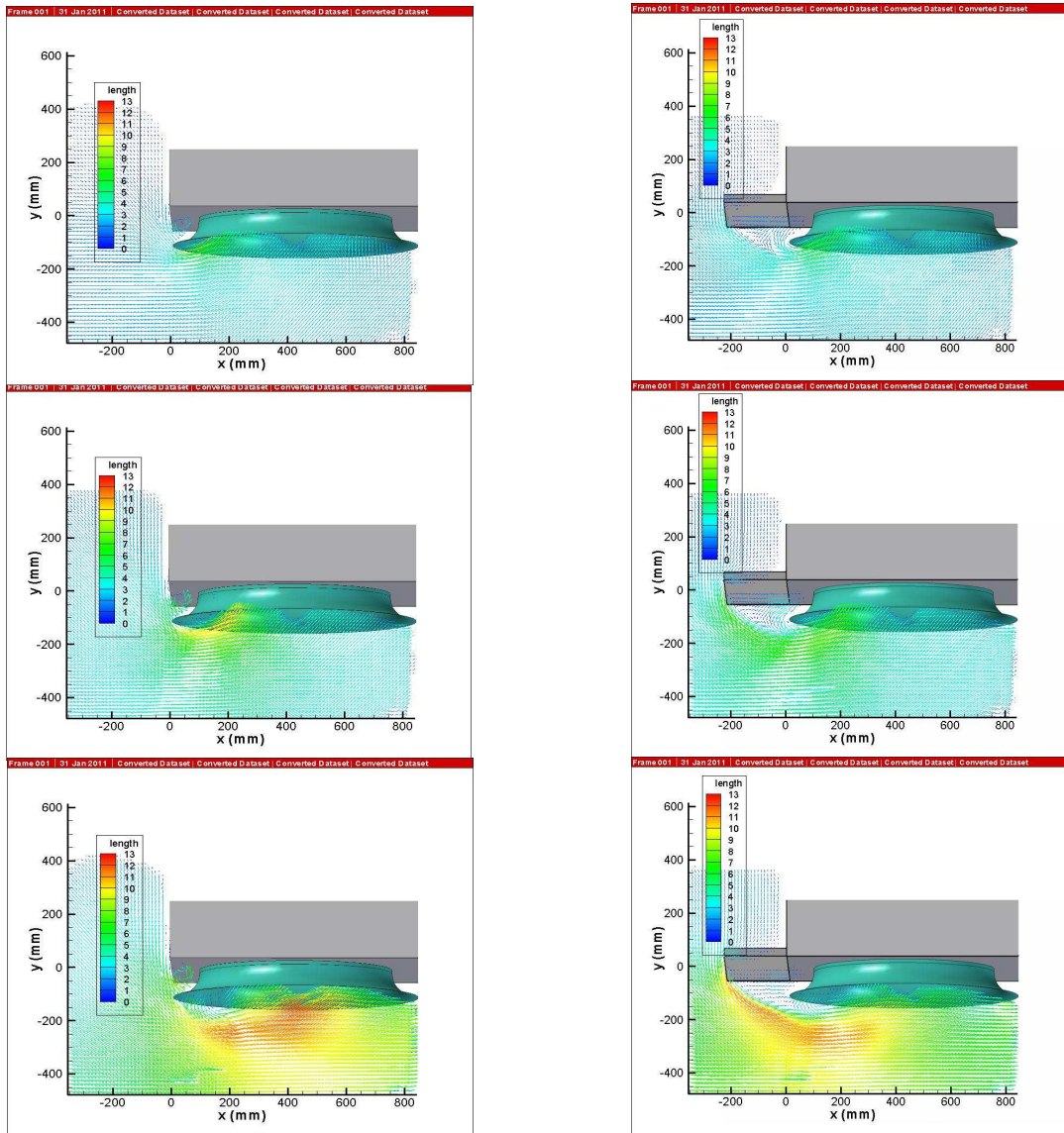


Figure F.22: PIV vector field for N_N_N configuration without walkway (left) and with walkway (right).

F.3.2. B_N_N configuration

Figures F.23 shows the PIV measurements for the B_N_N configuration at three different fan platform heights.

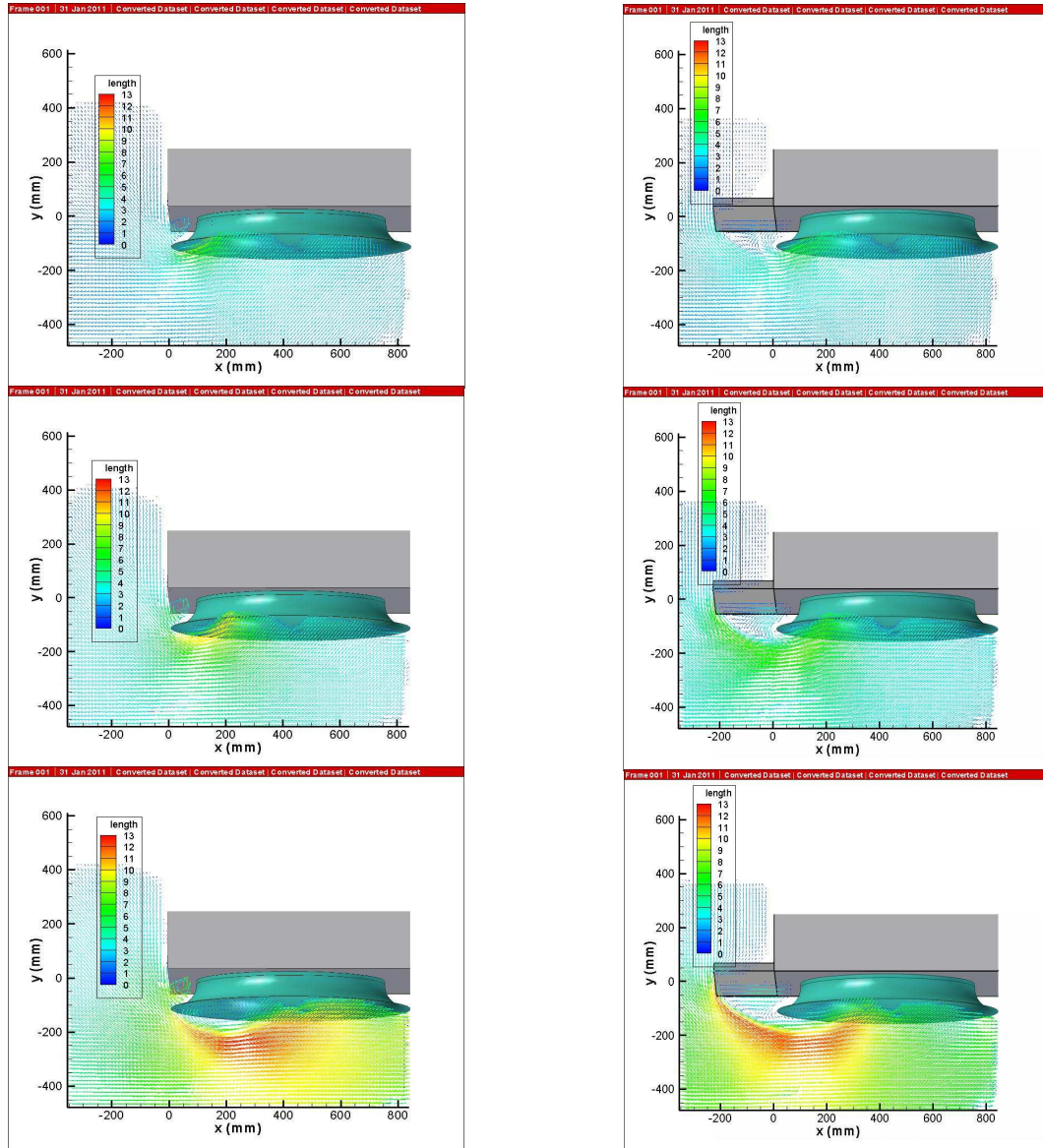


Figure F.23: PIV vector field for B_N_N configuration without walkway (left) and with walkway (right).

F.3.3. H10_N_N configuration

Figures F.24 shows the PIV measurements for the H10_N_N configuration at three different fan platform heights.

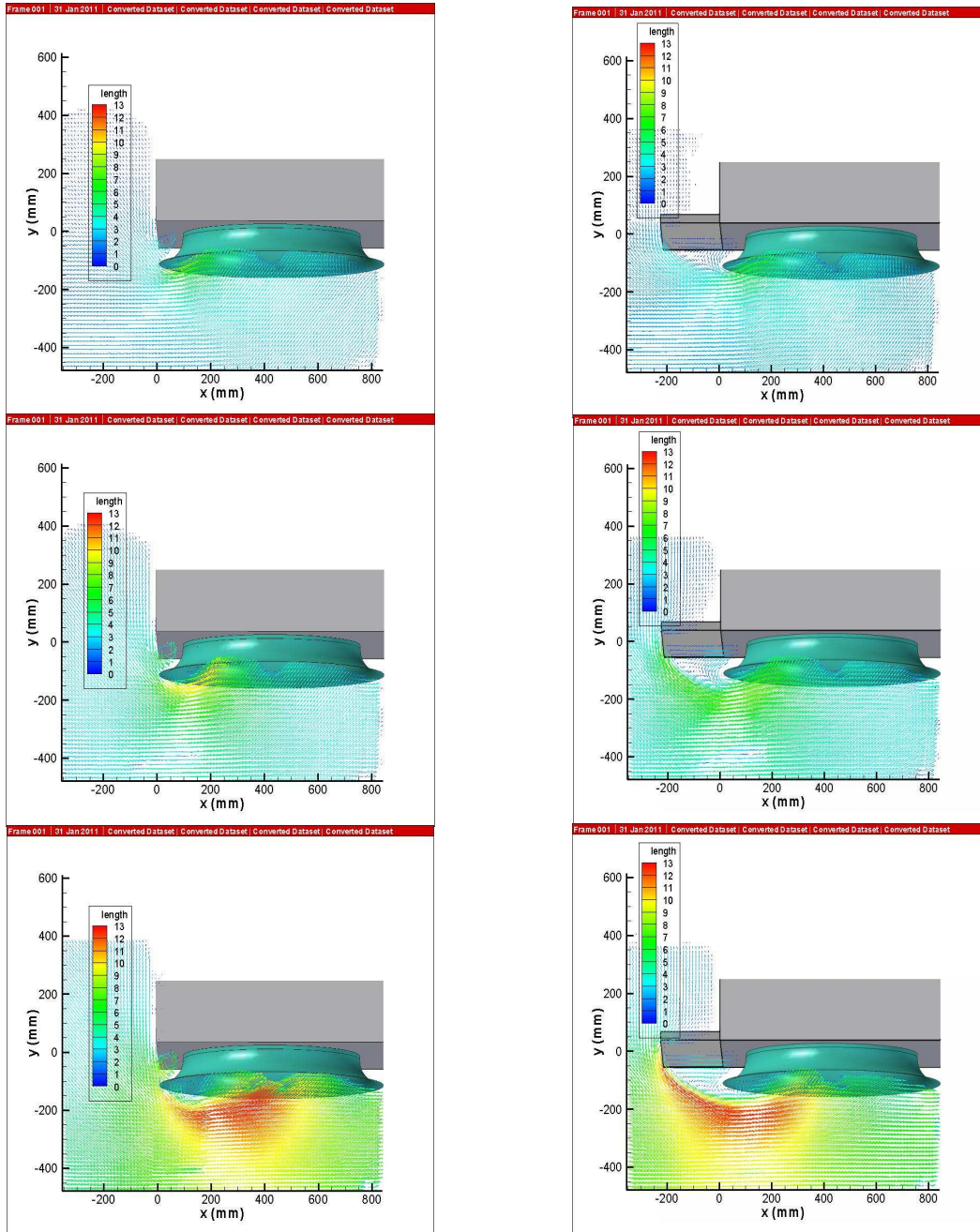


Figure F.24: PIV vector field for H10_N_N configuration without walkway (left) and with walkway (right).

APPENDIX G: DETAILED VELOCITY PROFILES

G.1 Experimental velocity profiles

Figure G.1 shows the velocity distributions along line 1, for the N_N_N multiple fan configuration.

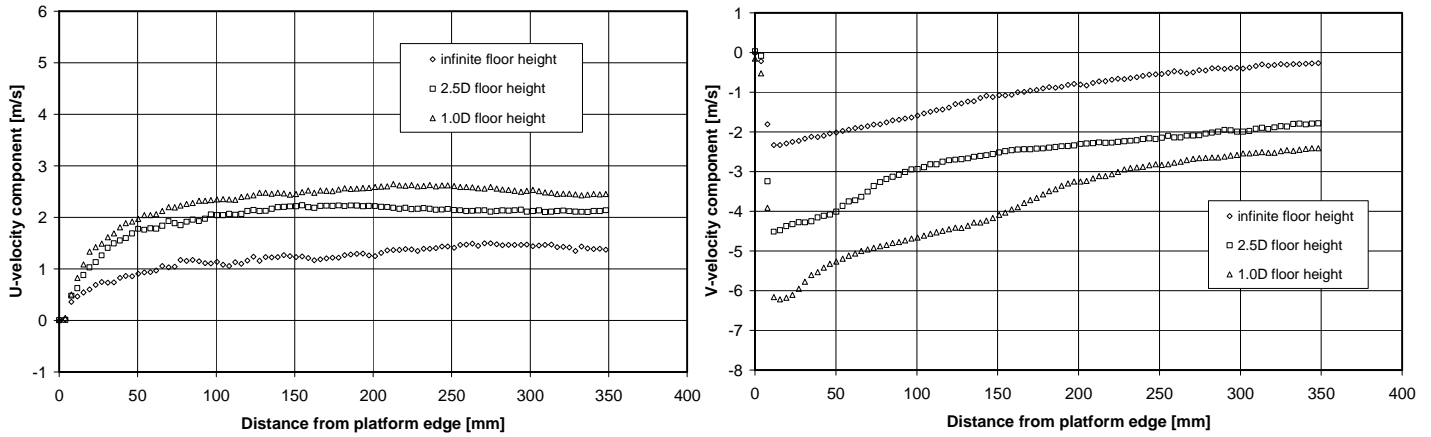


Figure G.1: U- and V-velocity components vs. distance from platform edge along line 1 for N_N_N fan configuration.

Figure G.2 shows the velocity distributions along line 2, for the N_N_N multiple fan configuration.

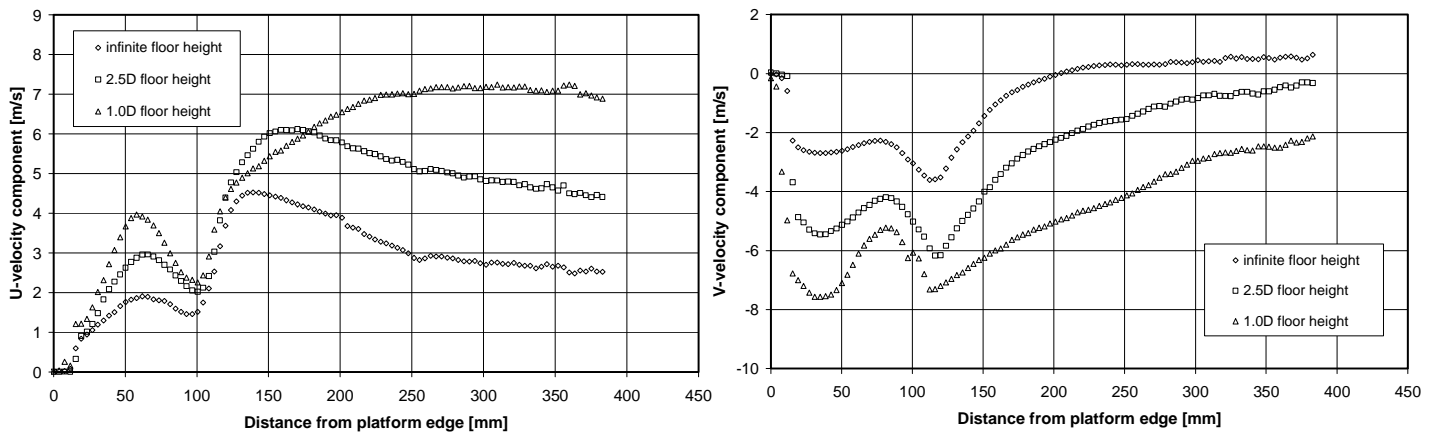


Figure G.2: U- and V-velocity components vs. distance from platform edge along line 2 for N_N_N fan configuration.

Figure G.3 shows the velocity distributions along line 3, for the N_N_N multiple fan configuration.

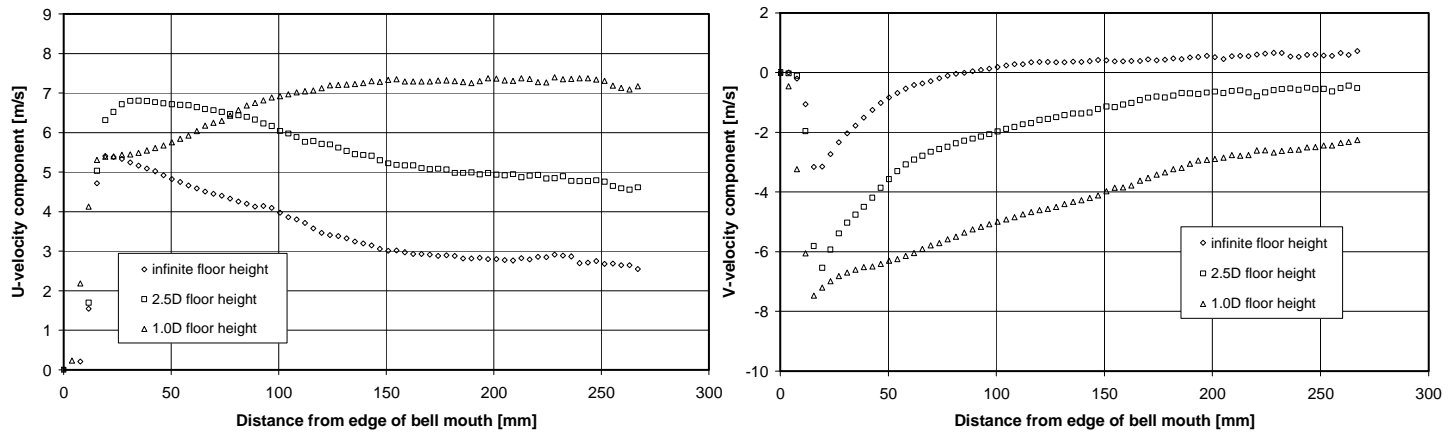


Figure G.3: U- and V-velocity components vs. distance from bell mouth edge along line 3 for N_N_N fan configuration.

Figure G.4 shows the velocity distributions along line 4, for the N_N_N multiple fan configuration. Note that the central section of zero velocity is caused by the presence of the fan shaft.

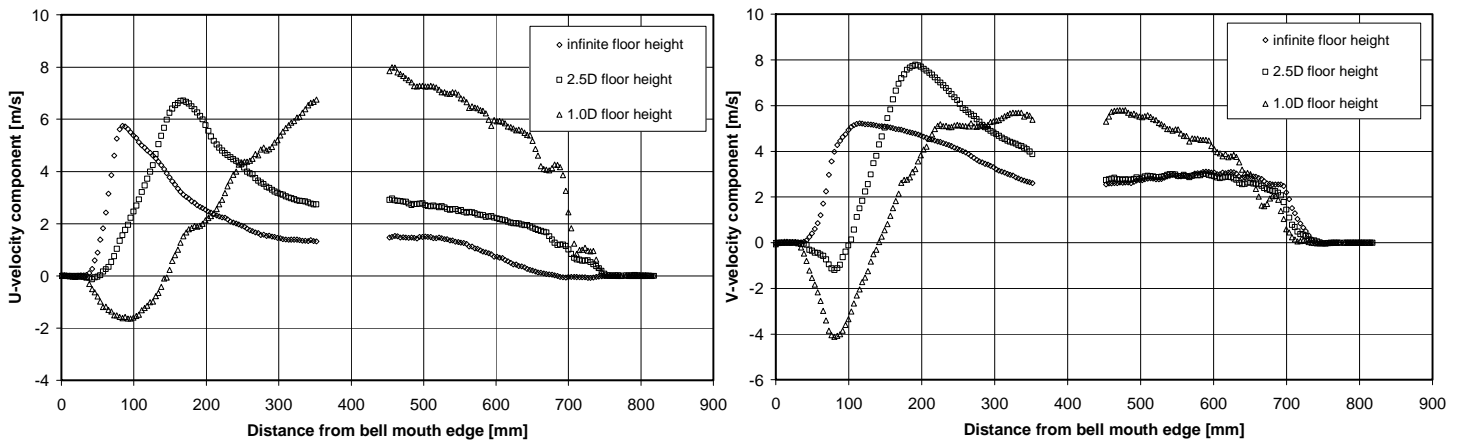


Figure G.4: U- and V-velocity components vs. distance from bell mouth edge along line 4 for N_N_N fan configuration.

Figure G.5 shows the velocity distributions along line 1, for the B_N_N multiple fan configuration.

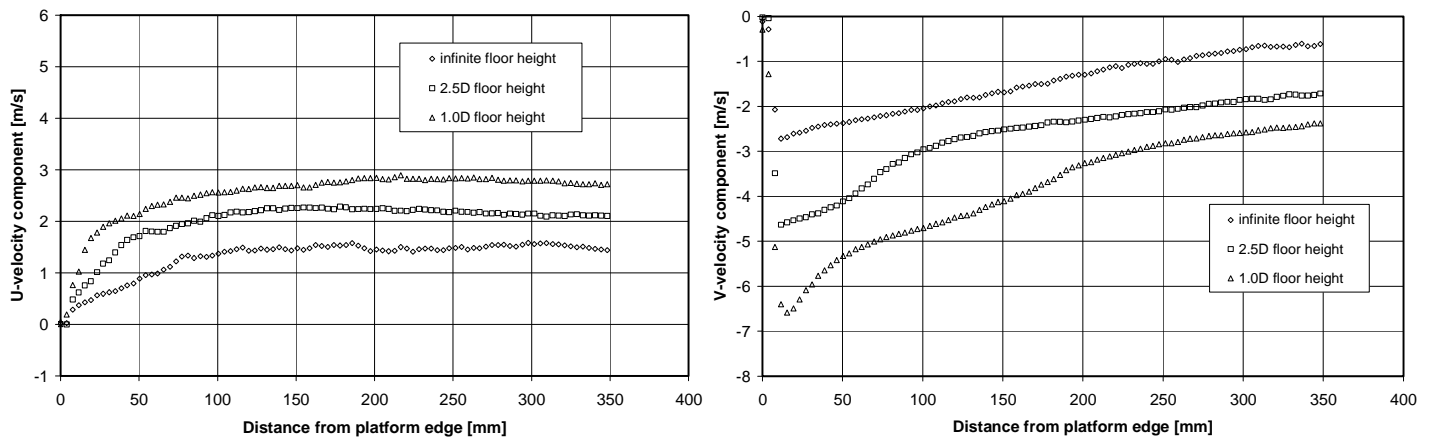


Figure G.5: U- and V-velocity components vs. distance from platform edge along line 1 for B_N_N fan configuration.

Figure G.6 shows the velocity distributions along line 2, for the B_N_N multiple fan configuration.

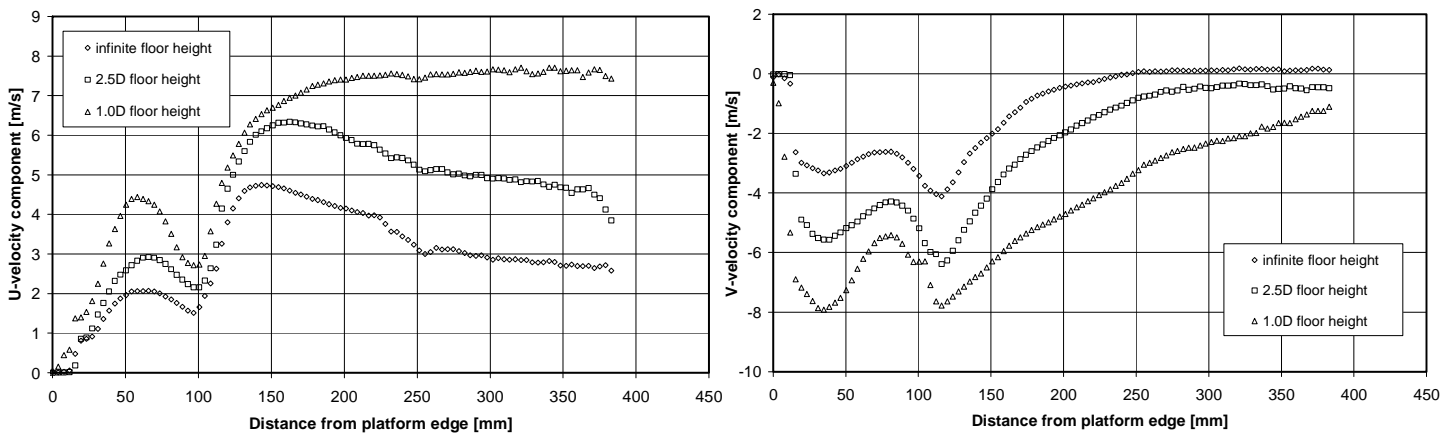


Figure G.6: U- and V-velocity components vs. distance from platform edge along line 2 for B_N_N fan configuration.

Figure G.7 shows the velocity distributions along line 3, for the B_N_N multiple fan configuration.

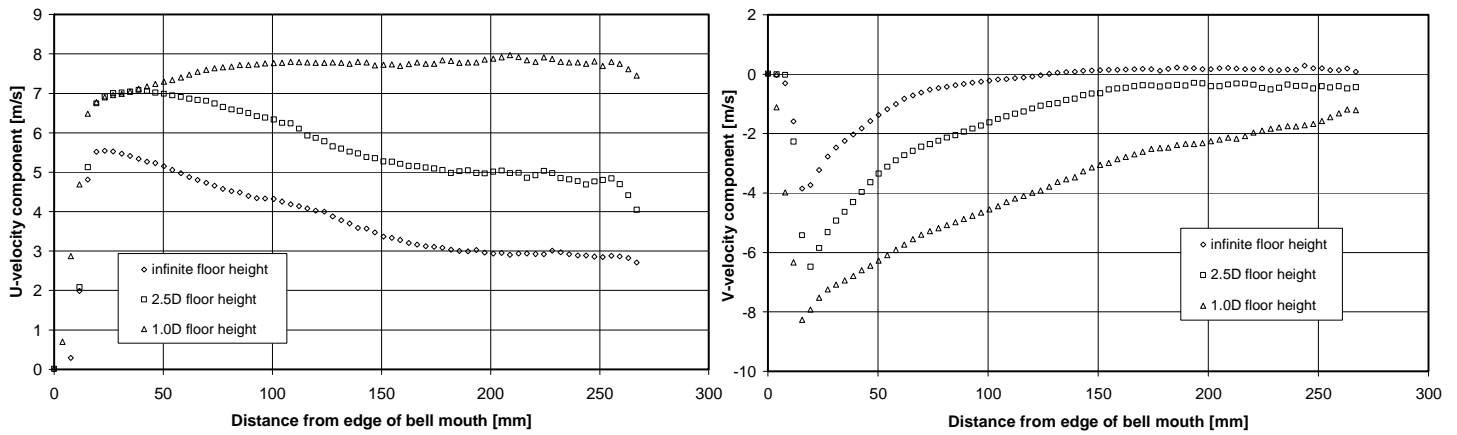


Figure G.7: U- and V-velocity components vs. distance from bell mouth edge along line 3 for B_N_N fan configuration.

Figure G.8 shows the velocity distributions along line 4, for the B_N_N multiple fan configuration. Note that the central section of zero velocity is caused by the presence of the fan shaft.

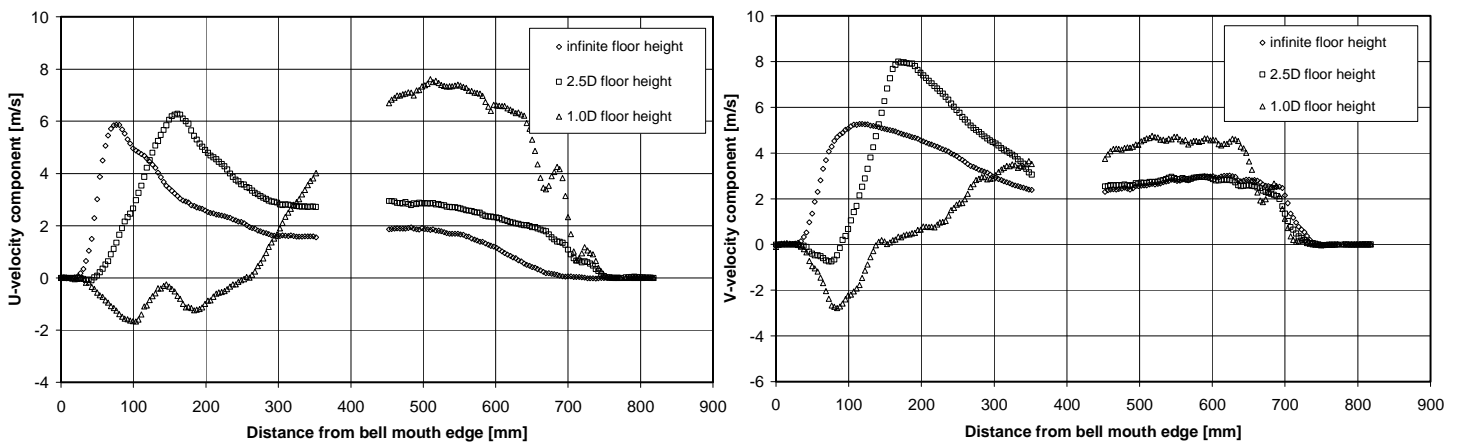


Figure G.8: U- and V-velocity components vs. distance from bell mouth edge along line 4 for B_N_N fan configuration.

Figure G.9 shows the velocity distributions along line 1, for the H10_N_N multiple fan configuration.

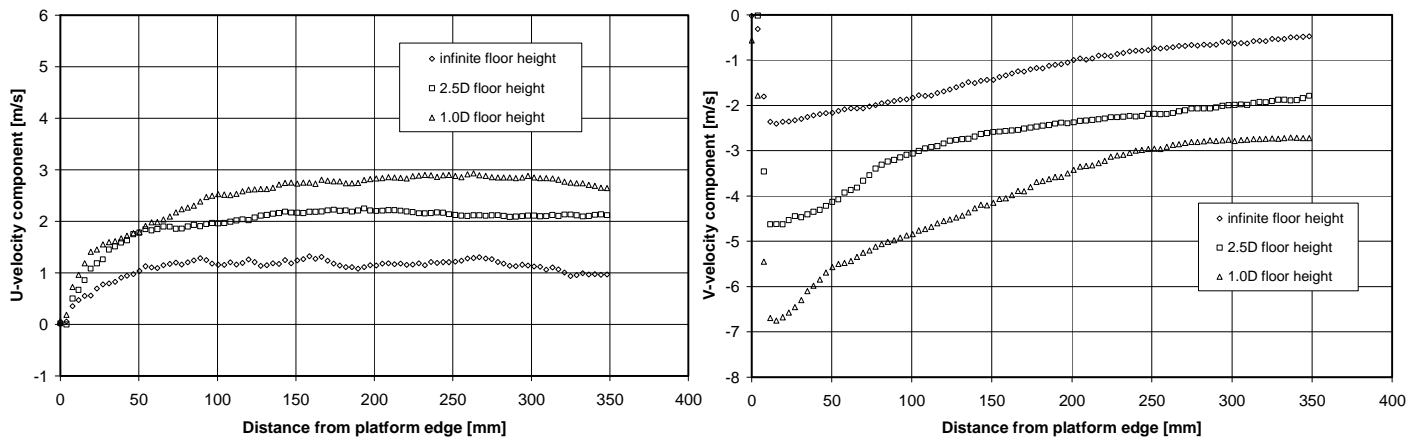


Figure G.9: U- and V-velocity components vs. distance from platform edge along line 1 for H10_N_N fan configuration.

Figure G.10 shows the velocity distributions along line 2, for the H10_N_N multiple fan configuration.

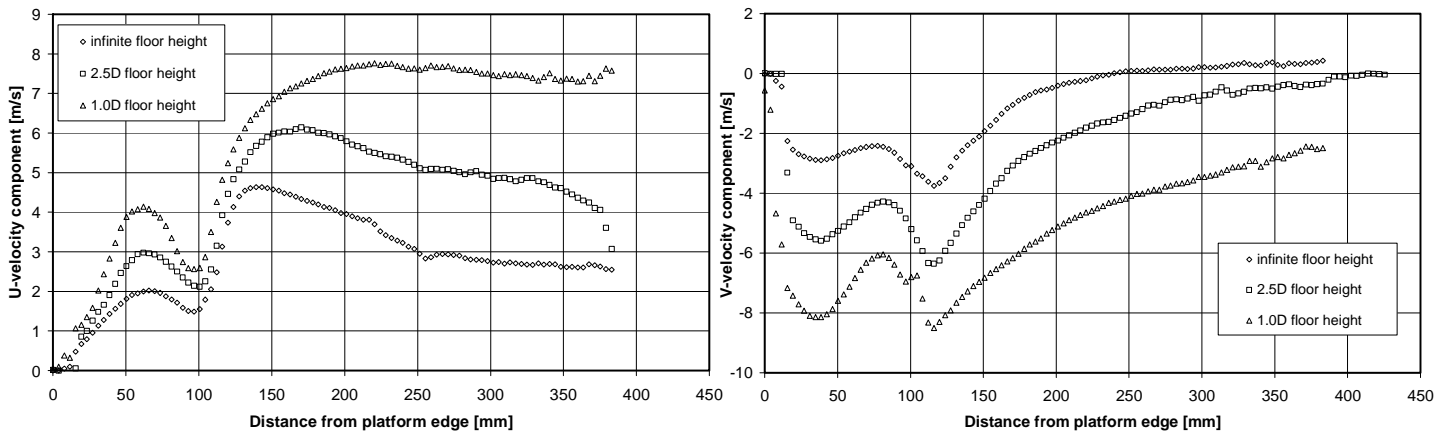


Figure G.10: U- and V-velocity components vs. distance from platform edge along line 2 for H10_N_N fan configuration.

Figure G.12 shows the velocity distributions along line 3, for the H10_N_N multiple fan configuration.

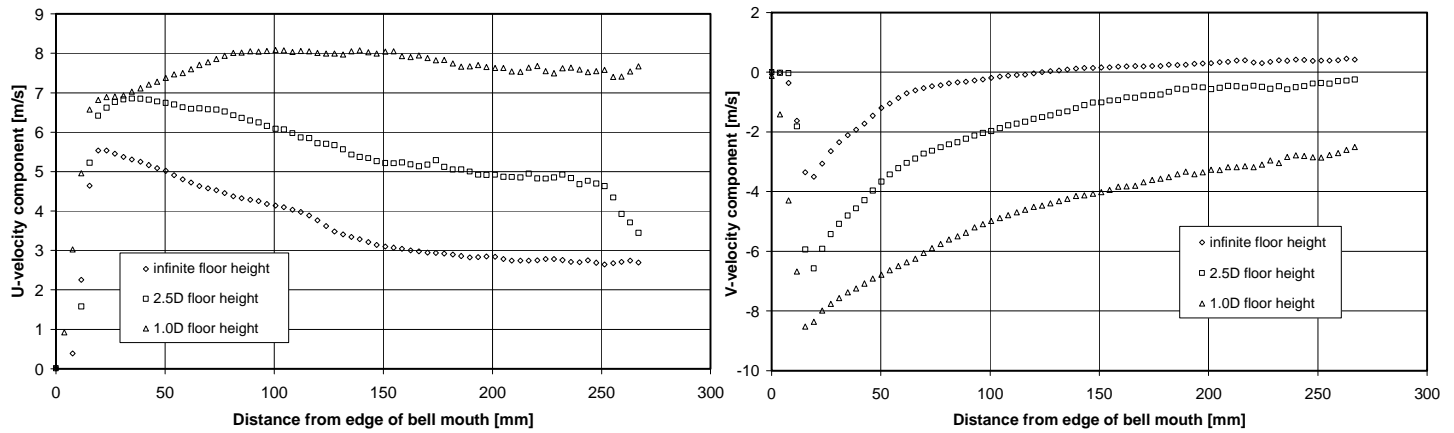


Figure G.11: U- and V-velocity components vs. distance from bell mouth edge along line 3 for H10_N_N fan configuration.

Figure G.12 shows the velocity distributions along line 4, for the H10_N_N multiple fan configuration. Note that the central section of zero velocity is caused by the presence of the fan shaft.

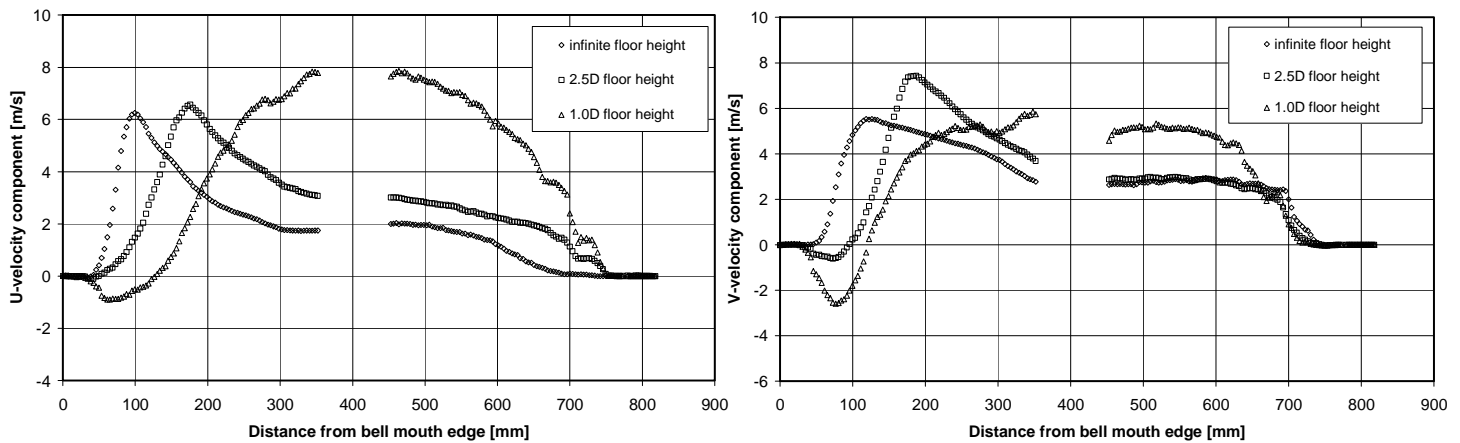


Figure G.12: U- and V-velocity components vs. distance from bell mouth edge along line 4 for H10_N_N fan configuration.

G.2 Comparison of CFD and experimental velocity profiles

A full set of detailed velocity profile results is shown for the N_N_N system configuration. Figures G.13 shows the velocity profiles along a horizontal line drawn from the edge of the plenum chamber (or platform) for an infinite floor height.

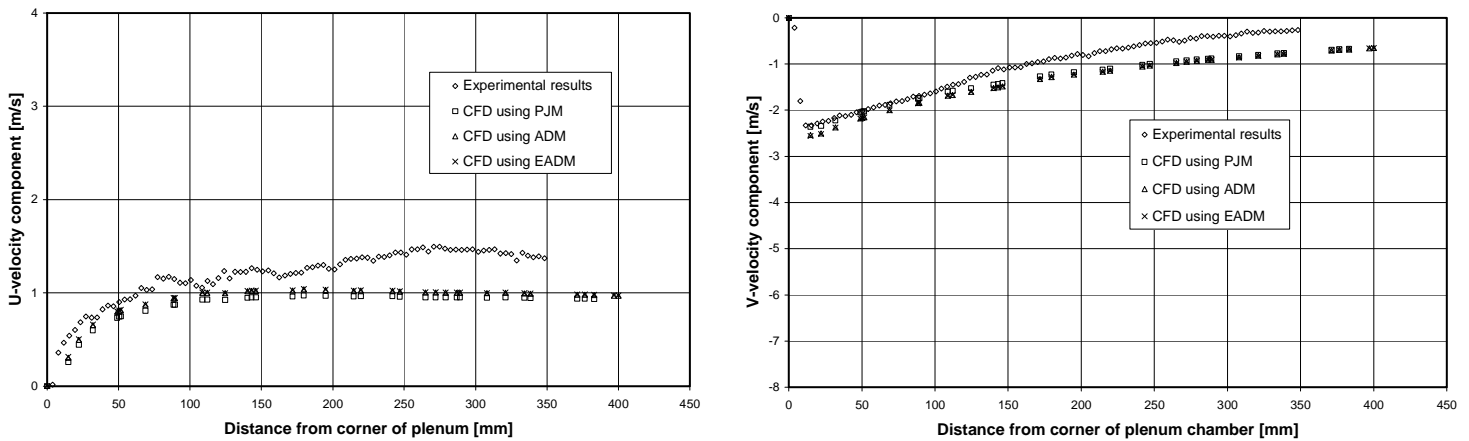


Figure G.13: Comparison of velocity profiles for N-fan at horizontal line from edge of plenum for infinite floor height.

Figures G.14 shows the velocity profiles along a vertical line drawn from the edge of plenum for an infinite floor height.

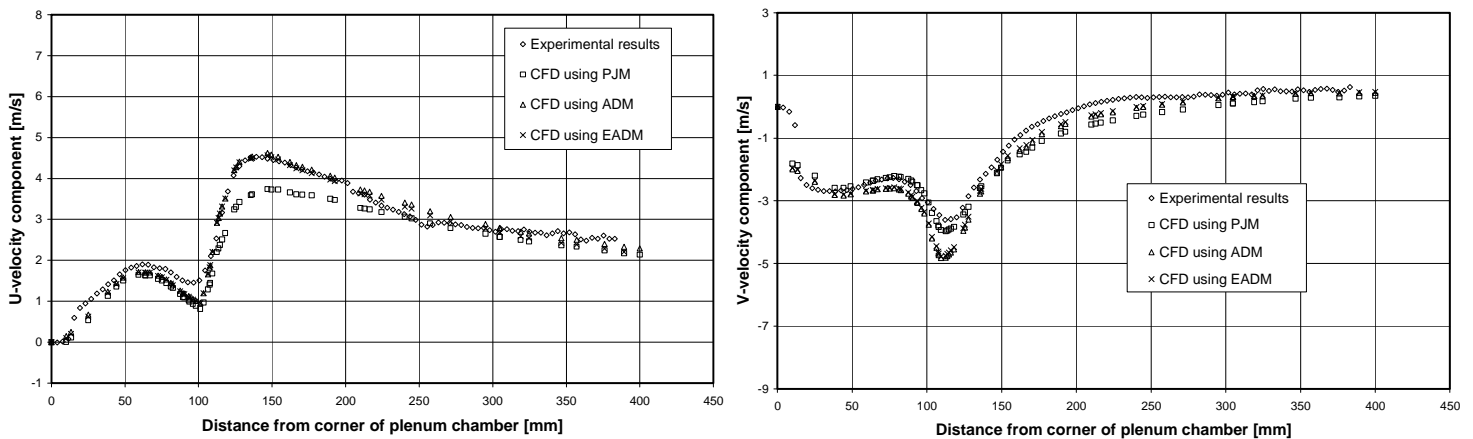


Figure G.14: Comparison of velocity profiles for N-fan at vertical line from edge of plenum for infinite floor height.

Figure G.15 shows the velocity profiles along a vertical line drawn from the edge of the edge fan bell mouth for an infinite floor height.

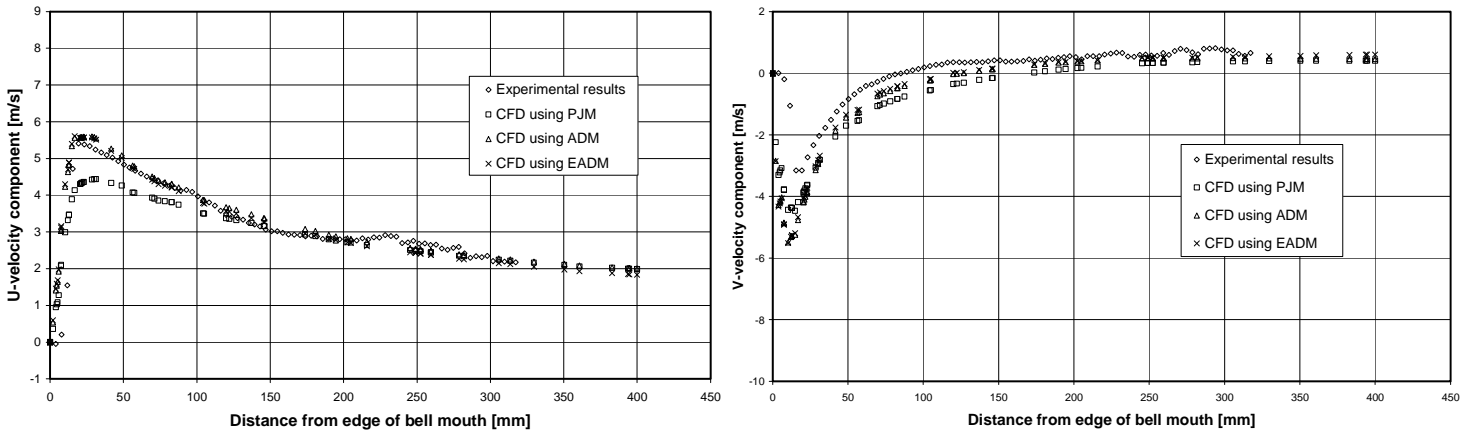


Figure G.15: Comparison of velocity profiles for N-fan at vertical line from edge of bell mouth for infinite floor height.

Figure G.16 shows the velocity profiles along a horizontal line drawn from the edge of the edge fan bell mouth for an infinite floor height.

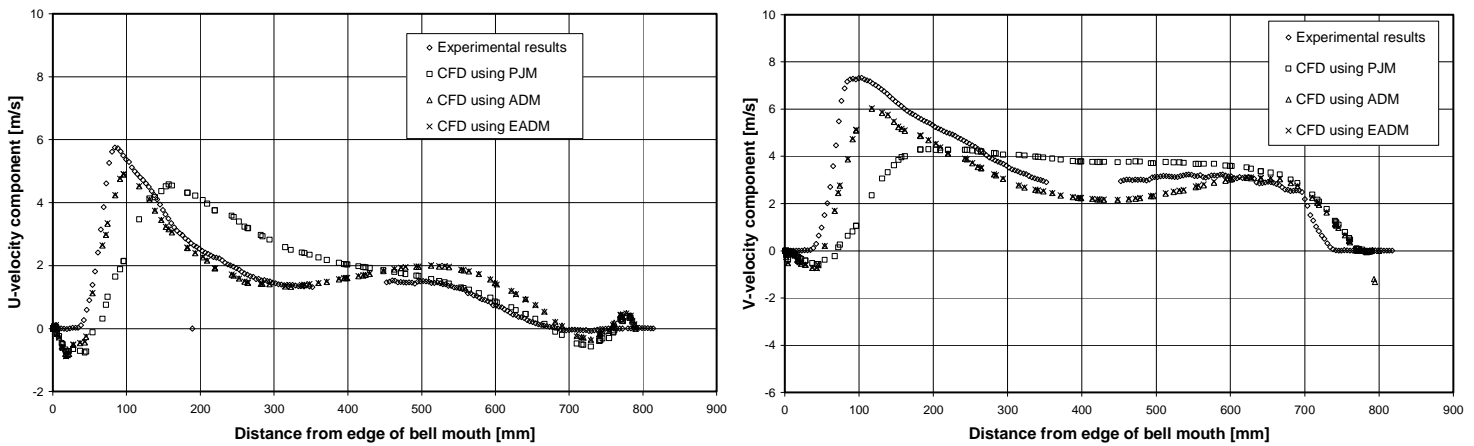


Figure G.16: Comparison of velocity profiles for N-fan at horizontal line from edge of bell mouth for infinite floor height.

Figure G.17 shows the velocity profiles along a horizontal line drawn from the edge of the plenum chamber for a 2.5 x fan diameter floor height.

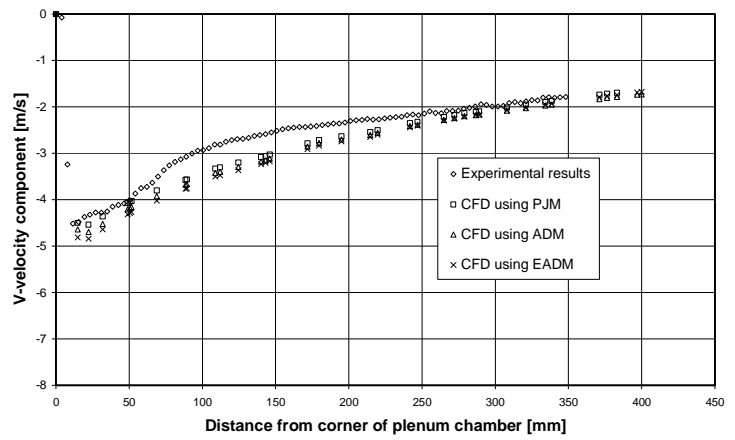
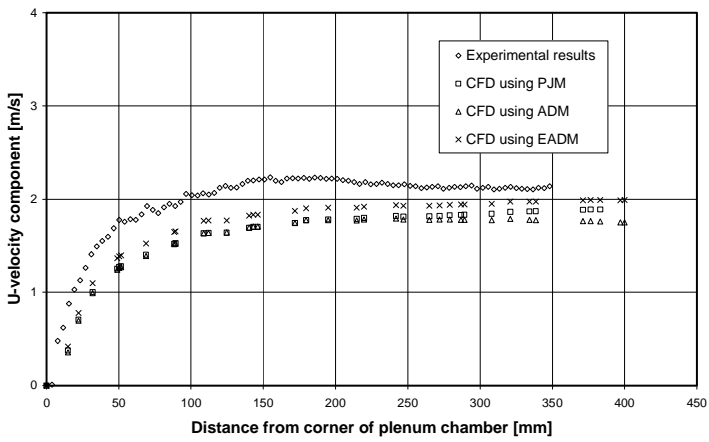


Figure G.17: Comparison of velocity profiles for N-fan at horizontal line from edge of plenum for 2.5 x fan diameter floor height.

Figure G.18 shows the velocity profiles along a vertical line drawn from the edge of the plenum chamber for a 2.5 x fan diameter floor height.

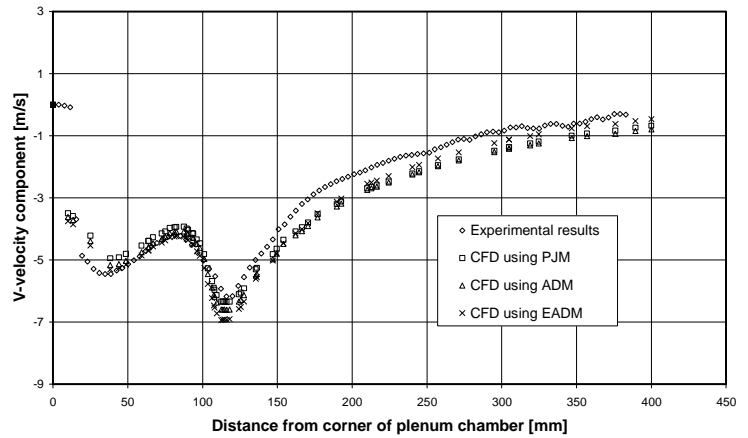
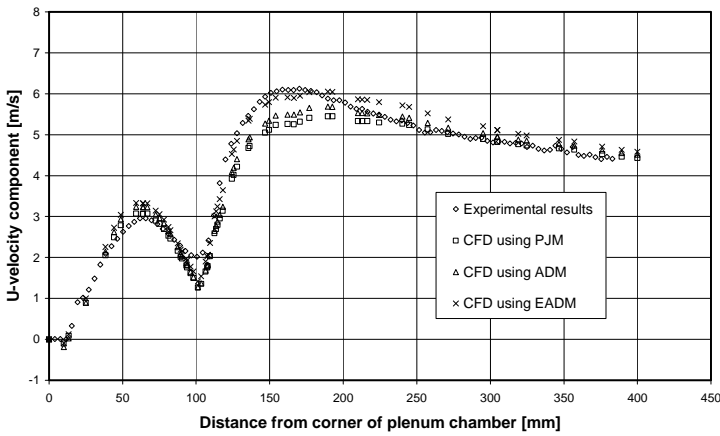


Figure G.18: Comparison of velocity profiles for N-fan at vertical line from edge of plenum for 2.5 x fan diameter floor height.

Figure G.19 shows the velocity profiles along a vertical line drawn from the edge of the edge fan bell mouth for a 2.5 x fan diameter floor height.

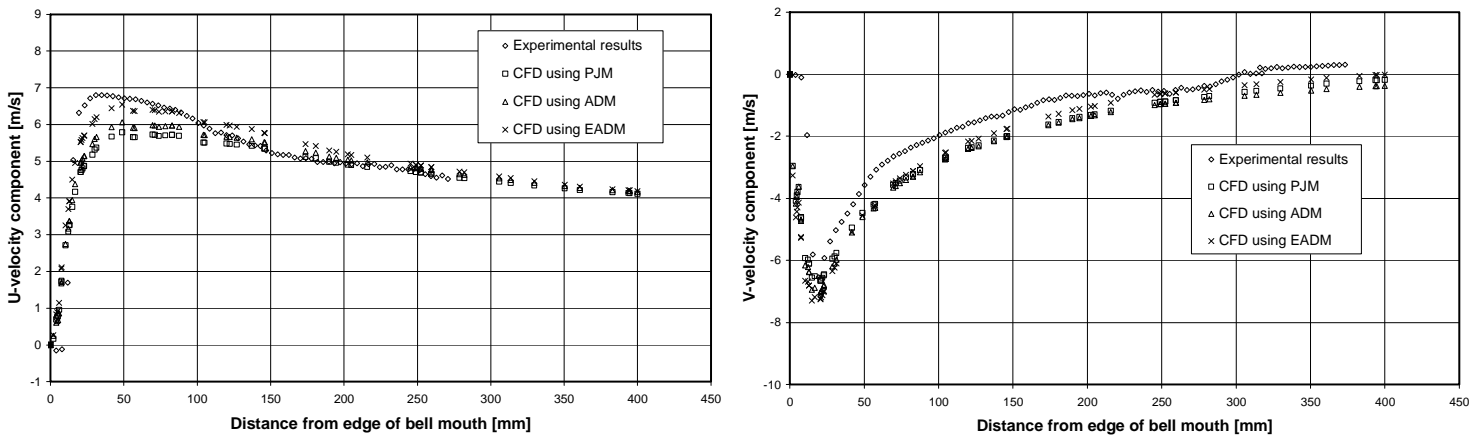


Figure G.19: Comparison of velocity profiles for N-fan at vertical line from edge of bell mouth for 2.5 x fan diameter floor height.

Figures G.20 shows the velocity profiles along a horizontal line drawn from the edge of the edge fan bell mouth for a 2.5 x fan diameter floor height.

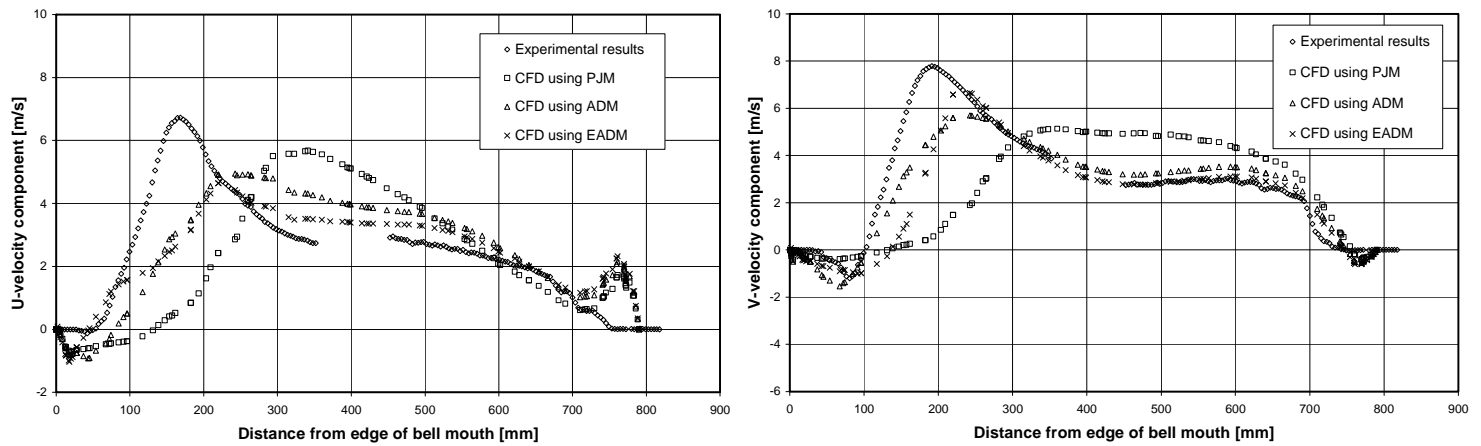


Figure G.20: Comparison of velocity profiles for N-fan at horizontal line from edge of bell mouth for 2.5 x fan diameter floor height.

Figure G.21 shows the velocity profiles along a horizontal line drawn from the edge of the plenum chamber for a 1.0 x fan diameter floor height.

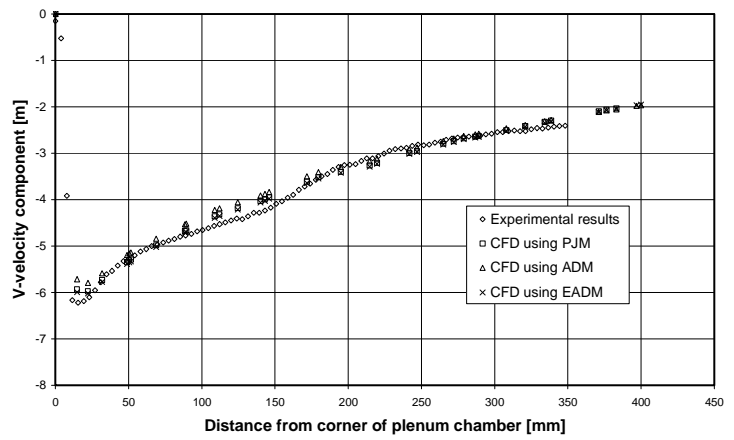
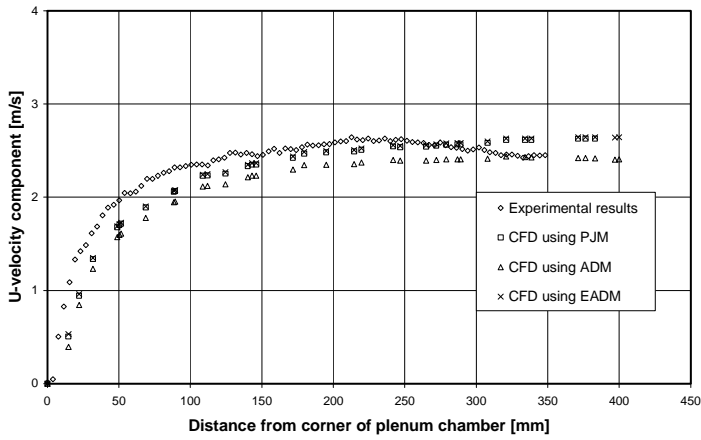


Figure G.21: Comparison of velocity profiles for N-fan at horizontal line from edge of plenum for 1.0 x fan diameter floor height.

Figure G.22 shows the velocity profiles along a vertical line drawn from the edge of the plenum chamber for a 1.0 x fan diameter floor height.

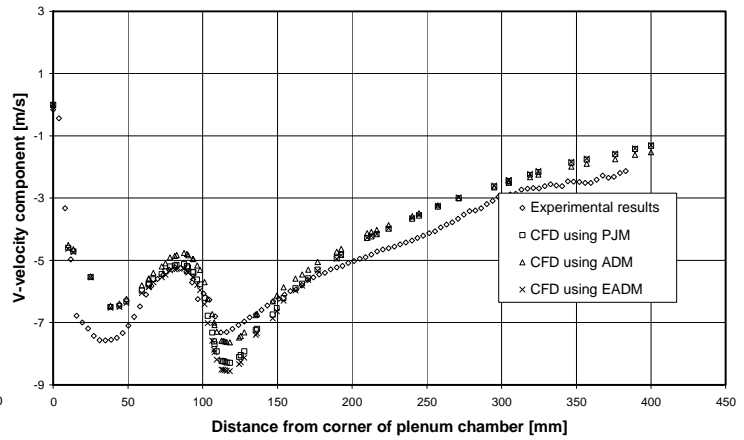
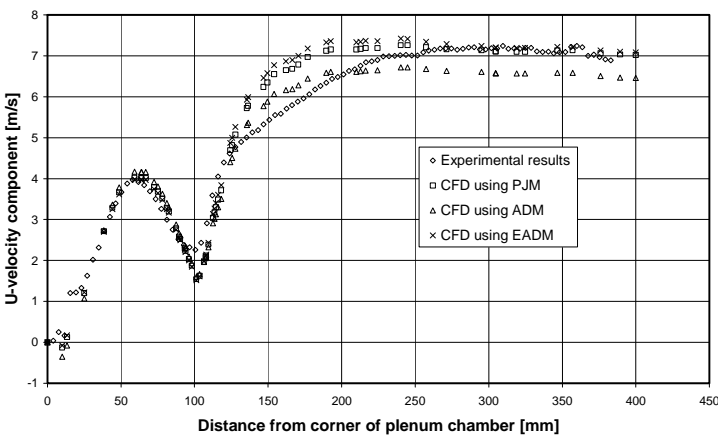


Figure G.22: Comparison of velocity profiles for N-fan at vertical line from edge of plenum for 1.0 x fan diameter floor height.

Figures G.23 shows the velocity profiles along a vertical line drawn from the edge of the edge fan bell mouth for a 1.0 x fan diameter floor height.

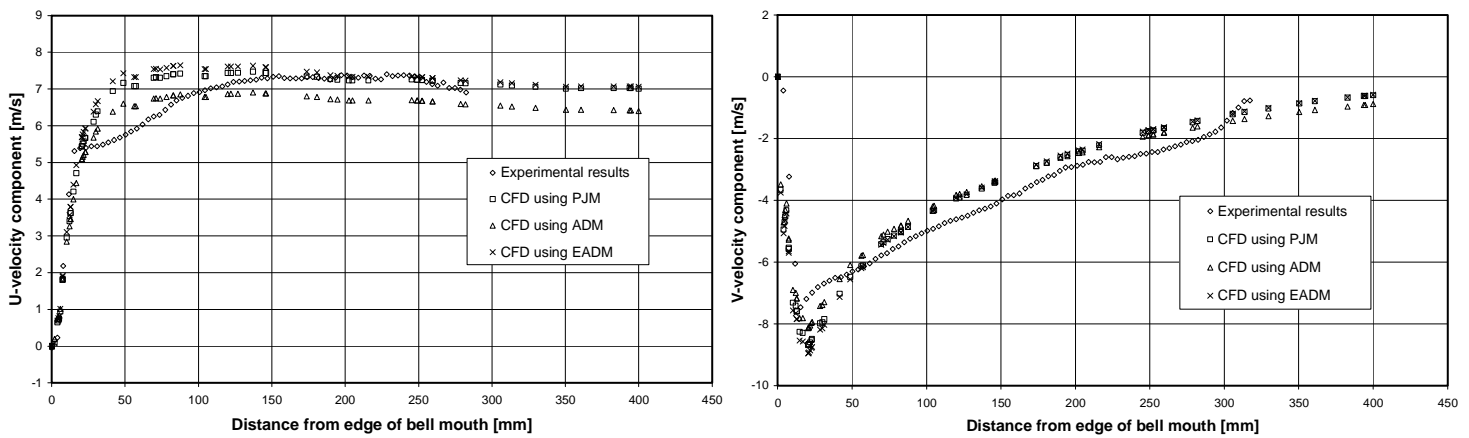


Figure G.23: Comparison of velocity profiles for N-fan at vertical line from edge of bell mouth for 1.0 x fan diameter floor height.

Figure G.24 shows the velocity profiles along a horizontal line drawn from the edge of the edge fan bell mouth for a 1.0 x fan diameter floor height.

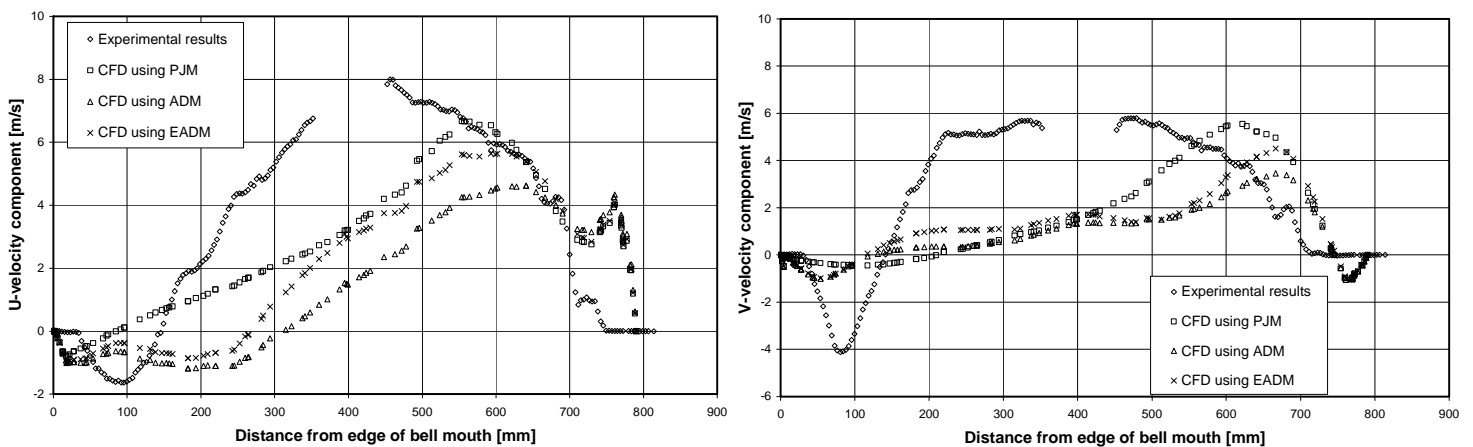


Figure G.24: Comparison of velocity profiles for N-fan at horizontal line from edge of bell mouth for 1.0 x fan diameter floor height.